HAL
open science

Transport and control of a laser-accelerated proton beam for application to radiobiology

Loann Pommarel

To cite this version:

Loann Pommarel. Transport and control of a laser-accelerated proton beam for application to radiobiology. Plasma Physics [physics.plasm-ph]. Université Paris Saclay (COmUE), 2017. English. NNT : 2017SACLX001 . tel-01509051

HAL Id: tel-01509051

https://pastel.hal.science/tel-01509051

Submitted on 15 Apr 2017

HAL is a multi-disciplinary open access archive for the deposit and dissemination of scientific research documents, whether they are published or not. The documents may come from teaching and research institutions in France or abroad, or from public or private research centers.

L'archive ouverte pluridisciplinaire **HAL**, est destinée au dépôt et à la diffusion de documents scientifiques de niveau recherche, publiés ou non, émanant des établissements d'enseignement et de recherche français ou étrangers, des laboratoires publics ou privés.

NNT : 2017SACLX001

THÈSE DE DOCTORAT
DE
L'UNIVERSITÉ PARIS-SACLAY
PRÉPARÉE À
L'ÉCOLE POLYTECHNIQUE

ÉCOLE DOCTORALE N°572 : ONDES ET MATIÈRE (EDOM)

Spécialité de doctorat : Physique des plasmas

par

M. Loann POMMAREL

Transport and control of a laser-accelerated proton beam for application to radiobiology

Thèse présentée et soutenue publiquement à Palaiseau, le 13 Janvier 2017

Composition du Jury :

M. Dimitri BATANI,	Professeur	Université de Bordeaux 1	Rapporteur
M. Marco BORGHESI,	Professeur	Queen's University of Belfast	Rapporteur
M. Tiberio CECCOTTI,	Ingénieur de Recherche	CEA Saclay	Président du jury
M. Régis FERRAND,	Ingénieur	Institut Universitaire du Cancer de Toulouse	Examinateur
M. Alessandro FLACCO,	Maître de Conférences	ENSTA ParisTech	Co-Directeur de thèse
M. Victor MALKA,	Directeur de Recherche	École polytechnique	Directeur de thèse

École polytechnique, ENSTA ParisTech, CNRS, Université Paris Saclay
Laboratoire d'Optique Appliquée (LOA)
UMR CNRS 7639, Palaiseau, France

"Life is short, and Art long; the crisis fleeting; experience perilous, and decision difficult."

Aphorisms of Hippocrates, Greek physician of the 4th century BC.

"La vie est courte, la science interminable, l'opportunité fugace, l'expérimentation faillible, le jugement difficile."

Aphorismes d'Hippocrate, médecin grec du IVe siècle av. J.-C.

"An investigator starts research in a new field with faith, a foggy idea, and a few wild experiments. Eventually the interplay of negative and positive results guides the work. By the time the research is completed, he or she knows how it should have been started and conducted."

Donald Cram, American chemist (1919 - 2001)

"Un enquêteur commence la recherche dans un domaine nouveau avec foi, une idée brumeuse, et quelques expériences sauvages. Finalement, le jeu des résultats négatifs et positifs guide le travail. Au moment où la recherche est terminée, il ou elle sait comment il aurait dû être commencé et mené."

Donald Cram, chimiste américain (1919 - 2001)

"The strongest arguments prove nothing so long as the conclusions are not verified by experience. Experimental science is the queen of sciences and the goal of all speculation."

Roger Bacon, English philosopher (1214 - 1292)

"On peut, sur les vérités de fait, se passer de la démonstration si l'on sait se servir de l'expérience."

Roger Bacon, philosophe, théologien et savant anglais (1214 - 1292)

Remerciements

Je dédie ces premières pages de ma thèse à toutes les personnes qui m'ont permis de mener à bien ce projet ambitieux. Bien que le reste du manuscrit soit écrit en anglais, je tiens à adresser mes remerciements directement dans la langue de la plupart de mes soutiens et amis. Ces trois dernières années que j'ai passées à travailler sur cette thèse ont été une aventure exaltante, édifiante et agréable, grâce aux nombreuses personnes qui m'ont soutenu. C'est pourquoi je veux remercier vivement tous ceux qui l'ont rendue possible et y ont contribué.

Je veux en premier lieu remercier mon directeur de thèse, Victor Malka, pour ses encouragements et son optimisme contagieux, ainsi que pour l'autonomie dont il m'a laissé bénéficier. Je remercie également chaleureusement mon co-encadrant Alessandro Flacco, pour m'avoir guidé tout au long de ce projet avec sa vaste expertise scientifique et sa pédagogie remarquable, ainsi que pour son aide et sa disponibilité. J'exprime ma gratitude aux rapporteurs Dimitri Batani et Marco Borghesi pour s'être intéressés à mes travaux et pour le temps qu'ils ont consacré à la lecture de ce manuscrit, ainsi que pour leurs remarques et les discussions qui en ont découlé. Je les remercie ainsi que les membres du jury Tiberio Ceccotti et Régis Ferrand, pour s'être libérés afin d'assister à ma soutenance, ainsi que pour leurs questions et remarques pertinentes à l'origine de réflexions fructueuses.

Merci à Gilles Rey pour m'avoir formé au domptage de l'installation laser SAPHIR. Un grand merci également à Benjamin Vauzour qui m'a accompagné dans cette épreuve, pour avoir démarré soigneusement le laser pendant de nombreuses matinées, pour être resté à maniper avec moi lors de longues soirées, puis pour avoir apporté son œil critique sur mes productions même après avoir quitté le laboratoire. Je remercie Olivier Delmas qui a pris la relève pour optimiser la chaîne laser avec sa main experte jour après jour au gré des aléas climatiques, mais aussi pour s'être intéressé et avoir participé aux expériences.

J'aimerais remercier les nombreuses personnes avec qui j'ai eu l'opportunité de collaborer au cours de ma thèse. Je remercie infiniment Émilie Bayart et Frédérique Mégnin-Chanet de l'Institut Gustave-Roussy pour m'avoir initié à la radiobiologie et pour nous avoir permis de réaliser ensemble les premières expériences d'irradiation de cellules sur SAPHIR, faisant entrer la thématique de la biologie au LOA. Les résultats probants sont le fruit de nombreuses heures passées à préparer, mettre en culture, puis traiter et analyser les échantillons. Merci à l'équipe italienne de l'INFN-LNS dans la communauté des accélérateurs de particules, pour m'avoir accueilli chaleureusement à Catane en Sicile et de nous avoir prêté leur système de quadripôles : Giuseppe A. Pablo Cirrone, Giacomo Cuttone, Francesco Romano, Antonio Domenico Russo, Valentina Scuderi, et tout particulièrement Francesco Schillaci qui m'a transmis ses compétences en simulation de transport de faisceaux d'ions sous les logiciels TraceWin et Simion. Merci à l'équipe du Centre de Protonthérapie d'Orsay qui nous a ouvert ses portes et nous a accordé du temps de faisceau pour que nous puissions calibrer nos instruments, notamment Farid Goudjil et Catherine Nauraye avec qui nous avons pu éclaircir de nombreux aspects ambigus dus aux différents points de vue des physiciens et cliniciens.

Merci aussi à tous ceux qui sont intervenus et à ceux qui m'ont aidé au cours des expériences sur SAPHIR. Tout d'abord Florian Mollica, co-thésard avec qui j'ai affronté les défis rencontrés sur SAPHIR, que ce soit des questions liées à la gestion des trigs ultra-rapides utilisés par les différents diagnostics, ou des problématiques faisant suite aux imprévus et pépins techniques survenus sur l'installation. Nous avons pu échanger des astuces pour surmonter ces difficultés et accomplir nos projets de recherche avec succès. Merci à Antoine Doche avec qui nous avons réalisé un essai d'irradiation de cellules avec un faisceau d'électrons en salle Jaune, mais aussi à Wan Yang, doctorant chinois qui m'a assisté pendant son séjour en France. À ce titre, je n'oublie

pas Dan Levy pour sa contribution dans les dernières expériences de radiobiologie alors que je finissais de rédiger mon manuscrit, et surtout pour sa curiosité et sa bonne humeur quotidienne, ainsi que pour ses conseils de jonglage à 4 balles !

J'exprime également ma reconnaissance envers Antoine Rousse pour m'avoir accueilli au LOA, pour son engagement à porter ce laboratoire à son statut de renommée mondiale, et pour la bonne ambiance qui y règne. Merci à tous mes collègues de bureau, post-docs, doctorants et stagiaires, avec qui j'ai partagé ces années et qui ont contribué à l'atmosphère de travail amicale et stimulante dont j'ai bénéficié : parmi les personnes avec qui j'ai eu de nombreuses discussions (scientifiques ou pas) et que je n'ai pas encore nommé, je citerai Igor Andriyash, Adrien Depresseux, Andreas Döpp, Emilien Guillaume, Gabrielle Grittani, Safir Lazar, Rémi Lehe, Francesco Massimo, Slava Smartsev. Plus généralement, je tiens à remercier tous les membres (anciens et actuels) du groupe SPL et avec qui j'ai eu la chance d'interagir : Sébastien Corde, Jean-Philippe Goddet, Guillaume Lambert, Agustin Lifschitz, Cédric Thaury.

Les travaux réalisés au LOA n'auraient pas été possibles sans les personnes ayant contribué au soutien technique. Merci à Grégory Iaquanello pour la conception assistée par ordinateur de la chicane magnétique puis du système de support des quadripôles qui furent les équipements à la base des résultats expérimentaux de ma thèse. Merci à Jean-Lou Charles, Mickaël Martinez et Bernard Allali pour toutes les pièces qu'ils ont fabriquées, ainsi que pour l'accueil cordial régnant à l'atelier de mécanique. Merci à Maxence Le Sourd pour le support informatique. Je remercie enfin fortement l'équipe administrative du LOA : Patricia Toullier, Sandrine Tricaud, Octavie Verdun, Carole Gratpanche, Lucie Huguet et Catherine Buljore, pour leur gentillesse et leur efficacité, et qui facilitent les corvées administratives liées aux commandes et aux missions.

Enseigner à l'École polytechnique pendant mon doctorat a également été une expérience enrichissante, et je remercie mes collègues chercheurs ou étudiants qui l'ont rendue plaisante, notamment Vincent Kemlin puis Lamiae Abdeladim du LOB.

Mes remerciements plus personnels vont à tous mes amis qui ont été présents pendant ces trois années et qui ont su me faire sortir la tête des protons ! Des anciens de Champo et Centrale aux confrères doctorants rencontrés à travers X'Doc, la CJC ou via les activités sur le plateau, merci pour tous ces excellents moments passés ensemble.

Je veux enfin remercier ma famille qui m'a apporté un soutien indéfectible et un intérêt prononcé envers mes travaux de recherche pourtant bien éloignés des domaines professionnels de chacun. Un merci tout particulier à mes parents envers qui je serais éternellement reconnaissant : vous avez toujours été là pour moi, vous m'avez soutenu sans faille pendant ces trois années de doctorat, et sans vous je n'aurais jamais pu réaliser tout le parcours qui m'y a mené. Merci à ma grande sœur pour ses précieux conseils. Merci encore à mes parents d'avoir préparé le pot qui a suivi ma soutenance, à Corie et Xavier d'avoir assuré la mise en place et le service, ainsi qu'à Sophie, Antoine et Faustine pour leur gentil coup de main.

Merci enfin à tous mes supporteurs qui ont osé s'aventurer à ma soutenance ce vendredi 13 !

Je terminerai sur ces mots pour exprimer et illustrer toute ma reconnaissance :

« *Ce n'est pas tant l'intervention de nos amis qui nous aide, mais le fait de savoir que nous pourrons toujours compter sur eux.*[1] »

[1] Citation d'Epicure, philosophe grec du IIIe siècle av. J.-C.

Contents

Remerciements iii

Résumé en français 1

Introduction 5

1 Physics of Laser Ion Acceleration 9
1.1 Lasers . . . 10
1.1.1 Electromagnetic wave . . . 10
1.1.2 Gaussian laser pulse . . . 11
1.1.3 Relativistic laser pulse . . . 12
1.1.4 Chirped pulse amplification . . . 13
1.2 Laser-matter interaction . . . 14
1.2.1 Plasma created by laser . . . 14
1.2.2 Laser-induced ionization . . . 14
1.2.3 Laser propagation in a plasma . . . 16
1.3 Mechanisms of electron acceleration by laser . . . 17
1.3.1 Ponderomotive force . . . 17
1.3.2 Laser absorption and energy transfer in a plasma . . . 17
1.3.3 Collisional absorption or inverse Bremsstrahlung . . . 18
1.3.4 Resonant absorption . . . 18
1.3.5 Vacuum heating or Brunel effect . . . 19
1.3.6 Relativistic j x B heating . . . 19
1.4 Laser-driven ion acceleration mechanisms . . . 20
1.4.1 Target normal sheath acceleration . . . 20
1.4.2 Acceleration from the target front side . . . 23
1.4.3 Radiation pressure acceleration . . . 25
1.4.4 Break-out afterburner . . . 27
1.4.5 Applications of laser-accelerated ion beams . . . 28
1.5 Conclusions . . . 28

2 Radiobiology basics 29
2.1 Physics of radiation interactions with matter . . . 30
2.1.1 Irradiation effects and types . . . 30
2.1.2 Passage of charged particles through matter . . . 30
2.1.3 Quantities and units . . . 33
2.2 Radiotherapy methods and techniques . . . 37
2.2.1 Mechanism of action . . . 37
2.2.2 Cellular biology techniques . . . 37
2.2.3 Fractionation and beyond . . . 41
2.2.4 Proton beam therapy . . . 41
2.3 Conclusion . . . 43

3 Proton Acceleration on SAPHIR **45**
3.1 Experimental infrastructure . . . 46
3.1.1 SAPHIR 200-terawatt laser system . . . 46
3.1.2 Laser characteristics . . . 49
3.1.3 Target irradiation conditions . . . 54
3.2 Ion diagnostics . . . 54
3.2.1 Thomson parabola spectrometer . . . 54
3.2.2 Detectors . . . 57
3.2.3 Detector stacks and filters . . . 59
3.3 Ion acceleration experiments . . . 59
3.3.1 Solid target developments . . . 61
3.3.2 Effect of the laser pulse temporal contrast . . . 62
3.3.3 Scan in focus position . . . 62
3.3.4 Ion beam energy spectrum . . . 65
3.3.5 Energy-resolved divergence of the proton beam source . . . 67
3.3.6 Front and back side acceleration relationship . . . 69
3.3.7 Spectroscopy with a synthetic diamond . . . 69
3.4 Conclusion . . . 71

4 Proton Beam Transport and Control **73**
4.1 Transverse Beam Magnetic Optics . . . 74
4.1.1 Linear beam optics . . . 74
4.1.2 Beam focusing with magnetic quadrupole . . . 75
4.2 Proton Beam Spatial and Spectral Shaping . . . 80
4.2.1 Beam transport with a magnetic chicane . . . 81
4.2.2 Beam focusing with PMQs . . . 87
4.2.3 Radiobiology transport beamline . . . 93
4.2.4 Pepperpot characterisation . . . 103
4.3 Conclusion . . . 107

5 Dosimetry **109**
5.1 Dose integrating devices . . . 110
Ionization chambers . . . 110
5.2 TIC calibration experiment at CPO in Orsay . . . 111
5.3 Simulations for absolute dose retrieval . . . 114
5.4 Irradiation conditions . . . 116
5.5 Conclusion . . . 118

6 Radiobiology Experiments on SAPHIR **119**
6.1 Cell handling : material and methods . . . 120
6.1.1 Cell lineage culture . . . 120
6.1.2 Cell irradiation . . . 120
6.1.3 Cell survival assay . . . 120
6.1.4 DNA damage foci immunofluorescent staining . . . 122
6.2 Experimental results . . . 123
6.2.1 Foci analysis . . . 124
6.2.2 Survival assay . . . 124
6.2.3 Exploratory work and outlook . . . 128
6.3 Conclusion . . . 132

Conclusion **133**

Bibliography **137**

Résumé en français

Cette thèse s'intéresse à la conception, l'implémentation et la caractérisation d'un système permettant de transporter et de mettre en forme un faisceau de protons accélérés par laser. L'objectif est de produire un faisceau dont la distribution spatiale et en énergie est utilisable pour des expériences de radiobiologie. Un point crucial est de contrôler la dose délivrée par le faisceau de protons généré par laser. Il est ainsi possible d'étudier précisément les effets du haut débit de dose associé à ce type de source de rayonnements ionisants sur des tissus vivants.

Accélération d'ions par laser

Le principe d'*accélération d'ions lors de l'interaction laser-plasma* à haute intensité représente le sujet d'étude de nombreuses recherches de par le monde, rendues possibles depuis le début de ce millénaire grâce aux progrès dans le domaine des lasers de puissance. La technologie permettant de générer des impulsions laser extrêmement intenses est basée sur la technique d'*amplification à dérive de fréquence*. Elle consiste à étirer l'impulsion laser dans le temps et l'espace grâce à une paire de réseaux optiques, qui séparent les longueurs d'ondes composant l'impulsion. L'intensité crête est donc réduite et il est alors possible d'amplifier l'impulsion de manière classique sans craindre d'occasionner de dommages sur les éléments optiques et les cristaux amplificateurs. L'impulsion ainsi amplifiée est ensuite recomprimée avec une autre paire de réseaux, arrangée de manière à inverser l'effet occasionné par la première paire. On peut ainsi obtenir des puissances laser de plusieurs centaines de TW, et des intensités du faisceau focalisé dépassant les 10^{21} W $\cdot$ cm^{-2}.

Ce faisceau laser ayant une intensité suffisamment élevée peut alors ioniser la matière et créer un *plasma*. Si la densité électronique du plasma dépasse une certaine valeur critique, le milieu est dit opaque, c'est-à-dire qu'il n'est plus transparent pour un faisceau laser à une longueur d'onde fixée.

Les ions étant des particules relativement lourdes, ils ne sont pas directement accélérés par l'onde électromagnétique aux amplitudes délivrées par les installations laser actuelles. Le transfert d'énergie se fait par l'intermédiaire des électrons qui gagnent de l'énergie cinétique, car étant près de 2000 fois plus légers que les protons, ils sont plus affectés par la force de Lorentz. Différents mécanismes d'accélération des ions par laser se produisent selon les paramètres expérimentaux relatifs au laser et à la cible utilisée. Les caractéristiques du faisceau d'ions émis sont spécifiques à chaque mécanisme, et le plus éprouvé est appelé le *Target Normal Sheath Acceleration* (TNSA) dont le principe d'action est le suivant.

Les électrons, chauffés par le laser, traversent la cible et commencent à se détendre dans le vide, aussi bien en face avant qu'en face arrière de la cible, ionisant les atomes à sa surface. L'inertie élevée des ions ainsi créés laisse le temps aux électrons d'établir un champ électrostatique ambipolaire. Ce champ résultant de la différence de charge d'espace est très fort, de l'ordre du TV/m. C'est lui qui est responsable de l'accélération des ions à des énergies de l'ordre de la dizaine de MeV. Le faisceau d'ions émis dans le régime du TNSA a la particularité d'avoir un spectre thermique suivant une distribution exponentielle décroissante avec une énergie maximale de coupure. Le faisceau possède également une forte divergence angulaire qui diminue néanmoins avec l'énergie.

Dans des conditions de haut contraste temporel de l'impulsion laser, le TNSA est un mécanisme d'accélération symétrique. Avec un contraste moins bon, un flux et des énergies de particules plus importants sont obtenus du côté non illuminé de la cible. D'autres mécanismes d'accélération sont à l'étude ainsi que des géométries de cibles particulières et ils permettraient d'obtenir des énergies d'ions plus élevées, des spectres quasi-monoénergétiques, ou encore des faisceaux mieux collimatés.

Sur l'*installation SAPHIR* du Laboratoire d'Optique Appliquée à Palaiseau, l'accélération de faisceaux de protons avec une énergie maximale dépassant 7 MeV a été obtenue en focalisant des impulsions laser d'une durée de 25 fs pour une énergie de 3 J sur des cibles en titane de 5 µm d'épaisseur où l'intensité pic était de $4 \times 10^{19}\,\mathrm{W \cdot cm^{-2}}$. La distribution en énergie des faisceaux d'ions générés est mesurée avec un spectromètre de masse résolue en énergie (Thomson Parabola) aligné sur l'axe perpendiculaire à la cible. Leur distribution spatiale est déterminée à l'aide d'empilements de films radiochromiques placés quelques centimètres derrière la source.

Mise en forme spatiale et spectral de faisceaux de protons

Une ligne de transport de faisceaux de protons a été développée à partir d'un système magnétique constitué de quatre *aimants permanents quadripolaires* (PMQs). Chacun des PMQs a l'effet d'une lentille cylindrique sur un faisceau de particules chargées, qu'il focalise dans une direction transverse et défocalise dans la direction transverse perpendiculaire.

Des simulations numériques de transport de faisceaux ont permis d'optimiser ce système pour plusieurs objectifs. D'une part, la possibilité de *focaliser* une composante en énergie du faisceau de protons a été démontrée. Une taille millimétrique a ainsi été atteinte expérimentalement pour des protons de 8.6 MeV à 44 cm de la source. Ce procédé ouvre la voie au filtrage en énergie du faisceau, en plaçant une ouverture dans le plan de focalisation et en exploitant les propriétés chromatiques des PMQs (des protons d'énergies différentes ne sont pas focalisés dans le même plan).

D'autre part, le système de transport a été optimisé pour délivrer dans l'air à 1 m de la cible un faisceau de protons adapté à l'irradiation d'échantillons biologiques minces. Le faisceau, extrait de la chambre d'interaction sous vide, possède un spectre en énergie présentant un pic à 1.5 MeV et sa distribution spatiale a été mise en forme afin de fournir une grande surface d'irradiation uniforme.

De plus, les prédictions de profils du faisceau le long de la ligne de transport, obtenues grâce aux simulations informatiques, sont en accord avec les observations expérimentales.

Dosimétrie

Pour étudier les effets du dépôt de dose par les faisceaux de protons sur des échantillons biologiques, il est crucial de connaître avec précision la dose absorbée par ceux-ci. C'est pourquoi une procédure rigoureuse a été établie afin de déterminer la dose délivrée lors de chaque tir laser.

Pour cela, une *chambre d'ionisation à transmission* a été calibrée sur l'accélérateur cyclotron à usage médical du centre de protonthérapie d'Orsay de l'Institut Curie. Cette chambre d'ionisation a ensuite été installée sur le trajet du faisceau de protons dans SAPHIR, pour un contrôle en temps réel des fluctuations tir à tir. Des *simulations Monte Carlo*, réalisées sous la plateforme logicielle Geant4, ont ensuite permis de relier les valeurs de charge mesurées par la chambre à des valeurs de dose déposée dans les échantillons.

Sur une surface de 1.5 cm^2, une dose moyenne de 1.1 Gy par tir est délivrée dans la couche monocellulaire, avec un écart type de 22 % lié à l'inhomogénéité spatiale.

Radiobiologie

Lorsqu'un *rayonnement ionisant*, tel qu'un faisceau de protons énergétiques, traverse la matière, il interagit avec elle en y déposant de l'énergie. Des atomes peuvent ainsi être excités et ionisés, perturbant la structure moléculaire du milieu et causant d'importants dommages chimiques et biologiques dans des tissus vivants.

La *protonthérapie* consiste à détruire une tumeur cancéreuse en l'irradiant avec un faisceau de protons. Cette technique de radiothérapie représente un intérêt par rapport aux traitements par électrons ou photons en raison de sa capacité à cibler précisément une tumeur à irradier en surface ou en profondeur dans le corps, tout en minimisant les dommages occasionnés aux tissus biologiques environnants. La courbe de dépôt d'énergie des protons présente en effet un maximum situé juste avant qu'ils ne s'arrêtent, spécificité appelée le *pic de Bragg*, contrairement à d'autres rayonnements ionisant (électrons ou photons) caractérisés par une décroissance monotone avec la profondeur de pénétration. Les protons sont donc préférentiellement utilisés pour traiter certains types de tumeurs où il est important de préserver les tissus alentours sains et radiosensibles. Ceci est particulièrement important pour les tumeurs situées près du cerveau, de l'œil, de la moelle épinière, ou encore en pédiatrie quand les effets secondaires à long, terme tels que le déclenchement de tumeurs radio-induite provoquées par la dose totale de radiation dans le corps, sont problématiques.

Les conséquences de l'irradiation de cellules vivantes in vitro ont été étudiées sur des monocouches de cellules avec deux méthodes utilisées en biologie cellulaire. La première est la mise en évidence des dommages provoqués sur l'ADN (cassures double brin) par des marqueurs moléculaires via la technique d'immunofluorescence. La seconde est la mesure de la survie cellulaire des échantillons suite à leur irradiation par différents niveaux de dose. Plusieurs lignées de cellules cancéreuses humaines ont été examinées, à savoir des cellules du cancer du côlon (HCT116 sauvage et p53 muté) ainsi que des glioblastomes (tumeurs du cerveau, SF763 et U87MG).

Conformément aux attentes, le nombre de dommages augmente et le taux de survie diminue plus la dose appliquée est élevée, et des variations quantitatives différencient le comportement des différentes lignées. Les effets des hauts débits de dose fournis par les faisceaux de protons pulsés générés par laser sur SAPHIR ($> 10^8\,\mathrm{Gy} \cdot \mathrm{s}^{-1}$) ont été comparés aux résultats obtenus avec des sources de rayonnements ionisant conventionnels (rayons X ou proton) à des débits de l'ordre de quelques $\mathrm{Gy} \cdot \mathrm{min}^{-1}$. Aucune différence significative n'a été observée, mais des expériences préliminaires visant à analyser l'impact de la cadence à laquelle les tirs multiples sont délivrés sur un même échantillon semblent manifester une tendance inattendue. S'il est confirmé, cet effet prometteur révélera un atout significatif pour l'utilisation d'ions accélérés par laser en médecine pour la définition de protocoles cliniques plus efficaces.

Introduction

Context

Cancer is a public health issue and is the second cause of death in the world. The trends are rising and in 2012 it was responsible for the death of 8 million people worldwide and 14 million new cases were diagnosed[2] including 355 thousands in France[3]. Radiation therapy, along with surgery and chemotherapy, is one of the cancer treatment pillars. Despite side effects caused by temporary DNA damage to nearby healthy tissues, radiotherapy can be a highly effective treatment for cancer, and it is involved in the treatment plan of 40 % of successfully cured cancers. Today, external radiotherapy relies mainly on linear electron accelerators, and a few hadrontherapy facilities based on the cyclotrons and synchrotrons technologies.

The main challenge of the last decades in radiotherapy has been to achieve maximal local dose deposition in tumours while causing minimal damage to the surrounding normal tissues. An increased selectivity reduces long-term secondary cancers due to induced mutations in the exposed cells. Protontherapy is offering a particularly suitable solution as protons have ballistic qualities (energy deposition at a depth in tissues, small lateral scattering) allowing a more accurate dose delivery compared to other ionizing radiations such as electrons or x-rays.

Proton beams have been used to treat 16 200 patients worldwide in 2015, and more than 130 000 since its first clinical application at Berkeley Radiation Laboratory in 1954. Its popularity has surged in recent years with now more than 50 facilities in clinical operation around the world, as it has proven to be a successful clinical approach leading to excellent results in several indicated cases.

However, the current installations are based on *conventional accelerators* such as cyclotrons or synchrocyclotrons, which are expensive, large and massive, limiting the availability of hadrontherapy treatments to patients. Progress has been made nonetheless in the conventional accelerator technology, and commercial devices (e.g. the Proteus®ONE S2C2 cyclotron sold by *IBA*) can deliver protons at an energy of 230 MeV with an average current of 135 nA while weighing less than 50 t and measuring less than 2.5 m in diameter. However, electromagnets and gantries used to transport the beam are very heavy and imposing (see Figure 2). Moreover, *radioprotection* demands massive protective walls (with a thickness in the order of meters) surrounding the entire ion beamline.

The SAPHIR project, within which this PhD work falls, aims at determining the technical, scientific and economical viability of laser-driven protontherapy, as an alternative to the classical particle acceleration techniques used for curing cancers. Laser baser ion sources would represent an advance in terms of cost and size, able to be installed directly in hospitals, thus making this treatment more accessible. Besides, laser beam transport does not require more than light shielding for eye and skin safety, limiting the radiation protection barriers required. This project

[2]Source: http://globocan.iarc.fr/Pages/fact_sheets_cancer.aspx

[3]http://www.e-cancer.fr/Professionnels-de-sante/Les-chiffres-du-cancer-en-France/Epidemiologie-des-cancers

FIGURE 1: Sketch of a conventional protontherapy facility.

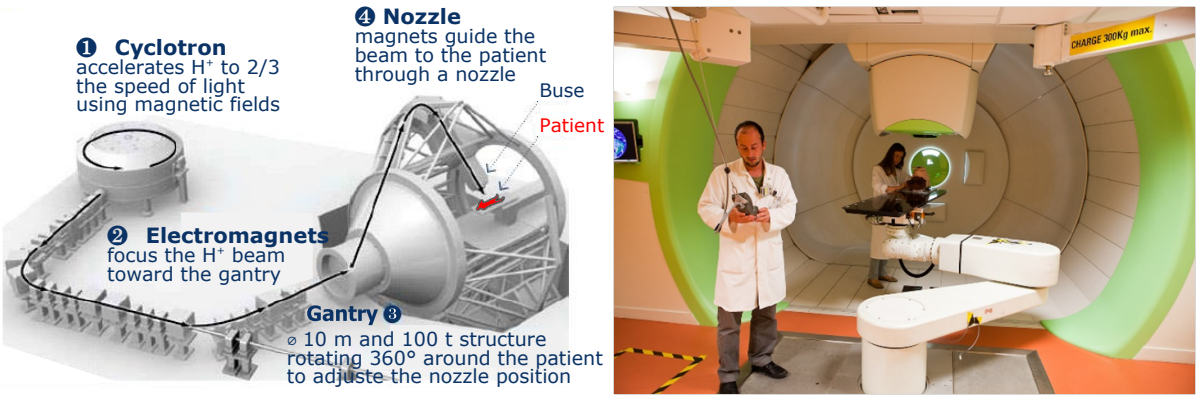

FIGURE 2: Diagram of a protontherapy facility, with the proton beam path from its production in the accelerator to the isocentric gantry (left [a]). Picture of a treatment room located inside the gantry with a mobile proton beam nozzle to choose its orientation, and a robotic arm to place the patient (right [b]).

[a] from http://itn-argent.eu/node/55
[b] from http://www.israelprotontherapy.com/about-proton-therapy.html

is the result of a wide collaboration between 5 laboratories and French institutions (LOA, CPO of Institut Curie, Institut Gustave Roussy, LIRM team of CEA DAM, and LIdyl IRAMIS team of CEA Saclay) and 4 industrial partners (Amplitude Technologies, Imagine Optic, Dosisoft and Propulse SAS) are involved in SAPHIR. This interdisciplinary project connects physics, biology, oncology, and is largely devoted to technology transfer from basic research to industry. The experimental system is installed at LOA in Palaiseau, where radiobiological experiments using laser-accelerated protons have been carried out, and whose implementation and results represent the content of this thesis.

Laser acceleration of ions is a young field in rapid development that could represent an alternative to the conventional accelerators for hadron cancer radiotherapy [Malka et al., (2004); Murakami et al., (2008); Ledingham et al., (2014)]. Ambitious prospects of compact gantry designs for ion beam therapy with laser accelerated protons were already proposed [Burris-Mog et al., (2011); Masood et al., (2014)] (see Figure 3). The beam energy and spatial distribution demands specific *laser-driven ion beam manipulation* methods, and several research teams worldwide have been developing systems for *cell irradiation studies*.

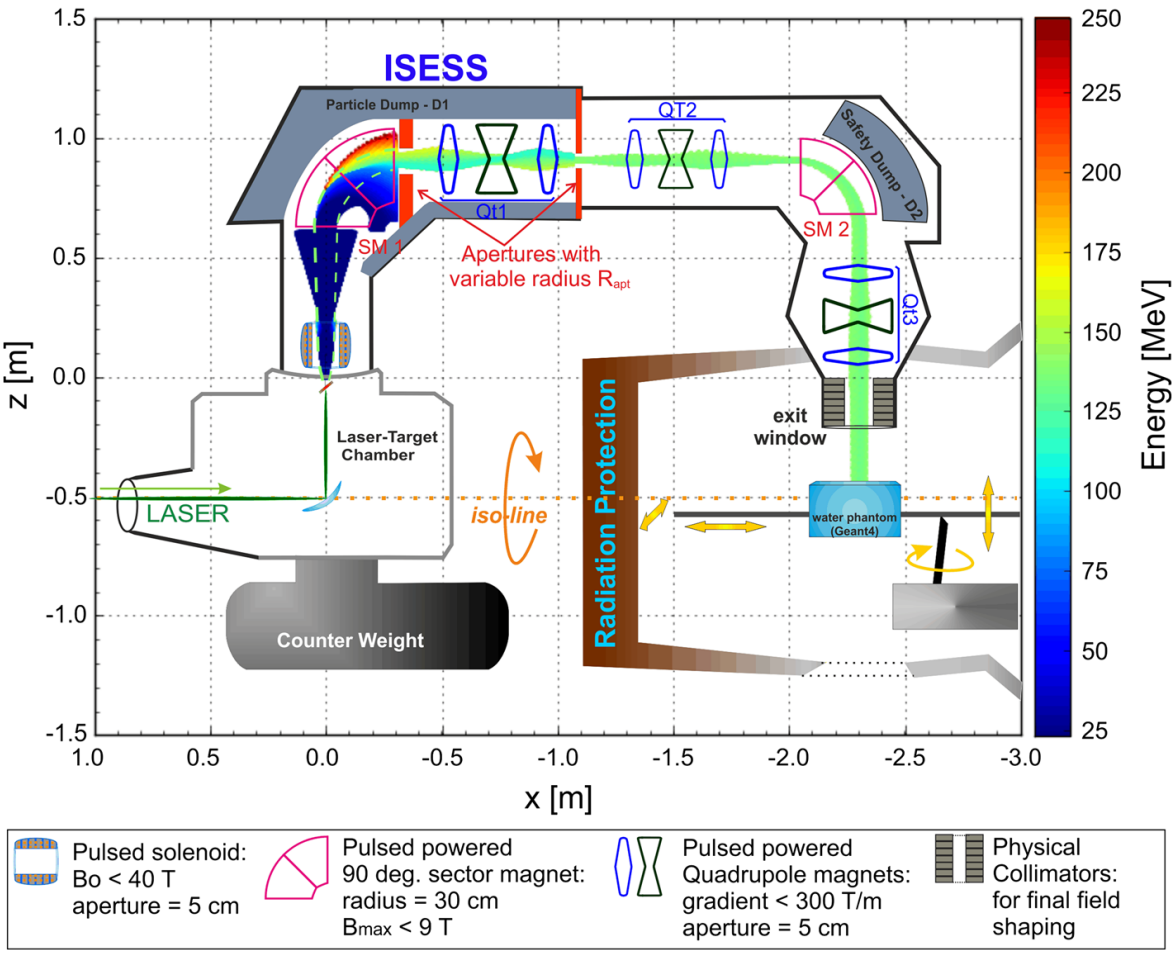

FIGURE 3: Schematic representation of 360° isocentric gantry concept for particle therapy with laser-plasma accelerators based on pulsed steering, focusing and spectral manipulation. (Reproduced from [Masood et al., (2014)])

Some used *dipole magnets* and their bending effect to make sure the electrons and x-rays that are generated simultaneously with the protons in the laser-induced plasma were removed and to perform energy filtering on the proton beam [Yogo et al., (2009); Kraft et al., (2010)]. Others transported the beam with *permanent magnet quadrupoles* [Bin et al., (2012)]. However the irradiation area provided by these systems remained small, making possible the demonstration of in vitro biological damage induction to the DNA of tumour cells by laser-accelerated proton beams, and sometimes the comparison of survival fractions with the results of irradiation using conventionally accelerated proton beams. A *pulsed solenoid* combined with a *dipole chicane* was realised as an energy-dependent beam collimation device allowing for the active shaping of the proton energy spectral intensity to perform in vivo volumetric irradiation [Zeil et al., (2012)].

Even if the ion beams generated by lasers are not readily suitable for patient treatment, their pulsed nature and the extremely high dose rate they provide motivate radiobiology studies to investigate the dose rate effects in comparison to continuous sources. Moreover, beam shaping systems have to be designed to better suit the needs of such experiments.

Objective and outline of this thesis

In this context, the objective of this thesis is the implementation of a beam transport and shaping system for a laser-ion accelerator to obtain a beam with configurable spatial and spectral distributions. A crucial issue is to develop a method for output dose monitoring, to be able to study precisely the experimental effects of such radiations on living cells. On the whole, the manuscript is organised as follows.

- Chapter 1 introduces the main theoretical concepts that underpin ion acceleration by super-intense laser-plasma interaction. The most relevant laser energy absorption mechanisms and ion acceleration regimes are mentioned.
- Chapter 2 presents some radiobiology concepts useful to understand the interaction of ionizing radiations, such as energetic protons, on living tissues. The effects they may cause and common methods used to quantify the induced damages are outlined. Reasons for employing protons in the medical field are also explained.
- Chapter 3 focuses on the SAPHIR facility, the diagnostics used and the results of the ion acceleration experiments there performed.
- Chapter 4 is dedicated to beam transport and shaping techniques. It starts with some beam optics concepts. Then, the magnetic systems that have been used experimentally to setup a proton beamline are detailed along with their characterisation in terms of resulting density profile and energy distribution.
- Chapter 5 proposes an dosimetry approach to rigorously control and retrieve the dose deposited by the laser-accelerated proton beam in a biological sample located at the beamline output. It relies on the absolute calibration of an ionisation chamber associated to Monte-Carlo simulations that are both delineated.
- Chapter 6 finally reveals the outcome of the cell irradiation experiments pursued in SAPHIR. The quantification of DNA damages following sample irradiation are presented, as well as dose-dependent cell survival curves.

Chapter 1

Physics of Laser Ion Acceleration

As explained in the introduction, the goal of this thesis is the production of proton beams by laser, their characterisation and shaping to make them relevant for radiobiological studies. The aim of this first chapter is to describe succinctly the processes occurring when a multi TW laser beam is focalised on a thin target to accelerate energetic ions. This chapter is therefore intended to set the fundamental bases for understanding relativistic laser-matter interactions. The main absorption mechanisms responsible for the energy transfer from a laser pulse to plasma particles are described, with the parameters needed for them to take place. Furthermore, several ion acceleration models are presented, along with the experimental conditions required to observe each of them. Finally, some ion beam applications are mentioned.

Contents

1.1 Lasers **10**
1.1.1 Electromagnetic wave 10
1.1.2 Gaussian laser pulse 11
1.1.3 Relativistic laser pulse 12
1.1.4 Chirped pulse amplification 13
1.2 Laser-matter interaction **14**
1.2.1 Plasma created by laser 14
1.2.2 Laser-induced ionization 14
1.2.3 Laser propagation in a plasma 16
1.3 Mechanisms of electron acceleration by laser **17**
1.3.1 Ponderomotive force 17
1.3.2 Laser absorption and energy transfer in a plasma 17
1.3.3 Collisional absorption or inverse Bremsstrahlung 18
1.3.4 Resonant absorption 18
1.3.5 Vacuum heating or Brunel effect 19
1.3.6 Relativistic j x B heating 19
1.4 Laser-driven ion acceleration mechanisms **20**
1.4.1 Target normal sheath acceleration 20
TNSA features and developments 22
1.4.2 Acceleration from the target front side 23
1.4.3 Radiation pressure acceleration 25
1.4.4 Break-out afterburner 27
1.4.5 Applications of laser-accelerated ion beams 28
1.5 Conclusions **28**

1.1 Lasers

The history of the **laser** (*Light Amplification by Stimulated Emission of Radiation*) began in 1916 with Albert Einstein setting the theoretical foundations for the processes involved in laser operation, defining the probability coefficients for *absorption*, *spontaneous emission*, and *stimulated emission* of electromagnetic radiation [Einstein, (1916)]. The first optical laser was built more than 40 years later in 1960 by Theodore Maiman, based on a synthetic ruby crystal [Maiman, (1960)]. Since then, many others lasers have been developed each year. Current research is dedicated to the development of solid state lasers (diode lasers, crystal or amorphous solids doped with active ions, optic fiber lasers) with the aim of obtaining shorter pulses (the present record is 67 as [Zhao et al., (2012)]) and greater powers.

Every *laser oscillator* is constructed from three main components. A *pump source* that provides energy to the laser system. An *amplifying or gain medium*, which can be solid, liquid or gaseous. It is excited by the pump source to produce a population inversion and lead to optical gain and amplification of the light wave through stimulated emission. The last element is an *optical cavity or resonator* that provides light feedback. In its simplest form, it consists in two parallel mirrors placed around the gain medium, with one of them called the *output coupler* that is a partial reflector to allow some of the light to leave the cavity and produce the laser's output beam to be used.

1.1.1 Electromagnetic wave

A laser is a device emitting coherent light through a process of optical amplification based on the stimulated emission of electromagnetic radiation. Thus, the waves forming the beam obey **Maxwell's equations**:

$$\nabla \cdot \mathcal{E} = \frac{\rho_0}{\varepsilon_0}, \qquad \text{Coulomb's law} \tag{1.1a}$$

$$\nabla \cdot \mathcal{B} = 0, \qquad \text{Gauss's law} \tag{1.1b}$$

$$\nabla \times \mathcal{E} = -\frac{\partial \mathcal{B}}{\partial t}, \qquad \text{Faraday's law} \tag{1.1c}$$

$$\nabla \times \mathcal{B} = \mu_0 \left(\mathbf{J} + \varepsilon_0 \frac{\partial \mathcal{E}}{\partial t} \right). \qquad \text{Ampère's law} \tag{1.1d}$$

where $(\mathcal{E}(\mathbf{r}, t), \mathcal{B}(\mathbf{r}, t))$ are the space and time dependent electric and magnetic fields respectively, ρ_0 and $\mathbf{J}(\mathbf{r}, t)$ are the total electric charge and current densities, and ε_0 and μ_0 are the permittivity and permeability of free space. The wave equations are derived from Faraday's and Ampère's law by applying the curl operator $\nabla\times$ and following the vector identity $\nabla \times (\nabla \times \mathbf{X}) = \nabla(\nabla \cdot \mathbf{X}) - \nabla^2\mathbf{X}$, making used of $\varepsilon_0\mu_0c^2 = 1$ with c the speed of light in vacuum:

$$\nabla^2\mathcal{E} - \frac{1}{c^2}\frac{\partial^2\mathcal{E}}{\partial t^2} = \mu_0\frac{\partial \mathbf{J}}{\partial t} + \nabla(\nabla \cdot \mathcal{E}), \tag{1.2a}$$

$$\nabla^2\mathcal{B} - \frac{1}{c^2}\frac{\partial^2\mathcal{B}}{\partial t^2} = -\mu_0\nabla \times \mathbf{J}. \tag{1.2b}$$

In a cold plasma, the quasineutrality assumption gives us $\rho_0 = e(Zn_i - n_e)$ with n_i and n_e being the ion and electron densities respectively, and $\mathbf{J} = -\rho_0\mathbf{v}$ with $\mathbf{v}$ the mean electron velocity. These two equations can be solved analytically to describe the behaviour of a laser field.

1.1.2 Gaussian laser pulse

Useful parameters can be calculated considering beams with a *temporal and spatial Gaussian profile*. Thus, some of their features are described in this section even though the real laser pulses differ slightly from this framework. The mathematical expression for the electric field amplitude of a Gaussian beam is a solution to the paraxial Helmholtz equation [Svelto, (2010)]. Assuming polarisation in the $\hat{\mathbf{x}}$ direction and propagation in the $+z$ direction ($\mathbf{k}.(x,y,z) = kz$ with the wavenumber $k = 2\pi/\lambda = \omega/c$), the electric field in phasor (complex phase vector) notation is given by:

$$\boldsymbol{\mathcal{E}}(r,z,t) = \mathcal{E}_0\,\hat{\mathbf{x}}\,\frac{w_0}{w(z)}\exp\left[\frac{-r^2}{w(z)^2}\right]\exp\left[-2\ln(2)\left(\frac{z-ct}{c\,\tau_0}\right)^2\right]e^{i(kz-\omega t)} \tag{1.3}$$

where the FWHM (Full Width at Half Maximum) temporal and spatial dependencies are set by the duration of the intensity envelope τ_0, and the radius $w(z)$ at which the intensity amplitude falls to $1/e^2$ of its axial value. The intensity envelope follows:

$$I(r,z,t) = I_0\,\exp\left[\frac{-2\,r^2}{w(z)^2}\right]\exp\left[-4\ln(2)\left(\frac{z-ct}{c\,\tau_0}\right)^2\right], \tag{1.4}$$

where the peak intensity is $I_0 = (c\varepsilon_0\mathcal{E}_0^2)/2$, and its dependence on the total energy contained in the pulse E_L can be determined by integrating $I(r)$ in polar coordinate over $rdrd\theta$:

$$I_0 = \frac{4\sqrt{\ln(2)}}{\pi^{3/2}}\,\frac{E_L}{\tau_0 w^2} \tag{1.5a}$$

$$\approx 0.6\,\frac{E_L}{\tau_0 w^2}. \tag{1.5b}$$

If we treat light propagation by approximating the distances at the second order (Fresnel integrals), a field amplitude with a Gaussian envelope is found to be an eigenstate (transverse electromagnetic mode (TEM) involving Hermite polynomial multiplied by a Gaussian function) so that the Gaussian envelope evolves keeping its formal structure. The TEM00 mode with the best quality and obtained from a confocal cavity has a pure transverse Gaussian profile. The optics of Gaussian beams is essential in laser optics as it defines the way energy evolves in space, and also determines boundaries and asymptotic behaviours. In the ideal case described here, the amplitude envelope radius $w(z)$ and the phase front radius of curvature $R(z)$ are simply described as a function of the propagation distance z:

$$w(z) = w_0\sqrt{1+\left(\frac{z}{z_\mathrm{R}}\right)^2}, \tag{1.6}$$

$$R(z) = z\left[1+\left(\frac{z_\mathrm{R}}{z}\right)^2\right], \tag{1.7}$$

where w_0 is the *beam waist size* and

$$z_\mathrm{R} = \frac{\pi w_0^2}{\lambda} \tag{1.8}$$

the *Rayleigh range* (see Figure 1.1). The waist formed by a lens of focal length f focusing a beam of diameter $2w$ is found by setting $z = f$ in (1.6), and if we are in the approximation that $w \gg w_0$,

it leads to:

$$w_0 \approx \frac{\lambda f}{\pi w}. \tag{1.9}$$

Inserting the longitudinal coordinate dependent waist (1.6) into (1.5) gives the peak intensity dependence on the distance from the focal plane:

$$I(z) = I_0 \cdot \left[1 + \left(\frac{z}{z_R}\right)^2\right]^{-1/2}. \tag{1.10}$$

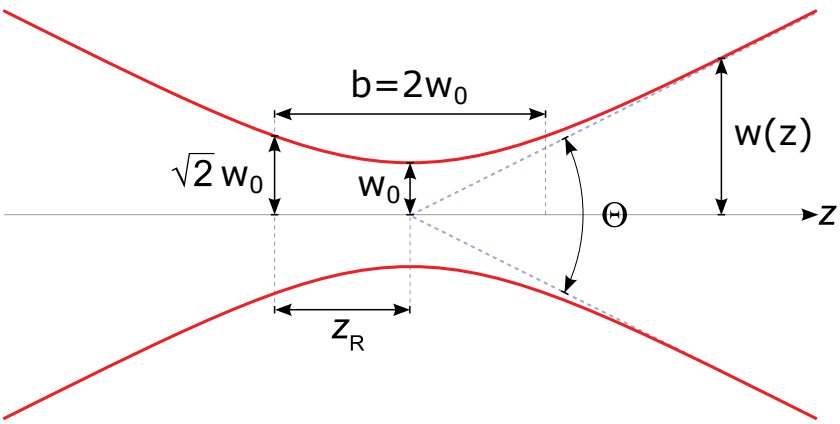

FIGURE 1.1: Gaussian beam width $w(z)$ as a function of the distance z along the beam. w_0: beam waist, b: depth of focus, z_R: Rayleigh range, Θ: total angular spread.

1.1.3 Relativistic laser pulse

A laser pulse is said to be of relativistic intensity if the electromagnetic wave is so intense that the electron kinetic energy W, in the quivering motion due to the electric field oscillation, is relativistic. Normalizing with respect to mc the electron momentum in the wave vector potential A (with $\boldsymbol{\mathcal{E}} = -\partial_t \mathbf{A} = -i\omega\mathbf{A}$ in complex notation), we obtain the dimensionless laser parameter or *normalized electric field amplitude*:

$$a_0 = \frac{eA}{m_e c} = \frac{e}{m_e c}\frac{E}{\omega_L} = \sqrt{\frac{2\, e^2\, \lambda_L^2\, I}{\pi\, m_e^2\, c^5}} \tag{1.11a}$$

$$\approx 0.855 \times 10^{-9}\, (I[W/cm^2])^{1/2}\, \lambda_L[\mu m] \tag{1.11b}$$

The wave is said to be **relativistic** for $a_0 > 1$. The total relativistic energy is:

$$< E_R > = \sqrt{p^2c^2 + m_e^2c^4} = \gamma\, m_e c^2 = < W > + m_e c^2, \tag{1.12}$$

where $\gamma = \sqrt{1 + \frac{a_0^2}{2}}$ is the *cycle-averaged relativistic Lorentz factor* and the average momentum for a linearly polarised wave is given by:

$$< p > = \frac{eA}{\sqrt{2}}, \tag{1.13}$$

so the average electron kinetic energy in the oscillation is:

$$< W > = < E_R > - m_e c^2 = (\gamma - 1)\, m_e c^2 = \left(\sqrt{1 + \frac{1}{2}\left(\frac{eA}{m_e c}\right)^2} - 1 \right) m_e c^2. \tag{1.14}$$

1.1.4 Chirped pulse amplification

In the two decades following the invention of the first laser, pulse intensities reached a level of $10^{15}\,\mathrm{W \cdot cm^{-2}}$ through Q-switching and then mode-locking techniques. Limitations on the peak intensity in high-power short-pulse laser systems arose from nonlinear pulse distortions and damages in the optical components through which pulses propagated, so it was necessary to increase the beam diameter to be able to work at higher laser intensities. A solution to this problem was found with the adaptation in 1985 by G. Mourou and D. Strickland [Strickland and Mourou, (1985)] of the **chirped pulse amplification** (CPA) method that was originally developed in the context of radar technology. Besides being spread out spatially on a larger surface, CPA stretches the pulse frequency components in time with a pair of gratings. The latter are arranged so that the low-frequency components of the laser pulse travel a shorter path than the high-frequency components, thus becoming positively chirped, with a longer pulse duration than the original by three to five orders of magnitude, typically ~100 ps out of a fs seed pulse. This lower peak intensity pulse of the same energy can then safely pass through the gain medium and be amplified conventionally to a high energy by a factor 10^6 or more, as the fluence on the optics is below their damage threshold. Afterwards, the pulse is recompressed by another grating pair, introducing this time negative group-velocity dispersion, as a very short pulse of high peak power (see diagram in Figure 1.2). CPA also makes it possible to miniaturize laser systems and build table-top compact high-power lasers capable of generating beams exceeding hundreds of TW and focused laser intensities above $10^{21}\,\mathrm{W \cdot cm^{-2}}$.

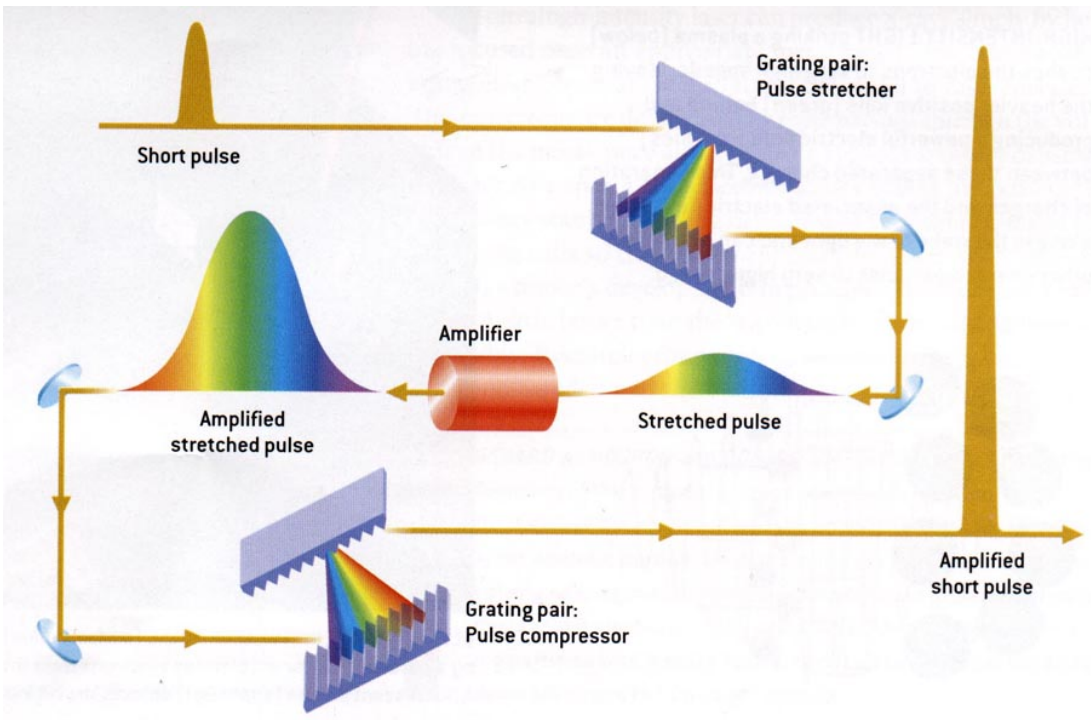

FIGURE 1.2: Schematic of the chirped pulse amplification technique.

1.2 Laser-matter interaction

When interacting with matter, high power laser beams enable to transform it into a plasma, a medium with particular properties that I am going to describe now.

1.2.1 Plasma created by laser

The **plasma** is a state of matter where components are no more neutral. It consists of an ionized gas with free charged particles, electrons and ions, in a fraction significant enough so that the system presents a collective behaviour due to electromagnetic interactions. A plasma can be created by exposing a gas to a strong electromagnetic field, applied for instance with a microwave generator or a laser. Matter is heated to a point where its internal energy is greater than its ionization potential, resulting in the loss of electrons by the atoms during collisions.

In a cold plasma, where the ions are at rest and the thermal motion of electrons is ignored ($T_e = 0$), the charge density of the specie α (here the electron, $q_e = -1$) with charge q_α, density n_α and mass m_α, oscillates at the **plasma frequency**:

$$\omega_{\mathrm{p}\alpha} = \sqrt{\frac{n_\alpha\, q_\alpha^2}{m_\alpha\, \varepsilon_0}}. \tag{1.15}$$

This fundamental parameter set the timescale at which the α-plasma will react to an external perturbation, and restore neutrality following a charge separation. In a plasma, electric fields are screened out by a redistribution of the mobile charge carriers. The charge distribution surrounding each individual charge balances its electrostatic potential, reducing the effective range of the Coulomb interaction. The distance over which the newly created electric field drops by a factor of $1/e$ is defined by the **Debye length** [Chen, (1984)]:

$$\lambda_{\mathrm{D}} = \sqrt{\frac{\varepsilon_0\, k_{\mathrm{B}}\, T_\alpha}{n_\alpha\, q_\alpha^2}}. \tag{1.16}$$

This length is independent of the mass, thus it is usually comparable for different species. The considered system has to have a length scale much bigger than λ_{D} for boundary effects to be neglected. In this ideal case, the plasma is described at thermal equilibrium by the **quasineutrality** condition $n_e = Zn_i$.

1.2.2 Laser-induced ionization

The threshold intensity at which a target starts to ionize is meaningful, especially with respect to the laser contrast that greatly influences the ion acceleration process. To estimate the threshold laser intensities, one can calculate the energy that electrons require to be free from their atomic orbits. The **ionization energy** for a hydrogen atom in its ground state is given in the Bohr model by the *Rydberg energy*:

$$R_{\mathrm{B}} = \frac{m_{\mathrm{e}}(k_{\mathrm{e}}e^2)^2}{2\hbar^2} = \frac{k_{\mathrm{e}}e^2}{2r_{\mathrm{B}}} \approx 13.6\,\mathrm{eV}, \tag{1.17}$$

where the *Bohr radius* is:

$$r_{\mathrm{B}} = \frac{\hbar^2}{k_{\mathrm{e}}m_{\mathrm{e}}e^2} \approx 5.29 \times 10^{-11}\,\mathrm{m}. \tag{1.18}$$

The *binding electric field* given by [Gibbon, (2005)] is:

$$E_b = \frac{k_e e}{r_B^2} \approx 5.1 \times 10^9\,\mathrm{V \cdot cm^{-1}} \tag{1.19}$$

Laser-induced ionization generally happens by **multi-photon ionization** at moderate intensities, above $10^{10}\,\mathrm{W \cdot cm^{-2}}$. When the photon density is high enough, a bound electron can be freed by the absorption of several photons, each with an individual energy lower than the work potential [Agostini et al., (1968); Mainfray and Manus, (1991)]. If more photons are absorbed than required to ionize the atom, electrons are ejected with non-zero energy:

$$E_{e^-} = (f + m)\hbar\omega - E_{bound} \tag{1.20}$$

where f is the number of photons necessary to free the electron, m the number of additionally absorbed photons, and E_{bound} is the binding energy of the considered electron. In the case of the hydrogen atom ($E_{bound} = 13.6\,\mathrm{eV}$) and a laser with a wavelength of $\lambda = 800\,\mathrm{nm}$ associated to photons with an energy of $1.55\,\mathrm{eV}$, we obtain $f = 9$.

When the laser intensity approaches I_i (see eq. 1.22), the laser electric field deforms the walls of the atomic binding potential well, and quantum mechanics allows **tunnel ionization** to occur, even though the atomic potential is higher than the binding energy of the electron (see the red potential curve in Fig. 1.3).

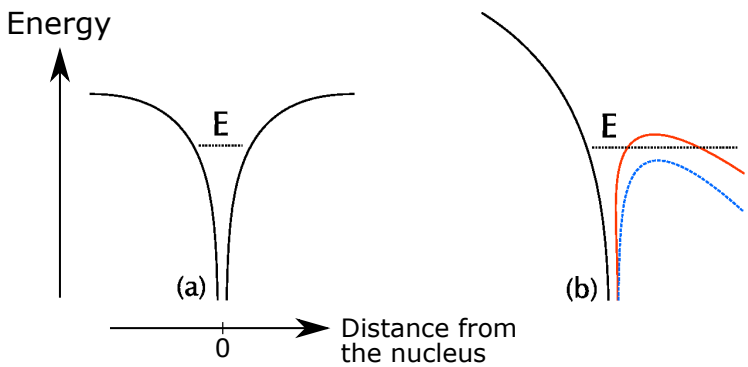

FIGURE 1.3: (a) Coulomb potential of a bound electron captive in the atomic core. (b) In the presence of an external field, the electron can tunnel through the residual potential (in red), or freed itself by suppression of the barrier (the maximum of the potential in blue is lower than the electron binding energy represented by the dotted line).

The relative importance of these non linear ionization mechanisms is indicated by the *Keldysh adiabaticity parameter*, equal to the ratio of the laser field frequency ω and the frequency of tunnelling through a potential barrier ω_t:

$$\gamma_K = \frac{\omega}{\omega_t} = \omega \frac{\sqrt{2 m_e W_i}}{eA}, \tag{1.21}$$

where ω_t is defined as the electron potential in the oscillating electric field eA divided by the ionization momentum $\sqrt{2 m_e W_i}$, with W_i being the work potential of the specific electron level. While multi-photon ionization dominates for $\gamma_K > 1$, when the frequency of the incident laser radiation decreases, it relaxes the timescale constraint dictating when an electron can undergo tunnel ionization, which is therefore the dominant process when $\gamma_K < 1$.

For $\gamma_K \gg 1$, the atomic potential is so much distorted by the high intensity laser radiation that its maximum is lower than the electron binding energy, as shown by the blue curve in Figure 1.3. There is no more confining barrier so the electron can spontaneously escape by the so-called **barrier suppression ionization** (BSI) or **over the barrier ionization** phenomenon. Plugging in the binding electric field in (1.19) into the laser intensity yields the threshold value above which any target material will be ionized solely by the laser electric field (the hydrogen ionization energy is among the highest besides noble gases, F, N and O)

$$I_{BSI} = 4 \times 10^9 \frac{E_i^4}{Z^2} \approx 1.4 \times 10^{14}\,\mathrm{W \cdot cm^{-2}}. \tag{1.22}$$

1.2.3 Laser propagation in a plasma

For a transverse plane wave (ordinary wave, $\vec{k} \perp \vec{B}_0$, $\vec{E}_1 \| \vec{B}_0$) travelling in a cold plasma, the collisionless **dispersion relation** is:

$$\frac{c^2 k^2}{\omega_L^2} = 1 - \frac{\omega_p^2}{\omega_L^2}. \tag{1.23}$$

We can deduce directly from this expression that the laser cannot propagate through the plasma if $\omega_L < \omega_p$. In this case, the plasma is said to be **opaque** to the laser light. Therefore, when the electromagnetic wave penetrates a plasma with a density gradient, it will propagate freely until it reaches the surface where $\omega_{pe} = \omega_L$, defining from Equation (1.15) the **critical density**:

$$n_c = \frac{\varepsilon_0 m_\mathrm{e}}{e^2} \omega_L^2 \approx 1.7 \times 10^{21}\,\mathrm{cm^{-3}} \text{ at } \lambda = 800\,\mathrm{nm}. \tag{1.24}$$

For a relativistic field amplitude, the electron plasma frequency (eq. (1.15)) has to be corrected considering the increase of the effective electron mass from its rest mass by the multiplying *Lorentz factor* $\gamma = \sqrt{1 + a_0^2/2}$, so that

$$\omega'_{\mathrm{p}e} = \frac{\omega_{\mathrm{p}e}}{\sqrt{\gamma}}. \tag{1.25}$$

Now the plasma is opaque and said *overdense* for $n_e/\gamma > n_c$, and it is still transparent for $n_e < n_c$ (*underdense* plasma), but **relativistic transparency** is induced in the range

$$n_c/\gamma < n'_e = n_e/\gamma < n_c. \tag{1.26}$$

1.3 Mechanisms of electron acceleration by laser

1.3.1 Ponderomotive force

When an intense laser pulse is focused, adiabatic and equilibrium conditions are violated, and strong radial gradients exist. Due to the space-time inhomogeneities of the oscillating electric field, the quivering motion of an electron transports it into regions of different intensities, and it experiences a net force after a full cycle, thus not returning back to its initial position. As a result, the electron gain energy and is pushed by a force, directed from the region with a higher field toward the weaker field region [Mulser and Bauer, (2010)]. The expression of this light pressure, named **ponderomotive force**, can be derived from the equation of motion of a charged particle subject to the *Lorentz force*:

$$\mathbf{F}_{\mathrm{L}} = q\left(\mathbf{E} + \mathbf{v} \times \mathbf{B}\right), \tag{1.27}$$

of an inhomogeneous TEM wave, leading to [Rax, (2005)]:

$$\mathbf{F_p} = -\boldsymbol{\nabla}\Phi_p\,, \text{ where } \Phi_p = -\frac{q^2 E_0^2}{2m\omega^2}\cos(2\omega_0 t), \tag{1.28}$$

giving a time average of:

$$\langle \mathbf{F_p} \rangle = -\frac{q^2}{4m\omega^2}\boldsymbol{\nabla}|\mathbf{E}|^2. \tag{1.29}$$

It has the effect of depleting regions of higher intensity of all its charged particles independently of their sign. Nevertheless the force is inversely proportional to the carrier mass, so its effect is predominant on electrons. This push is responsible for the **hole boring** effect [Wilks et al., (1992); Kodama et al., (1996); Pukhov and J. Meyer-Ter-Vehn, (1997)] (deformation of the critical surface during the interaction), as well as for the steepening of the density gradient [Fedosejevs et al., (1977)].

1.3.2 Laser absorption and energy transfer in a plasma

Laser absorption is a crucial physical process governed by many parameters, occurring in the interaction of a high intensity and short laser pulse with a plasma, and resulting in an energy transfer between the laser pulse and the target. The laser fields currently produced are not strong enough to directly accelerate the ions of the plasma, so their acceleration is mediated by the energy gain of the oscillating plasma electrons due to the electric field. They will in turn transmit some of their gained energy to the plasma ions. At relativistic intensities (in the order of $10^{20}\,\mathrm{W}\cdot\mathrm{cm}^{-2}$), the nanosecond pulse pedestal, due to a non perfect laser contrast, will start to ionize the target surface before the main pulse reaches it. We will therefore consider the situation where the main laser pulse (in the order of tens of femtoseconds) interacts with a preformed plasma expanding into vacuum, instead of a solid.

Depending on laser characteristics such as energy, intensity, contrast, polarisation, incidence angle and pulse duration, coupled to target characteristics and conditions of the pre-plasma, different absorption regimes take place. Extensive review of various absorption mechanisms proposed are described in [Gibbon, (2005); Kruer, (2003); Sentoku et al., (2014)]. To classify the energy transfer regimes between the laser pulse and the plasma electrons, responsible for generating a suprathermal electron population, we introduce the electron-ion **collision**

frequency [Cohen et al., (1950); Spitzer and Härm, (1953); Dendy, (1995)]:

$$\nu_{ei} \propto \frac{n_e Z}{T_e^{3/2}}. \tag{1.30}$$

Inverse Bremsstrahlung [Schlessinger and Wright, (1979)] is a *collisional* process that is the dominant absorption mechanism for high density plasmas (and high Z) at low electron temperatures, but as the intensity (and thus the temperature) increases, the fraction of the light energy absorbed by collisions becomes smaller and the following *collisionless* processes prevail. When the plasma density gradient is long compared to the scale length of the electron quivering motion:

$$L_g = \left(\frac{\partial \ln(n)}{\partial x}\right)^{-1} > v_e/\omega_L, \tag{1.31}$$

resonant absorption [McAlister and Stern, (1963); Freidberg et al., (1972)] is effective, while **vacuum/Brunel heating** [Brunel, (1987); Brunel, (1988)] dominates for steep gradients. **Relativistic $j \times B$ heating** [Kruer and Estabrook, (1985)] also intervenes at high intensities.

1.3.3 Collisional absorption or inverse Bremsstrahlung

In the laser electric field, electrons start oscillating and gain energy. When they undergo collisions with ions while absorbing laser energy, their trajectory changes, converting kinetic energy into thermal energy. The thermalisation collisions results in plasma heating, as the coherent oscillations of the electrons are converted into an isotropic Boltzmann velocity distribution. The magnetic term of the Lorentz force can be neglected, and adding a damping term taking into account electron-ion collisions to the equation of motion, we get:

$$\frac{d\mathbf{v}}{dt} = -\frac{e}{m_e}\mathbf{E} - \nu_{ei}\mathbf{v}. \tag{1.32}$$

Substituting variables in this equation (1.32) with complex notations of the form:

$$\mathbf{F}(\mathbf{r}, t) = Fe^{i(\mathbf{k}\cdot\mathbf{r}-\omega t)}, \tag{1.33}$$

we obtain an expression for the electron oscillating velocity:

$$v = \frac{eE}{m_e(i\omega - \nu_{ei})}. \tag{1.34}$$

Inverse Bremsstrahlung is most effective at low laser intensities, below $10^{15}\,\mathrm{W}\cdot\mathrm{cm}^{-2}$. As the intensity increases, the electron-ion collision frequency ν_{ei} decreases, so the electron velocity in the laser field v is not anymore efficiently converted into thermal motion.

1.3.4 Resonant absorption

Resonant absorption is a non-collisional mechanism of energy transfer occurring for *p-polarised* light waves obliquely incident on a plasma with a long density scale length compared to the laser wavelength. p-polarisation and oblique incidence are needed as a tangential electric field component normal to the critical surface is required to partly tunnel into it and drive plasma oscillations at ω_{pe} across this surface. These oscillations grow resonantly with the successive laser cycles, since $\omega_L = \omega_{pe}$ at the critical surface. The electron plasma wave propagates and

is transferred to the plasma through collisions (at low intensities), wave breaking or *Laudau damping* (at high laser intensities).

To explain more formally this process, injecting in eq. (1.32) variables with a harmonic behaviour in time, so that the following expansion can be used:

$$f(\mathbf{r},t) = f_0(\mathbf{r}) + f_1(\mathbf{r})e^{-i\omega t} + f_2(\mathbf{r})e^{-2i\omega t} + ... \tag{1.35}$$

leads, in a first order approximation and using the definition of the electron plasma current, to:

$$\mathbf{v_1} = \frac{-ie}{m_e(\omega + i\nu_{ei})}\mathbf{E_1}, \tag{1.36a}$$

$$\mathbf{J_1} = -en_e\mathbf{v_1} = \frac{i\omega_{pe}^2}{\varepsilon_0(\omega + i\nu_{ei})}\mathbf{E_1}. \tag{1.36b}$$

Plugging these solutions into the wave equation for the electric field (1.2a) comes to:

$$\boldsymbol{\nabla}^2\boldsymbol{E_1} + \frac{\omega^2}{c^2}\mathbf{E_1} = \frac{\omega}{\varepsilon_0^2(\omega + i\nu_{ei})}\frac{\omega_{pe}^2}{c^2}\mathbf{E_1} + \boldsymbol{\nabla}(\boldsymbol{\nabla}\cdot\mathbf{E_1}) \tag{1.37}$$

The first term on the right-hand side is the collisional contribution, while $\boldsymbol{\nabla}(\boldsymbol{\nabla}\cdot\mathbf{E_1})$ is linked to the resonant absorption. We now understand that for a s-polarised wave oriented perpendicular to the surface, or for normal incidence, $\mathbf{E_1} \perp \boldsymbol{\nabla}n_e$ so $\boldsymbol{\nabla}\cdot\mathbf{E_1} = 0$ and the resonant process is ineffective.

1.3.5 Vacuum heating or Brunel effect

Again for p-polarised light, but penetrating a steep plasma density gradient, with a scale length of the critical surface smaller than the electron oscillation amplitudes, coupling is not efficient and resonantly driven plasma waves are not generated. However vacuum heating comes into play in the laser absorption, in a mechanisms introduced by Brunel in 1987 [Brunel, (1987)] as the "not-so-resonant, resonant absorption". The electric field, acting orthogonally on the sharp interface between the conducting plasma and the vacuum, pulls the electrons out of the plasma and sends them back into it when the laser field reverses. The laser is able to penetrate the overdense plasma only to its skin depth, so the electrons that are pushed deeper are not dragged back as the restoring forced is screened out, and they can then thermalise and lose their energy through collisions.

1.3.6 Relativistic $\mathbf{j} \times \mathbf{B}$ heating

At relativistic intensities when $a_0 > 1$, the magnetic term of the Lorentz force is no longer negligible and the electron motion is dominated by the $\mathbf{v} \times \mathbf{B}$ term. Because of the 2ω term in the expression of the time-dependent ponderomotive force described in eq. (1.28), electrons oscillate at twice the laser frequency at the plasma-vacuum boundary, and can be accelerated at plasma vacuum boundary. Some electrons are pushed in the overdense plasma, escaping the area where they can be pulled back by the laser field. This process is similar to vacuum heating, but it works best under normal incidence and linearly polarised light. The conversion efficiency of laser energy into hot electrons increases with the intensity, and it has been observed above 30 % at the high intensities considered [Key et al., (1998)].

1.4 Laser-driven ion acceleration mechanisms

This section aims at introducing ion acceleration by super-intense laser-plasma interaction [d'Humières, (2012)], based on the physical concepts presented previously. In the last decades, several acceleration mechanisms have been proposed theoretically, and some have been demonstrated experimentally, as detailed in this review by Macchi et al., [2013]. Due to their heavy mass, ions are not directly accelerated by the laser pulse in the current facilities. The relativistic regime for electrons being in the order of $10^{18}\,\mathrm{W}\cdot\mathrm{cm}^{-2}$, considering protons as the lightest ions but still almost 2000 times heavier than electrons, we obtain an intensity threshold for *direct relativistic acceleration* scaled by the square of the mass ratio, above $10^{24}\,\mathrm{W}\cdot\mathrm{cm}^{-2}$. This is a couple orders of magnitude higher than the records achieved up to date, so the ion energy gain to MeV energies is mainly mediated by the strong electrostatic fields that are generated by the charge separation resulting from the electron displacement occurring during the interaction [Mourou et al., (2006)]. The accelerating fields reach several tens of $\mathrm{TV}\cdot\mathrm{m}^{-1}$, which is six orders of magnitude higher than what is attained in conventional rf-accelerators.

The ion acceleration processes have been investigated theoretically and numerically, by means of two- and three-dimensional *particle-in-cell* (PIC) computer simulation codes [Petrov and Davis, (2009)]. The mechanisms in action depend on the specific experimental conditions of the laser-target interaction, and reviews of different acceleration mechanisms can be found in [d'Humières et al., (2005); Borghesi et al., (2006); Borghesi, (2014)]. Experiments have reported collimated beams of high-energy ion during laser pulse interactions with solid targets [Fews et al., (1994); Clark et al., (2000b); Clark et al., (2000a)], with the first measurements dating back to more than four decades ago [Yamanaka et al., (1972); Luther-Davies and Hughes, (1976)]. Fast ions have also been observed in the interaction with gas jets [Sarkisov et al., (1999); Krushelnick et al., (1999)] (due to *Coulomb explosion* [Esirkepov et al., (1999)] during which the laser blows away electrons from the plasma cloud, leaving positively ions to explode under the resulting Coulomb repulsive force), clusters [Ditmire et al., (1997); Lezius et al., (1998)] or preformed underdense plasmas [Young et al., (1996)].

Two acceleration mechanisms based on space charge effects can work independently and at the same time, with ions coming both from the back and front surfaces, depending on the processes involved [Maksimchuk et al., (2000); Zepf et al., (2003); Karsch et al., (2003)].

1.4.1 Ion acceleration from the rear side of thin foil targets : target normal sheath acceleration

In the year 2000, ion acceleration from the back unirradiated target surface was realized experimentally, when a low contrast laser pulse interacted with a thick solid density slab target, generating protons up to 55 MeV with a 7 % conversion efficiency of the laser energy incident on the target [Hatchett et al., (2000); Snavely et al., (2000)]. Modelled theoretically a year later, the mechanism was named **Target Normal Sheath Acceleration** (TNSA) [Wilks et al., (2001)].

In this mechanism, a relativistic laser pulse with $a_0 > 1$ is incident on a relatively thick solid target, consisting in a foil with a thickness of several micrometers that remains opaque to the laser light during the entire interaction. The illuminated target surface is quickly ionized by the pedestal of the laser pulse, creating a plasma expanding into vacuum. When the main pulse arrives, it is partly absorbed at the plasma critical surface, and generates a huge amount of *hot electrons*, with a temperature T_h, which penetrate the target and ionize the rear surface upon arrival by resistive heating and collisions. The electrons manage to escape the rear surface over

a distance λ_D of a few micrometers before being pulled back into the plasma, generating strong ambipolar electrostatic fields, equilibrating the charge imbalance, on the order of TV $\cdot$ m^{-1} and scaling as $E_s = k_B T_h / e\lambda_D$ [Passoni and Lontano, (2004); Schreiber et al., (2006); Albright et al., (2006)]. Ions are, in turn, accelerated in the forward direction into vacuum (see cartoon in Figure 1.4). The electron transport through the overdense plasma is supported by *return currents* of *cold electrons*, constrained to a maximum value set by the Alfvén limit.

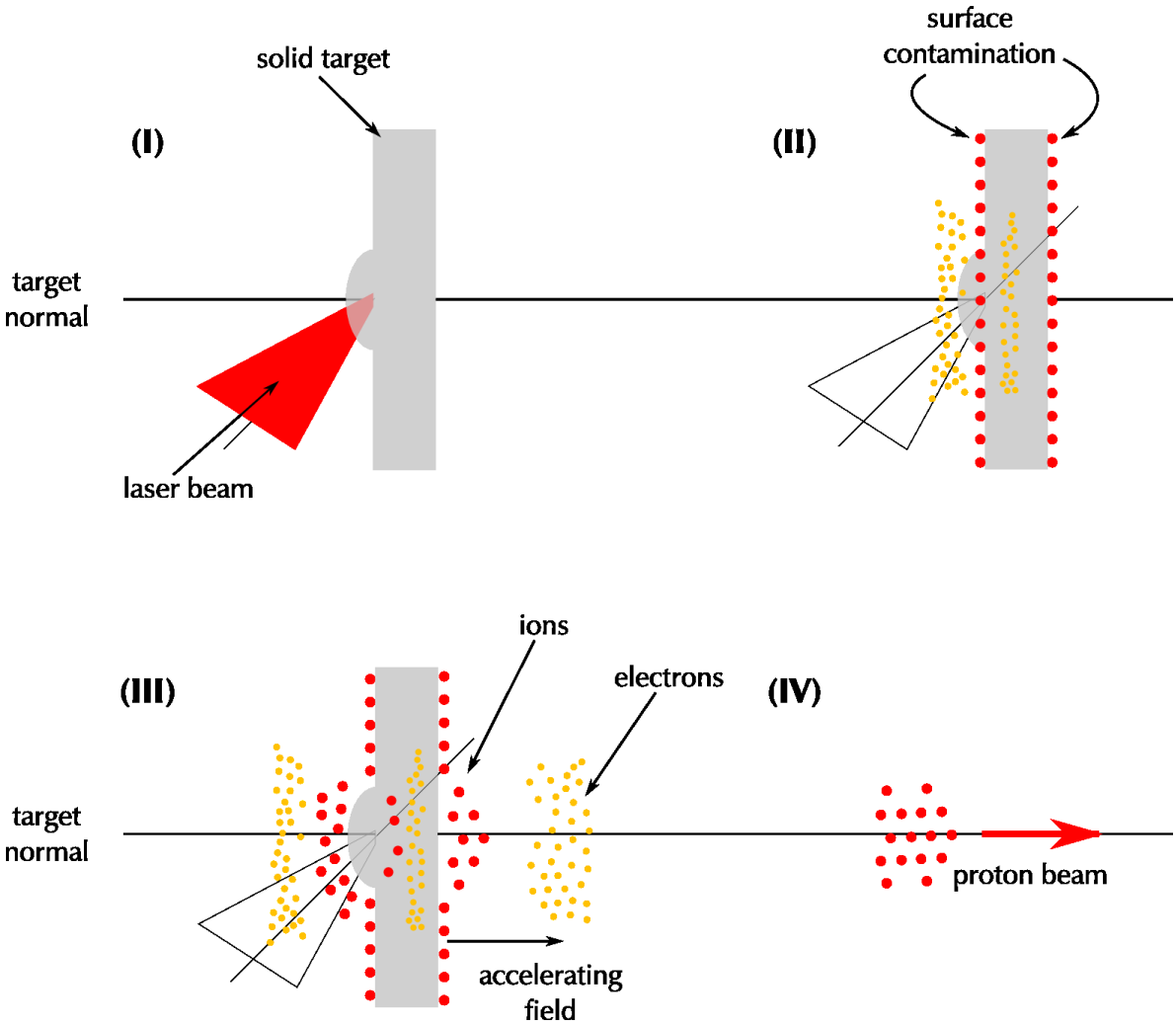

FIGURE 1.4: TNSA proton acceleration scheme (from [Flacco, (2008)]). The ultra high intensity laser pulse impinges on a slab of solid matter (I); the matter is ionized and the plasma heated, producing a suprathermal electron population (II). Following the propagation of electrons through the target (III), an electrostatic accelerating field is set up on the rear surface, extracting and accelerating ions from the back surface impurities (IV).

TNSA features and developments

The acceleration lasts for several times the laser pulse duration, and the ion beam is emitted in a direction perpendicular to the target rear surface. As the ion energy increases, the ion collimation toward the target normal axis increases, while the source size in the hundred micrometer scale on the target backside decreases (see [Roth et al., (2002)] and Figure 6.6 p.71 in [Hegelich, (2002)]). The ions originate from impurities, as a nm-thin layer of hydrocarbon contaminants inside the solid target or adsorbed on its surfaces.

The TNSA mechanism can operate on each target surface, generating two ion beams: one escaping from the back surface and one coming from the front illuminated surface in a counter-propagating direction with respect to the laser. Ions emitted at the front are generally less energetic due to the presence of a preplasma, but during the interaction of a high contrast ($> 10^{10}$) laser pulse with thin targets, it was shown that proton beams originating from both target sides were similar, with the peak proton energy increasing with thinner targets, as it was demonstrated by Ceccotti et al., [2007] (see the illustration in Figure 1.5).

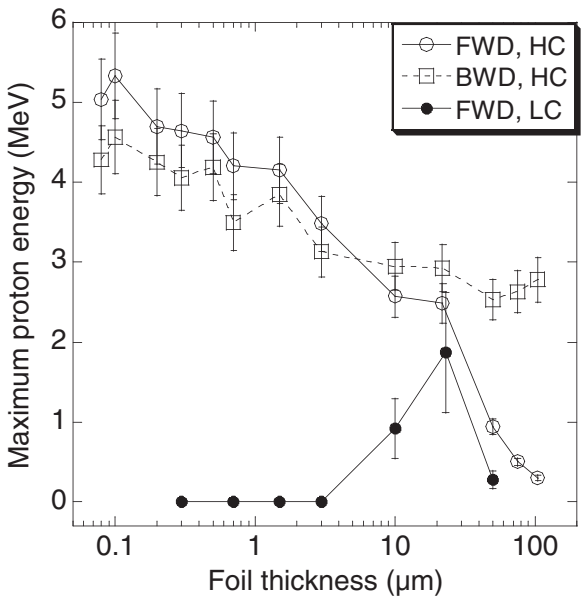

FIGURE 1.5: Maximum proton energy detected as function of target thickness, both in the forward (circles) and backward (squares) direction, with a high contrast of 10^{10} (open markers) or lower one of 10^{6} (solid markers). (Adaptated from Ceccotti et al., [2007])

The accelerated ions are in majority protons, independently of the target foil material, because they have the highest charge-to-mass ratio and the lowest inertia. Nonetheless, their presence can be removed in favour of heavier ion species if the target is cleaned, through resistive heating, ion gun etching, cw-laser heating or laser ablation [Hegelich et al., (2002); Roth et al., (2002); Hegelich et al., (2005)]. In this way, ion energies up to about 7 MeV/u have been measured for carbon, fluorine, aluminum and lead, and energies greater than 10 MeV per nucleon for iron ions [McKenna et al., (2004)].

The resulting ion beam has a broad quasi-thermal energy spectrum (exponentially decaying) with a sharp high energy cutoff. Scalings of the maximum ion energy have been proposed based only on the laser intensity with a square-root dependence [Wilks et al., (2001); Mora, (2003);

Schreiber et al., (2006)]:

$$E_{max} \propto T_h \propto a_0 \propto \sqrt{I_L}. \tag{1.38}$$

The effect of the target thickness and the laser pulse duration on the maximum proton energy has been investigated for a high-contrast-laser, showing that two proton acceleration regimes can take place depending on the ratio between the density gradient and the hot electron Debye length at the rear target surface [Flacco et al., (2010)]. It is worth noting that the highest intensity is not necessarily suitable for reaching maximum ion energies, underlining the important role of the laser pedestal, with a perfect contrast not desirable in this regime. It was found that the laser-driven ion energy could be considerably enhanced by optimizing the preplasma scale-length, compared to perfect conditions with a clean laser pulse (without a prepulse) irradiating a clean target (without a preplasma) [Esirkepov et al., (2014)]. However, it was suggested that for shorter laser pulses, the maximum proton energy would increase proportionally to the laser intensity I, as the laser irradiance goes from the subrelativistic domain $I < 10^{18}\,\mathrm{W \cdot cm^{-2}}$ to higher intensities, with the ponderomotive force passing from being proportional to I to being proportional to $\sqrt{I}$ [Borghesi et al., (2006); Kim et al., (2013)]. The evolution of the recorded maximum proton energy, reported in various facilities around the world as a function of pulse duration or laser irradiance, is shown in Figure 1.6. In Figure 1.6-(a) one can see a clear increase of the maximum proton energy with the laser pulse duration, with a roughly parallel trend for different laser irradiances. This same tendency is seen in Figure 1.6-(b), which shows the evolution of the maximum proton energy as a function of laser irradiance, and where the two scalings as function of the laser intensity can be identified. It was also discussed that other parameters could dictate the scaling laws [Fuchs et al., (2006)], such as the *electron areal density* $\sigma = n_e l_t$, involving the target thickness l_t. Laser absorption would be optimal for ion acceleration at a value of σ proportional to the square-root of the intensity: $\sigma_{opt}/n_{cr}\lambda \approx 3 + 0.4a_0$ [Esirkepov et al., (2006)].

In an attempt to get narrower energy spectrum out of laser–plasma accelerators, proof-of-principle experiments manufactured solid microstructured targets and managed to produce quasi-monoenergetic proton beams [Schwoerer et al., (2006)], or C^{5+} ions with a relative energy spread of 17 % centred on 3 MeV/u obtained from a solid palladium foil undergoing several phase changes during heat treatment [Hegelich et al., (2006)]. It was also demonstrated in [Ceccotti et al., (2013)] that the cutoff energy could be increased by a factor 2.5 with a more efficient laser absorption by grating targets, resulting in the resonant excitation of surface waves. However, these expensive techniques to enhance TNSA and shape the beam properties require a cumbersome and time-consuming target preparation, making them inapplicable as is, in practical applications requiring multi-shots in a limited period of time. Maximum proton energy reported were 67 MeV using flat-top hollow microcone targets in 2010 [Gaillard et al., (2011)], with record published to date of 85 MeV [Wagner et al., (2016)] in the TNSA regime, and 93 MeV [Kim et al., (2016)] in the RPA regime.

1.4.2 Acceleration from the target front side

In another scenario, ions are accelerated at the illuminated target surface by the charge separation field induced in the expanding plasma by the ponderomotive force. This force acts on plasma electrons in the laser focus, expulsing them from high intensity interaction regions. The resulting electrostatic potential is maintained as long as its effect on electrons is balanced by the ponderomotive force. This lasts for the duration of the main laser pulse, a time long enough to accelerate ions. **Front Side Acceleration** (FSA) was studied with 1-D PIC simulations, and

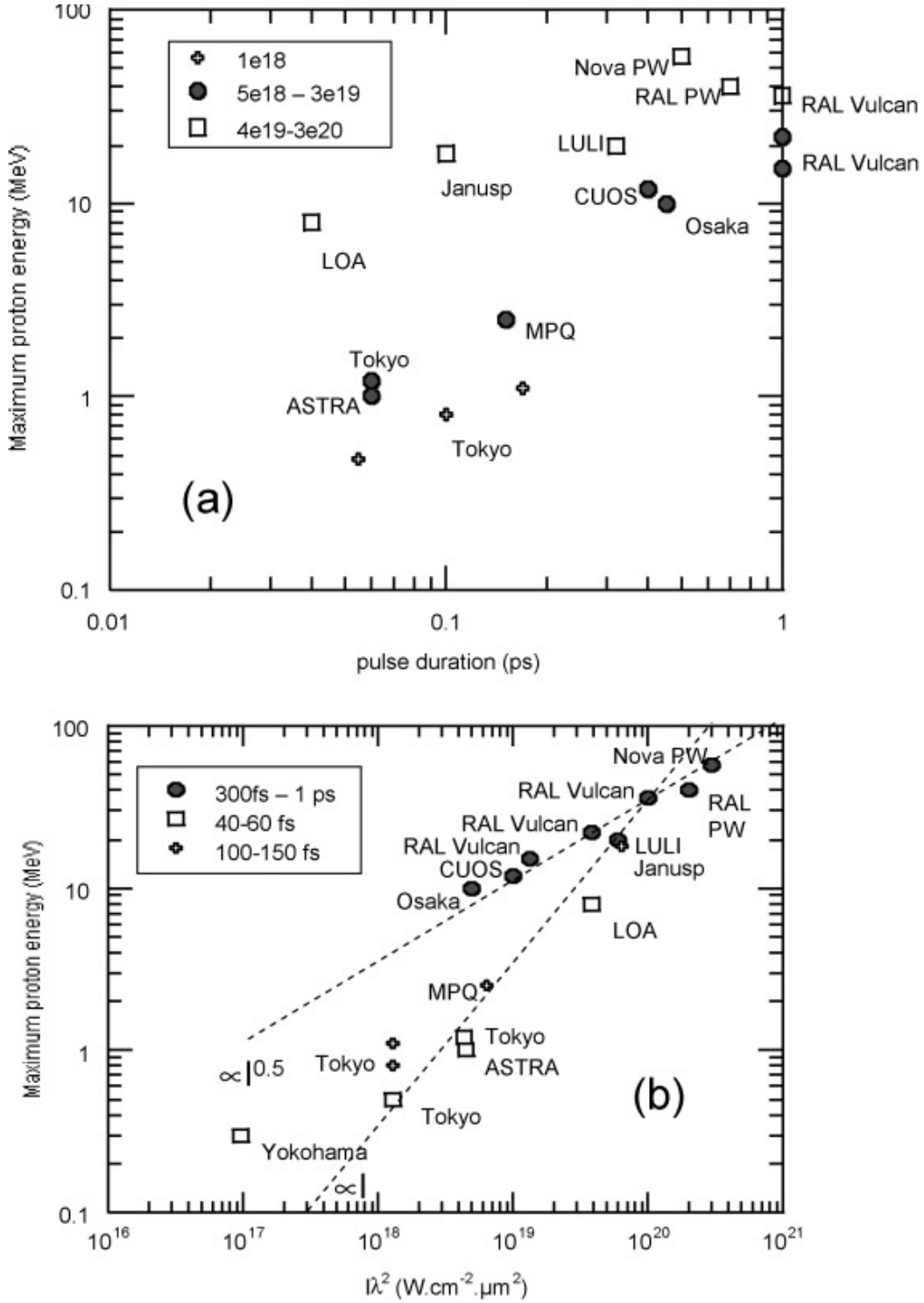

FIGURE 1.6: (a) Maximum proton energy from laser-irradiated thin (5 to 10 µm, except for the data points marked "RAL PW" and "Nova PW" where the thickness is 100 µm) metal (Al or Cu) targets for different experiments as a function of the laser pulse duration and for three different ranges of laser irradiances. (b) Same but as a function of the laser irradiance and for three ranges of pulse durations. The two dashed lines are trend lines proportional to I and $I^{0.5}$. The data have been grouped so that similar conditions in experiments carried out in different laboratories could be compared. (Extracted from Borghesi et al., [2006])

details about the influence of the laser-target interaction are given in [Sentoku et al., (2003)]. Electrostatic fields on the illuminated surface scales as $E_s = k_B T_h / e L_g$ with L_g the plasma gradient length, representing usually a larger scale length than on the back surface, thus smaller fields. This is why rear-surface acceleration seems to produce higher energy particles with smaller divergence and a higher efficiency than front-surface acceleration [Fuchs et al., (2005)], also because the illuminated surface is more prone to be bent and the acceleration time there is more limited.

Another process can compete with TNSA at relativistic intensities. When the ponderomotive force is strong enough to launch a collisionless electrostatic shock wave with a high Mach number, ions at the front and in the bulk of the target can be reflected at twice the shock velocity [Denavit, (1992)].

They are driven into and through the target by **shock acceleration** [Silva et al., (2004); Henig et al., (2009b); Fiuza et al., (2012)]. For a peak plasma density equal to a few times the critical plasma density, the ion beam produced has a narrow feature or a plateau in its energy spectrum [Haberberger et al., (2012)].

1.4.3 Radiation pressure acceleration

The **Radiation Pressure Acceleration** (RPA) regime takes place at relativistic laser intensities $a_0 \gg 1$, with *circular polarisation* (CP) and under normal incidence on a sufficiently thin foil. In the **Light Sail** (LS) scheme, the electromagnetic radiation pressure of the laser light is able to push the whole laser-irradiated target area as a single block of plasma, an idea dating back half a century ago and initially envisioned for laser-driven spacecraft propulsion [Marx, (1966)]. The spatial distribution of electrons and ions evolves dynamically to maintain an equilibrium condition, where the electrostatic and ponderomotive forces acting on the electrons balance each other. It has the promising characteristic of accelerating all plasma ions with a quasi monoenergetic spectrum. It is attracting lots of attention, and was recently investigated in numerous publications using analytical models and PIC simulations in the search for new acceleration mechanisms that could lead to higher energies than the well-known TNSA [Esirkepov et al., (2004); Macchi et al., (2005); Klimo et al., (2008)].

Achieving RPA-LS experimentally is difficult, as for instance to fulfill the quasi one dimensional geometry. The laser focus has to be significantly larger than the target thickness, hence the large laser energy needed to reach a high intensity. Moreover, the focal spot should be uniform and the target surface must be perfectly flat, as any denting will bring about a linear polarization component seen by the bent target out of the CP pulse, which will induce some electron heating and prevent the RPA regime from occurring. The laser contrast should also be very high, not to have a pedestal deforming the target surface. Its first experimental signature was reported in [Henig et al., (2009c)], when a peak in the fully ionized carbon spectrum appeared when laser polarization is changed from linear to circular, and was attributed to a reduction in electron heating. Similar narrow-band features, with stronger fluences but still not monoenergetic, were seen by [Kar et al., (2012)].

Due to the CP light, there is no oscillating component in the $\mathbf{j} \times \mathbf{B}$ force that would heat the electrons and lead them out of the interaction area. Instead, electrons are pushed inward adiabatically by the steady part of the $\mathbf{j} \times \mathbf{B}$ force, leaving a depletion area behind them at the plasma surface followed by a compression area. Electrons quickly reach a stationary state, as an equilibrium between the electrostatic field and the ponderomotive force settles. Ions are accelerated from the depletion layer on the target front surface and toward the dense electron

cloud. The electrostatic field, generated via the space charge displacement, evolves linearly along the target normal axis, and peaks at the interface of both areas (see Figure 1.7), according to the assumption that the electrons follow quasiequilibrium dynamics. The field felt by an ion is constant over its trajectory and depends only on its initial longitudinal position, so all ions in the compression region reach the end of it at the same time and with the same velocity, but ions starting in the depletion region will never catch up. The ions crossing the singularity surface at the end of the compression region are injected into the unperturbed plasma region, breaking the force balance acting of the compressed electrons.

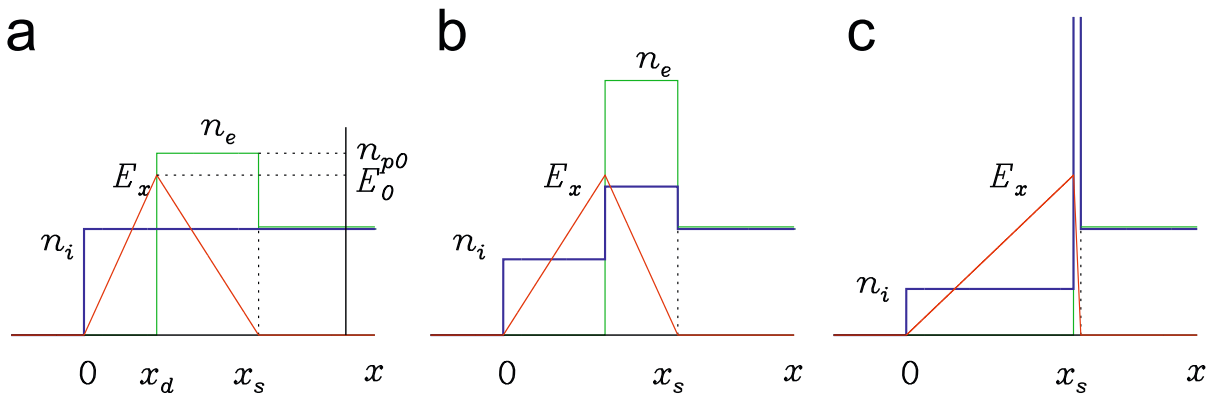

FIGURE 1.7: Schematic of the evolution of the density profiles (electrons in green, ions in blue) and the electrostatic field (in red) at several steps of the RPA scheme. Owing to the CP laser light, there is no electron heating so they are pushed into the target until the charge separation field balances the radiation pressure. An electron depletion area ($0 < x < x_d$) and an electron compression area ($x_d < x < x_s$) are formed. The ponderomotive force peaks at $x = x_d$ and vanishes at $x = x_s$. (extracted from Ref. [Macchi and Benedetti, (2010)])

The entire process can then repeat in cycles until the compression layer gets to the rear target surface, allowing monoenergetic ions and electrons to copropagate together ballistically, as a quasineutral plasma volume continuously gaining energy from the laser field. This scheme is called the **hole boring** mechanism [Macchi and Benedetti, (2010)], and it is also referred to as **phase stable acceleration** (PSA) in [Yan et al., (2008)]. Long laser pulses are required for this mechanism to operate, with the condition $v_i \tau_L > l_t$ satisfied, where v_i is the average ion velocity, τ_L the laser pulse duration, and l_t the target thickness.

For very thin targets having low inertia, the RPA regime was appropriately named **light sail** [Macchi et al., (2009); Macchi et al., (2010)]. Nonlinear self-induced transparency effects have to be considered, and the acceleration process repeats successively leading to very high ion energies. The radiation pressure regime would become dominant for ion acceleration at intensities in the order of 5×10^{21} W $\cdot$ cm^{-2} [Esirkepov et al., (2006)], where monoenergetic ion beams up to GeV are predicted, with a scaling of the ion energies as $E_{max} \propto (\tau_L I_L)^2$ [Macchi and Benedetti, (2010)].

1.4.4 Break-out afterburner

As opposed to the ion acceleration mechanisms presented so far, where the laser interacts with an overdense target, the **Break-Out Afterburner** mechanism (BOA) [Yin et al., (2006); Albright et al., (2006); Yin et al., (2007)] has the particularity of happening when the target becomes relativistically underdense. During the plasma expansion, the electron density is reduced down to the relativistic critical density. Here, this effect improves the ion acceleration, while it was limiting the energy attainable with RPA. Besides, the volumetric heating of the target electrons enhances the field accelerating the ions. For a given set of laser conditions, there would be an optimal target thickness enabling BOA to accelerate quasi-monoenergetic ion bunches with better efficiency and to energies one order of magnitude higher than what is attained with traditional TNSA. The effectiveness would be best when the occurrence of relativistic transparency corresponds with the laser pulse peak. Carbon energies as high as 500 MeV/nucleon has been reached in some experiments [Hegelich et al., (2011)].

When an ultra-high contrast, prepulse-free and very-intense laser pulse interacts with a very thin solid target tens of manometers thick, the linearly polarized light ionizes rapidly the target, similarly to TNSA. As the plasma expands, the electron density decreases and the *plasma skin depth* l_s (depth to which the electromagnetic radiation can penetrate) increases, as $l_s = c/\omega_{pe} \propto c/\sqrt{n_e}$. The target thickness becomes comparable to the laser skin depth, the laser evanescent field reaches deeper in to the target and eventually all the cold electrons in the target area are heated through $j \times B$ heating, enhancing the ion acceleration. The target, that is classically opaque to the laser light, turns relativistically transparent: $n_e/\gamma < n_c < n_e$. As the laser penetrates the rear of the target, a strong accelerating longitudinal electric field is generated and moves together with the ions, hence the expression laser breakout afterburner (see Figure 1.8).

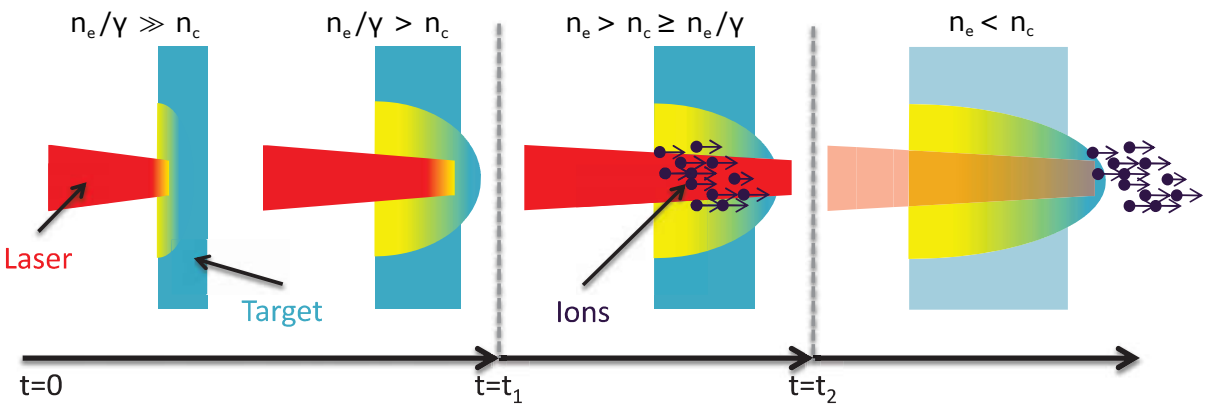

FIGURE 1.8: Schematic of the BOA scheme. From $t = 0$ to $t = t_1$, the target is volumetrically heated, and all electrons are subsequently promoted to hot electrons. At time $t = t_1$, the plasma density has dropped so that the target turns relativistically transparent to the laser light. It follows a period of rapid and extreme ion acceleration, where the electrons energy is continuously replenished by the laser light. The acceleration ceases when the target turns classically underdense at $t = t_2$ due to the strong plasma expansion. (Adapted from [Jung, (2012)])

Nonlinear processes related to the cohabitation of highly relativistic electrons and comparatively slow plasma ions support the growth of electromagnetic instabilities, which further enhances energy coupling into the ions. Since the target is transparent, electrons keep regaining

energy from the laser, which sustains the instabilities and the ion acceleration. 1D PIC simulation analysis associated the BOA mechanism with the *relativistic kinetic Buneman instability* that efficiently converts energy from the electron drift into the ions [Albright et al., (2007)]. The acceleration goes on until the plasma becomes classically underdense, and the beam that was initially monoenergetic gradually spread into an exponentially decaying energy spectrum, as observed experimentally [Henig et al., (2009a)]. By virtue of their low charge-to-mass ratio, light ions such as protons could propagate far enough ahead during the initial TNSA phase, to leave BOA operating on a *self-cleaned* layer.

1.4.5 Applications of laser-accelerated ion beams

Ion beams are widely used in medical, industrial and research fields. They have a peculiar energy deposition profile, compared other sources of ionizing radiation such as x-rays or electrons, with a maximum loss of energy at the end of their trajectory (more details on this particularity in the next chapter). This property makes them particularly suitable for applications requiring a localised energy deposition, such as ion beam cancer therapy [Bulanov and Khoroshkov, (2002)]. Laser-driven ion accelerators also represent compact sources of energetic particles with many established or potential applications [Malka et al., (2008)], owing to a number of unique characteristics that distinguish them from conventional accelerators (cyclotrons, synchrotrons, linear and circular radiofrequency accelerators), such as an ultrashort bunch duration, very high flux rate and a low emittance [Cowan et al., (2004)]. With the advent of multi-MeV proton acceleration, several applications where proposed including laser triggering and control of nuclear reactions [McKenna et al., (2003); Yang et al., (2004); Hannachi et al., (2007)], and the production of warm dense matter via isochoric heating [Koenig et al., (2005); Mančić et al., (2010)]. Energetic proton beams are used in laser-plasma research for ultrafast probing of transient electric and magnetic fields in dense plasmas [Borghesi et al., (2002b); Borghesi et al., (2002a); Rygg et al., (2008); Li et al., (2009); Volpe et al., (2011)], for medical imaging in the production of short-lived isotopes for positron-emission tomography [Fritzler et al., (2003); Ledingham et al., (2004)] or as an imaging tool in tomography [Cormack and Koehler, (1976); Attanasi et al., (2009); Attanasi et al., (2010)]. The low emittance of laser-accelerated ion beams also makes them interesting candidates as injectors for large conventional accelerators (storage ring or RF cavity) and colliders [Krushelnick et al., (2000)]. Lower proton energies are exploited in industry-related topics for ion implantation in substrates [Hong et al., (2001); Klug et al., (2011)], for spectroscopic surface characterisation [Smith, (1971)], and in manufacturing techniques such as lithography [Melngailis et al., (1998); Ottevaere et al., (2002)] and micromachining [Rajta et al., (2003)]. Growing interest is shown in focusing high ion density beams into the core of a highly compressed deuterium-tritium plasma to ignite a fusion reaction, according to the fast ignition approach to laser-driven inertial confinement fusion [Bychenkov et al., (2001); Roth et al., (2001)].

1.5 Conclusions

Laser-plasma interactions can result in the acceleration of energetic ion beams. The properties of the generated beams depend mainly on the laser and target parameters and it is possible to obtain desired features, for instance in terms of energy spectrum and spatial distribution, using adapted targets and laser pulses to select the appropriated interaction regime.

Chapter 2

Radiobiology basics

Radiobiology is the study of the action of ionizing radiations on living organisms. Hence, this chapter presents the various types of ionizing radiations and describes some physical, chemical and biological processes involved during their interaction with matter. Then some methods used in radiotherapy to study the damages radiation may cause on biological material are described. Finally the interest of using energetic protons in medicine for the treatment of cancer is discussed.

Contents

2.1 Physics of radiation interactions with matter **30**
2.1.1 Irradiation effects and types 30
2.1.2 Passage of charged particles through matter 30
Charged particle energy loss 30
Charged particle range 32
2.1.3 Quantities and units 33
Radiation dose 33
Relative biologic effectiveness 35
2.2 Radiotherapy methods and techniques **37**
2.2.1 Mechanism of action 37
Radiation effects at the molecular level 37
2.2.2 Cellular biology techniques 37
DNA damage detection by immunofluorescence 37
Cell survival assay 39
2.2.3 Fractionation and beyond 41
2.2.4 Proton beam therapy 41
2.3 Conclusion **43**

2.1 Physics of radiation interactions with matter

2.1.1 Irradiation effects and types

Many phenomena can happen when matter is subject to irradiation. The energy absorption from radiation may excite or ionize the material. For low energy radiations, an electron in an atom or molecule may simply be raised to a higher energy level, which is called **excitation**. Typical non-ionizing radiations include electromagnetic waves in the range of ultraviolet and less energetic waves. However the process is called **ionization** if the radiation has enough energy to eject orbital electrons from the atoms, producing positively charged ions. The ejected electrons may possess sufficient energy to cause secondary ionizations, and so on. Ionizing radiations have the characteristic of releasing locally large amount of energy, as ionizations are discrete events. The average energy dissipated by an ionizing event is about 33 electronvolts (eV), which is more than enough to break strong chemical bonds (for example, the energy associated with a carbon-carbon double bond is 4.9 eV) [Cox and Ang, (2009)]. These physical perturbations lead to physicochemical reactions, then chemical and finally biological effects.

Ionizing radiations are ejected in the decay process of unstable nuclei or emitted by de-excitation of atoms in nuclear reactors, X ray machines, cyclotrons and other devices such as laser-plasma accelerators. They can also be divided into two categories, depending on the way they interact with matter :

- **Directly ionizing radiations** consist of charged particles : electrons, protons and heavier ions. They can directly cause ionizations and excitations during interactions with electrons encounter on their trajectory, disrupting the molecular structure of the medium they are traversing. The Coulomb force acting between an incident charged particle and electrons of the medium leads to a kinetic energy transfer. This energy deposition produces intense chemical and biological damage to molecules on their track inside living tissues.
- **Indirectly ionizing radiations** consist of electromagnetic radiations and uncharged particles such as neutrons. They do interact strongly with matter but they give up energy to the material, producing secondary fast moving charged particles. These secondary electrons generated by photons, or secondary protons generated by neutrons, can then ionize the medium.

Besides interacting with electrons from the medium, charged particles can also slow down during their interaction with nuclei, leading to the emission of **Bremsstrahlung radiation** (from the german bremsen meaning "to brake" and Strahlung "radiation", i.e. "braking radiation" or "deceleration radiation") in the form of photons. However, this process is negligible in interactions with biological materials, except for high energy electrons.

2.1.2 Passage of charged particles through matter

Charged particle energy loss

When a charged particle with energy E travels a short distance dx along its trajectory through a material, it undergoes many collisions with electrons present around its path at various distances, associated to diverse energy transfers. The sum of all these transfers represents the energy dE lost by the particle during its propagation over the length dx. The **stopping power** is defined as the retarding force acting on charged particles due to interaction with matter, resulting in loss of

particle energy. The **linear stopping power** S is numerically equal to the loss of energy dE per unit path length dx, that is :

$$S(E) = -\frac{dE}{dx}. \tag{2.1}$$

The minus sign makes the quantity S positive, and it is usually measured in $\mathrm{MeV} \cdot \mathrm{cm}^{-1}$. It depends on the material as well as on the velocity v and charge z of the particle. To easily compare values for various materials in different state forms, one often divide the force by the density of the material, to obtain the **mass stopping power**. It is measured in $\mathrm{MeV} \cdot \mathrm{cm}^2 \cdot \mathrm{mg}^{-1}$ and it depends only very little on the density of the material.

As a first approximation, the energy transfer q for each collision can be considered proportional to z^2/v^2, so will be E and therefore S. A more exact formula was established by Bethe, taking into account close collisions and the electron-atom bond. The relativistic Bethe-Bloch formula is given by [Sigmund, (2006)] :

$$-\frac{dE}{dx} = \frac{4\pi}{m_e c^2} \cdot \frac{nz^2}{\beta^2} \cdot \left(\frac{e^2}{4\pi\varepsilon_0}\right)^2 \cdot \left[\ln\left(\frac{2m_e c^2 \beta^2}{I \cdot (1-\beta^2)}\right) - \beta^2\right] \tag{2.2}$$

where c is the speed of light and ϵ_0 the vacuum permittivity, $\beta = \frac{v}{c}$, e and m_e the electron charge and rest mass respectively, n the electron number density and I the mean excitation potential of the target material in which the particle is travelling a distance x.

The stopping power depends on the nature and kinetic energy of the particles, which impacts their radiobiological properties. However, particles carrying a single charge and with the same velocity have the same stopping power, as for instance a proton with a kinetic energy of E_p and an electron with a kinetic energy of $E_e = E_p \times \frac{m_e}{m_p} = E_p/1836$.

The rate at which an ionizing radiation loses its energy, while passing through a particular medium, depends on the energy and type of radiation as well as on the material density. The **linear energy transfer** (LET) of the radiation is defined as the average energy deposited in matter per unit length of track, and is generally expressed in $\mathrm{keV} \cdot \mu\mathrm{m}^{-1}$. It describes the density of ionizations along the track and it varies as the radiation energy decreases during its propagation. It is used to describes the effect and action of radiation upon matter (in biology, electronics, ...). Typical LET values for radiations commonly used in radiotherapy are listed in Table 2.1.

The LET derives from the stopping power, but it describes the energy transfer to the material nearby the particle track, by secondary electrons. As a result, it does not include the nuclear stopping power. Besides, the LET represents an average quantity that does not take into account the discretisation of the energy transfers that are, in reality, occurring only during successive and separate events. It cannot be determined experimentally but is obtained from calculations.It indicates the quality of different types of radiation and is important in radiobiology because the biological effect of a radiation depends on it. Charged particles generally have higher LET than X and γ rays because of their greater energy deposition along the track. Notice that the higher their energy is, the lower their LET and therefore their biological effectiveness are.

Energy loss events are essentially randomly distributed along the track of a radiation. For low LET radiations like photons, the energy deposition events are sparsely distributed relative to the dimensions of biomolecules such as DNA. The amount of energy deposited by these radiations in a region of the track with such a scale size varies widely from a few eV to hundreds of eV. However for high LET radiations, energy loss events are much more closely spaced so the energy deposition is uniform at a biological molecule scale.

TABLE 2.1: Linear energy transfer values for typical radiations in water [Hall and Giaccia, (2012); Shapiro, (2002); Sprawls, (1995)].

Radiation		**Linear Energy Transfer**
Type	Energy	[keV · µm^{-1}]
Cobalt-60 γ-rays	1.2 MeV	0.2
x-rays	250 keV	2.0
Electrons	4 to 20 MeV	0.2
	100 keV	0.42
	10 keV	2.3
	1 keV	12
Protons	150 MeV	0.5
	10 MeV	4.7
	3 MeV	12
	1.5 MeV	20
	1 MeV	27
	0.1 MeV	93
Neutrons	14 MeV	75
α-particles	2.5 MeV	166
Fe ions	2 GeV	1000

Charged particle range

The **range** of a charged particle, with a given initial kinetic energy E_0 and propagating inside a certain medium, is the distance R over which it progressively losses (almost) all its energy to come to rest. A second related quantity, the **projected range**, is defined as "the farthest depth of penetration of the particle in its initial direction" [Attix, (1986)]. It is represented for protons as function of their energy up to 200 MeV in Figure 2.1. A third quantity, the **CSDA range** is a close approximation to the average path length travelled by the charged particle as it slows down to rest, calculated in the *Continuous Slowing Down Approximation*. In this approximation, the rate of energy loss at every point along the track is assumed to be equal to the total stopping power (sum of collision and nuclear stopping powers for ions), and energy-loss fluctuations are neglected. Its value is obtained by integrating the reciprocal stopping power with respect to energy :

$$R_{CSDA} = \int_0^{E_0} \frac{1}{S(E)} \, \mathrm{d}E. \tag{2.3}$$

The deposited energy can be obtained by integrating the stopping power over the entire path length of the particle while it travels in the material. The **detour factor** is the ratio of the projected range to the CSDA range. Particle trajectory is wiggly rather than straight, due to multiple scattering so the detour factor is always smaller than unity.

Heavy particles are not much deviated during collisions, so their trajectories are almost straight lines, with a similar range for a certain initial energy. Their detour factor is close to one except at very low energies. Because electrons are about two thousand times lighter, remote collisions (i.e. at large impact parameters) do not affect them much, but the occasional close collisions lead to major deviations. Thus, their trajectory is made of rectilinear segments with a few sudden angulations. The energy loss associated to close collisions changes randomly

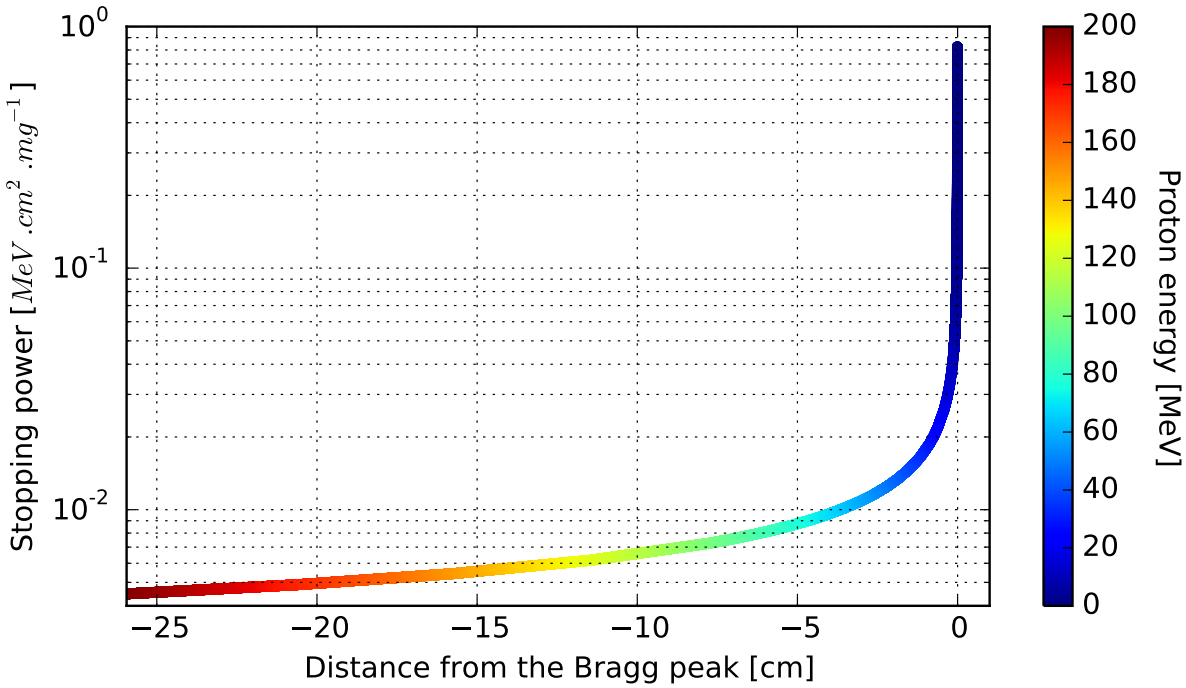

FIGURE 2.1: Mass stopping power of a proton with an initial energy of 200 MeV as function of the opposite of the projected range in liquid water. The colorscale is associated to the proton energy.

from an electron to another, so their range fluctuates significantly, and their detour factor is relatively low. As an example in liquid water, a 1 MeV proton as a detour factor of 0.99 and it only goes down to 0.5 at 17 keV, while it is 0.57 for a 1 MeV electron and reaches just 0.88 at 50 MeV [Berger et al., (1999); Fernández-Varea et al., (1996)]. This explains the shape of the relative transmission curves for various radiations as function of the thickness of an absorbing material, illustrated in Figure 2.2. Heavy ions are all stopped at the same absorber thickness, while the electron behaviour is more probabilistic with a transmission experiencing a slower and smoother decrease.

All the phenomena described previously contribute to an energy transfer, from the radiation giving up energy to the irradiated medium. This leads to the concept of absorbed dose.

2.1.3 Quantities and units

Radiation dose

The biochemical changes produced by ionizing radiations are the fundamental events leading to radiation damage in tissues. The biological effects were experimentally found to be proportional to the amount of energy deposited per unit mass of matter, with a dependence on the type and energy of the radiation, as well as on many factors concerning both the radiation and the absorbing material. It is therefore necessary to use specific quantities, and the most common ones are introduced in this section.

Radiation can be measured as **exposure** based on its ability to produce ionization in air under standard temperature and pressure, and it is the quantity indicated by some detectors such as

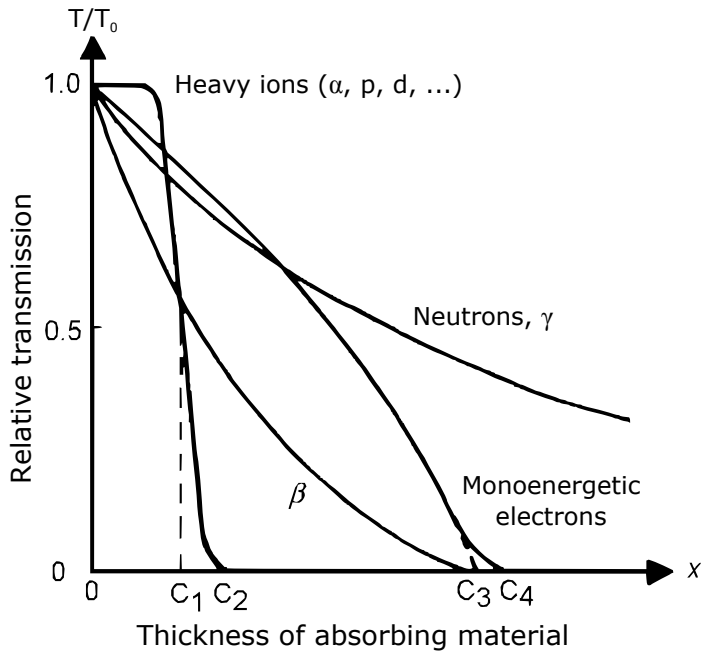

FIGURE 2.2: Curves showing the relative transmission T/T_0 of various types of radiation beams as function of the absorber thickness x. C_1 and C_3 are average, C_2 and C_4 maximum range. (Adapted from Choppin et al., [2013])

ionization chambers or Geiger-Müller tubes. Its S.I. unit is Coulombs/kg in air, or Roentgen in old units, with $1\,\mathrm{R} = 2.58\times10^{-4}\,\mathrm{C/kg\cdot air}$. A second quantity is generally preferred, describing the amount of energy absorbed in a system. It is the **absorbed dose** D representing the mean energy imparted by ionizing radiations to matter per unit mass.

$$D = \frac{dE_{dep}}{dm} \tag{2.4}$$

where dE_{dep} is equal to the kinetic energy of all ionizing particles entering the volume of mass dm, minus the sum of the kinetic energy of all ionizing particles leaving this volume, plus the sum of all the changes in rest energy of the nuclei and elementary particles involved in the interactions ($Q > 0$ if the rest energy decreases, and $Q < 0$ if it increases). It has the unit of joules per kilogram, named as Gray, and the Rad (for radiation absorbed dose) is still used sometimes: $1\,\mathrm{Gy} = 1\,\mathrm{J\cdot kg^{-1}} = 100\,\mathrm{rad}$. It can quantify exposure to any type of ionizing radiation with respect to any type of absorbing matter, so it is inadequate to estimate biological harmful effects because at equal levels of absorbed dose, different radiations may cause remarkably different damages.

The **dose rate** is the absorbed dose per unit time, expressed in the SI unit of Gray per second ($\mathrm{Gy\cdot s^{-1}}$).

Relative biologic effectiveness

The biological effectiveness of different types of radiation varying with a number of factors such as their LET and the irradiated biological system, the **equivalent dose** $H_{T,R}$ in a tissue T, irradiated by a radiation R, is defined as the absorbed dose $D_{T,R}$ in the tissue, multiplied by the radiation weighting factor w_R :

$$H_{T,R} = w_R \times D_{T,R}. \tag{2.5}$$

The **radiation weighting factor** w_R (unitless), formerly known as the quality factor, varies between 1 and 20, and some of its values are given in Table 2.2.

TABLE 2.2: List of radiation weighting factors w_R (in accordance with Euratom basic standards 1996).

Radiation		w_R
Type	Energy range	
Photons	all energies	1
Electrons and muons	all energies	1
Neutrons	<10 keV	5
	10 to 100 keV	10
	100 keV to 2 MeV	20
	2 to 20 MeV	10
	>20 MeV	5
Protons (other than recoil)	>2 MeV	5
Alpha particles, fission fragments, heavy nuclei		20

$H_{T,R}$ has the same fundamental unit of joule per kilogram as the absorbed dose, but it is given its own special name, the *sievert* (Sv), to acknowledge that it is derived from the gray by multiplying by a dimensionless scale factor. The equivalent dose cannot be measured but has to be calculated. This quantity enable to sum, for radioprotection purposes, the effects of irradiation of tissue by several types of radiation, leading to different risks for the same level of absorbed dose. As an example, the annual dose delivered by the radioelements naturally incorporated in the human body (mainly potassium 40 and carbon 14) is about 0.25 mSv, and the French regulatory dose limit is 20 mSv/year for radiation-exposed workers.

In addition to considering the type of radiation, it is necessary to take into account the different sensitivities of various tissues in order to estimate the health risk on the entire organism. For that purpose of representing the stochastic health effect on the whole body, the **effective dose** is defined as the tissue-weighted sum of the equivalent doses in all specified tissues and organs :

$$E = \sum_T w_T \times H_T \tag{2.6}$$

and according to the definition of the tissue weighting factor, their summation over all the tissues in normalized to one, that is $\sum_T w_T = 1$.

The effective dose to the entire organism can also be expressed, in an expanded form, as the summation of the absorbed doses multiplied by the appropriate radiation and tissue factors :

$$E = \sum_R w_R \cdot \left(\sum_T w_T \cdot D_{T,R} \right) = \sum_T w_T \cdot \left(\sum_R w_R \cdot D_{T,R} \right). \tag{2.7}$$

This relationship reflects the fact that the same effective dose is received either if the whole body is exposed homogeneously, or if all the organs are separately irradiated by the same equivalent dose. This quantity allows to calculate the cumulative risks associated to several partial irradiations.

The **relative biological effectiveness** (often abbreviated as RBE) of some test radiation under scrutiny compared with a reference radiation is defined by the absorbed dose ratio required for producing equal biological effects: RBE $= D_{ref}/D_{test}$. It is an experimental value which should be reported for well defined conditions. The RBE depends on many factors: irradiation (dose level and rate, fractionation) and biological (system studied, its sensibility, endpoint effect considered, oxygenation level) conditions.

In general, the RBE of a particular radiation increases with its LET up to a peak at about 100 keV · µm^{-1}, which corresponds to an energy of 0.1 MeV in the case of protons. It usually declines above this value due to energy deposition in excess of that needed to cause the biological outcome, an effect called *overkill* [IAEA, (2010)] (see Figure 2.3). As higher the radiation dose, the LET and/or the RBE, as more likely damages may occur. The effects are typically described by empirical *dose-response curves* (see section 2.2.2).

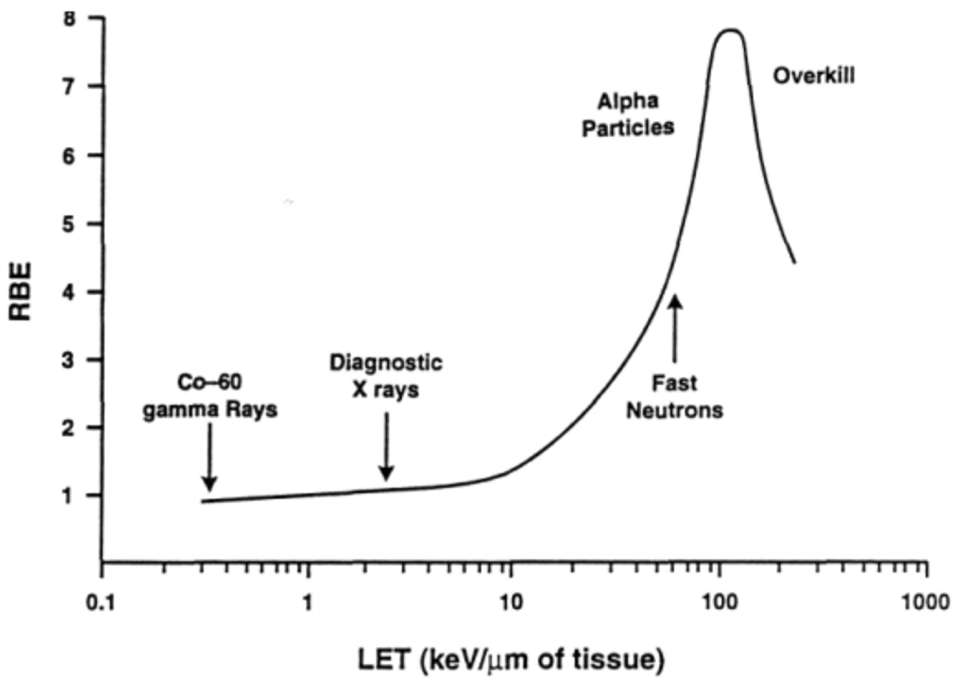

FIGURE 2.3: Dependance of the relative biological effectiveness on the linear energy transfer. For low LET radiation, the RBE is proportional to the LET. For higher LET, the RBE increases to a maximum. The subsequent drop is caused by the overkill effect. (Taken from [IAEA, (2010)])

In the present work, the reference radiation is 200 kV[1] x-rays, and RBE values are calculated from survival curves. The endpoint chosen for comparison is the D_{10} value, the dose required to cause a surviving fraction of 10 %.

[1]Voltage corresponding to the maximum electric potential used by the linear accelerator to produce the photon beam ; the maximum output photon energy is approximately equal to this maximum electric potential times the electron charge.

2.2 Radiotherapy methods and techniques

2.2.1 Mechanism of action

Cancer cells have mutations that make them to behave differently to normal cells. They tend to divide more often, proliferate and take over the body as they move through the mitosis phases more quickly. Because replication is a critical process, DNA damages caused when a cell is undertaking division will be more likely to unable it. If it concerns a cancer cell, the growth of a tumour is inhibited. Hence, cytotoxic treatments (chemical or via radiations) affecting the cell division process are used to treat cancers.

The irradiation of a living tissue can induce various effects at different physical and time scales, through processes that are illustrated in Figure 2.4.

Radiation effects at the molecular level

When a radiation strikes a living cell, it deposits energy while interacting with water, the main constituent of the cell at 70 %. The energy loss causes ionizations and breaks up molecules along a narrow track. The radiation decomposition or **radiolysis of water** leads to the production of *free radicals* like hydroxyl radicals $HO^{\bullet}$ and *oxidizing products* like hydrogen peroxide H_2O_2, that have a short lifetime of about 10^{-7} s. These hydrolysis products are highly reactive and can transfer excitation energy to the DNA, breaking the bonding between the two helices or between nucleotides of the same strand. This process is called **indirect action** of radiation, as pictured in Figure 2.5. To a lesser extent, the radiation may interact directly with the molecules of the cell in a **direct hit**. The DNA helix has a diameter of about 2 nm and it is estimated that outside nucleosomes, free radicals produced in a cylinder with twice that diameter can affect the DNA [Hall and Giaccia, (2012)]. Indirect action is dominant for sparsely ionizing radiation, but direct action dominates in the interaction of high LET particles. In both cases, biological damages are more severe if they affect the cell nucleus and DNA, as they are the hardest to repair.

2.2.2 Cellular biology techniques

DNA damage detection by immunofluorescence

In the absence of any external attack, cell DNA is deteriorated by free radicals formed by the natural oxygen metabolism. Cells have acquired during their evolution an ability to repair damages caused by usual environmental conditions (in the order of mSv/year but with a large geographic variability). But a therapeutic irradiation can generate lesions that are more concentrated in space and time. The most deleterious DNA lesions are **double-strand breaks** (BSBs), which may lead to chromosome aberrations or cell death if left unrepaired. Cells react by activating the *DNA damage response*, a complex molecular mechanism that senses, signals and repairs DNA lesions.

The formation of DSBs triggers many reactions, among which *phosphorylation of the histone variant H2AX*, producing **γH2AX** [Rogakou et al., (1998); Podhorecka et al., (2010)]. This event plays a key role in the repair process and the interruption of the cell cycle progression. The presence of γH2AX can be measured as an intracellular marker of DSBs, and used to detect the genotoxic effect of toxic substances. It also allows to monitor the efficiency of a treatment

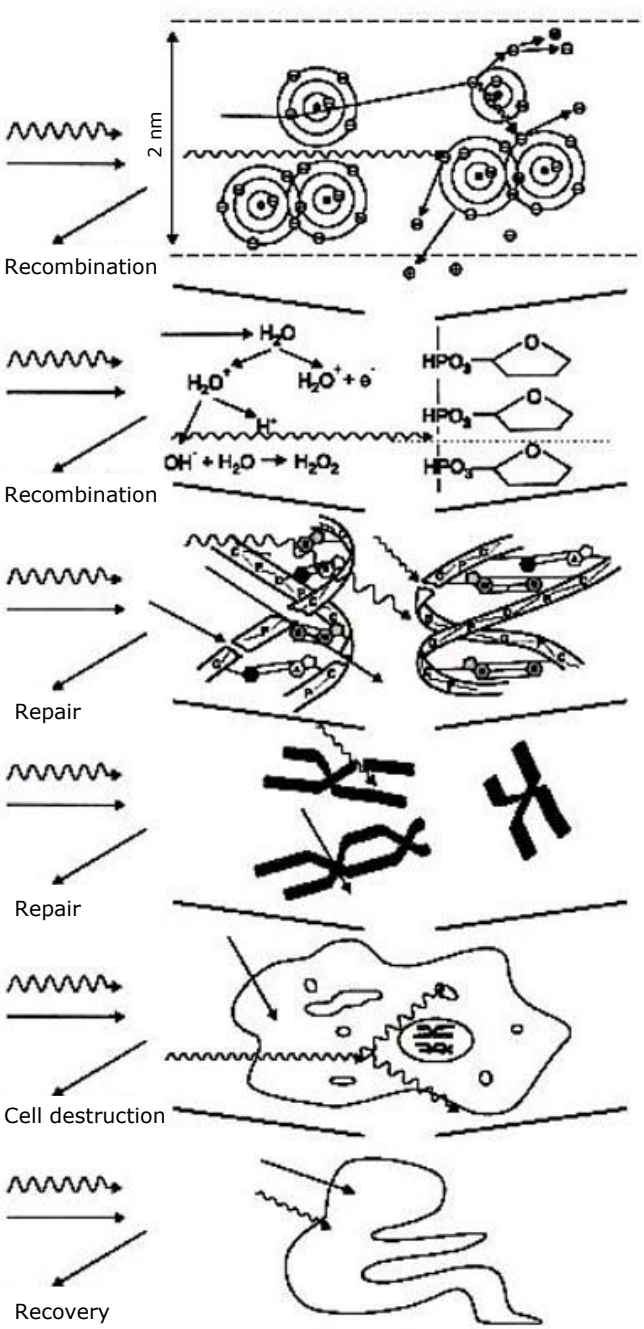

Process	Time scale
Ionization excitation	ns, μs
Producing radicals, Radiolysis, Breaking chemical bonds	μs, ms
Single and double strand breaks, Strand cross-links	s, hours
Chromosome aberrations	hours, days
Cell damages	days, weeks
Somatic and hereditary diseases	weeks, years, decades

FIGURE 2.4: Development of early and late radiation effects in a living system and time scale of the processes involved, modified from [Nagy, (2009)].

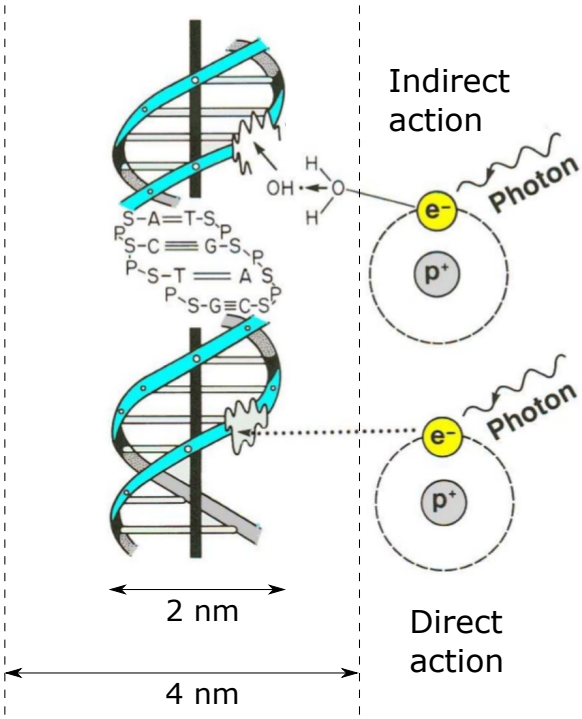

FIGURE 2.5: Direct and indirect actions of radiation on the DNA structure shown schematically on the left. In direct action, a secondary electron interacts with the DNA to produce an effect. In indirect action, the secondary electron interacts with, for example, a water molecule to produce a OH• radical, which in turn produces the damage to the DNA. (Modified from Hall and Giaccia, [2012])

and assess the sensitivity of tumour cells to irradiation. Each **nuclear foci** sites of a DNA damage contains thousands of γH2AX molecules that can be detected using *antibody staining and fluorescence microscopy*, and their number is directly correlated to the number of DSBs.

An advantage of γH2AX compared to other DNA damage markers is its high sensitivity that enables to detect small changes in genome integrity at a single cell level. In return, a non-zero background level of nuclear foci is usually observed in unstressed cells, hence the need for control samples. It is thought that residual foci at late delays following irradiation ($> 12\,\mathrm{h}$) represent unrepaired DSBs that could lead to subsequent cell death. Some damages being repaired with time, care should be taken on the delay between irradiation and fixation of the sample.

Immunofluorescence microscopy is an immunostaining technique used with fluorescence microscopy to visualise the location of proteins of interest through specific antibody fixation on biological samples thanks to fluorophores. A *fluorophore* is a chemical compound that can emit fluorescent light at a characteristic wavelength upon excitation by absorption of a photon.

Cell survival assay

The graphical representation of the relationship between the survival proportion of a cell lineage and the absorbed radiation dose constitutes a **cell survival curve**. "Survival" may mean different things in different context, but the gold standard for measuring the *radiosensitivity* of a cell population is the *retention of reproductive integrity*, that is the ability of a cell to undergo several divisions and produce in a period varying from one to two weeks a viable colony containing at

least 50 cells. Such a survivor able to proliferate indefinitely to produce a large colony is said to be *clonogenic*. However, these clonogenic assays requires a large and uniform irradiation area as the colonies that grows should not merge if one wants to make an accurate counting.

This is why, as in our case, one may start with a simpler test and turn toward **cell viability assays** that only evaluate the cell survival rate. In this case, the cell concentration on the sample can be much higher, up to filling the dish surface with a cell monolayer. The sample is also usually cultured for 5 times the cell *doubling time* between the irradiation and the counting analysis. This ensures that the cells damaged beyond possible repair have the time to die. For each assay, the survival of a control unirradiated sample is used to determine the reference value in untreated conditions (0 Gy).

Survival curves are best shown as a semilog plot of survival (on a logarithmic scale) against irradiation dose (on a linear scale), as shown in Figure 2.6. The most common model is the **linear-quadratic model**, fitting the experimental results of the survival decline S with increasing dose D using a second-order polynomial described by two constants α and β:

$$S = e^{-(\alpha D + \beta D^2)}. \tag{2.8}$$

This model assumes the existence of two components to cell killing by radiation: one that is proportional to the dose (represented by the parameter α) and another proportional to the square of the dose (represented by β). For α-particles and other densely ionizing radiations, the dose-response curve is almost a straight line from the origin. The survival is an exponential function of the dose and $\beta \approx 0$.

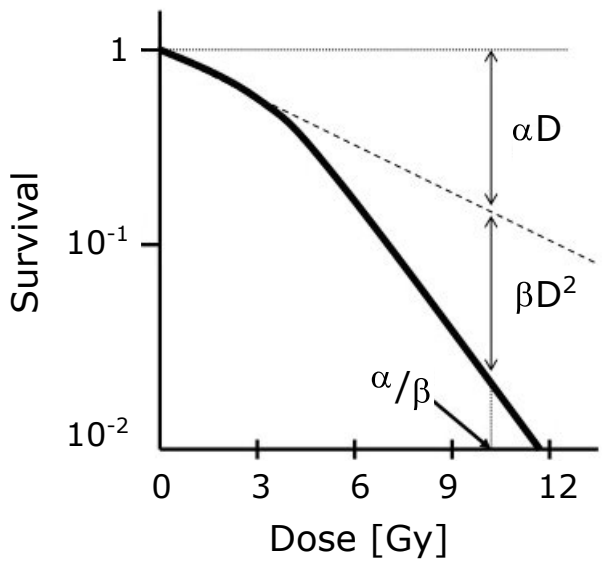

FIGURE 2.6: Typical shape of survival curve for cells exposed to radiation. The fraction of cell surviving is plotted on a logarithmic scale against dose on a linear scale. The experimental data are fitted to a linear-quadratic function. There are two component of cell killing: one is proportional to the dose, while the other is proportional to the square of the dose. The dose at which the linear and the quadratic components are equal is the ratio α/β.

2.2.3 Fractionation and beyond

When cells are exposed to several acute irradiations separated by a variable delay, it was found that the clonogenic survival increases with the time gap to reach a plateau after a few hours [Elkind and Sutton, (1959)]. This phenomenon was explained with the concept of *sub-lethal damage*. The radiation tolerance of normal tissues is enhanced by *fractionating* the dose over a number of days due to repair of damages between the fractions followed by proliferation of the surviving cells. Thus, higher doses can be given with this **fractionation** approach, which is prevailing in today's radiotherapy treatments.

The most common protocol in fractionated external radiotherapy is to deliver a dose of 2 Gy per day, 5 days per week, for several weeks until the desired cumulative dose is reached [Tubiana, (2008)]. A typical adjuvant therapy dose to cure a cancer is 50 Gy. With this method, each fraction contains a small dose that is tolerated by healthy tissues, but that gradually accumulates to form the total dose in the tumour. Sub-lethal damages are induced but the 24 h delay ensure that all of them are repaired in the healthy cells, while a significant portion of cancer cells are exposed to radiations during the most vulnerable phases of their cell cycle. To preserve even more healthy tissues, the incident angle of the irradiation beam is changed for at least each session. Because malignant cells replicate faster without taking time to recover after suffering damages, this technique allows to treat effectively the cancerous cells, whilst leading to less damage affecting normal tissues. Fractionation also has an effect on RBE values ; they are lower for high-dose administered all at once and larger for multiple small fractions [Joiner and Johns, (1987)].

Other fractionation schedules are currently under research, to test if they may either be more effective or more convenient than traditional fractionation, for instance:

- *accelerated fractionation*: treatment given in larger daily or weekly doses to reduce the total treatment time;
- *hyperfractionation*: smaller doses of radiation given more than once a day;
- *hypofractionation*: larger doses given in fewer visits, once a day or less often.

When pulsed radiation beams with high dose rates are used, one can also consider alternatives beyond these regimen variations that are on an hour time scale. The **pace** at which the shots are delivered could be varied on a shorter time scale in the order of seconds, leading to potentially different biological responses and new more suitable treatment schemes. A preliminary exploration of this effect was investigated during the radiobiological experiments performed in SAPHIR, as delay between shots is a parameter that can easily be varied. The results are presented in the last chapter (section 6.2.3).

2.2.4 Proton beam therapy

High energy ions, including protons, are attractive for radiotherapy because of their peculiar behaviour. They do not interact much with matter and are sparsely ionizing except for a short region at the end of their trajectory, when they have a low velocity just before they stop. This maximum in their *percentage depth dose curve* close to the end of their range is called the **Bragg peak**, and its depth depends on initial energy of the particle as shown in Figure 2.7. Besides, the RBE of protons is similar from that of 250 kV x-rays, with a value of about 1.1 relative to high-energy photons [Paganetti, (2014)]. A second advantage of ions their smaller average *scattering angles* compared to electrons, leading to a reduced *penumbra* especially for heavy ions. Therefore protons offer special advantages specially in medical applications, enabling to deposit high energy densities at a given depth in a body while sparing the nearby tissues as illustrated in Figure 2.8.

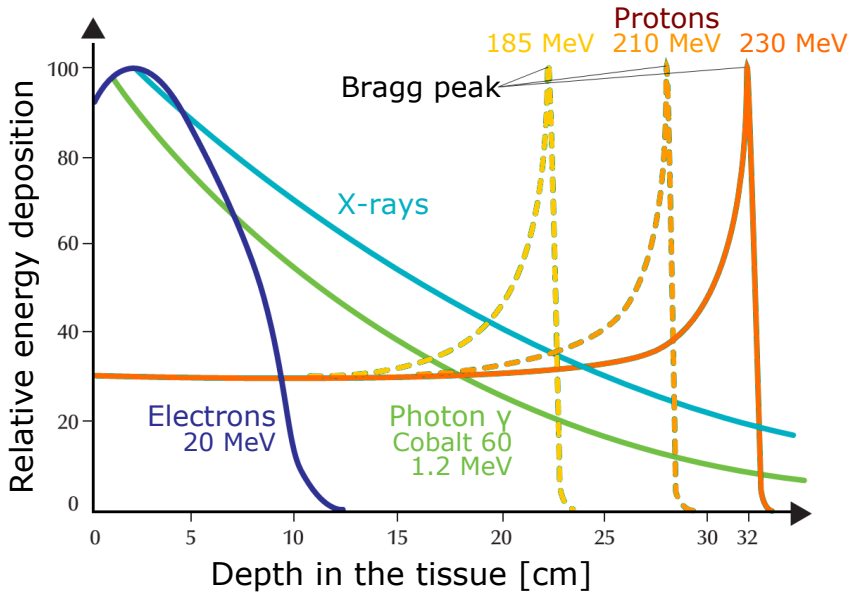

FIGURE 2.7: Relative energy deposition of various ionizing radiations. Note the peak at the end of the proton range, called the Bragg peak, and its shift in depth as function of the proton initial energy.

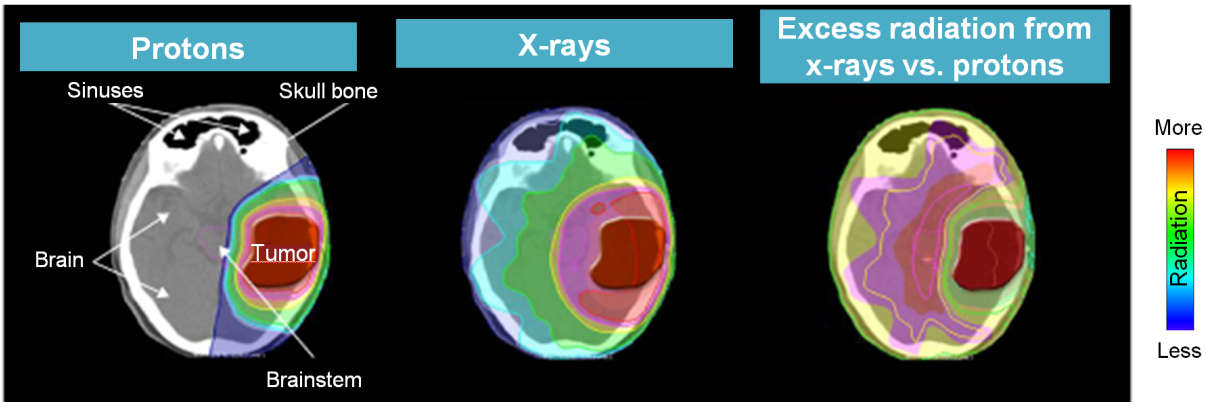

FIGURE 2.8: Less healthy tissue around the brain tumour receives radiation with protontherapy (left) compared to x-rays radiotherapy (center). The dose received in excess is represented with the colorscale on the right.

Protontherapy is a type of external beam radiotherapy that uses a beam of protons in cancer treatment to irradiate diseased tissues. Thanks to the ballistic qualities of protons allowing high doses to be delivered to small tumours with limited damage to the surrounding normal tissues, it is a medical procedure particularly recommended to treat tumours that are invasive or located close to sensitive organs such as the brain, the eye or the spinal cord. It is also prescribed in paediatrics, where the reduction of the integral dose to the normal tissues lessens potential unwanted side effects in the long run, such as the occurrence of radio-induced cancers.

2.3 Conclusion

When a radiation interacts with matter, it leads to various effects. They are nonetheless all related to a transfer of energy that is absorbed by the material. Specific quantities are defined to assess the consequences this may have on living things, as radiation may be generated artificially for medical use. Biologists have developed a number of procedures that enable to monitor the reaction of tissues to damages caused by their exposure to radiations. Protons have a distinctive physical dose deposition distribution, compared to other ionizing radiations such as electrons or x-rays, which makes them notably adapted for the treatment of certain cancerous tumours.

Chapter 3

Proton Acceleration on SAPHIR

The experimental activities described in this thesis were performed on the SAPHIR facility at LOA in Palaiseau (France), that comprises a laser delivering high-intensity ultrashort pulses and a target interaction chamber required for particle acceleration experiments. I witnessed the first shots of the facility in December 2013, which were followed by a period of characterisation and optimization of the laser chain, including an upgrade during the summer 2015. The experimental setup used for ion acceleration is described at the beginning of this chapter. Then, some of the used ion beam characterisation techniques are outlined. Finally, experimental results of the ion beam measurements are presented.

Contents

3.1 Experimental infrastructure **46**
3.1.1 SAPHIR 200-terawatt laser system 46
3.1.2 Laser characteristics 49
Enhancement of the temporal contrast ratio 49
Pulse duration 52
Focal spot and adaptive correction of the phase front 52
3.1.3 Target irradiation conditions 54
3.2 Ion diagnostics **54**
3.2.1 Thomson parabola spectrometer 54
3.2.2 Detectors 57
CR-39 etched track detector 57
Radiochromic film 57
Image plate 58
3.2.3 Detector stacks and filters 59
3.3 Ion acceleration experiments **59**
3.3.1 Solid target developments 61
3.3.2 Effect of the laser pulse temporal contrast 62
3.3.3 Scan in focus position 62
3.3.4 Ion beam energy spectrum 65
3.3.5 Energy-resolved divergence of the proton beam source 67
3.3.6 Front and back side acceleration relationship 69
3.3.7 Spectroscopy with a synthetic diamond 69
3.4 Conclusion **71**

3.1 Experimental infrastructure

In this section, the laser system is presented, along with its technical specifications and achieved performances. The elements encountered from the initial light source to the target, place of the laser-matter interaction, are described.

3.1.1 SAPHIR 200-terawatt laser system

The **SAPHIR laser** was implanted at Laboratoire d'Optique Appliquée by *Amplitude Technologies* in 2013. It is a femtosecond, double CPA laser chain, designed as follows to reach an energy per pulse of 6 J before compression and a peak power of 200 TW at a repetition rate of 5 Hz, hence an average power of 25 W (see scheme in Figure 3.2 and a picture in Figure 3.1). Since its upgrade in June 2015, the system is made of two CPA modules.

- The *oscillator* is a commercial Synergy pro laser manufactured by *Femtolasers*. This Ti:Sapphire, Kerr-lens mode-locked laser produces a train of pulses with a duration below 10 fs, at a repetition rate of 76 MHz and with an energy per pulse of 6 nJ. Its central wavelength is $\lambda = 800$ nm and the FWHM spectrum is 100 nm.
- The repetition rate of the oscillator is cut down to 10 Hz by a Pockels cell. The selected pulse is stretched, pre-amplified to 4 mJ and compressed back to 35 fs, before being injected in the XPW system. The *Superbooster* or CPA1 is composed of the following elements:
  - *Booster*: the beam is amplified before being cleaned while passing through a *saturable absorber* (SA) which operates nonlinear filtering to remove residual ASE background coming from the oscillator. A *Pockels cell* selects the pulse to be amplified.
  - *Öffner-type stretcher*: it stretches the oscillator output spectrally before amplification. An *acousto-optic programmable dispersive filter* [Tournois, (1997)] (AOPDF or Dazzler) is inserted to shape the spectral phase and amplitude of the ultrashort pulse, and compensate for group delay time dispersion within the chain.
  - *Regenerative amplifier*: the pulse is amplified in a Ti:sapphire crystal pumped by a frequency doubled Nd:YAG laser with a high gain while providing a beam with a good spatial quality.
  - *Compressor*: the pulse is then recompressed by a grating compressor.
- *XPW*: the contrast ratio of the pulse is enhanced in a nonlinear crystal after spatial filtering of the beam passing through a hollow-core fiber. It has a very low efficiency hence the requirement of having the first CPA stage.
- *CPA2*: similarly to the CPA1, it is comprised of:
  - a stretcher including a Dazzler;
  - a regenerative cavity; an *acousto-optic programmable gain control filter* [Oksenhendler et al., (2006)] (AOPGCF or Mazzler) is inserted to optimize the spectral losses inside the regenerative cavity and maintain an ultra short pulse duration.
  - a multipass *Ampli* 600 mJ is used to amplify the beam with a low gain.
  - a *cryogenically-cooled* multipass amplifier: this is the last amplification stage, bringing the pulse energy up to 6 J;
  - a compressor.

- End of the transport line toward the experimental chamber, with:
  - turning boxes: bringing the laser beam downstairs in the pit where is located the experimental chamber;
  - a *deformable mirror*: correcting the beam phase front, reducing some of the distortions added during propagation throughout the chain.

FIGURE 3.1: Picture of the SAPHIR laser system of which details are provided in the explanatory diagram of Figure 3.2.

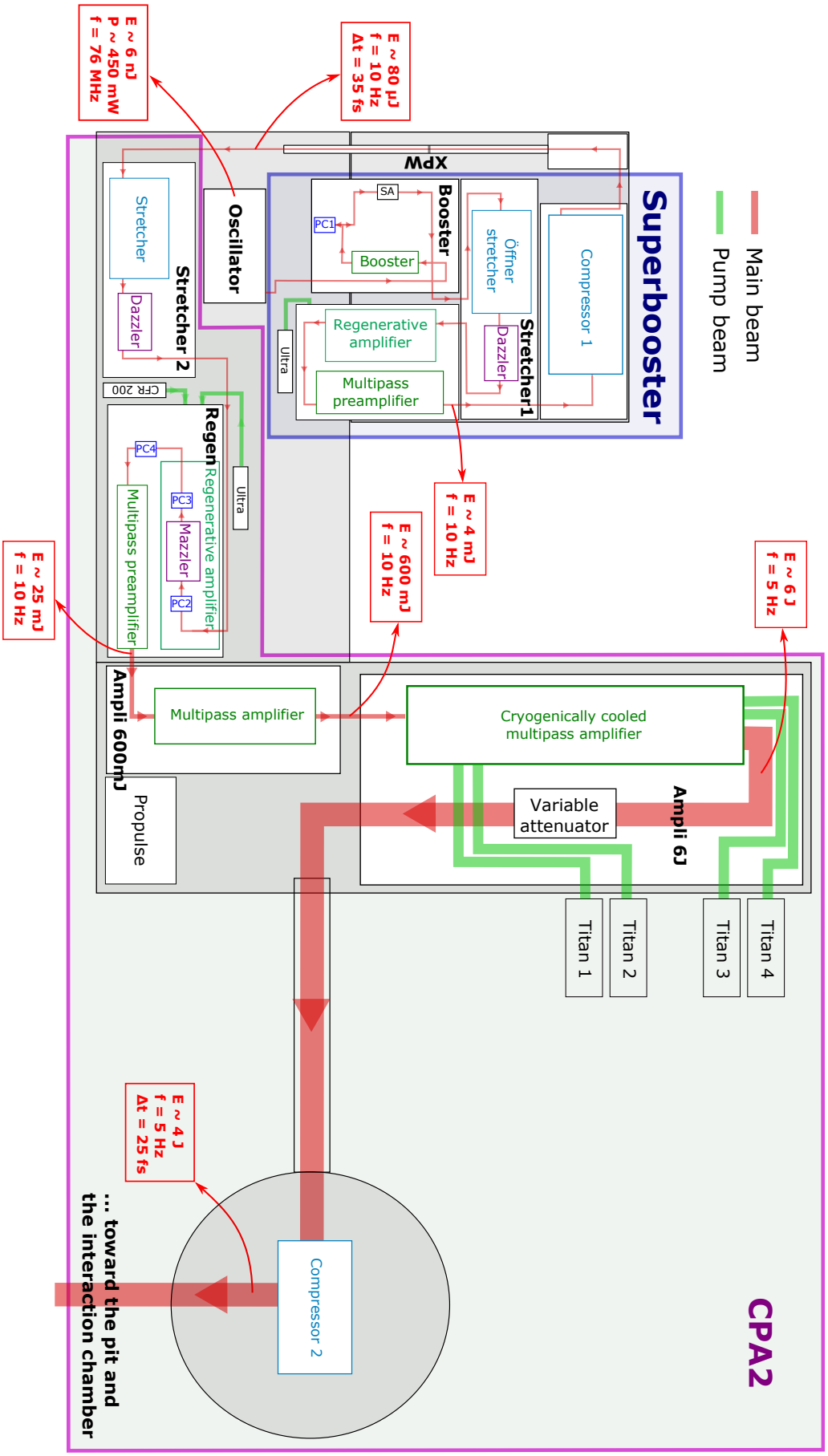

FIGURE 3.2: Diagram of the SAPHIR laser system, a double CPA Ti:sapphire laser chain.

3.1.2 Laser characteristics

The laser parameters are tuned in order to reach the highest intensity on target, with the lowest surrounding spatial and temporal background. This can be attained by shortening the pulse duration and concentrating the beam on a small spot.

Enhancement of the temporal contrast ratio

The **temporal contrast** of a laser pulse is the ratio of the peak intensity of the main pulse to its background level, as illustrated in Figure 3.3. Several effects may be observed in a CPA chain.

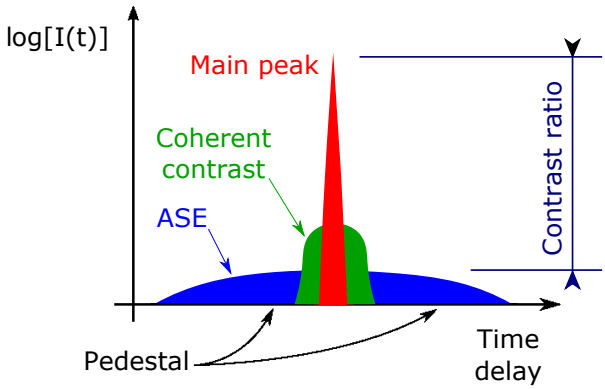

FIGURE 3.3: Schematic time dependence of a short laser pulse intensity, to illustrate the contrast ratio dimensionless quantity.

Pre- and post-pulses are replicas of the main femtosecond pulse that can be before and after the main pulse. They can originate from an insufficient extinction of the Pockels cells selecting the pulse from the oscillator and the regenerative cavities, cuts in the spectrum, or multiple reflections and shortcuts in the optical path.

Amplified Spontaneous Emission (ASE) comes from the spontaneous emission from the pumped gain media, that is amplified by stimulated emission in the crystals of the forthcoming stages before the passage of the main pulse. The contrast worsening is directly correlated to the gain in the amplifiers and to the timing between the pump laser pulses (used to charge the media) and the seed laser pulse (to be amplified). Together with the *coherent contrast* coming from the spectral shape and its deformations, they represent the nanosecond scale *pedestal* surrounding the main laser pulse.

The contrast plays a major role in laser-matter interaction at high intensities, as it is one of the main factors determining the dominant ion acceleration mechanism in action and the maximum achievable ion energies. In the TNSA theoretical framework, the transverse spreading of the electron beam passing through the target is reduced with the target thickness. It results in a higher electron density in the rear surface sheath, hence a higher accelerating field and higher ion energies with better conversion efficiencies [Neely et al., (2006)]. But for a laser pulse with a non perfect contrast, there is an optimal target thickness, below which the acceleration conditions worsen [Kaluza et al., (2004)]. The laser pedestal associated to a low contrast can significantly change the foil properties, with premature ionization, heating and expansion of the target leading to its deformation and eventually its destruction (for nm scale target thicknesses) prior to the arrival of the main pulse. The deleterious effects of prepulses have also been examined by Batani et al., [2010].

The temporal contrast is measured via a *high dynamic third-order cross-correlator* SEQUOIA fabricated by *Amplitude Technologies*, which is able to measure intensity profile over more than 10 orders of magnitude and works as follows. The main pulse is split in two lines, with one being frequency doubled and delayed. The two beams are recombined into a third harmonic generator (THG) producing a signal proportional to the temporal overlap between the two pulses into the THG crystal. The evolution of the signal with respect to the time delay gives the pulse temporal profile.

If what is of most concern is the pulse temporal shape before the main peak, recordings for positive delays is also useful to determine if the features observed are real or simply replicas coming after the main peak, as it can be understood from the principle of the measurement based on THG. If a peak is observed in the negative delay region along with a symmetrical and stronger peak in the post-pulse domain, then both are just related to a post-pulse replica. However if a negative delay peak does not have a higher counterpart in the positive region, then it is a real pre-pulse.

The contrast was measured in April 2014 at the end of the chain, which included only a *saturable absorber*, around 1×10^{-8} about 40 ps before the main pulse, as shown in Figure 3.4. The contrast was measured again after the XPW upgrade in June 2015, after the first CPA stage

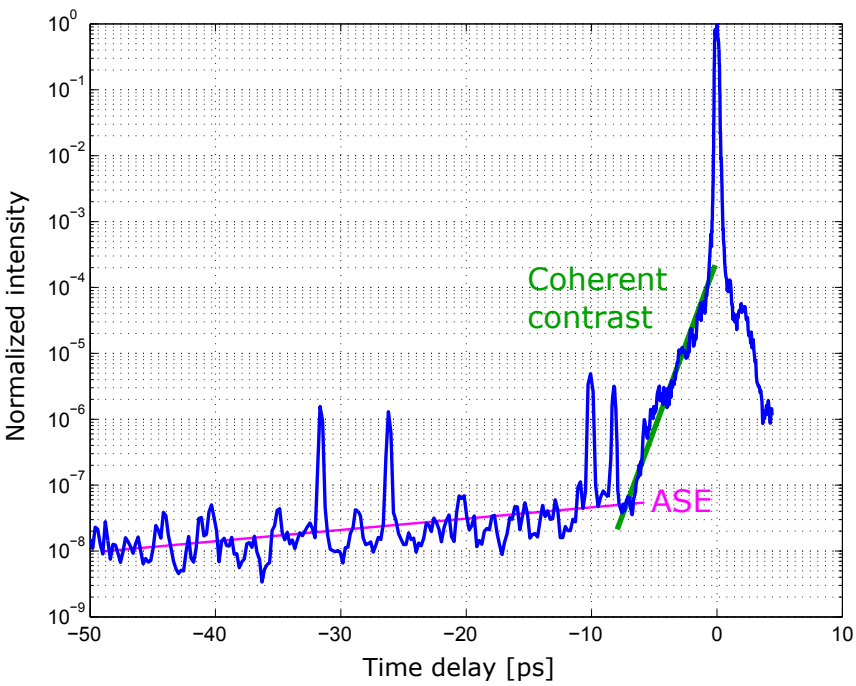

FIGURE 3.4: SAPHIR laser contrast before the upgrade.

at 2.5×10^{-10} about 50 ps before the main pulse (see Figure 3.5), and after XPW cleaning at the output of the second compressor at 4×10^{-11} about 100 ps before the main pulse (see Figure 3.6).

The **cross polarized wave** (XPW) generation [Jullien et al., (2005); Jullien et al., (2006); Jullien et al., (2007)] is a technique used for contrast enhancement, developed at the *Laboratoire d'Optique Appliquée* and based on nonlinear and anisotropic properties of $\chi^{(3)}$ tensor in cubic crystals such as BaF_2.

The nonlinear crystal plate is sandwiched by a polarizer–analyzer pair, and a linearly polarized wave is generated at the same frequency but with a polarization rotated with respect to

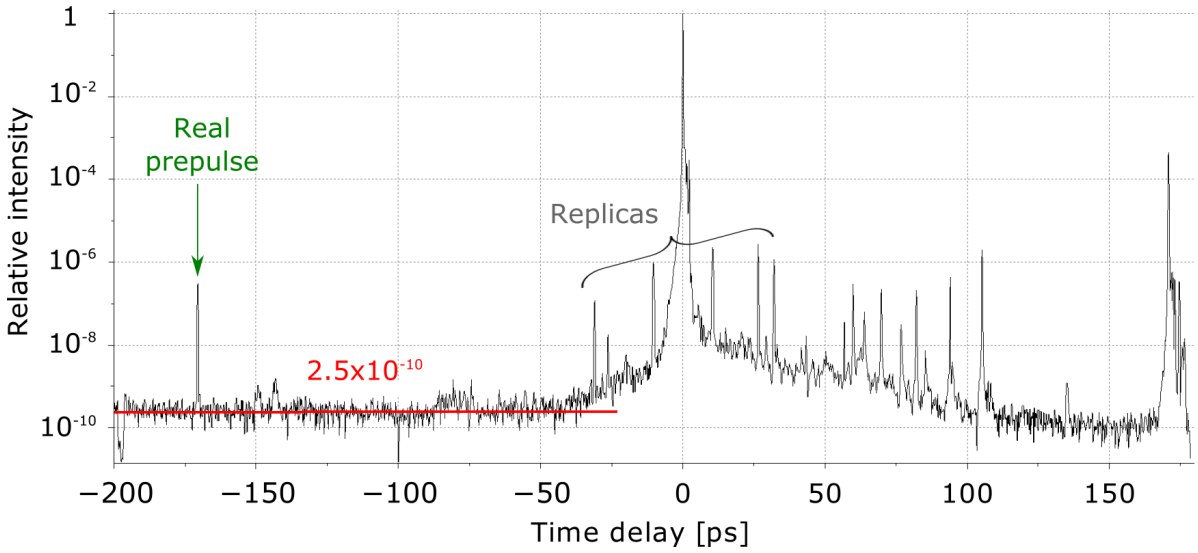

FIGURE 3.5: Contrast at the CPA1 output.

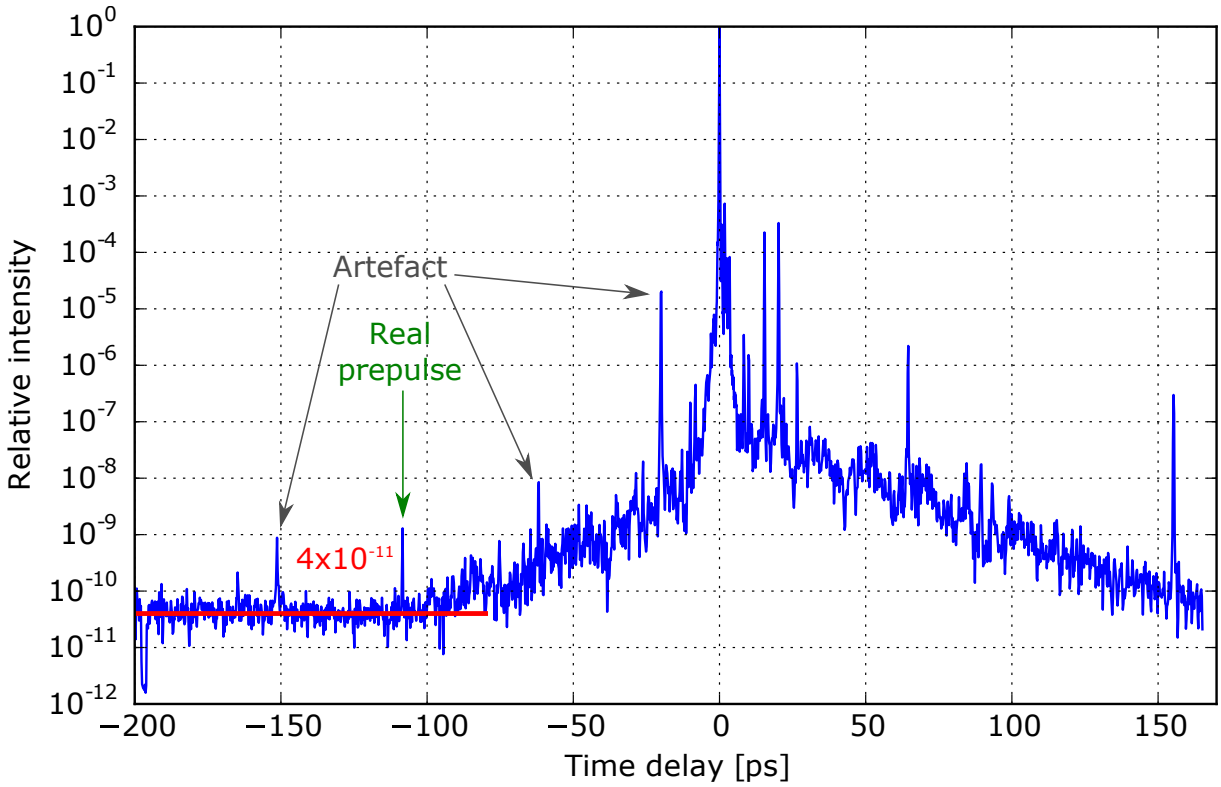

FIGURE 3.6: Temporal contrast of the SAPHIR laser after XPW at the CPA2 output.

the input fundamental wave. The temporal filtering results from the third order dependency of the XPW output field on the input field, and the contrast enhancement is limited only by the extinction ratio of the polarization discrimination device.

Pulse duration

The laser *pulse duration* is measured after the first and second compressor, in the latter case using a leakage mirror. Optimizing the distance between the two gratings in the compressors, a FWHM pulse duration of respectively 35 and 25 fs is obtained.

We used a Wizzler, a single-shot high contrast pulse measurement device manufactured by *Fastlite*, which is based on self-referenced spectral interferometry [Oksenhendler et al., (2010)].

Focal spot and adaptive correction of the phase front

The $D = 80$ mm diameter beam is focused with a 30° off-axis parabolic (OAP) mirror having a 100 mm diameter and a focal length of $f = 240$ mm, hence an *f-number* or *relative aperture* of $N = f/D = 3$. The theoretical beam waist diameter is $2w_0 = 4\lambda f/\pi D = 3.1$ µm, hence a Rayleigh range (see eq. (1.8)) of $z_R = \pi w_0^2/\lambda = 9.2$ µm, which sets the precision scale required for the target alignment. The laser **focal spot** is imaged at the *target chamber center* (TCC) by a microscope objective ×20, used out of its working distance, on a 12-bit CCD PCO Pixelfly VGA camera. The imaging system has an effective magnification of ×82, and a resolution of 0.12 µm/pixel.

The ability to focus the beam, and concentrate the laser energy into the smallest spot as possible, depends on the quality of its transverse profile. Inevitable distortions are introduced by the many refractive optics and nonuniform effects in the amplifying crystals present along the laser chain.

First, the focal spot shape and size were optimized manually. Two types of astigmatisms are minimized independently, adjusting in parallel the last mirror and the focusing parabola with their lateral or vertical motor. The focal spot can be improved further with a **deformable mirror** (DM), allowing to correct aberrations such as coma, trefoil or remaining astigmatism. The DM operates using 52 mechanical actuators, with astatic floating heads and arranged in cylindrical symmetry, that perform wavefront shaping with a nanometric precision by correcting up to the 6th order of aberration in Zernike polynomials [Zhu et al., (1999)]. The beam transverse profile is measured with a *Shack–Hartmann wavefront sensor* (HASO by *Imagine Optic*), that is used to build the correlation matrix. It represents the action of each actuator movement on the phase-front projected on the space of Zernike polynomials. Then, a numerical interpolation finds the best configuration for the actuator set.

Some distortions are still visible in Figure 3.7, but no adaptive optics were available to correct the phase front of the laser beam for this experiment. The analysis of the image indicates that 26 % and 59 % of the laser energy is located respectively in the FWHM (marked in violet) and I_0/e^2 (in green) intensity contour lines, with an average diameter of 10 µm and 24 µm. The integrations of the contoured areas were calculated numerically after subtracting the background level.

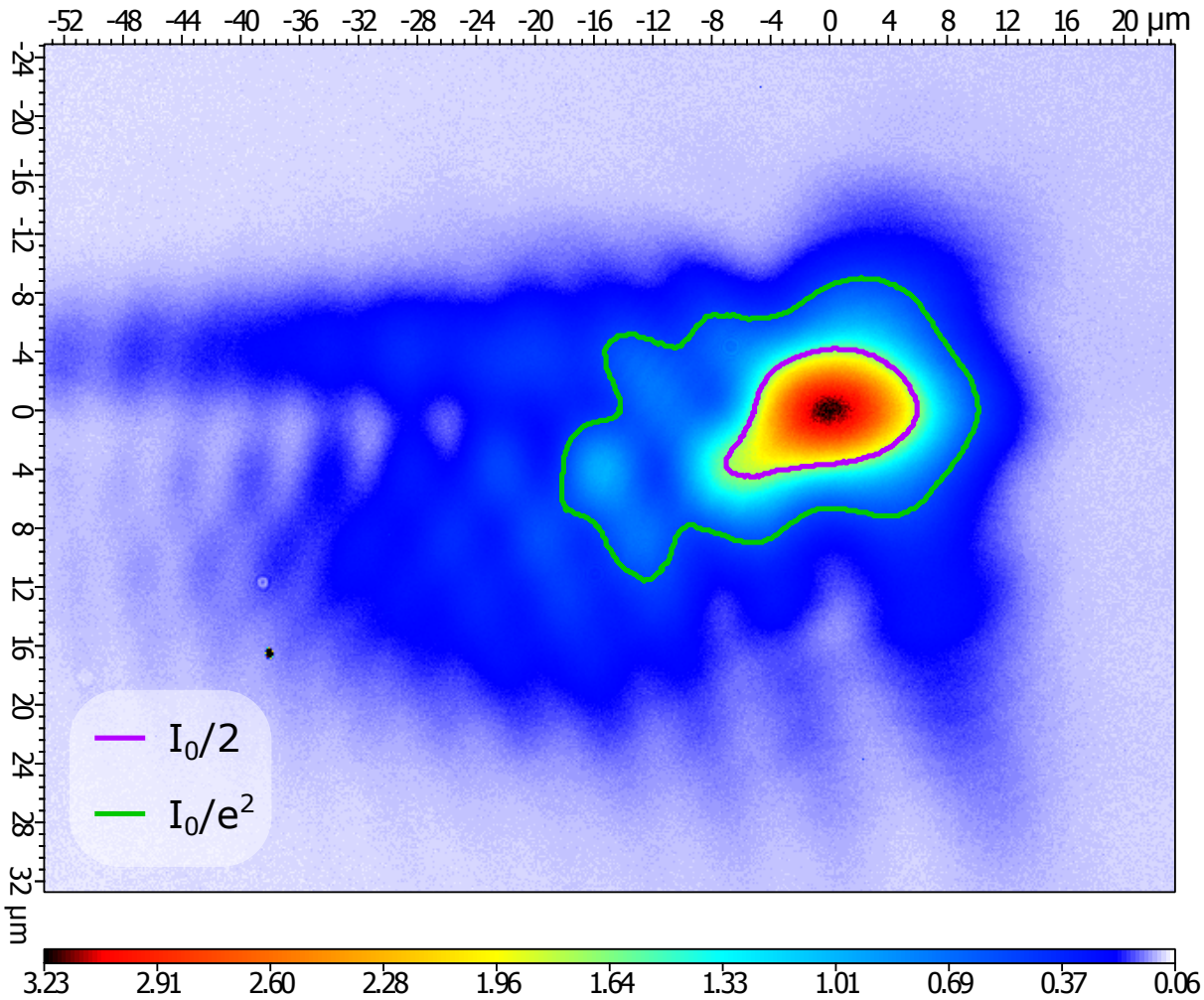

FIGURE 3.7: CCD image of the SAPHIR laser focal spot, with contour lines at half (in violet) or $1/e^2$ (in green) of the maximum intensity. The laser intensity was reduced to prevent from damaging the camera during the measure: the propulse and 2 titans were turned on, the transmission was at 0 % and 6.5 neutral optical density filters were placed in the CPA2 between the attenuator and the compressor. The deformable mirror was not available at this time.

3.1.3 Target irradiation conditions

The optical losses occurring along the laser beam transport were measured with a calorimeter (QE50LP-H-MB-QED by *Gentec Electro-Optics*), from the output of the last amplification stage right after the CPA2 crystal (where the pulse energy is maximum and reaches 6 J) to the target in the interaction chamber (skipping the deformable mirror). The *transmission efficiency* is $T = 52\,\%$, hence a total energy on target of $E_t = 3.1\,\mathrm{J}$ per pulse with a $\Delta\tau = 25\,\mathrm{fs}$ duration. Given a 59 % of energy in the $2w_0$ contour (displayed in green in Fig. 3.7) encircling an area of $A_{e^2} = 370\,\mu\mathrm{m}^2$, the resulting peak power and intensity on target are:

$$\mathrm{P}_0 = \frac{TE_t}{\Delta\tau} = 74\,\mathrm{TW} \;\text{ and }\; \mathrm{I}_0 = \frac{2\mathrm{P}_0}{A_{e^2}} = 4\times10^{19}\,\mathrm{W}\cdot\mathrm{cm}^{-2}. \tag{3.1}$$

The FWHM wavelength bandwidth is about $\Delta\lambda = 70\,\mathrm{nm}$ or $\Delta\nu = 33\,\mathrm{THz}$ with $\nu = c/\lambda$, hence a time-bandwidth product of $\Delta\nu\Delta\tau = 0.82$ (above the 0.44 limit obtained for an ideal transform-limited pulse). The pulse has a horizontal polarisation (linear).

3.2 Ion diagnostics

Besides the dose integrating detectors widely used in the medical and physics field (such as CR39, RCF or IP), real-time detection systems (like a MCP associated with a Thomson parabola to provide spectral information) are crucial to characterise ion beams. Other methods and tools exist but have not been used systematically, for example time-of-flight mass spectrometry, scintillators or nuclear activation schemes [Bolton et al., (2014)].

3.2.1 Thomson parabola spectrometer

A **Thomson parabola** (TP) is an *ion mass and energy spectrometer* [Rhee, (1984)] that was invented more than a century ago in 1911 by Sir Joseph John Thomson, the discoverer of the electron, to investigate *Kanalrays* or rays of positive electricity [Thomson, (1911)]. Coupled with a Micro Channel Plate (MCP) detector for conversion, it is now the most common diagnostic for real time measurement of the ion beams accelerated in laser-plasma interactions.

The device has a parallel electric and magnetic field arranged perpendicularly to the initial direction of the particles to be analysed. Ions are separated according to their charge-to-mass ratio and dispersed according to their energy, forming parabolic traces in the detector plane. Charged particles propagating through the system axis in the $\hat{\mathbf{z}}$ direction are deflected by the Lorentz force in the $\hat{\mathbf{x}}$ direction parallel to the electric field E with the acceleration $a_x = q_iE/m_i$, and in the $\hat{\mathbf{y}}$ direction perpendicular to the magnetic field B with the acceleration $a_y = q_iv_iB/m_i$. The time $t_{e/m} = L_{e/m}/v_i$ spends by a particle in the electromagnetic field, depends on its velocity v_i and the length $L_{e/m}$ of the field region. Ignoring effects due to fringe fields, assuming a constant field strength and small deviations, the deflections are expressed as [Harres et al., (2008)]:

$$x = \frac{1}{2}a_xt_e^2 = \frac{EL_e^2}{2}\cdot\frac{q_i}{m_iv_i^2} = \frac{EL_e^2}{4}\cdot\frac{q_i}{K_i}, \tag{3.2a}$$

$$y = \frac{1}{2}a_yt_m^2 = \frac{BL_m^2}{2}\cdot\frac{q_i}{m_iv_i} = \frac{BL_m^2}{2}\cdot\frac{q_i}{p_i}. \tag{3.2b}$$

The final deflection angle due to the electric field is obtained from the particle equation of motion as follows:

$$\theta_e = \frac{v_x}{v_z} = \frac{q_i E t_e}{m} = \frac{q_i E L_e}{m v_z} \approx \frac{q_i E L_e}{2K_i}. \tag{3.3}$$

When the ions hit the detector, positioned at a distance $D_{e/m}$ from the center of the electric and magnetic fields, the total deviations after the drift are given by:

$$X = \theta_e D_e = \frac{2D_e}{L_e} x = \frac{q_i D_e L_e E}{2K_i}, \tag{3.4a}$$

$$Y = \theta_m D_m = \frac{2D_m}{L_m} y = \frac{q_i D_m L_m B}{\sqrt{2 m_i K_i}}. \tag{3.4b}$$

Combining them yield the equation describing the parabola:

$$X = \frac{m_i}{q_i} \frac{D_e L_e E}{(D_m L_m B)^2} Y^2 \tag{3.5}$$

Looking at this expression, we can deduce that particles with the same charge-to-mass q_i/m_i ratio but different kinetic energies K_i are deviated along parabolic trajectories, while ion species with different charge-to-mass ratios lie on parabolas with different slopes. Protons, which have the highest charge-to-mass ratio $q_h/m_h = 1\,e/u$, are the least bent and form the parabola trace the closest to the $\hat{\mathbf{x}}$ axis. Deflections in both directions are independent, so the fields may overlap without affecting the validity of the calibration equations, and it allows to build more compact devices.

Faster particles spend less time in the E field, so they are less deviated in the $\hat{\mathbf{x}}$ direction. For this reason, more energetic particles are less spaced compared to particles with the same energy difference but in a lower energy range, leading to a worse resolution of the spectrometer towards higher energies, as shown in Figure 3.8. Several factors contribute to the TP intrinsic resolution [Jung et al., (2011)]. First, the ions enter the spectrometer through an entrance collimator, which limits the acceptance angle of the device and sets the width of the traces. Second, a greater drift distance $D_{e/m}$ will enlarge the figure on the detector. A third parameter is the magnetic field. A stronger B or longer L_m will improve the resolution thanks to a greater dispersion, and it will not have the unfavourable effect of reducing the output particle flux associated to a smaller collimator.

Experimentally, the deviation distances are measured from the origin marked by a bright spot aligned on the point-source to entrance collimator axis, due to photons or neutral radiations produced in the interaction. It would also correspond to the limit position of a charged particle with infinite velocity, and the maximum proton energy is inferred from the distance between this zero position and the beginning of the proton trace.

The TP used in this work had a 200 µm entrance pinhole located at 80 cm from the interaction point, upstream from the regions where acts the magnetic and electric fields. A magnetic field of 0.3 T is generated in the center of a permanent magnet dipole with a 5 cm long yoke. An electric field of $300\,\mathrm{kV \cdot m^{-1}}$ was generated between two electrodes 4 cm long and spaced by 2 cm, to which was applied 6 kV. The electrodes follow the dipole and both are mounted on a rail, allowing to choose between the observation of low energy ions when the stage is close to the MCP, or a better resolution at higher energies when the stage is moved further from the detector. A picture of the interior of the TP can be shown in Figure 3.9. The imaging system is a two stage MCP, mounted in Chevron design, amplifying the signal by a factor 10^6 through the production of a secondary electron cascade. It is revealed with a phosphor screen and recorded with a 16 bit

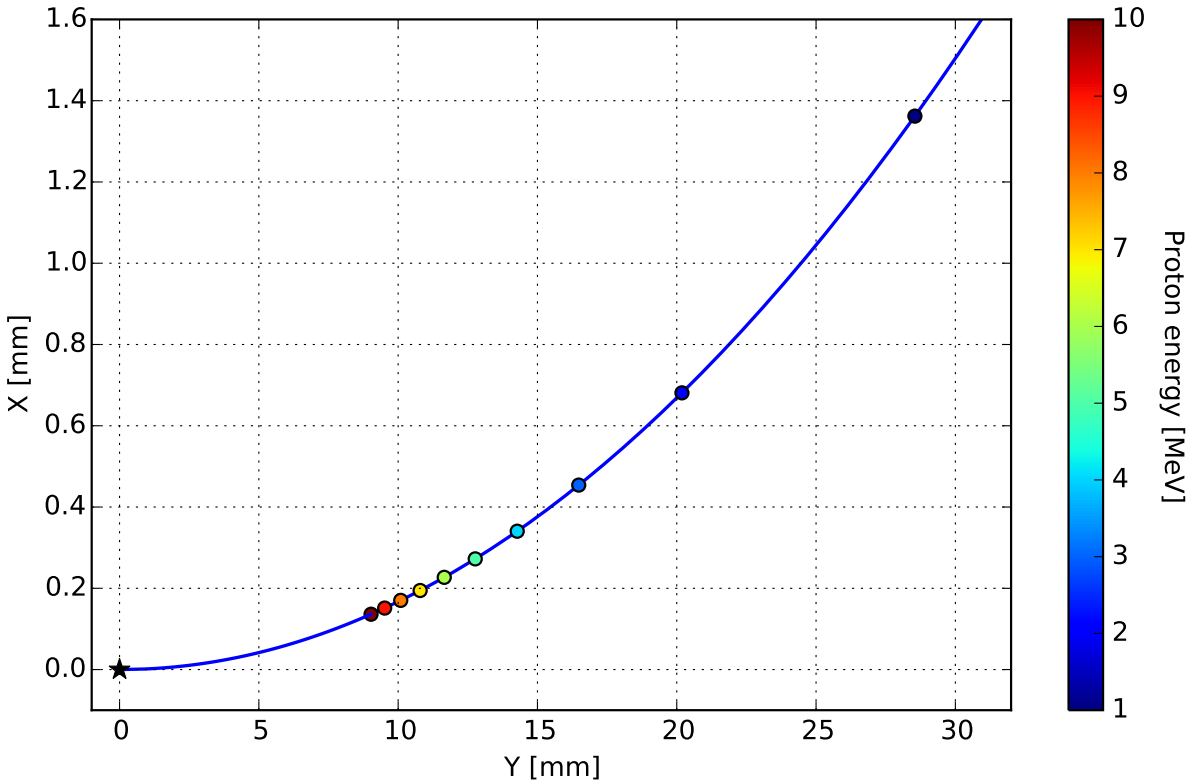

FIGURE 3.8: Deviation of protons as function of their energy in the sensing plane for our Thomson Parabola configuration (color circles associated to proton energies ranging from 1 to 10 MeV). Notice that the impacts get closer so the resolution worsen as the proton energy increases. The blue line depicts the trace along which protons are impacting the detector. The black star indicates the zero axis that is the limit position towards which all ions tends when their energy goes up.

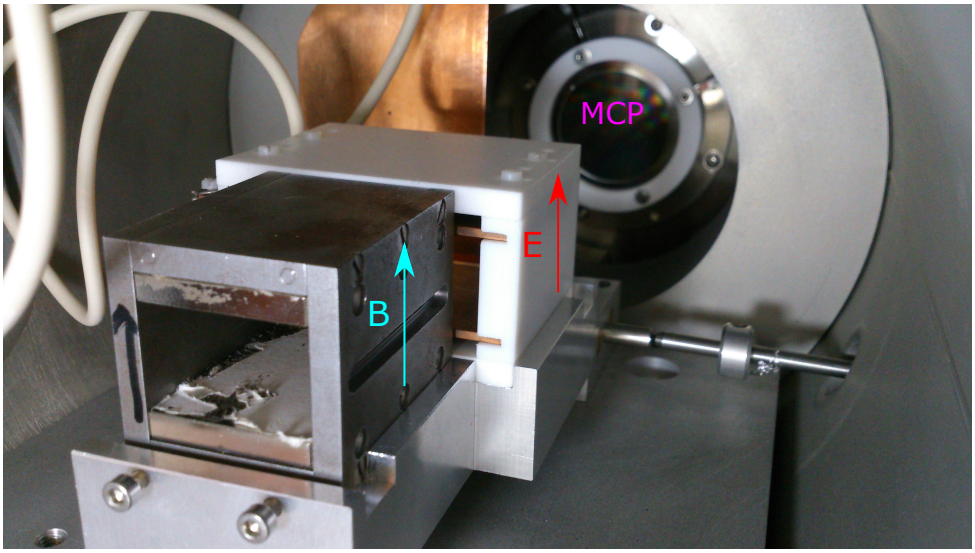

FIGURE 3.9: Picture of the inside of the vacuum chamber hosting the Thomson Parabola. The magnetic dipole is at the forefront with the electrodes next. The circular MCP detector is visible in the background. Between the field regions and the MCP, a copper plate can be translated to hide the halo generated around the strong zero axis signal.

CCD camera. Typical high-voltage power supply values are -1.3 kV on the MCP and 3.5 kV on the phosphor. The system operates under vacuum to prevent any electric breakdown arcing, and at a pressure below 10^{-5} mbar to limit the noise observed on the screen.

This real time detection device allows single shot characterisation of the ion beam, providing detailed information about the emission. However, data are related to a narrow solid angle of the beam situated on the target normal axis, and the information about the spatial energy dependence and beam divergence is lost. Moreover, the MCP needs to be calibrated to allow absolute spectrum estimations. A calibration method for protons and carbon ions utilizing respectively RCF stacks and CR-39 detectors is proposed in [Harres et al., (2008)].

3.2.2 Detectors

CR-39 etched track detector

CR-39 (*Columbia Resin* ♯39 [1]) is a Solid State Nuclear Track Detector (SSNTD) [Fleischer et al., (1965)] made of rigid thermosetting plastic that has found many applications in medicine and technology [Henshaw, (1982)], as well as for the detection of energetic protons emitted from plasma produced by intense lasers [Szydlowski et al., (2009)]. It is robust, easy-to-use, persistent and sensitive to single particle interactions, so it yields information on individual particles. On impact, in principle only heavily ionizing particles form damage tracks along their flight path in the polymer structure, so CR-39 are ideal to detect ions within a background of light, x-ray and electron radiations, strongly generated in laser-matter interactions.

A drawback of CR-39 is that it remains transparent without any visible alteration after irradiation. It has to be developed in a basic solution, for instance of 20 % sodium hydroxide (NaOH) diluted in water, and heated at 80 °C to speed up the reaction. The etchant dissolves the damaged regions faster than the bulk material, gouging out the impact spots and enlarging them [Durrani and Bull, (1987)] linearly with time, until they become visible under an optical microscope after about an hour. A traveling ion digs a hole, with depth equal to its range, and its interaction cross section increases as the particle energy decreases, according to the Bragg peak. As a result, it gives up most of its energy before it stops, so more energetic ions leaves smaller pits. Ions with energy above a threshold of 100 keV/nucleon are revealed. Another limitation of CR-39s is their dynamic range. If the particle flux is too high, the pits will overlap making accurate counting impossible.

Radiochromic film

Initially created for medicine as self-developing dosimetry films mainly used in radiotherapy, **radiochromic films** (RCF) are now a common diagnostic in particle beam physics. A variety of films with different sensitivities are commercially available among *Ashland*'s GAFChromic™ products. They consist of a single or double layer of radiation-sensitive organic microcrystal monomers on a thin polyester base with a transparent coating. The active layer turns to a shade of colors in a chemical process occurring upon irradiation, and its darkness increases with the absorbed dose. The types HD-V2 and EBT3, in addition to their respective previous generations HD-810 and EBT2, have been used in the context of this thesis. Their respective sensitivity range is 10 to 1000 Gy, and 1 cGy to 40 Gy. RCF were used as a diagnostic to measure the proton beam

[1] namely poly-allyl-diglycol-carbonate (PDAC), also known as TasTrak, with the chemical formula $C_{12}H_{18}O_7$.

divergence, and to characterize the transport system by checking the transverse beam profile along the beamline.

Even so instantaneous and not requiring any specific treatment, RCFs have some limitations to be considered when one wants to determine the experimental dose distribution delivered by a proton beam. Each lot should be calibrated with a given scanner to determine the dose to optical density relationship, keeping in mind that the following factors can affect the absolute dose retrieval: temperature during calibration and experimentation [Klassen et al., (1997)], sensitivity to electrons, x-rays and ultraviolet radiations, film orientation and alignment during use and scanning, time lapse between exposure and scanning [Muench et al., (1991)], energy range of the radiation.

Image plate

An alternative to measure the spatial profile or energy spectrum of an ion beam is to use an **image plate** (IP). An IP commercialised by FUJiFILM typically consists of a protective layer, a phosphor film sensitive to ionizing particles, a support and a magnetic layer to ease handling. The IP response depends on the energy deposited in the phosphor layer[2]. This active layer has a linear response to x-rays over a large range of wavelengths starting at a few nanometers, and with a dynamic range of 105 [Miyahara et al., (1986)], but it is also sensitive to electrons and ions. Their sensitivity to all kinds of ionizing radiations is the main issue when IPs are used as diagnostic in laser-matter interactions at high intensities, making difficult to discriminate the proton beam contribution to the recorded signal.

When an ionization radiation hits the IP active layer, electrons from Eu^{2+} ions are promoted into a long lived metastable state where they remain trapped into the lattice defects. To extract the data stored in the IP, relaxation to the ground state can be stimulated by light with a wavelength of 632.8 nm. It is accompanied by the emission of a blue photon around 400 nm, that is detected using a photomultiplier tube. This photo-stimulated luminescence (PSL) is detected by a special scanner (*Fuji* FLA-7000 scanner in the scope of this thesis) to generate a digital image of the irradiation pattern within minutes. Recombination of the electron-hole pairs can also happen spontaneously, inducing a natural *fading* of the recorded signal [Paterson et al., (2008)], hence the necessity to scan IPs after a fixed time following their exposure to obtain meaningful and comparable data. The information stored on the IP can then be completely erased, with exposition to incoherent bright white light for a quarter-hour, to be re-used afterwards. The resolution is theoretically limited in our case by the beam waist of the scanner stimulating laser, that is 25 µm. A difficulty with IPs is to get an absolute calibration, as it is specific to each of the many IP types and scanner models available. Some calibrations for protons are reported in [Mančić et al., (2008); Boutoux et al., (2015)]. Assuming linearity of the IP response [Bonnet et al., (2013)], if the signal is partly saturated on the first scan, a successive one can be performed and a corrective factor applied, estimated from the signal reduction in a non-saturated area.

[2] made of barium fluorohalide phosphor crystals with europium bi-ionized dopants [$BaF(Br, I) : Eu^{2+}$], with a thickness of 50 and 120 µm for TR and SR IP types respectively [Bonnet et al., (2013)]

3.2.3 Detector stacks and filters

When the range of some accelerated protons exceed the thickness of a detector, it is interesting to mount several detectors one after the other in a stack configuration. The notable stopping range of ions in matter allows the front detectors to act as a high-pass energy filter for the next ones, because there is a well-defined energy threshold below which all ions of a given specie are blocked. The thinner the detectors are, the more layers will be traveled across by the beam, and the better will be the energy resolution.

For instance, stacks of RCF may be used to reconstruct the spatial energy distribution of a proton beam, as described in section 3.3.5. As each proton deposits most of its energy in the layer corresponding to its stopping range, it is possible to infer a rough energy spectrum, but with a good spatial resolution (~10 µm), from the color density in each layer.

If the detector is too thick or the ion energies too low, one may place strips of filters in front of a given detector, typically 13 µm thick aluminium foil. Making use of the symmetries or invariance by rotation of the beam profile, and varying the numbers of filter layers, similar step-like and spatially-resolved energy spectra are obtained, as shown in Figure 3.10.

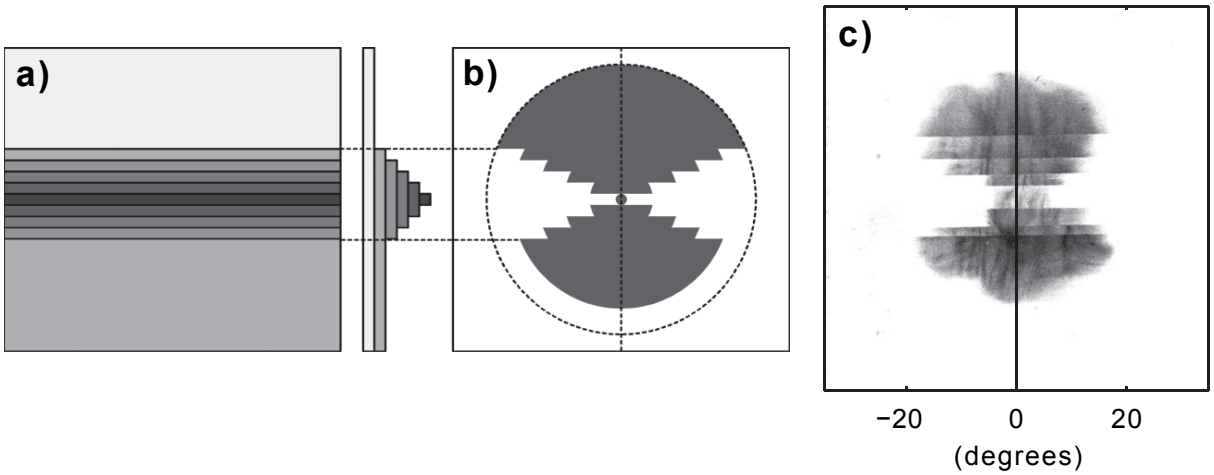

FIGURE 3.10: (a) An Al filter mask is placed in front of a CR-39 plate to enable measurement of both the proton spatial and energy distributions. The expected pattern on the detector plates is schematically illustrated in (b), assuming a proton beam directed along the target normal and with a divergence decreasing with increasing proton energy. An example of observed distribution is illustrated with (c). (Modified from [Lindau et al., (2005)])

3.3 Ion acceleration experiments

The presence at different timings of various unwanted prepulses emerging from the freshly built laser system hindered the achievement of proton energies in the tens of megaelectronvolts expected by comparison with other laser facilities. The priority was not to study in details the laser-matter interaction process and try to achieve higher ion energies thanks to new acceleration regimes. Instead, my work focused on the characterisation of the ion beam produced via TNSA (energy spectrum, angular divergence distribution) to be able to then manipulate the beam for practical applications.

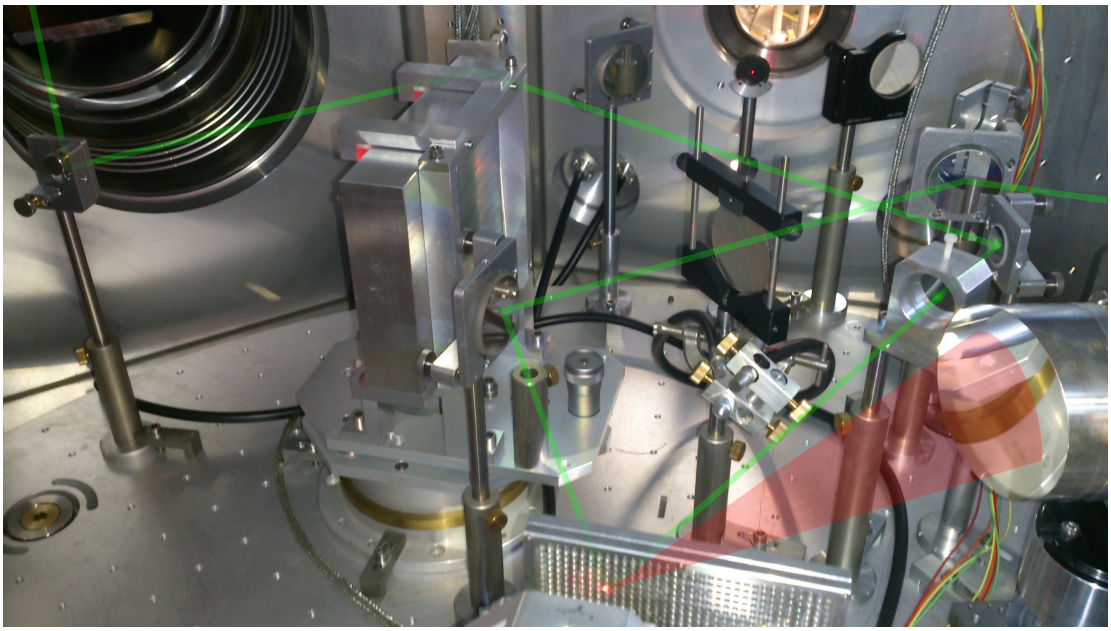

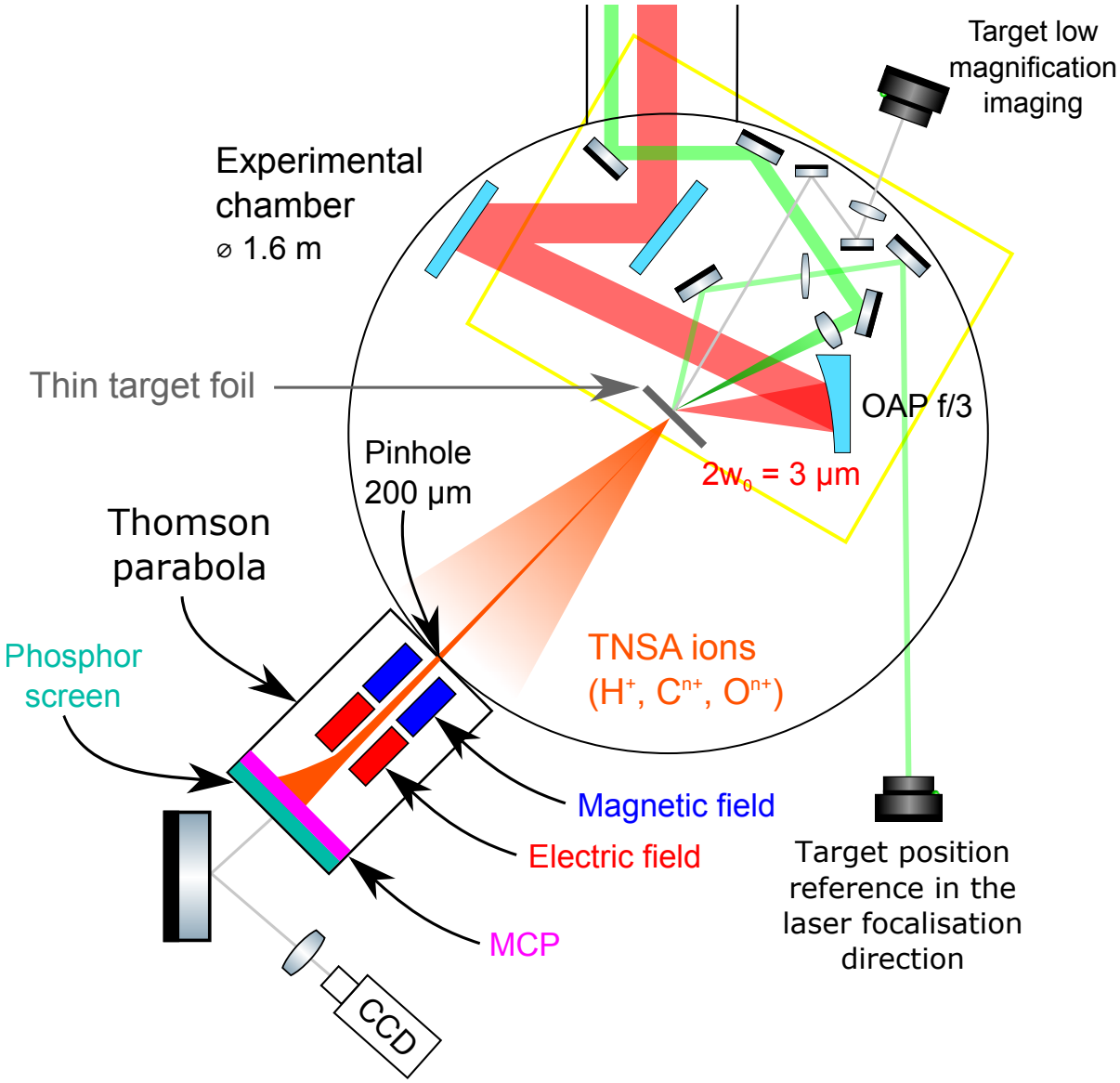

FIGURE 3.11: Sketch of the SAPHIR experimental chamber with the setup used for solid target experiments. The picture at the top shows the imaging diagnostic region pointed out by the yellow rectangle in the bottom diagram.

3.3.1 Solid target developments: assembly, thickness, material and alignment

Aluminium targets of various thicknesses ranging from 3 to 15 µm were used initially, and the highest proton energies were generated with the most consistency with 6 µm thick foils. In 2015, *titanium* targets (2, 5 and 10 µm thick) were tested and proved to be more stable, which can be explained by several factors. The Ti foils are stiffer so the target surface is less inclined to be deteriorated during the mounting process. They also have better optical surface quality, which facilitates their alignment. Titanium has a melting point at 1941 K whereas it is substantially lower at 933.5 K for aluminium. Hence, more energy is needed to turn the Ti targets into the liquid state. Finally, the first ionization energy is 14 % higher for Ti than for Al (658.8 kJ · mol^{-1} against 577.5 kJ · mol^{-1}), so more energetic prepulses are required to turn the Ti target surface into a plasma. The target foils used to be sandwiched between two grids, each with a thickness of 80 µm, but bending of the grid prevented from maintaining the target well flat. From May 2016, we tried to simply glue the foil with a Neoprene spray on a new target holder grid made thicker (2 mm, visible in the background of Figure 3.12) to prevent it from becoming distorted.

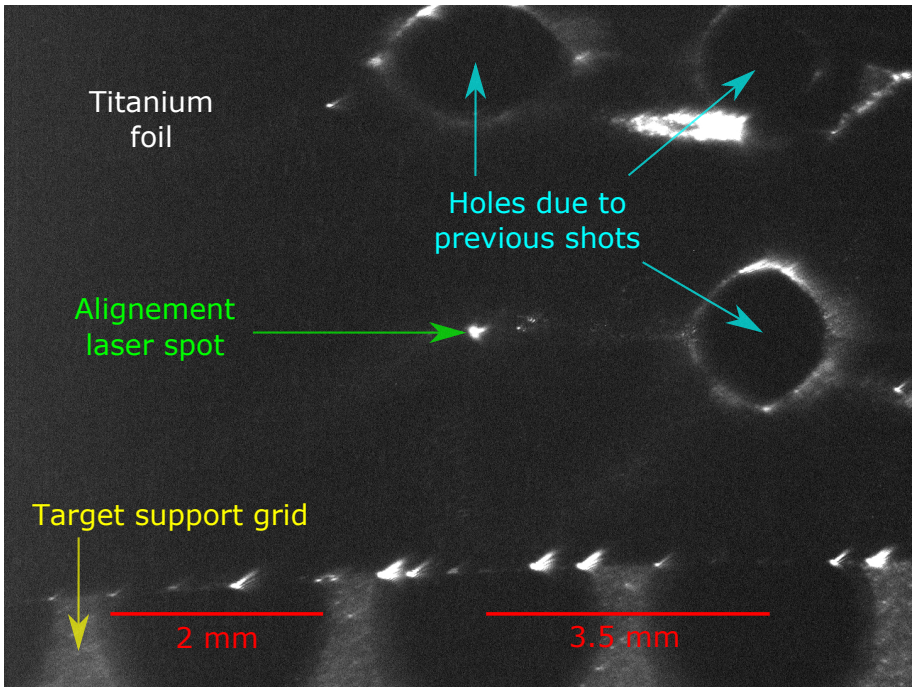

FIGURE 3.12: Low magnification image of the target front surface aligned on a clean area. Three holes in the titanium target surface, where the laser was shot previously, are visible in the top right corner. The target was glued on top of the holding grid that can be seen at the bottom of the image after the edge of the foil.

The target holder is positioned on a 5-axis mount: 2 manual tilts and 3 motorized translations. The 2 rotations allow to align the target vertically and in a plane leading to a laser incidence angle of 45°. These rotations are adjusted by autocollimation each time the mount is moved to change the target. This is done by sending a HeNe laser, aligned on a diameter of the chamber corresponding to the target normal axis, back on itself after reflection on a small mirror fixed on the support grid. Two translations are aligned on the target vertical and horizontal axis, allowing to refresh the target surface after each shot thanks to a camera imaging with a low magnification the target front surface, where an alignment laser superimposed on the IR beam path is visible. The third spatial stage is aligned on the laser incident direction at a 45° angle from the target plane, and is used to finely correct the position of each new target in the laser

focusing direction to assure the repeatability of the interaction conditions. These adjustments are monitored with a high magnification optical line, imaging the alignment laser light diffused by the target surface to give a precise spatial reference position of the target in respect of the focal spot (see the layout in Figure 3.11). The resolution of the positioning is about 20 µm or 2.2 z_R, which corresponds to the displacement of the alignment laser image by half its spot size on the camera.

3.3.2 Effect of the laser pulse contrast on the maximum proton energy cutoff

Proton spectra were measured for different laser contrast conditions (see Figure 3.13), while prepulses were diagnosed and removed along the laser chain. As the ion acceleration process strengthens with the improved contrast, higher energies were obtained. The best more stable acceleration conditions were obtained on Titanium target with a thickness of 5 µm.

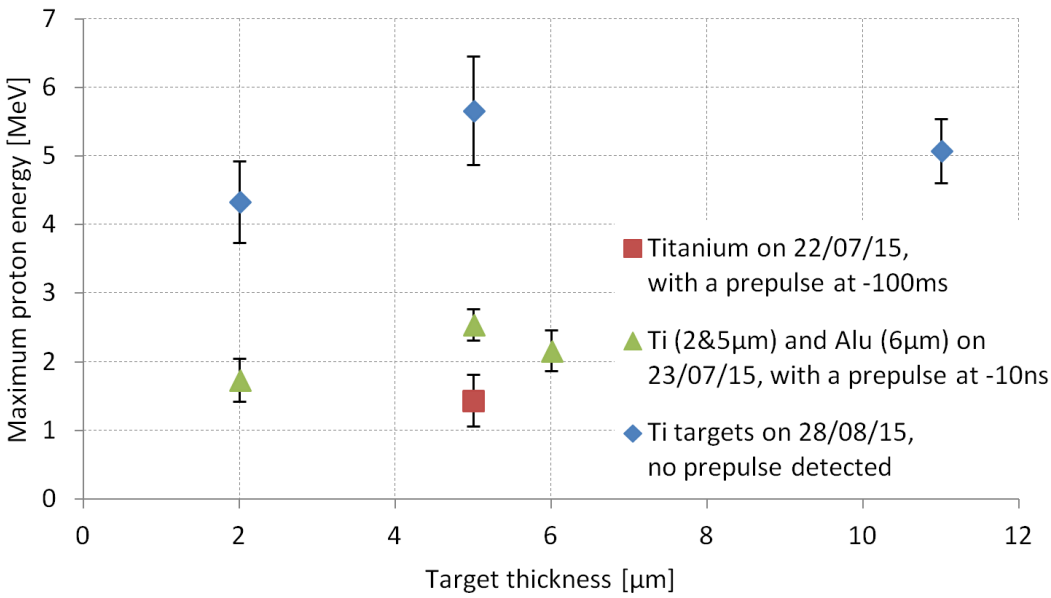

FIGURE 3.13: Forward proton beam energy cutoff for different targets and various prepulse conditions.

3.3.3 Scan in focus position

The correct target position with respect to the focusing laser beam is searched experimentally by studying the accelerated proton beam as the focusing parabola is moved by successive steps toward or away from the target. The peak intensity on target for a Gaussian beam would evolve as a Lorentzian function according to equation (1.10), with a drop to 71 % of its maximum at one Rayleigh range from the waist. The proton energy cutoff depends on the laser intensity on target, so in normal conditions, an optimum is found when the target is positioned in the laser focal plane, as shown in Figure 3.14.

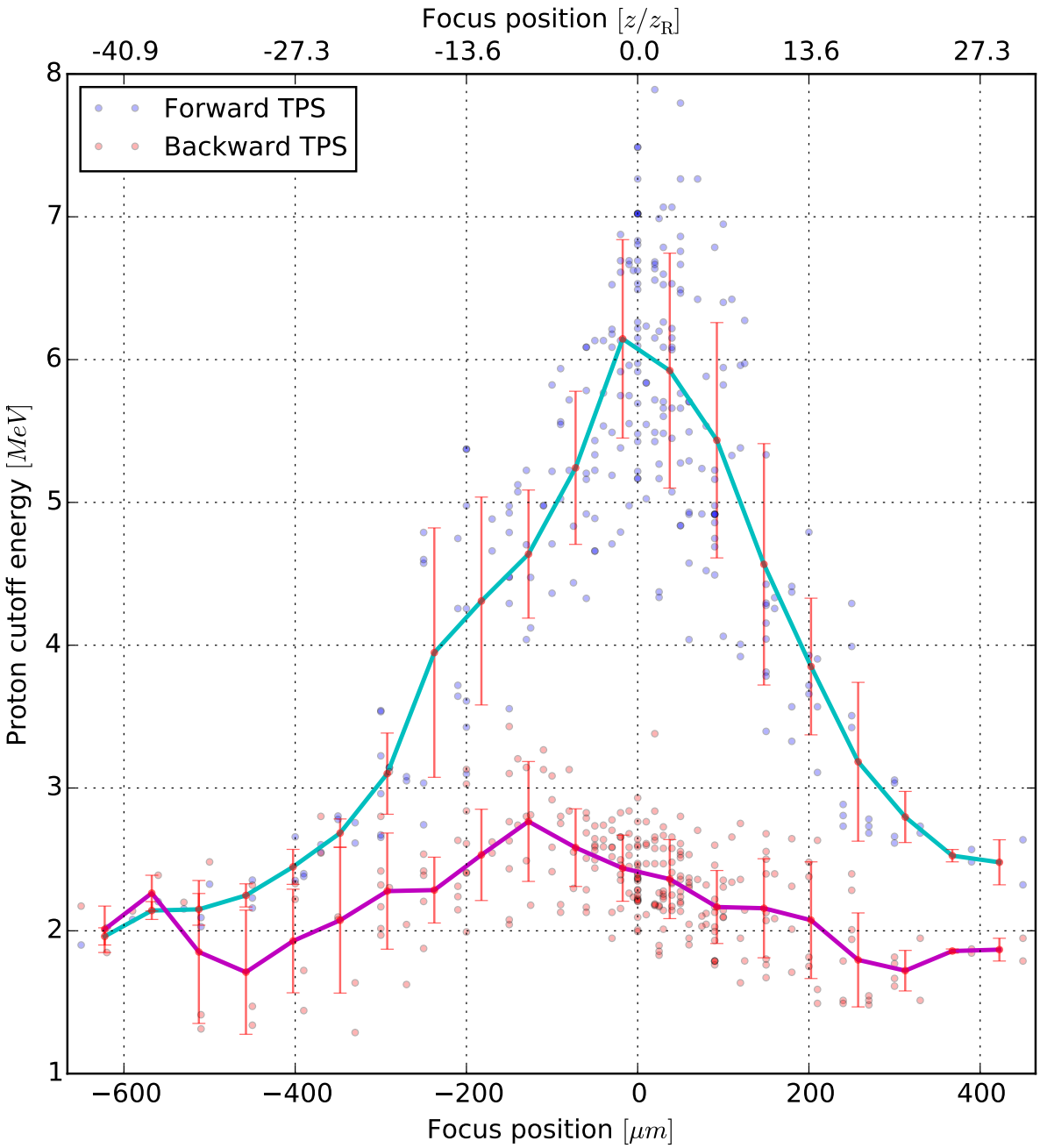

FIGURE 3.14: Cutoff energy of the forward (in blue) and backward (in red) proton beams obtained for different focus positions during the Fall 2015 on titanium targets of 5 µm thickness. A maximum is found at the focus position in the forward direction.

However, our laser beam is far from being comparable to this framework (many distortions in the focal spot, see Fig. 3.7), which explains why we are still accelerating protons to a couple MeV even half a millimeter away from the focus, corresponding to several tens of theoretical Rayleigh ranges. Indeed, the peak laser intensity does not decreases as fast as expected, as shown in Figure 3.15.

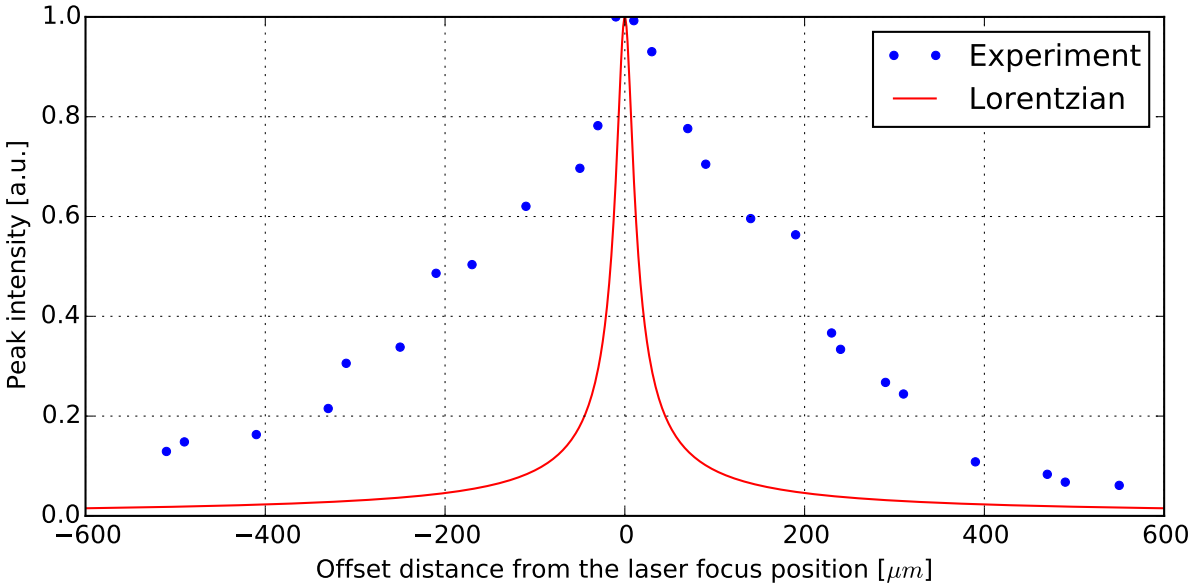

FIGURE 3.15: Evolution of the peak laser intensity in the focus direction (parabola to target axis). The blue points are the experimental values, while the red curve corresponds to the Lorentzian function in eq. (1.10) describing a Gaussian beam.

Besides, a different response with two peaks is observed in poor contrast conditions (before the XPW upgrade), as in Figure 3.16. When the target is moved away from the beam waist, both the peak and pedestal intensities decrease. Better interaction conditions can be found with a reduced overall intensity on target, if the pedestal intensity is lowered enough not to disrupt too much the target surface and hinder the acceleration process.

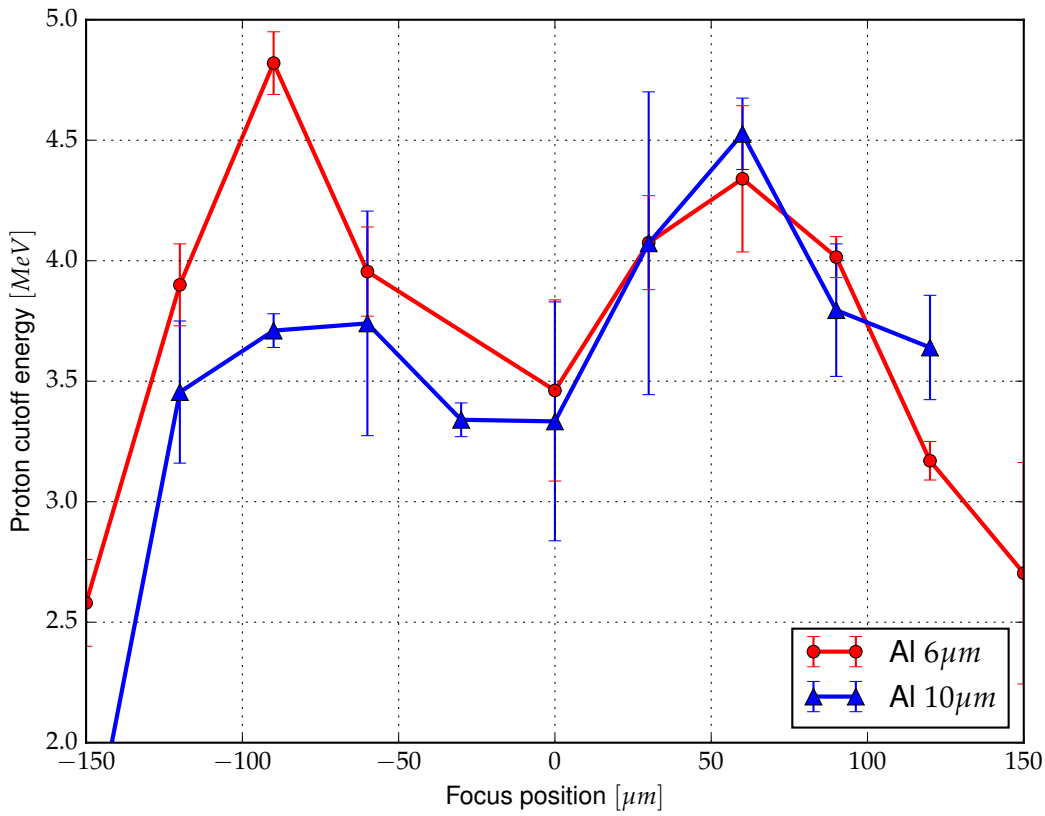

FIGURE 3.16: Cutoff energy of the forward proton beam obtained for different focus positions on Aluminium targets in July 2014 (before the laser upgrade). A local minimum is found at the focus position.

3.3.4 Ion beam energy spectrum

The energy spectrum of the laser-accelerated protons available for the experiments presented in the next chapters was measured in the forward direction on the target normal axis with the Thomson parabola spectrometer. Simulations of the ion trajectories enable to fit the traces observed on the phosphor screen and retrieve spectra.

Protons and carbon ions (ionized from 1 to 4 times) are the main species accelerated, but traces of C^{5+} and oxygen ions are also detected (see Figure 3.17a). The ion energy spectra are typically described by a thermal-like exponentially decreasing distribution, leaving only few accelerated particles close to the maximum energy cutoff. The Boltzmann distribution temperature of the average proton beam in Figure 3.17c is approximately 5 MeV, with a cutoff around 7 MeV, but a calibration of the MCP would be necessary to get a more accurate estimation.

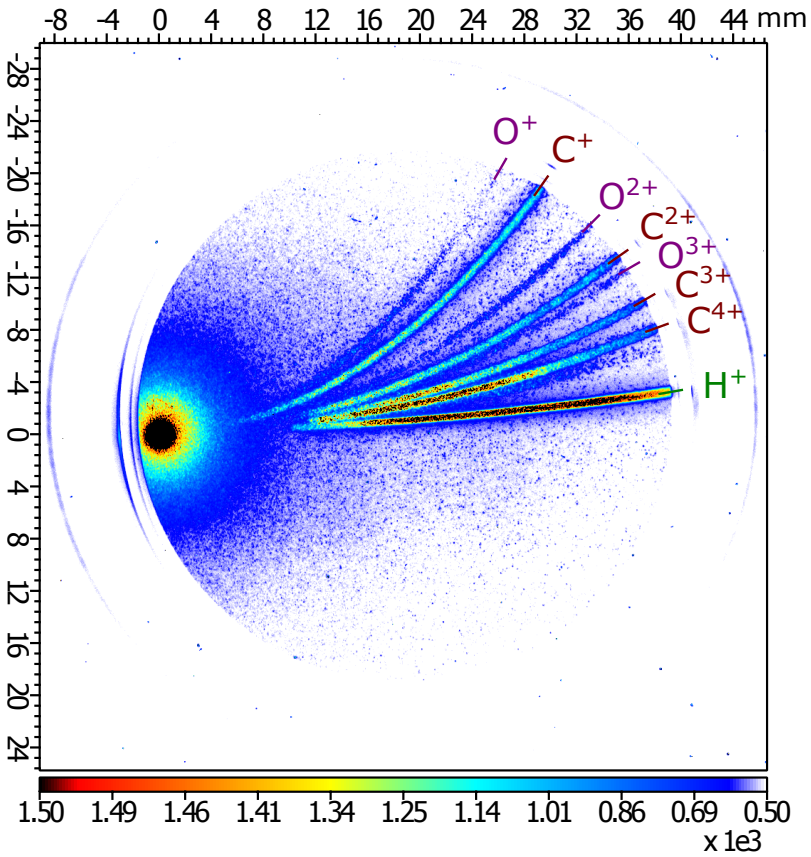

(a) Imprint on the TPS of the ion beam accelerated in the forward direction.

Ion specie	Energy range	
	min	max
H^+	< 0.5	7
C^+	< 0.07	1
C^{2+}	< 0.2	2
C^{3+}	< 0.4	3
C^{4+}	< 0.7	6
O^{n+}	Faint traces	

(b) Energy range in MeV of the main ion species observed in a.

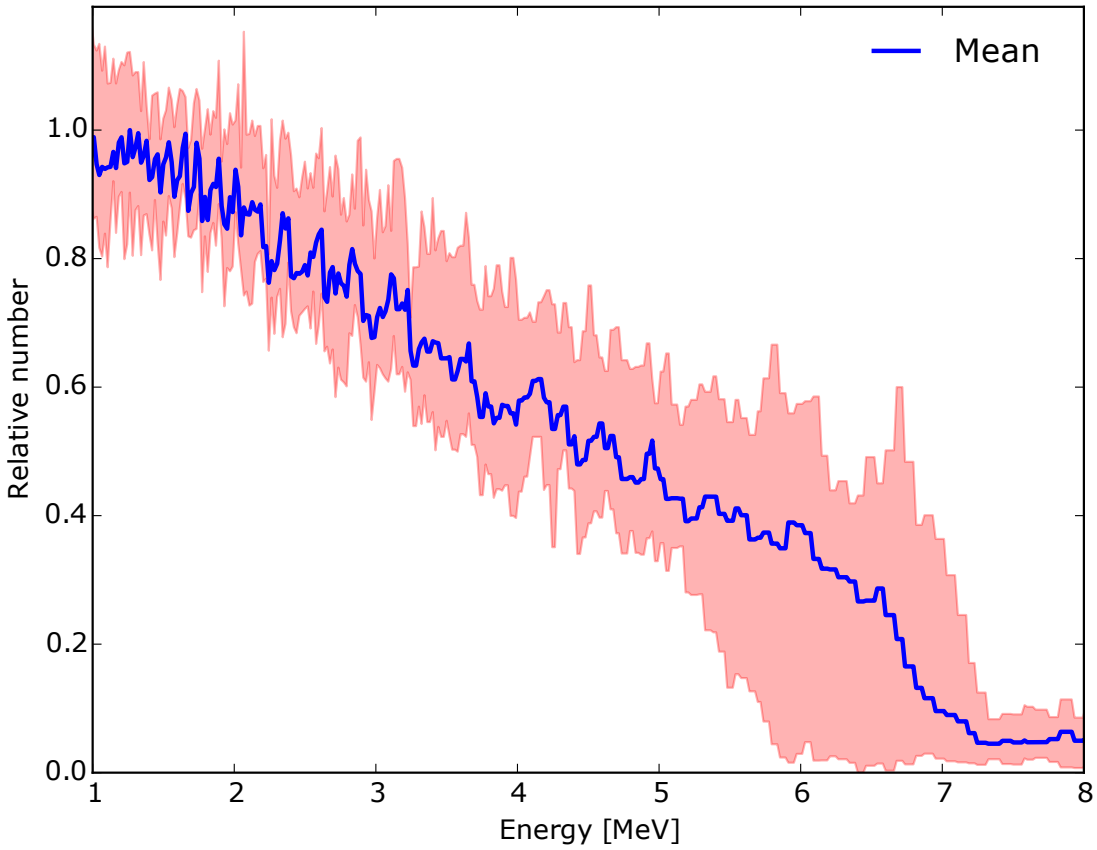

(c) Proton energy spectrum: average over 9 shots (in blue) and extremal range (in red).

FIGURE 3.17: Energy spectrum analysis with a Thomson parabola spectrometer of the ion beam accelerated on the target normal axis.

3.3.5 Energy-resolved divergence of the proton beam source

The divergence of the forward proton beam source was determined from a stack of RCF detectors, placed 4 cm behind the target and protected with 13 µm of aluminium, to record transverse spatial profiles of the beam at different energies. The opening angle of the cone in which the protons are emitted is deduced for each energy from the measurement of the spot FWHM. RCF HD-V2 type were used to make the stack, because of their thinner total thickness (105 µm) compared to EBT types more than twice thicker, enabling a relatively good energy resolution. However their sensibility is lower, so 25 shots were accumulated to have enough signal on the films. Energy deposition is measured up to the 6th layer (see Figure 3.18a), corresponding to a cutoff energy of 7.3 MeV. The net optical density retrieved from the scanned RCFs was converted into dose deposition in the films according to a calibration of our scanner. Contour lines at half the maximum dose on each layer are shown on the beam profile in Figure 3.18b. A continuous decrease of the average divergence angle with increasing proton energy is found (see Figure 3.18c).

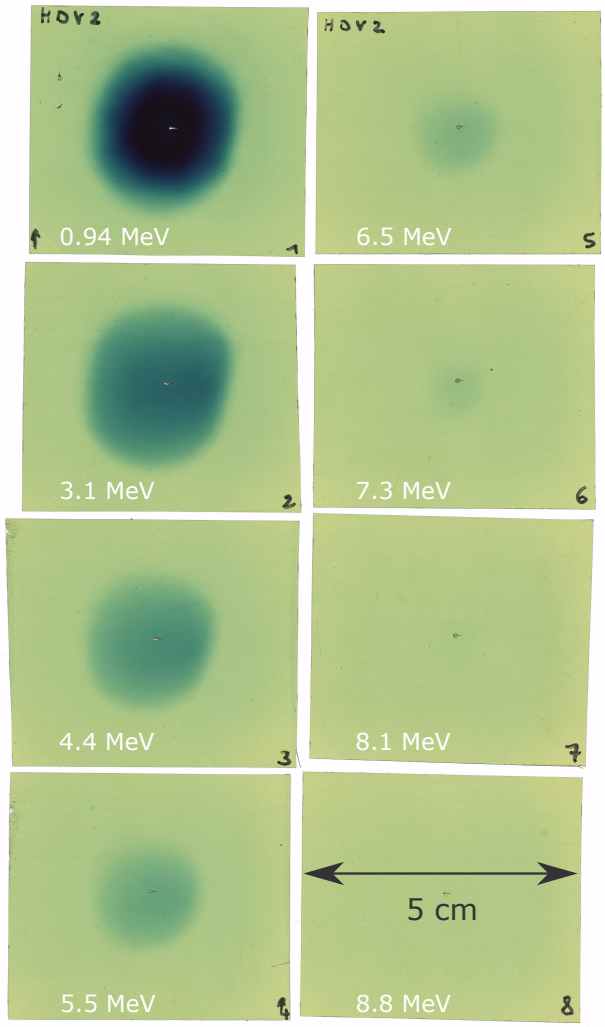

(a) Scan of the RCF HD-V2 stack recording the proton beam spatial profile 4 cm after the interaction point. The labels refers to the energy cutoff of protons on each layer.

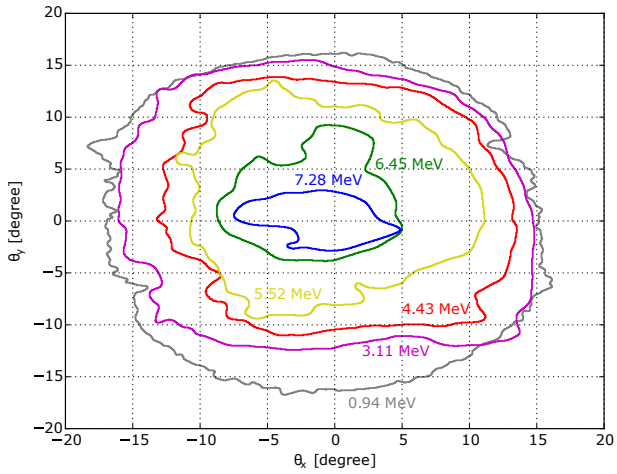

(b) Isodose contour lines drawn at 50 % of the maximum dose deposited on each radiochromic film layer. The labels indicate the minimum energy required for a proton to reach the corresponding layer.

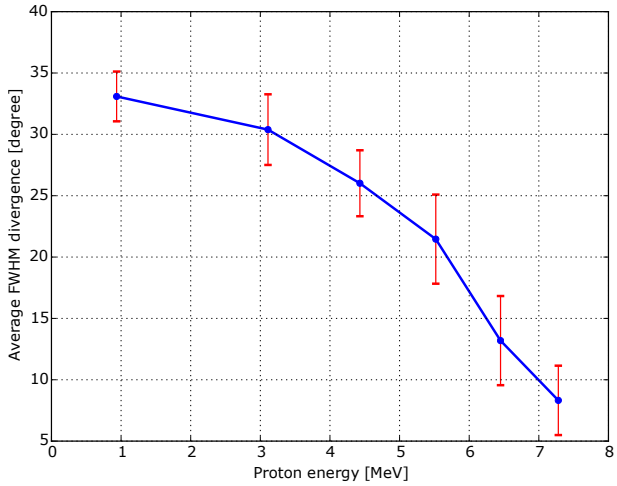

(c) Average beam divergence calculated for a discrete set of energies from the contour lines in b.

FIGURE 3.18: Energy dependent divergence of the proton beam source.

3.3.6 Front and back side acceleration relationship

Following the literature, describing a correspondence between the ion beams accelerated in the forward and backward direction as referred in section 1.4.1, we measured simultaneously the beam generated in each direction with two TPS both aligned on the target normal axis. The idea was to identify a possible correlation on both proton spectra, for the purpose of using later the backward TPS as a diagnostic about the forward beam, when we want to use the main beam for another goal and the setup behind the target prevent from characterising it with the forward TPS.

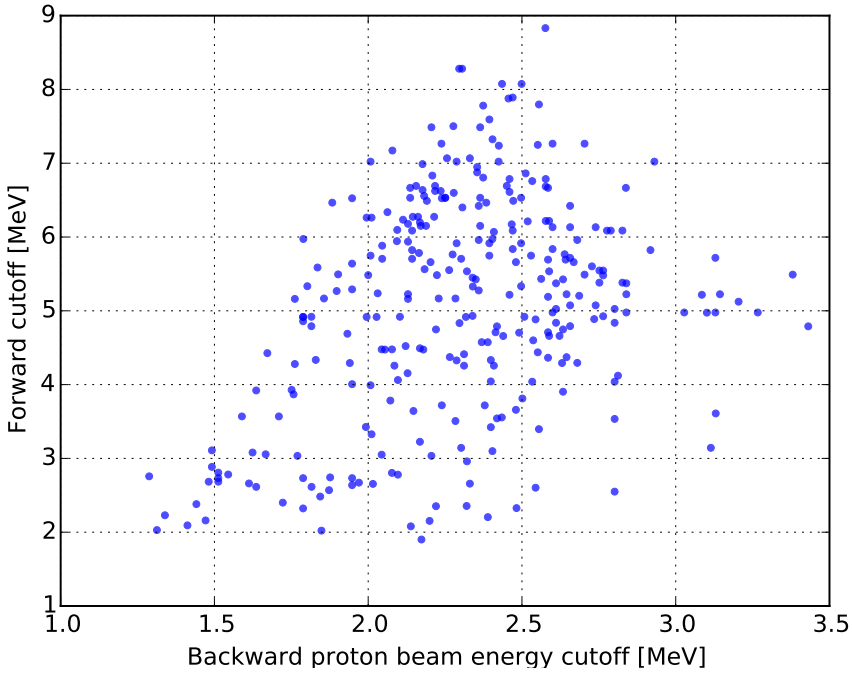

FIGURE 3.19: Relationship between the energy cutoff of the forward and backward proton beams, measured during the Fall 2015 with the XPW.

As shown in Figure 3.19, no correlation appears between the maximum energies achieved in both directions, in relatively good contrast conditions during the Fall 2015 after the laser upgrade. It could be due to a not sufficient contrast, responsible for the generation of a significant preplasma on the target front surface before the arrival of the main pulse, hence bad acceleration conditions and lower energies in the backward direction.

3.3.7 Spectroscopy with a synthetic diamond

During a diagnostic campaign performed in collaboration with a team of researchers from the INFN-LNS in Catania (Italy), a **poly-crystalline diamond film grown by chemical vapor deposition** (pCVD) [Tuvè et al., (2007)] was used as detector for **time-of-flight** measurements. Synthetic diamonds are known for their ability to carry out time-resolved recordings of ultrafast signals coming from ionizing radiations [Franklin et al., (1992); Berdermann et al., (2010); Margarone et al., (2011)]. An example of spectrum obtained this way with a preliminary analysis of the observed features is shown in Figure 3.20. The photopeak induced by x-rays is measured first, with a tail resulting from the fast electrons (electrons with energies between 10 MeV and 0.1 MeV reach the detector after a delay ranging respectively from 2.3 ns and 4.3 ns). Then

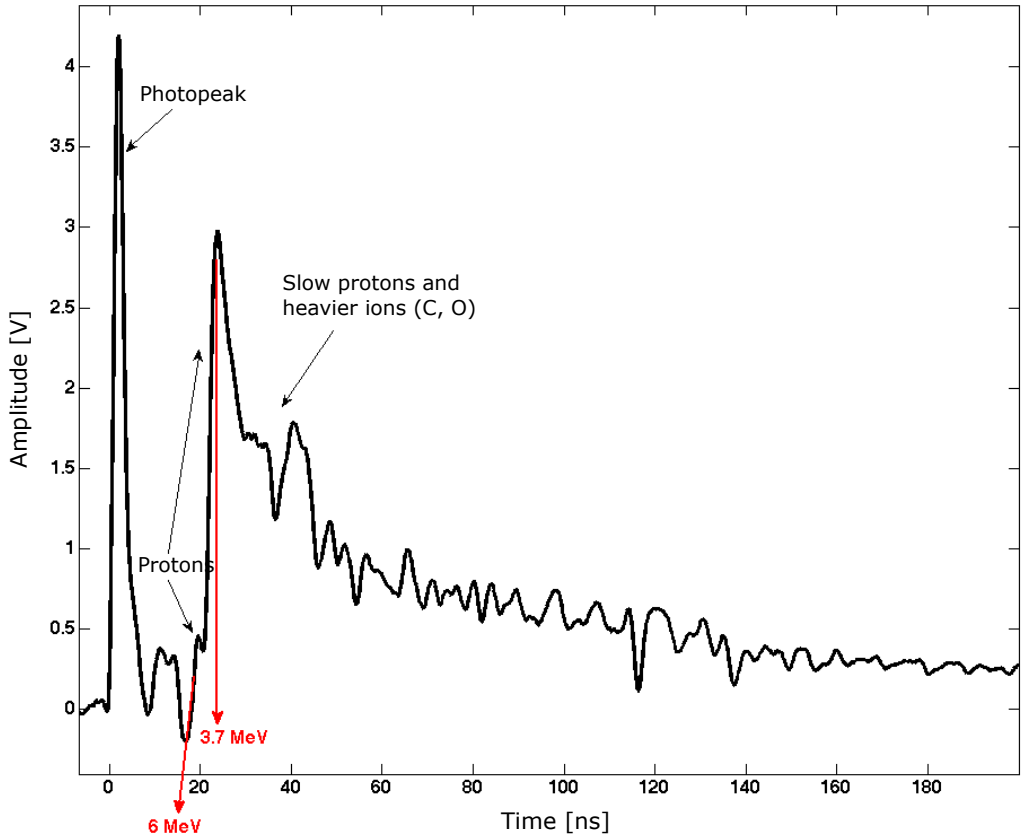

FIGURE 3.20: Time-of-flight spectrum recorded with a pCDV detector placed on the target normal axis 69.5 cm from the source in the forward direction.

follows some other patterns due to protons and other ions. The retrieval of the full spectra for the multiple ion species accelerated is not immediate as the output signal must be deconvoluted taking into account parameters of the electronic circuit, in particular its time constant.

Such a detector has the advantage of a very small size (sensitive area with a few mm diameter), hence the possibility to place and move it conveniently to study for instance spatial dependence of the spectrum. However, the detector should be placed further to improve the resolution. It requires special electronics to handle the fast signal, and a post processing of the data to extract individual spectra for each ion specie when possible. This preliminary test has a limited utility as many radiations are mixed together in the incident beam, hence it is not trivial to retrieve individual spectra for each component. It is nonetheless adapted to the measurement of the proton cutoff energy, as in our case it corresponds to the particles in the lead of the positive ions beam.

A relevant application considered is the measurement of the proton bunch duration after propagation through the quadrupole system. At that point, the beam will be cleaned of heavy ion species and electrons, and the proton beam will be filtered in energy, hence this device will allow to confirm some output spectrum estimations.

3.4 Conclusion

The laser facility, the experimental setup, the diagnostic equipments and the procedures established on SAPHIR enables to generate and monitor multi-MeV proton beams, ready for practical use. The laser-accelerated proton beam has been well-characterised, both in terms of energy spectrum and spatial divergence. This accurate description enables the reliable transport simulations presented in the next chapter.

Chapter 4

Proton Beam Transport and Control

This chapter begins with an introduction to accelerator physics, covering a few particle beam optics principles and focusing methods with a highlight on quadrupoles. They are also discussed in the scope of laser-plasma accelerators. Then some of the quadrupole setups experimented are described together with their effects on the energy spectrum and spatial profiles of the transported beams.

Contents

4.1 Transverse Beam Magnetic Optics **74**
4.1.1 Linear beam optics 74
4.1.2 Beam focusing with magnetic quadrupole 75
Quadrupole magnetic field 75
Other beam tailoring techniques 77
The quadrupoles used in our experiments 78
4.2 Proton Beam Spatial and Spectral Shaping **80**
4.2.1 Beam transport with a magnetic chicane 81
4.2.2 Beam focusing with PMQs 87
PMQ setup for focusing 8 MeV protons 87
Energy filtering with PMQs 90
4.2.3 Radiobiology transport beamline 93
Comparison between experimental and simulated beam profiles 93
Output beam spatial properties 100
Energy selection and output spectrum 102
4.2.4 Pepperpot characterisation 103
4.3 Conclusion **107**

4.1 Transverse Beam Magnetic Optics

4.1.1 Linear beam optics

A given transport system for charged particle beams has a fixed *nominal trajectory* so the motion of each individual particle in its vicinity is generally defined relatively to this trajectory. The particles trajectories are guided by the Lorentz force through the applied electric or magnetic fields. Its magnetic term is proportional to the particle velocity, as opposed to the electric term, so magnetic fields become much more effective with increasing speed, which is why highly energetic charged particles are typically guided with magnetic devices. We introduce a Cartesian coordinate system $K = (x, y, s)$ whose origin moves along the nominal beam trajectory s, and we will assume that the particles moves essentially in the s direction ($\mathbf{v} = (v_x, v_y, v_s) \approx (0, 0, v_s), v_{x,y} \ll v_s$), and that the magnetic fields have only transverse components ($\mathbf{B} = (B_x, B_y, 0)$). For a particle passing through the magnetic field in the defined moving frame, there is a balance between the Lorentz force $F_x = -qv_sB_y$ and the centrifugal force $F_r = m\gamma v_s^2/R$, with R the radius of curvature of the trajectory and $p = \gamma m v_s$ the momentum, leading to:

$$\frac{1}{R(x,y,s)} = \frac{q}{p}B_y(x,y,s). \tag{4.1}$$

Since the transverse dimensions of the beam are small compared to R, we can expand the magnetic field around s, which gives the *multipole expansion*:

$$\begin{aligned}
\frac{q}{p}B_y(x) &= \frac{q}{p}B_{0y} + \frac{q}{p}\frac{dB_y}{dx}x + \frac{1}{2!}\frac{q}{p}\frac{d^2B_y}{dx^2}x^2 + \frac{1}{3!}\frac{q}{p}\frac{d^3B_y}{dx^3}x^3 + \dots \\
&= \frac{1}{R} + kx + \frac{1}{2!}\mu x^2 + \frac{1}{3!}ox^3 + \dots \\
&= \text{dipole} + \text{quadrupole} + \text{sextupole} + \text{octupole} + \dots
\end{aligned} \tag{4.2}$$

The magnetic field around the beam can be decomposed into poles of various orders, each having a particular effect on the beam. Dipoles are used to steer the beam, while quadrupoles to focus it. If only these two lowest multipoles are used, we speak of **linear beam optics** since the forces are either constant or change linearly with the transverse displacement from the nominal trajectory. Higher order multipoles are *non-linear* components, used to compensate for higher order fields, such as chromatic aberrations with sextupoles or field error with octupoles, but they are not taken into account in the following linear approximation.

The linear equations of motion of a particle propagating through the magnetic structure are [Wille, (2000)]:

$$\begin{cases} x''(s) + K(s)\,x(s) = \dfrac{1}{R(s)}\dfrac{\Delta p}{p} \quad \text{where} \quad K(s) = \left(\dfrac{1}{R^2(s)} - k(s)\right) \\ y''(s) + k(s)\,y(s) = 0 \end{cases} \tag{4.3}$$

with $\frac{\Delta p}{p}$ the relative momentum deviation. The transverse coordinates x and y are decoupled and they represent the relative deviations from the nominal path s, along which dipole fields are applied only in the vertical **y** direction resulting in **x** horizontal bending.

In a simplified picture, a beam transport system consists of dipole and quadrupole magnets separated by drift sections. The particle trajectories can be calculated by operating *transfer matrices* on the transverse beam vector $X = (x, x', y, y')$. This notation of the equations of motion's

solution is particularly useful if $K(s)$ is piecewise constant, because when $K(s) = const$, the matrix elements can be expressed analytically, as described in the next section. The transformation matrices for a drift, dipole and quadrupole, depend only on three parameters: the longitudinal position s, the dipole bending radius R and the quadrupole field gradient k. This transfer matrix method provides a fast and easy tool for beam transport calculations, analogous to ray transfer matrix analysis used in the design of optical systems.

4.1.2 Beam focusing with magnetic quadrupole

This section concentrates on the description of quadrupole magnets, with an insight on the strengths and weaknesses of this tool compared to some of its alternatives to focus proton beams.

Similar to the properties of Gaussian light beams introduced in section 1.1.2, particle beams also have a tendency to spread out due to an inherent beam divergence caused by space charge effects. To keep the beam together and shape it as desired to obtain specific properties at selected points along the transport line, focusing devices are required. In photon optics, focusing is achieved with glass lenses. A *focusing lens* performs its duty deflecting light rays by an angle α proportional to its distance r from the axis of the lens (see Figure 4.1). Incoming parallel rays

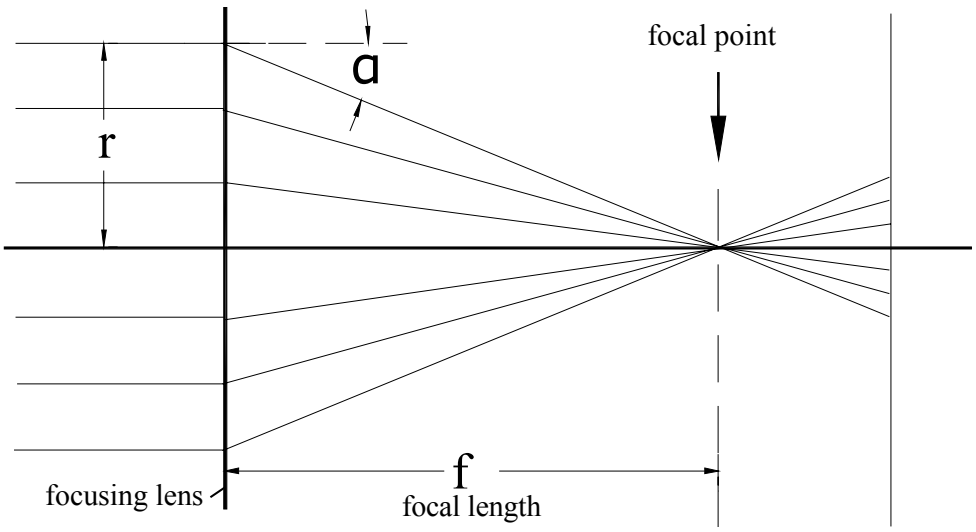

FIGURE 4.1: Principle of beam focusing (adapted from [Wiedemann, (2007)]).

will converge to a single point, at a distance from the lens equal to its focal length $f = r/\alpha$. Applying this same principle to charged particle beams from the multipole expansion (4.2), we see that focusing will be provided by the azimuthal quadrupole magnetic fields.

Quadrupole magnetic field

Quadrupole fields are used to focus beams [Lim et al., (2005)], and according to equation (4.2), they vanish on the beam axis and increase linearly with the transverse distance. The vertical field component along the x-axis is

$$G_y(x) = gx \quad \text{with} \quad g = \frac{\partial B_y}{\partial x}. \tag{4.4}$$

The second derivative of G_y disappears, so the required potential is [Wille, (2000)]:

$$\Psi(x,y) = g\,x\,y. \tag{4.5}$$

It follows that equipotentials for a given value Ψ_0 are hyperbolae of the form

$$y(x) = \frac{\Psi_0}{gx}, \tag{4.6}$$

and field lines are perpendicular to them. Hence, a quadrupole consists of four poles arranged with alternating polarity, as shown in Figure 4.2. Its field has the shape of a saddle, which has the effect of focusing a charged particle beam along one axis and defocusing it along the other one. To properly focus a beam, it is necessary to used at least two quadrupoles, rotated by 90°

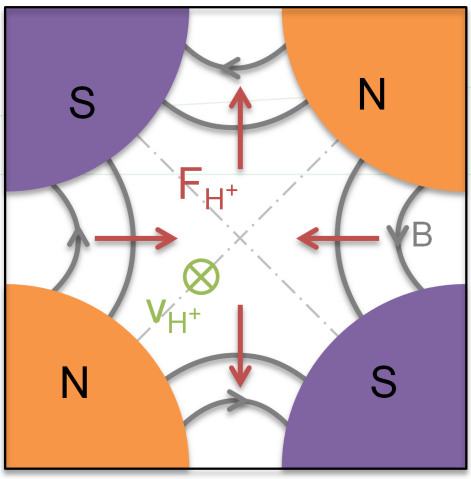

FIGURE 4.2: Transverse schematic of a magnetic quadrupole with field lines represented in gray. For a positively charged particle moving into the page, the force components (in red) are focusing in the horizontal plane and defocusing in the vertical direction.

relative to each other in order to focus along the two transverse axes.

The field gradient can conveniently be related to its optical effect, by normalisation to the particle momentum, thus defining the *quadrupole strength* [Wiedemann, (2007)]:

$$k = \frac{e\,g}{p} = \frac{e\,c\,g}{\beta E}, \tag{4.7}$$

with $pc = \beta E$ where E is the total particle energy, leading to the following numerical expression:

$$k[\mathrm{m}^{-2}] = 299.792\,\frac{g[T/m]}{p[MeV]}. \tag{4.8}$$

The *deflection angle* of a particle is defined by $\alpha = \int \frac{ds}{R}$, hence for a uniform field in the particle path of length l and using (4.1), we get:

$$\alpha = \frac{l}{R} = \frac{q}{p} B_y l = \frac{qc}{\beta E}\,g\,x\,l. \tag{4.9}$$

To obtain the focusing property $\alpha = x/f$, either the magnetic field or the magnet length must depend linearly on the transverse coordinate x. The convenient option is to have a constant

magnet length, while the magnetic field increases linearly with the distance from the axis of the focusing device. Its *focal length* f, alike than for light as described in Figure 4.1, is given by:

$$\frac{1}{f} = \frac{\alpha}{x} = k \times l. \tag{4.10}$$

where l denotes the length of the quadrupole.

An interesting property with quadrupoles (true with dipoles too) is that the horizontal component of the Lorentz force depends only on the horizontal position but not on the vertical position of the particle trajectory, and vice versa [Rossbach, J and Schmüser, P, (1994)]:

$$\begin{cases} F_x = evB_y(x,y) = -evgx, \\ F_y = -evB_x(x,y) = evgy. \end{cases} \tag{4.11}$$

Therefore in a *linear machine*, containing only dipole and quadrupole fields, the horizontal and vertical motions are completely *decoupled*. However, this decoupling would be lost if quadrupole magnets were rotated by some angle around their longitudinal axis, inducing beam distortions.

Thanks to this property, we can consider only one plane, for example the horizontal $x-s$ plane. Equation (4.3) may be solved analytically, leading to the following transfer matrices:

$$\mathbf{M} = \begin{cases} \begin{pmatrix} \cos\Omega & \frac{1}{\sqrt{|k|}}\sin\Omega \\ -\sqrt{|k|}\sin\Omega & \cos\Omega \end{pmatrix} & \text{if } k < 0 \text{ (focusing)} \\ \begin{pmatrix} 1 & s \\ 0 & 1 \end{pmatrix} & \text{if } k = 0 \text{ (drift section)} \\ \begin{pmatrix} \cosh\Omega & \frac{1}{\sqrt{k}}\sinh\Omega \\ \sqrt{k}\sinh\Omega & \cosh\Omega \end{pmatrix} & \text{if } k > 0 \text{ (defocusing)} \end{cases} \tag{4.12}$$

acting on the vector $X = (x, x')$, with $\Omega = \sqrt{|k|}s$. To get the transformation matrix of the complete quadrupole, one has to substitute the variable s by the length of the magnet. In any case, we have $\det \mathbf{M} = 1$, which holds true for all transfer matrices in linear beam optics in general.

Other beam tailoring techniques

To focus a charged particle beam, *solenoids* may also be used, as for instance in low energy sections of accelerators or in electron microscopes [Kumar, (2009)]. For their use on laser-accelerated particle beams, some advantages of quadrupoles over solenoids are described below:

- The focusing power of quadrupoles is stronger than of solenoids [Hofmann, (2013)]. At energies above a few MeV, solenoids require pulsed or superconducting technology, which increases the size and complexity of the system, whereas quadrupoles can still be built with permanent magnets.
- The first quadrupole of a system can be placed close to the particle source which increases the overall capture efficiency, as opposed to pulsed solenoids which can be perturbed by Eddy currents induced by magnetic field rising in the target region [Sekine et al., (2015)].

- Space charge effects observed with solenoids [Harres et al., (2010)] will not occur using quadrupoles. This is because solenoid focusing is independent of the charge, so neutralizing comoving electrons will be strongly focused towards the axis and will interact with the proton distribution [Almomani et al., (2012)]. When entering a quadrupole, electrons will instead be defocused in the axis along which positive ions are focused.

Concerning drawbacks of quadrupoles, we can mention the following:

- The largest disadvantage of a transport line made with quadrupoles is that the defocusing of the beam in one transverse direction induced by the first magnet results in significant particle losses, compared to solenoids which directly focus the beam in the radial direction.
- The transmission of equivalent systems (a quadrupole triplet or a solenoid with the same overall geometrical length and aperture) is slightly lower by 25 % for the triplet vs the solenoid. This is mainly due to the unsymmetrical focusing of quadrupoles mentioned in the first point.
- A quadrupole system is less flexible. While the magnetic field, hence the focal energy and position, can be adjusted with the current injected in a solenoid coil, it requires a rearrangement in the case of a quadrupole setup.

Lastly, we should cite alternative ion beam focusing and energy selection methods that have been investigated. Some approaches rely directly on target engineering, which imply relatively complex target fabrication or preparation procedures. They are less flexible but exempt from the need of installing any additional apparatus. For instance, *hemispherically shaped targets* have been used to generate focused proton beams [Patel et al., (2003)], but this technique has been limited for now to millimeter-scale focal lengths and low proton energy components. Spectral shaping has also been obtained from *microstructured targets* [Pfotenhauer et al., (2008)]. Other approaches operate with single-shot devices that need to be replaced after each shot, and need additional fs laser pulses. A compact laser-driven *plasma microlens* arrangement provided simultaneous focusing and energy selection [Toncian et al., (2006)], thanks to a hollow cylinder irradiated by a second laser pulse. The transmitted energy distribution of this interesting system was tunable with the optical delay between the two laser beams. Strong magnetic fields in the order of a kilotesla were obtained driving miniature single-loop *capacitor-coil targets* with ns laser pulses [Fujioka et al., (2013)]. A compact and versatile solution was proposed by Kar et al., [2016] using *miniature helical coil targets* (see Figure 4.3). The structure, excited by the electromagnetic pulse, surrounded the ion beam to provide simultaneously focusing, energy selection and post-acceleration of laser-driven ions.

The quadrupoles used in our experiments

A set of four **permanent magnet quadrupoles** (PMQs), designed with a *hybrid Halbach geometry* by INFN-LNS researchers and built in collaboration with SIGMAPHI, as an ion collection system for the INFN ELIMED Project [Schillaci et al., (2015a); Schillaci et al., (2015b)], was used to tailor our laser-produced proton beam. PMQ lenses have the advantage of being relatively compact while producing high field gradients within a relatively large aperture. In the present case, the system consists of two sets of two PMQs of 40 mm and 80 mm length, with a magnetic field gradient of about $100\,\mathrm{T}\cdot\mathrm{m}^{-1}$ inside a 2 cm diameter net bore (see Figure 4.4). The compact size enables us to install the device inside the interaction chamber as close as possible to the interaction point. The minimum distance between the target and the entrance of the first PMQ was 5 cm to prevent the target mount from hitting the PMQ system during the target

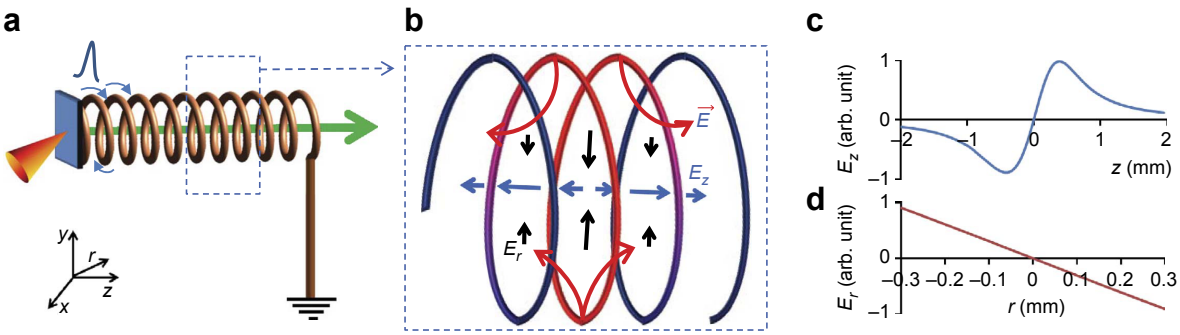

FIGURE 4.3: (a) Schematic representation of the target designed for optimizing the beam parameters of laser-driven protons. A helical coil is attached to the laser-irradiated thin foil and guides the EM pulse carrying the neutralizing charge around the proton-beam axis. (b) Snapshot showing the electric field configuration inside the coil. The red section of the coil represents the segment charged by the travelling pulse at a given moment of time. (c,d) Radial $E_z|_{(r=0)}$ and longitudinal $E_r|_{(z=0)}$ profiles of the electric field inside the coil at a given time, where $z = 0$ corresponds to the location of the peak of charge density along the coil at that time. (Adapted from [Kar et al., (2016)])

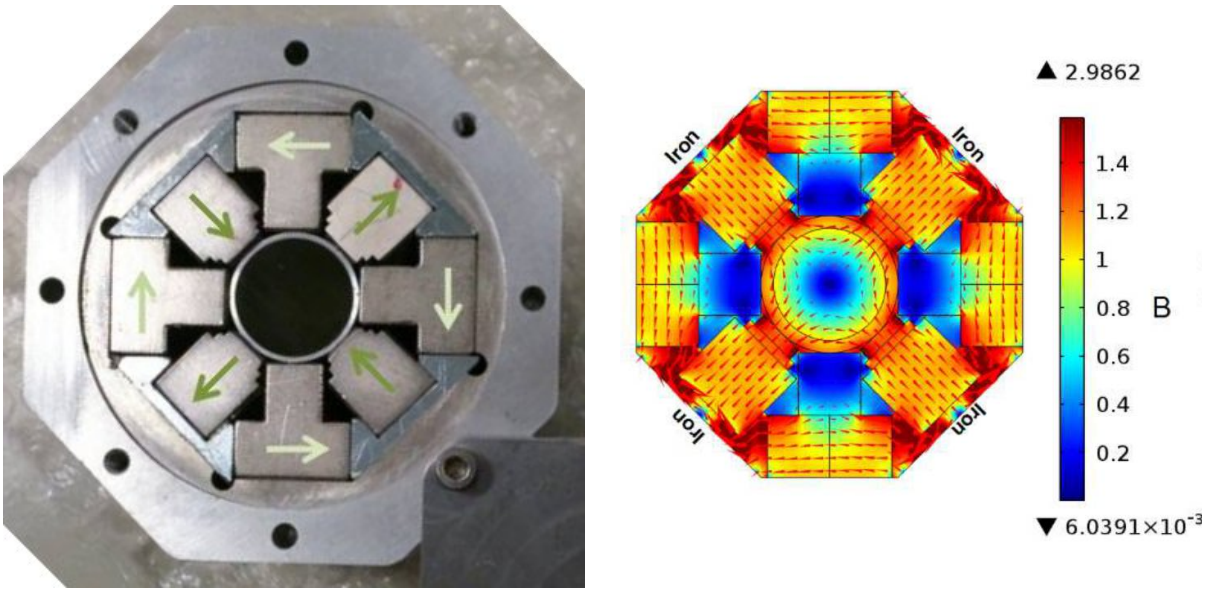

FIGURE 4.4: Picture taken in the axis of one of the permanent magnet quadrupole used (left). Simulated magnetic flux density (colour scale) and field lines directions (red arrows) inside the hybrid Halbach geometry of the PMQ (right, adapted from [Schillaci et al., (2015b)]).

replacements and alignments. These properties make PMQs specially suitable to handle laser-accelerated beams [Schollmeier et al., (2008); Sakaki et al., (2010)], when the device has to operate under vacuum.

As the permanent magnets have a fixed field strength, the system is tuned by adapting the position of the elements along the beam line axis, in analogy to familiar optics. However, the system being chromatic, a given configuration is optimized for a single energy component of the beam, because it impossible to adjust the position of the various PMQs to get the desired profiles for several proton energies independently. This is demonstrated by simulations showing generally large losses for protons with energies outside the range for which the setup was implemented. To adjust the output beam according to the required size and energy, the available parameters are the respective order and polarity of the PMQs, as well as the distance separating them, in the limits of the physical constraints (minimum gap between two PMQs of about 11 mm).

The spacings between the elements are first optimized with single energy simulations performed with TraceWin[1], in which field maps of the PMQs are used. Size, divergence and current diagnostics are inserted in the simulated setup to define goal values for the beam characteristics and losses. Once a configuration fits the needs for the selected energy, thorough polychromatic simulations are run using Simion® Ion and Electron Optics Simulator, for which the experimentally measured energy-dependent divergence of the beam (see Fig. 3.18) is implemented. Several configurations have been tested, but the only ones effectively transporting the beam without prohibitive losses where the following (the subscript **S** and **L** are used to designate the **short** and **long** PMQs, while the superscript is related to their polarity).

- Setup used for radiobiological experiments: $Source \rightarrow Q_L^+ \rightarrow Q_L^- \rightarrow Q_S^+ \rightarrow Q_S^-$
- Setup used for focusing 8 MeV protons: $Source \rightarrow Q_S^+ \rightarrow Q_L^- \rightarrow Q_L^+ \rightarrow Q_S^+$
- Other simulated setups potentially useful: $Source \rightarrow Q_L^+ \rightarrow Q_S^- \rightarrow Q_S^- \rightarrow Q_L^+$
  $Source \rightarrow Q_L^+ \rightarrow Q_S^- \rightarrow Q_S^+ \rightarrow Q_L^-$
  $Source \rightarrow Q_L^+ \rightarrow Q_S^- \rightarrow Q_S^- \rightarrow Q_L^+$
  $Source \rightarrow Q_S^+ \rightarrow Q_S^+ \rightarrow Q_L^- \rightarrow Q_L^+$
  $Source \rightarrow Q_L^+ \rightarrow Q_L^- \rightarrow Q_S^+ \rightarrow Q_S^+$
- 3 PMQ setups may also be used, but they proved to be less efficient and flexible.

Following equations (4.8) and (4.10), with reference field gradients of $k_S = 104\,\mathrm{T}\cdot\mathrm{m}^{-1}$ and $k_L = 114\,\mathrm{T}\cdot\mathrm{m}^{-1}$ and effective lengths of $l_S = 43.5\,\mathrm{mm}$ and $l_L = 84\,\mathrm{mm}$ [Schillaci et al., (2015b)], the PMQ focal lengths for proton energies of 5 MeV and 8 MeV are: $f_{S5} = 71.5\,\mathrm{mm}$, $f_{L5} = 34.8\,\mathrm{mm}$, and $f_{S8} = 90.5\,\mathrm{mm}$, $f_{L8} = 42.8\,\mathrm{mm}$.

4.2 Proton Beam Spatial and Spectral Shaping

This section starts with the preliminary results obtained with a magnetic chicane. Then, the characterisation of the different PMQ setups used for distinct purposes is presented in this section, namely to focus an energy component of the proton beam, or transport efficiently a narrow range of energies to perform radiobiological experiments.

[1] code developed by the CEA, available at http://irfu.cea.fr/Sacm/logiciels/index3.php

4.2.1 Beam transport with a magnetic chicane

Following the energy selection systems for laser-driven proton beam applications described in the literature [Fourkal et al., (2003); Luo et al., (2005); Yogo et al., (2011a); Scuderi et al., (2014)] (see Figure 4.5), a **magnetic chicane** was built. It consists of four *magnetic dipoles*, each made of a pair of rectangular cuboid permanent magnets[2]. They are enclosed in a ferromagnetic alloy assembly 1 cm thick, and generate a magnetic field of 0.38 T in the center of their air gap with a 3 cm height (see a picture and drawing of the system in Figure 4.6). The second and third magnetic fields are parallel with each other and oriented antiparallel to the first and fourth ones.

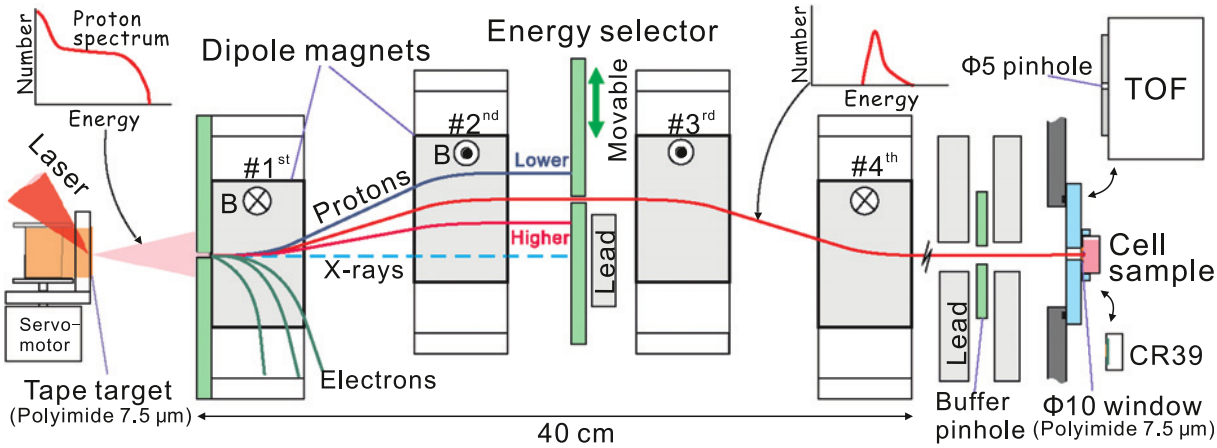

FIGURE 4.5: Schematic of a magnetic chicane for an experimental laser-driven quasi-monoenergetic beam line. (Extracted from [Yogo et al., (2011a)])

This spectrometer-like particle selector uses the magnetic field configuration to spread the protons spatially according to their energy and emitting angle. Protons are laterally displaced from the target normal axis in the midplane (half way between the second and third dipoles) by the first two dipoles. The beam energy range is set by a motorised movable vertical slit aperture located in this midplane. The last two magnets steer protons back to the target normal axis to refocus the beam using the opposite gradient. Protons are finally extracted from vacuum into air through a thin Mylar window behind which is placed the biological samples to irradiate.

The central energy and energy spread of the output proton beam spectrum could in principle be precisely tuned by moving transversely the midplane slit, if the incoming beam is initially well collimated by an entrance aperture. This will limit the spatial mixing of different proton energies once they travelled through the magnetic system, making the selection more accurate but at the cost of a reduced fluence. Moreover, the central slit and dipoles are mounted on a translation stage allowing transversal movement to select energy over a larger range. The first and fourth dipoles are mounted on a rail so that they can move in the longitudinal direction allowing possible magnetic field asymmetries to be compensated. The central slit is provided with a remote controlled actuator allowing to set the relative position of the slit and the two central dipoles.

[2]made of sintered neodymium NdFeB / N42 with a nickel coating; dimensions: 4 cm length, 4 cm width, 2 cm height; 239 g dead weight; flux density inside the magnet of $B_r = 1.28$ T and on its surface of $B_s = 384$ mT; holding force on a steel plate of $F = 524$ N ; https://www.hkcm.de/HKCM_allinone.php?id=7352

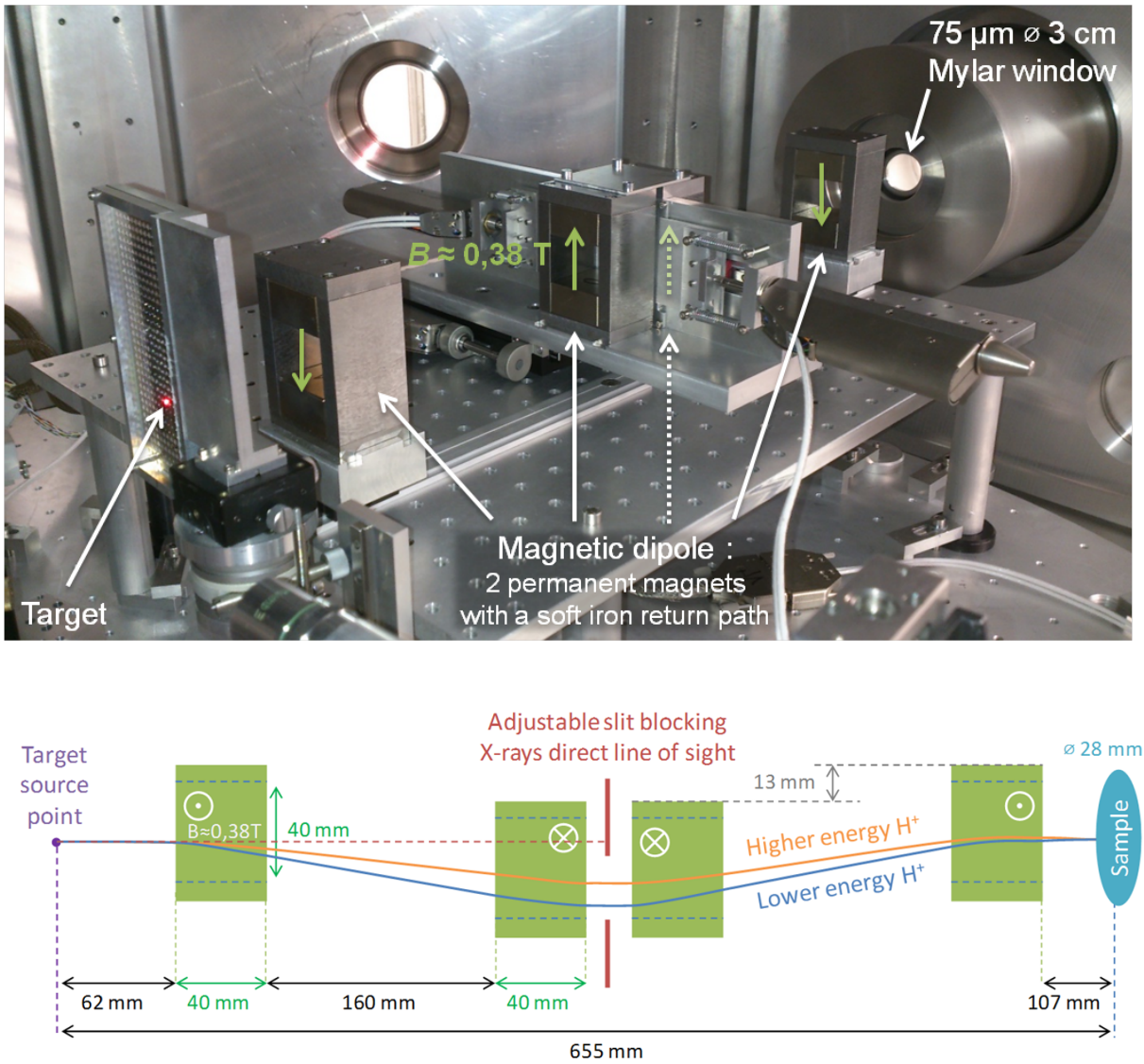

FIGURE 4.6: Picture and sketch of the magnetic chicane.

This chicane was assembled on a 55 cm long breadboard and tested in December 2014. The output proton beam profiles shown in Figure 4.7 were recorded in vacuum on a 9 cm diameter *plastic scintillator* and on an IP both placed 52 mm behind the exit of the last dipole. The non uniformities observed are due mainly to the fringe field of the magnetic dipoles that have a rather big air gap (chosen so to match the biological sample size). The scintillator image in Figure 4.7a features an intense horizontal line on the left that is almost suppressed for a narrower slit aperture blocking the lower energies in Figures 4.7b and 4.7d.

The system was characterised numerically with a Python code assuming a magnetic field with a super-Gaussian longitudinal profile, uniform in the transverse directions. For an input beam without any divergence, each transverse position in the slit plane corresponds to a given proton energy, as shown in Figure 4.8. A realistic beam with an energy-dependent divergence was also simulated (see Figure 4.9), indicating high output losses.

In fact, such a chicane could be useful to generate a thin and tunable quasi-monochromatic beam because to achieve a good energy selection and a uniform output beam, a well collimated input beam and a narrow slit opening are required. A compromise has to be found between the monochromaticity and homogeneity of the output beam or its charge and size. It is therefore suitable for conventional particle accelerator beams with a small divergence, but it is less appropriate for raw laser-accelerated proton beams with a high divergence. However, it can be relevant on laser accelerators if used in combination with an initial capture and collection device providing a collimated beam to the chicane, as described in [Fourkal et al., (2003); Cirrone et al., (2013)].

To cope with the chicane main drawback, which is a non uniform output dose deposition and a low transmission efficiency, an alternative solution was considered to handle the beam divergence. The next multipole order after dipoles was used, that is quadrupole magnetic fields.

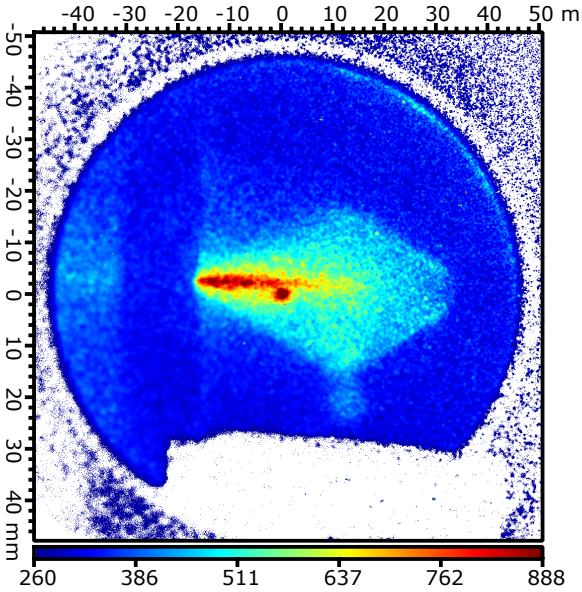

(a) Scintillator picture, central slit range: −10 mm to −33 mm.

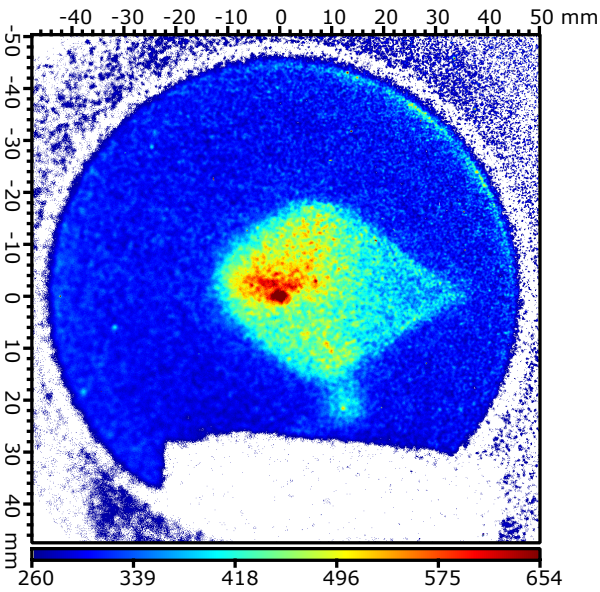

(b) Scintillator picture, central slit range: −11 mm to −21 mm.

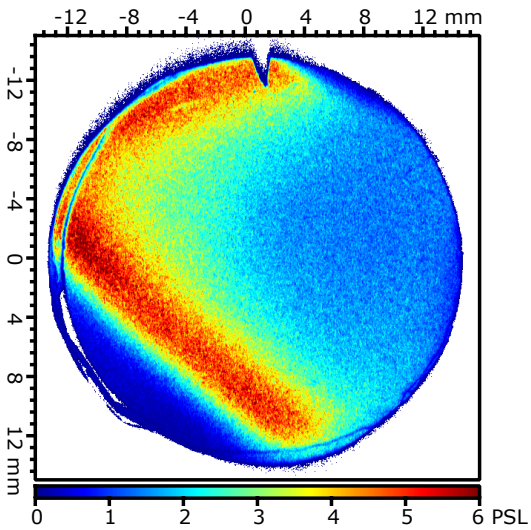

(c) Scan of an IP placed in air at the sample location 66 cm away from the source right after the Mylar window.

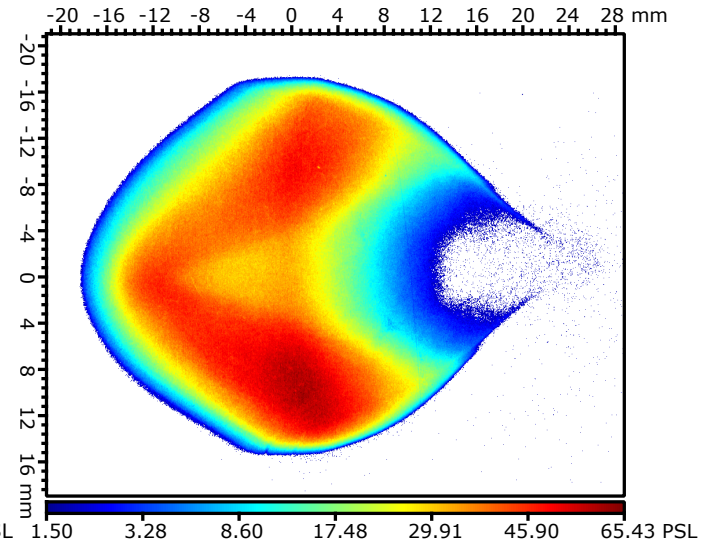

(d) Scan of an IP placed in vacuum in front of the scintillator, for the same slit configuration as in Fig.b.

FIGURE 4.7: Proton beam profile recorded with various detectors for different opening ranges of the central energy selecting slit. The central dipoles were offset by 13 mm from the axis of the extreme ones, and the slit range limits are referred with respect to this axis. The scintillator was placed in vacuum at the chicane output, 60 cm behind the source. Its center is marked by a hole, hence the strong signal spot observed at this position.

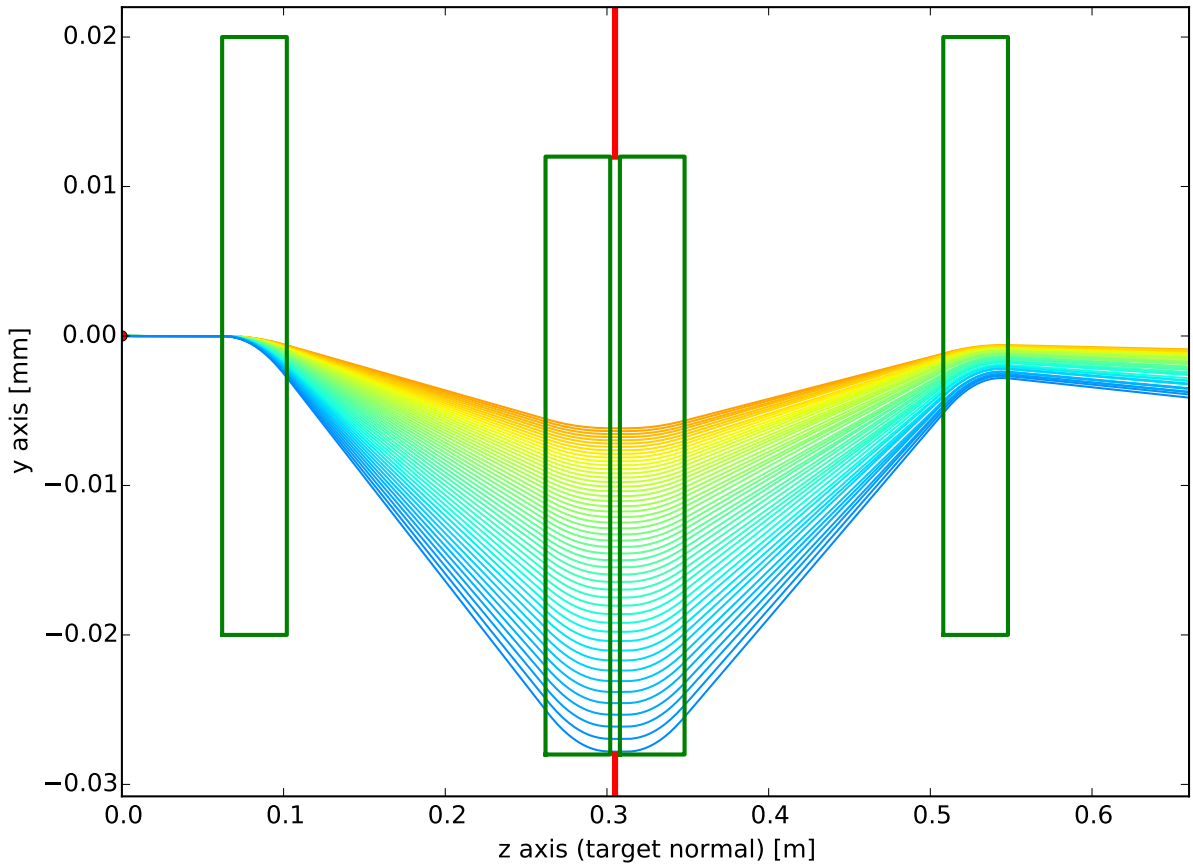

(a) Proton trajectories inside the device. The green rectangles represent the dipole field regions. Notice that the beam does not recollimate perfectly at the output, which is due to the inhomogeneous magnetic field profile.

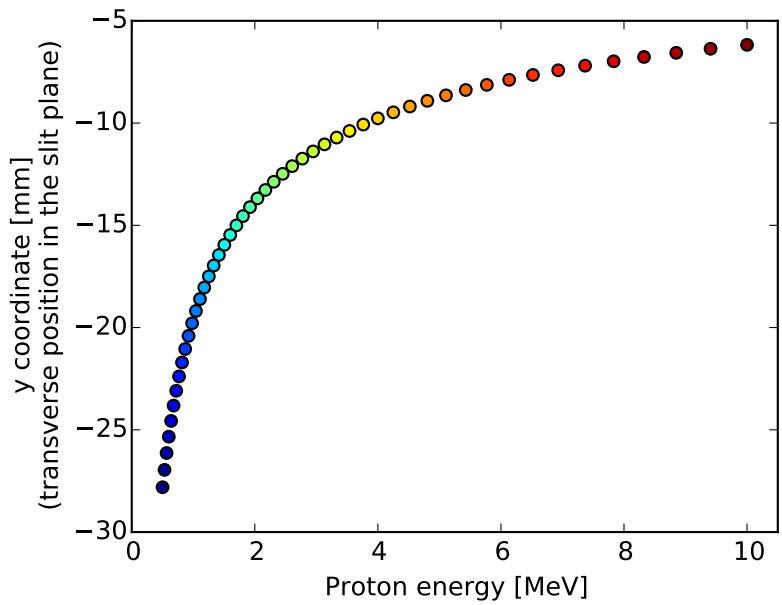

(b) Correspondence between the proton energy and the y transverse coordinate of its trajectory in the filtering slit plane.

FIGURE 4.8: Numerical simulation of a proton beam, without any initial divergence but including a range of energies, propagating inside the chicane.

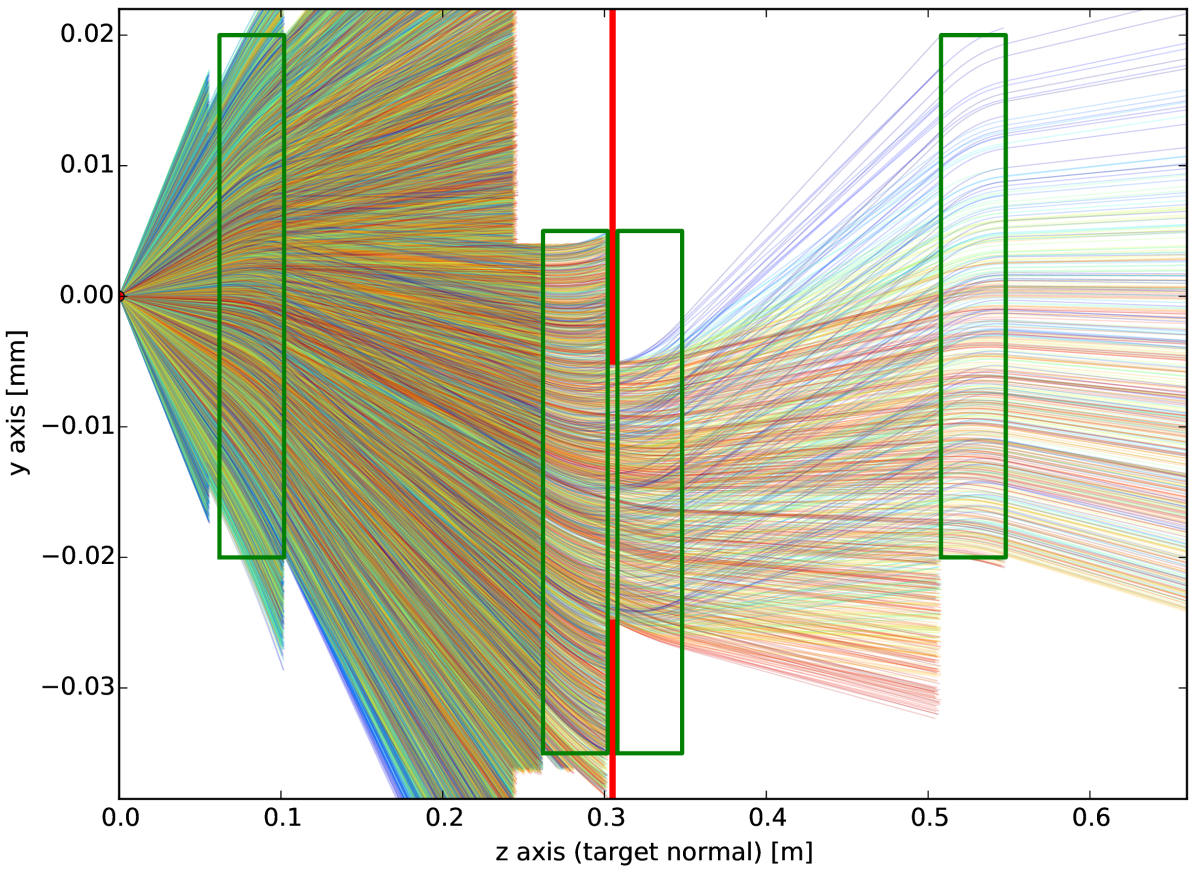

FIGURE 4.9: Numerical simulation of a realistic TNSA proton beam propagating through the chicane. The transmission efficiency is about 1 %.

4.2.2 Beam focusing with PMQs

PMQ setup for focusing 8 MeV protons

The PMQ system has been optimized in order to focus 8 MeV protons 442 mm behind the laser-target interaction point, as shown in Figure 4.10 and published in [Schillaci et al., (2016)]. The relative distances between the elements of the beamline are detailed in the sketch of Figure 4.11.

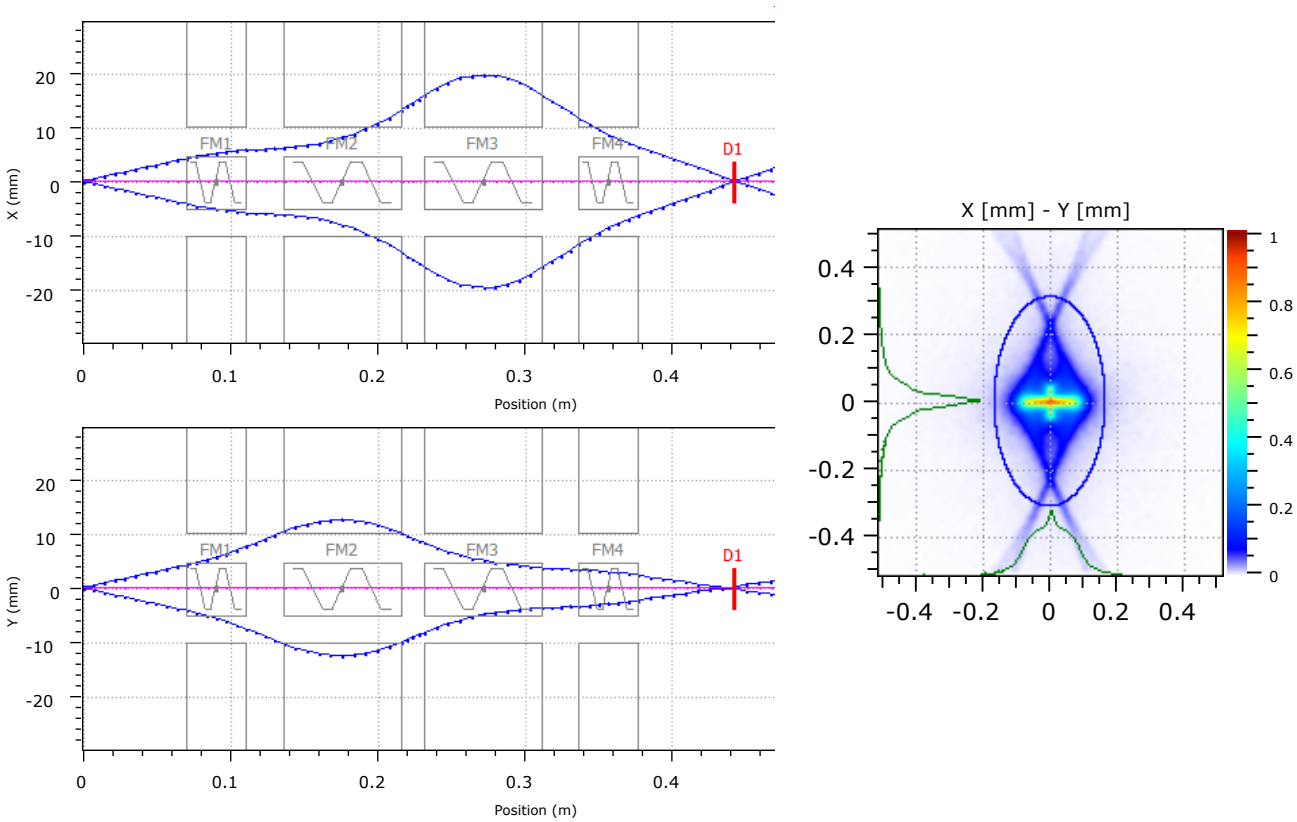

FIGURE 4.10: TraceWin simulations showing the multiparticle beam envelope of the 8 MeV protons computed in the two transverse directions (left), for the PMQ setup described in Figure 4.11 leading to a focus point 442 mm downstream the source, in the plane marked D1 in red. The transverse profile in that plane is plotted on the right, where the rms fit of the beam with an ellipse has diameters of size 0.33 mm × 0.63 mm.

A stack of six RCF films HD-810 has been set in the plane of the expected focal point. This type of films has a low sensitivity, in fact 25 laser shots have been fired in order to accumulate enough energy deposition to have visible traces. On the other hand, they are thin enough (105 µm) to guarantee a good energy resolution when they are used in a stack configuration. Experimental and simulation results are compared in Table 4.1.

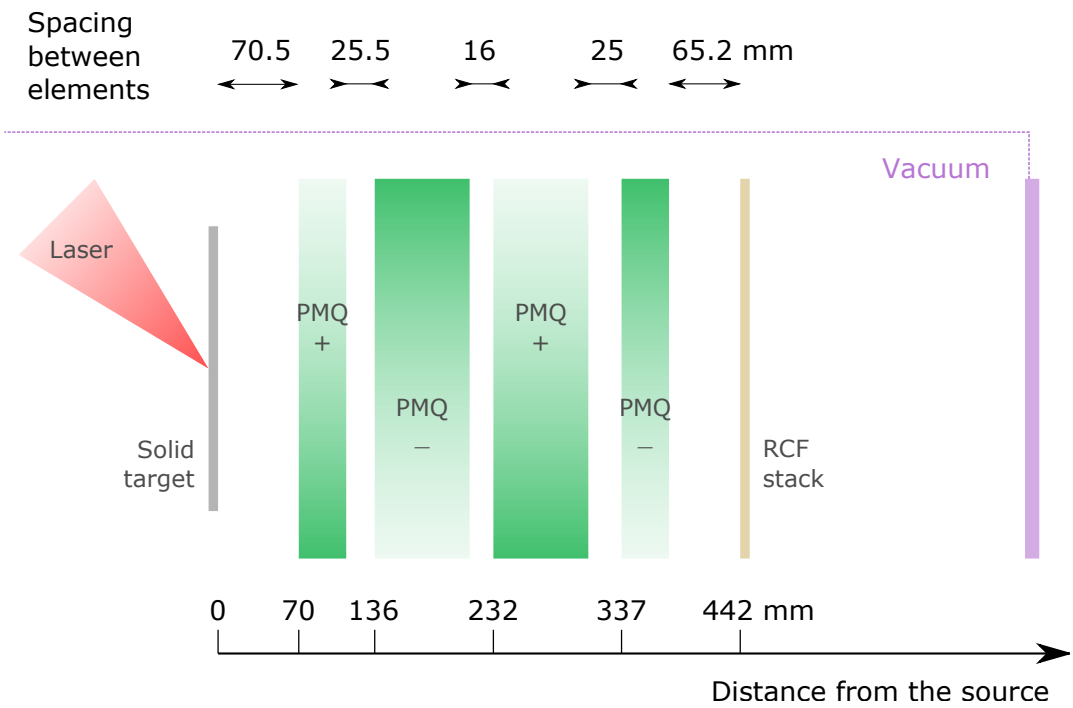

FIGURE 4.11: PMQ setup for 8 MeV proton beam focusing.

The RCF stack has been shielded with aluminum foil 130 µm thick filtering heavy ions, protons with energy lower than 3.98 MeV, and some photons. The calculated lower energy cutoff of protons reaching each layer of the stack is specified in the first column, and it corresponds to the monochromatic energy of the proton beam simulated with TraceWin (third column, colors are related to the particle density), and to the minimum energy of the realistic TNSA beam spectrum simulated with Simion (fourth column, the color scale represents the proton energy). The contrast of the RCF scanned images (second column) has been enhanced to bring out the proton energy deposition marked by the blue coloration of the film. The scanned images of the RCF films and the simulation plots have the same scale.

Lower H^+ energy cutoff	Experimental RCF HD-810 scan	TraceWin monochromatic simulation	Simion polychromatic simulation
4.0 MeV	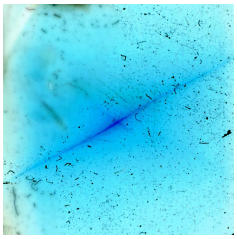	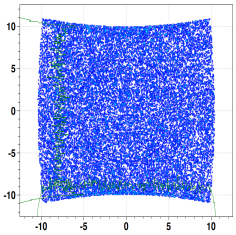	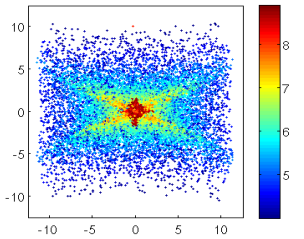
5.18 MeV	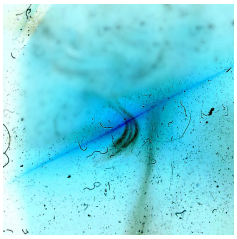	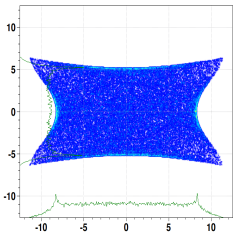	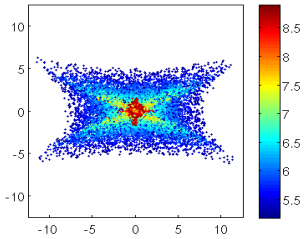
6.17 MeV	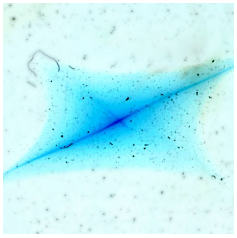	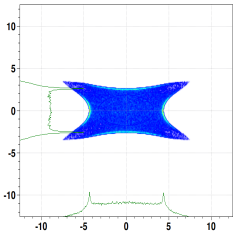	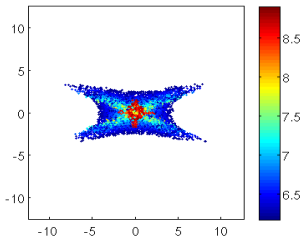
7.05 MeV	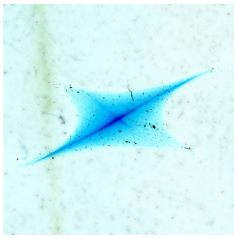	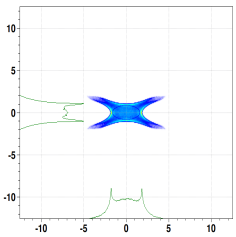	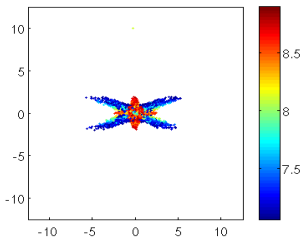
7.83 MeV	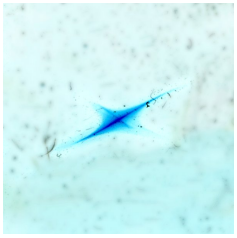	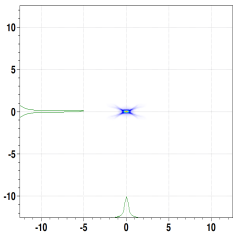	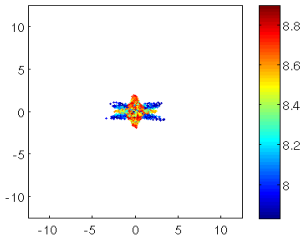
8.56 MeV	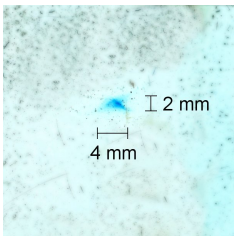	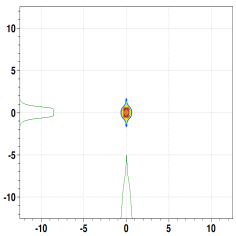	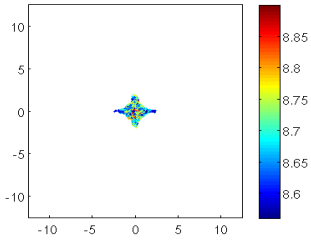

TABLE 4.1: Comparison of experimental results and simulations of the proton beam transverse profile 442 mm behind the source in the plane of focus with the PMQ system of the 8 MeV proton component. The scanned images of the RCF films (second column) and the simulation plots have the same scale.

The proper characterization of the proton source, both in terms of energy and spatial distribution, and hence emittance, allows to simulate the system with good precision. The results in Table 4.1 demonstrate the possibility to have a precise control on the beam optics. The cross-like trace, due to the high energy components, is well visible and in agreement with polychromatic beam simulations. However, small discrepancies in the experimental and simulated profiles may be related to different factors discussed below. The experimental beams imprinted in the first layers have slightly bigger beam size. This difference could be due to dispersion of the beam by scattering during the interaction with the filter and the previous layers, and also to the space charge effect, not considered in the simulations. A small spreading of the traces could result from the spatial averaging of the signal, deriving from the accumulation of multiple shots, for which the interaction conditions and hence the emitted beam direction could fluctuate. Even so, the diagonal feature looks sharp, with no evident blur, eliminating this possible effect at least on the higher proton energy range. In the last layer (row number six, recording signal from protons with energies above 8.56 MeV), the low amount of particle interacting with the film, as we are approaching the beam energy cutoff, leads to a low energy deposition and the apparently smaller beam spot size than in the Simion simulation. The PMQ field quality and errors, analysed in [Schillaci et al., (2015b)] can also be responsible for distortions and differences in the beam shape. The cross-like shape, which reflects the magnetic field of the quadrupoles, is due to the fact that the amount of particles moving outside the good field region of the PMQs (which has a 6 mm radius for a 10 mm bore radius) is significant. Also, non-linear effects on the beam optics cannot be neglected, but they are well reproduced by the simulations, and can be limited using collimators if required. In addition to alignment errors of the quadrupole mechanical system, these non-linear fields are responsible for the non symmetrical shape, with for instance a stronger bottom-left to top-right diagonal compared to the signal along the other one.

Lastly, the 8.56 MeV protons are focused to a noteworthy tiny spot size of less than 4 mm $\times$ 2 mm at 442 mm from the target. By comparison, the focusing of 2.4 MeV laser-driven protons to a spot size of 3 mm $\times$ 8 mm at 640 mm downstream from the target was demonstrated with two PMQs in [Nishiuchi et al., (2009); Nishiuchi et al., (2010)].

Energy filtering with PMQs

The PMQ setup described earlier has demonstrated the possibility to partly focus a proton beam, which offers the chance to perform energy selection to a certain extent. The PMQs having an intrinsic chromatic behaviour, a setup designed to focus a given energy component will not concentrate the other energies at the same location (if they actually are focused). In the present case, higher energy components are focused further from the source while lower energy components are focused closer, with the smallest size achieved in both cases in a slightly different longitudinal plane, as shown in Figure 4.12. By inserting a fitting aperture in the plane of focus, the selected energy component will be well transmitted, while the others will suffer from high losses due to a beam spot size larger than the aperture in its plane. The simulated transverse profile of the proton beam in the plane of the aperture is plotted in Figure 4.13 (as function of the proton energy in (a) and as function of the proton density distribution in (b)). The spectra before and after the filter are represented in Figure 4.13c, along with in (d) the deduced energy-dependent transmission efficiency of such a system, made of 4 PMQs and a 1 mm diameter aperture.

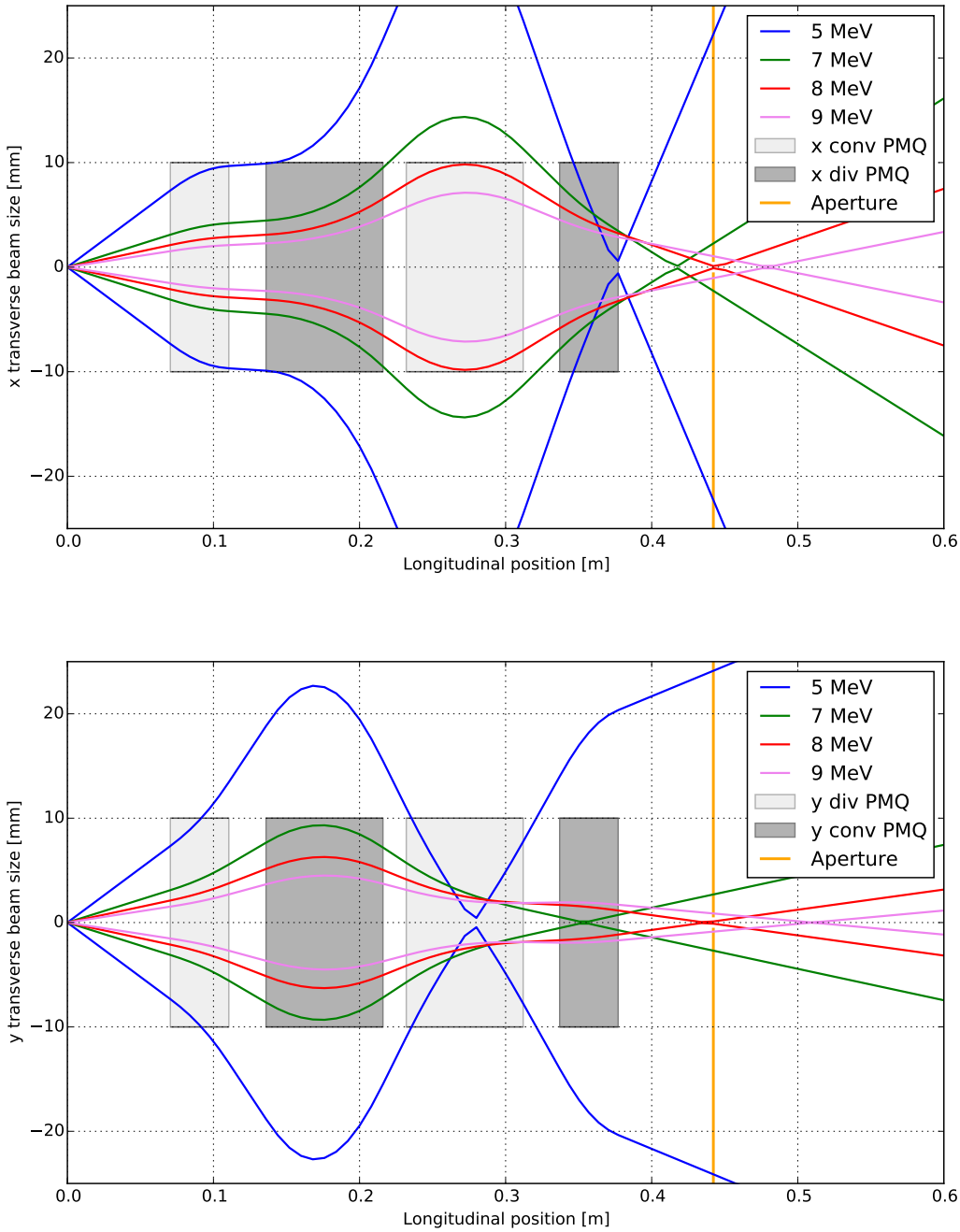

FIGURE 4.12: Beam envelope simulated in the two transverse directions for different proton energies in TraceWin. The orange line represents the filtering aperture placed in the plane of focus of the 8 MeV protons. The graph shows the full size of the beam envelope as if the PMQ field was not limited in the transverse direction and no clipping was cutting the beam due to the finite PMQ bore diameter.

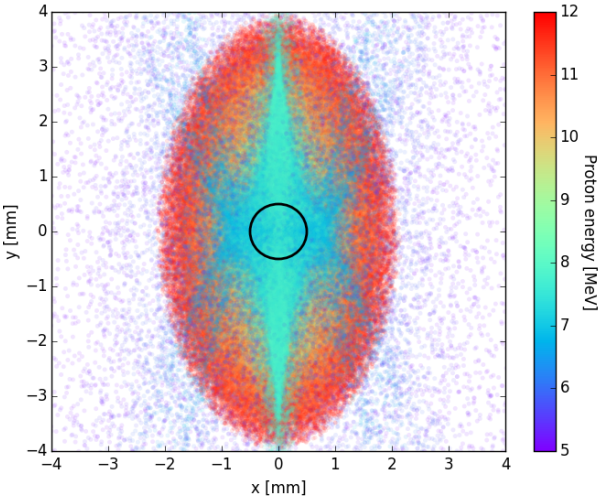

(a) Beam profile represented with a colorscale related to the proton energy.

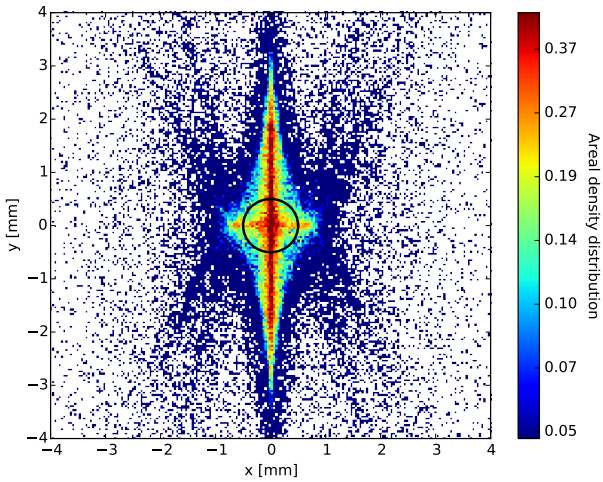

(b) Density distribution of the transverse beam profile.

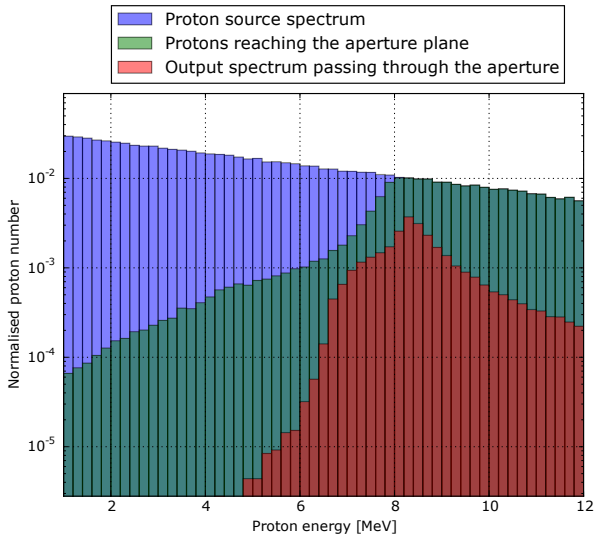

(c) Proton energy spectra, with a logarithmic vertical scale, of the source beam (in blue), of the beam reaching the aperture plane 442 mm downstream (in green), and of the output beam passing through the 1 mm diameter aperture (in red).

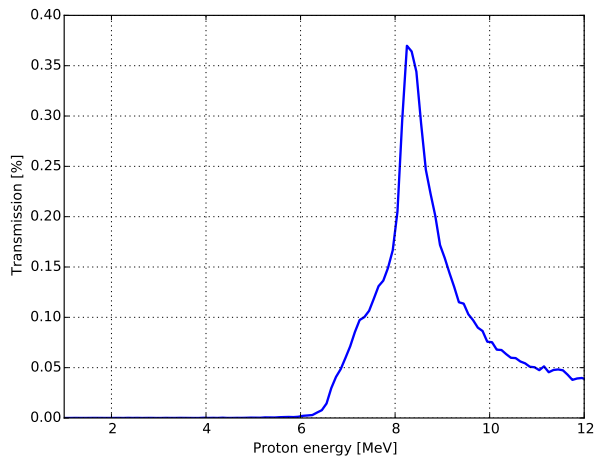

(d) Transmission efficiency of the system, calculated in function of the proton energy, as the ratio between the output and source spectra shown in c.

FIGURE 4.13: Simion simulation of the energy filtering system made of 4 PMQs and an aperture, for a TNSA beam (polychromatic and with an energy-dependent divergence). a and b show the proton beam profile in the transverse plane of the aperture 442 mm away from the source. The central black circle depicts the edge of a 1 mm diameter aperture.

A concentration of protons with energies around 8 MeV is observed in the enclosure of the aperture in the simulated density profile, and the calculated transmission efficiency demonstrates the good energy filtering exerted by the system. This type of setup, with an aperture located in the transverse focus plane of one energy of a proton beam, enable to extract, from a continuous energy spectrum, a beam with a narrower energy spread and a peak in its spectrum. This quasi-monoenergetic output spectrum can only be obtained with a small filtering aperture at the expense of high particle losses, which are nonetheless reduced down to 63 % at the peak of the beam transmission in the setting examined. The efficiency of the energy filtering is also dictated by the shift in the focus longitudinal position with the proton energy. A setup maximising the system chromaticity, hence leading to a faster increase of the beam size in the aperture plane as the proton energy move away from the selected energy, would improve its performance.

4.2.3 Radiobiology transport beamline

In this section, the transport system designed for sample irradiation, illustrated in Figure 4.14, is studied in details. The same configuration was kept since November 2015 for the cell irradiation tests, to be able to compare results and conclude on the observed effects. The beamline proved to be robust indeed, providing a stable output beam with similar profiles even after dismounting and repositioning the entire PMQ system, besides millimetric adjustments of the sample position. At the time, it was the most preferable setup given the proton acceleration conditions available, even though after improvements of some laser parameters, the setup could have been optimize to provide a more homogeneous output dose distribution, making use of the increased proton beam fluence in the higher energy range.

The examined setup was chosen to have a wide and relatively uniform output proton beam with a peak in its spectrum at 5 MeV. This initial proton energy was selected far enough from the 8 MeV cutoff so that the output charge would be significant and less sensitive to fluctuations of the source. Besides, it had to be high enough so that its Bragg peak would be located closely after the cell layer at the output. The protons at the peak in the output spectrum have a Bragg peak occurring past the cells, hence fluctuations of the received dose due to fluctuations in sample positioning are limited while maximising the dose deposition in the sample to be irradiated in air. After the PMQ system, protons with energies above 2.3 MeV are allowed to exit the vacuum chamber through a 75 µm thick Mylar film serving as a chamber window. Its thickness was chosen thin enough to limit the energy range filters out, but thick enough to sustain, with a safety margin, atmospheric pressure over its 3 cm diameter surface. A few centimeters behind is inserted the transmission ionization chamber, and the biological sample is placed at the end of the line, 1 m from the target (see Figure 4.15). The sample dish is fixed on a holder mount with a magnetic base, to facilitate a quick installation and removal, and ensure repeatability of the exact same positioning of every sample. After this brief description of the experimental system, let us examine its effect on the transported proton beam.

Comparison between experimental and simulated beam profiles

An accurate beam optics study has been carried out for this setup, recording the beam transverse profile at several positions along the PMQ system, shown in Figure 4.14. The beam envelopes for different proton energies obtained with TraceWin Multiparticle calculations are shown in Figure 4.16. RCF films type EBT3 were used in stacks of two layers (each with a 280 µm

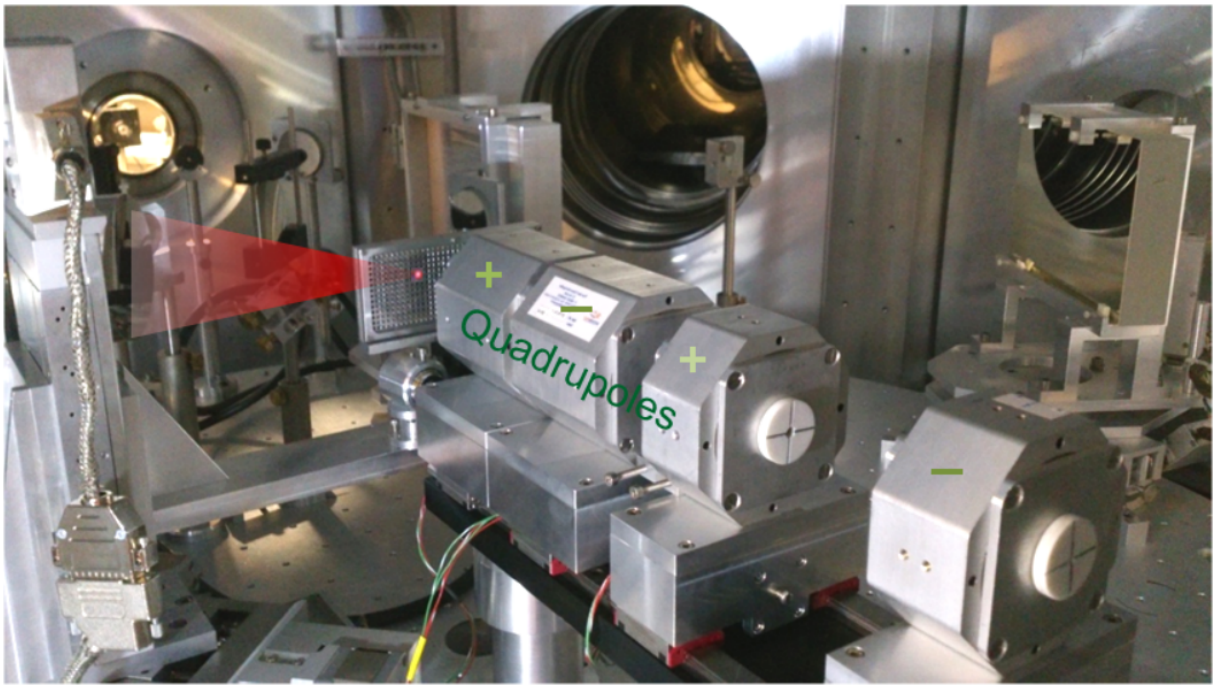

(a) Picture of the PMQ setup mounted inside the experimental chamber.

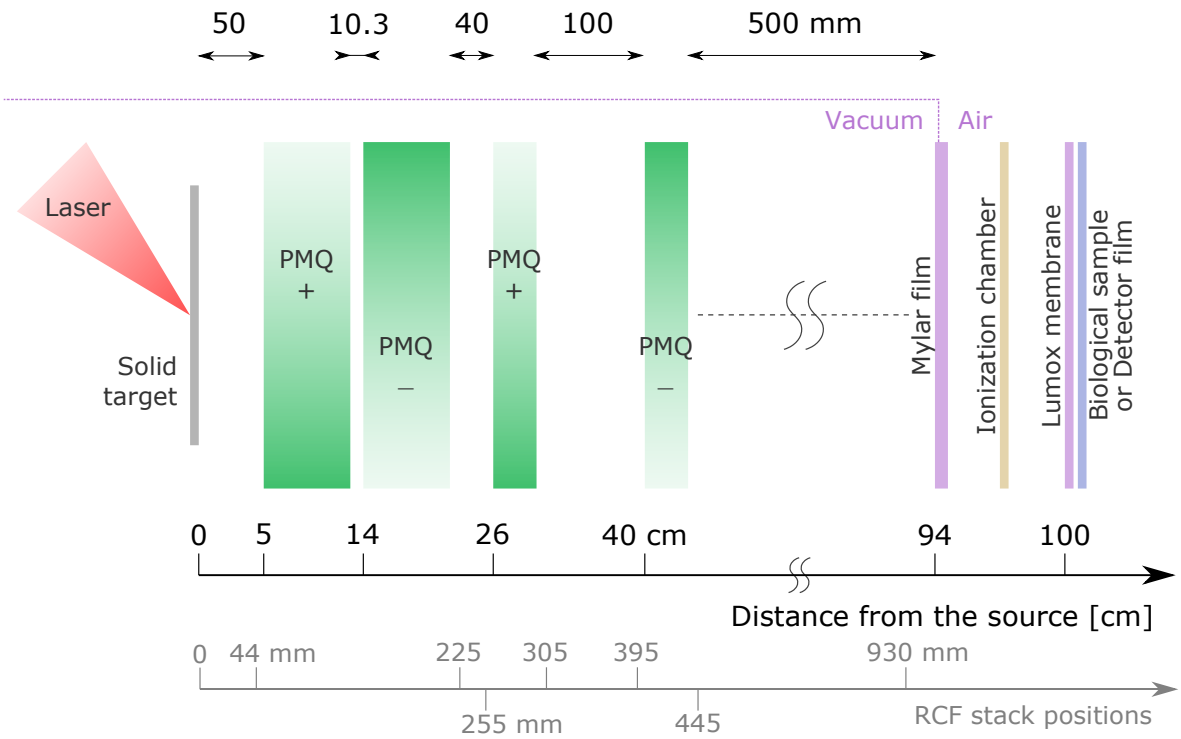

(b) Sketch of the setup used for radiobiological experiments, with details on the spacing and position of the elements marked on the black scale. It includes the 75 µm Mylar film ensuring the vacuum/air separation, as well as the transmission ionisation chamber and the sample located in the in-air region (see a picture in Figure 4.15). The gray scale indicates the distances from the source of the RCF stacks used for beam profile characterisation.

FIGURE 4.14: SAPHIR beamline designed for radiobiological experiments. The plus and minus symbols indicate the relative polarity of each PMQ that focuses a charged particle beam along one axis (as would a cylindrical lens) and defocuses it along the other.

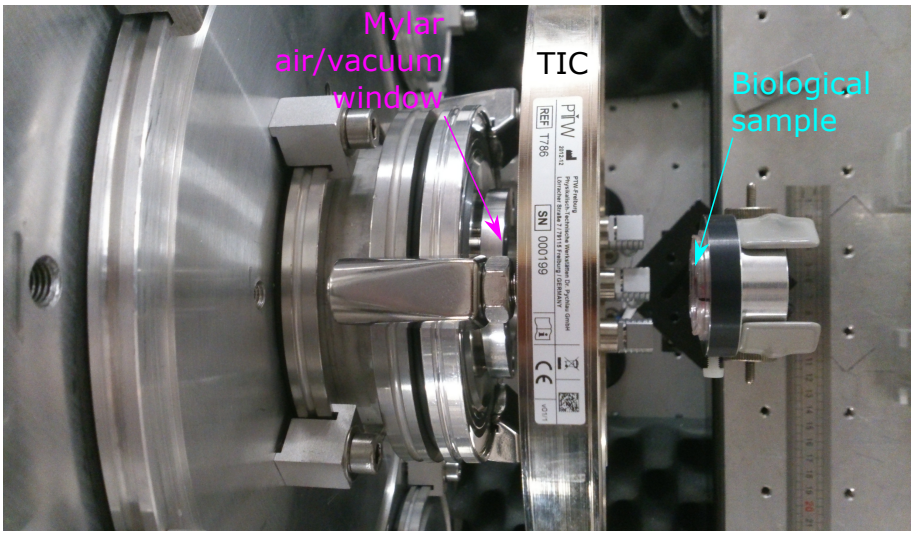

(a) Top view.

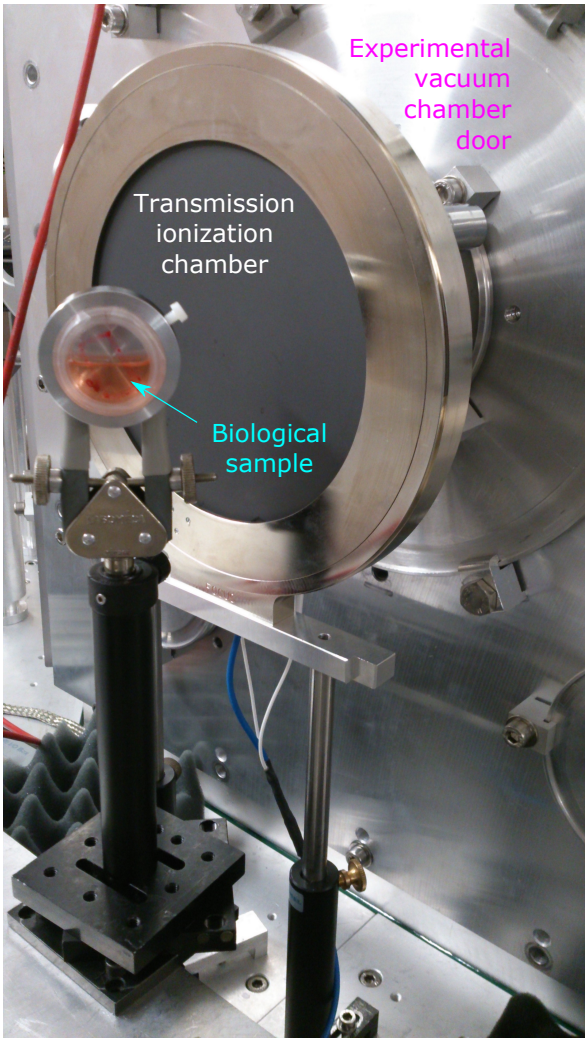

(b) Back view. The sample mount was rotate to show it; the TIC is hiding the Mylar film.

FIGURE 4.15: Picture of the transmission ionization chamber inserted between the biological sample and the vacuum chamber window.

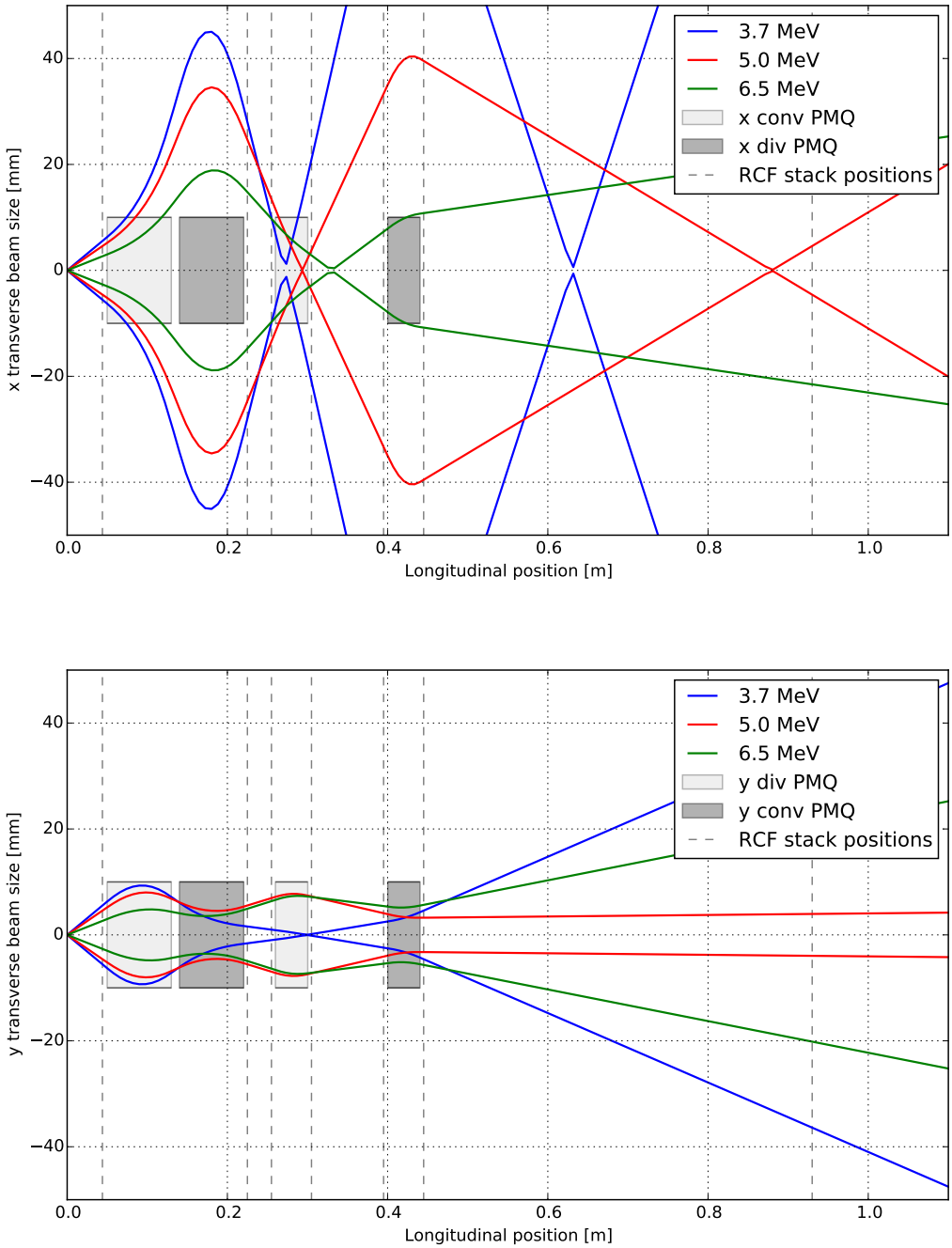

FIGURE 4.16: Proton beam envelope calculated in the two transverse directions in the described PMQ setup with the TraceWin Multiparticle tool. Beams with different energies, corresponding to the energy for which the line was optimized (5 MeV) and associated to the protons observed in the different layers of the RCF stack, are simulated. The vertical dash lines mark the various planes where a RCF stack was placed to record the transverse beam profile. The graph shows the full extent of the beam envelope as if the PMQ field and bore diameter were not limited in the transverse direction, not inducing any loss of particles while clipping the beam.

thickness), shielded with a 26 µm thick aluminum foil, to record the transverse beam profile along the propagation path of the beam. The energy resolution is worst than in the previous case (protons were penetrating only two layers) but these thicker films are more sensitive and only 6 laser shots were fired.

The results of the PMQs optics effect on the proton beam observed on each RCF film are reported in tables 4.2 and 4.3, with comparison of simulations done with TraceWin and Simion. In particular, table 4.2 refers only to the first film layer of each stack, whose lower energy cutoff is 3.66 MeV. Table 4.3 refers only to the second film of each stack, whose lower energy cutoff is 6.48 MeV. The distance from the source to the transverse plane of measurement is indicated in the first column. In the tables, a scanned image of the first and second layers of each RCF stack irradiated is shown in the second column. Their sensitive layer were reached by protons with energies above 3.66 and 6.48 MeV respectively, which is the energy of the monochromatic beam simulated in TraceWin (third column, colors are related to the particle density), and it also corresponds to the minimum energy of the realistic TNSA beam spectrum simulated in Simion (fourth column).

Longitudinal position and transverse size	Experimental scan of the first layer of the RCF EBT3 stack	TraceWin 3.66 MeV monochromatic simulation	Simion polychromatic simulation
225 mm, 29.6x29.6 mm	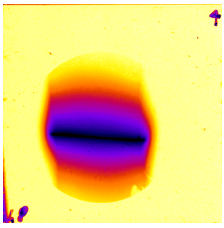	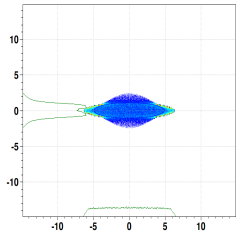	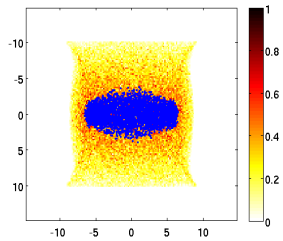
255 mm, 29.6x29.6 mm	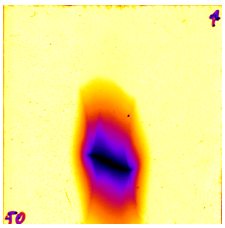	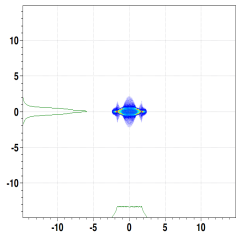	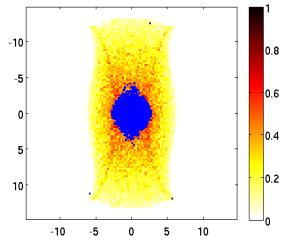
305 mm, 29.6x29.6 mm	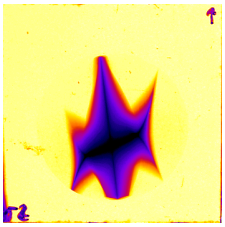	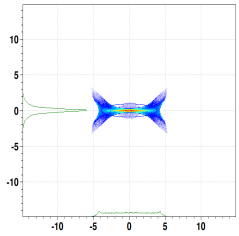	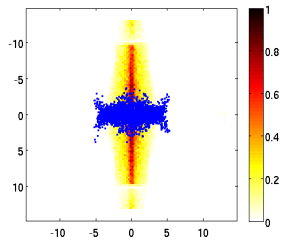
395 mm, 51.6x29.6 mm	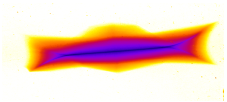	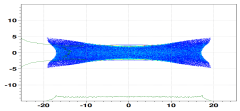	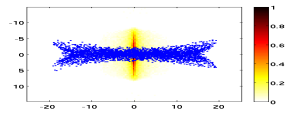
445 mm, 29.6x29.6 mm	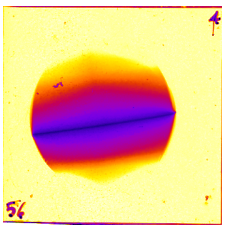	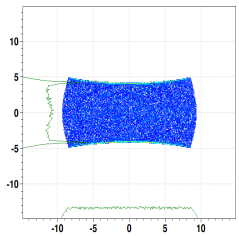	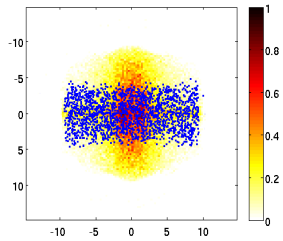
930 mm, 57.8x57.8 mm	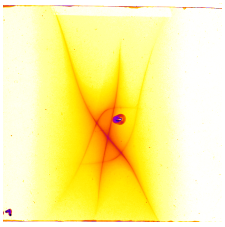	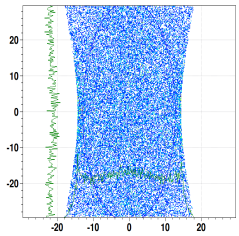	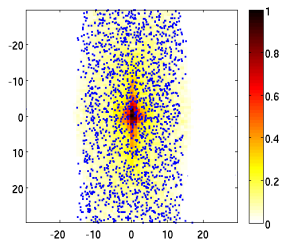

TABLE 4.2: Comparison of experimental results and simulations of the proton beam transverse profile, measured along the axis of the setup for a broad initial energy spectrum. For the Simion simulation in the last column, the particles in the lower energy range $[3.66 - 4]$ MeV are plotted in blue, while above the colorscale is related to the particle density. The scanned images of the RCF films (second column, contrast enhanced and rendered in false colours) and the simulation plots have the same scale, and the real dimensions of the films are specified in the first column.

Longitudinal position and transverse size	Experimental scan of the second RCF EBT3 layer	TraceWin 6.48 MeV monochromatic simulation	Simion polychromatic simulation
225 mm, 29.6x29.6 mm	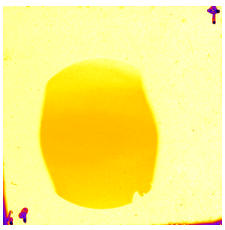	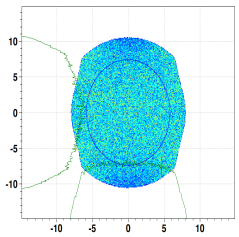	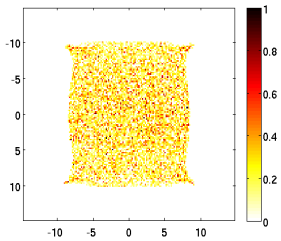
255 mm, 29.6x29.6 mm	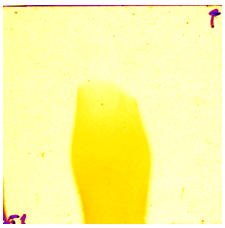	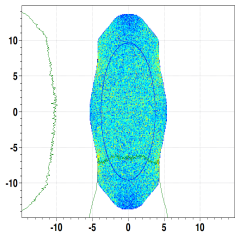	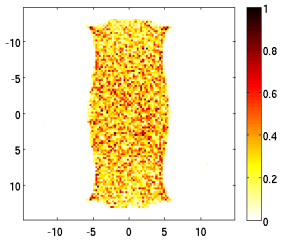
305 mm, 29.6x29.6 mm	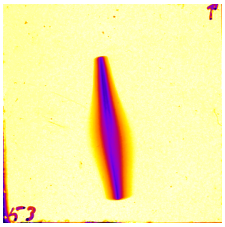	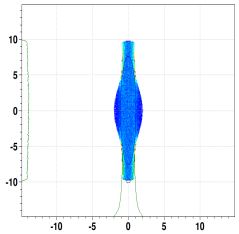	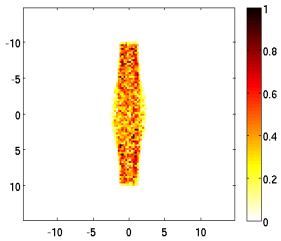
395 mm, 51.6x29.6 mm	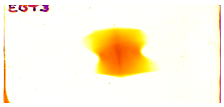	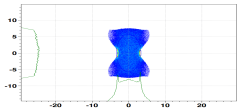	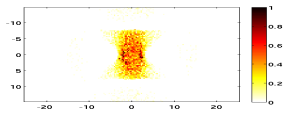
445 mm, 29.6x29.6 mm	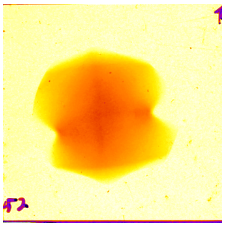	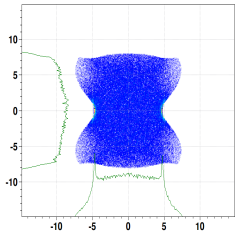	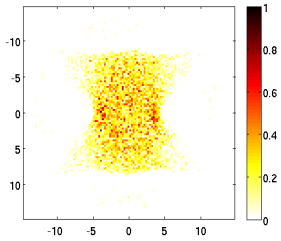
930 mm, 57.8x57.8 mm	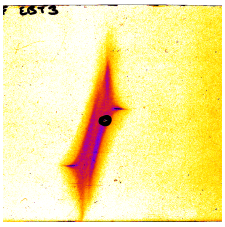	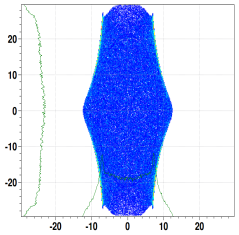	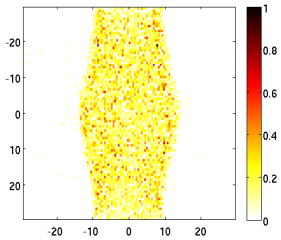

TABLE 4.3: Experimental results compared to simulations (with density colorscales) of the beam transverse profile for the higher range of initial proton energies, reported along the axis of the setup. The contrast was enhanced to the same setting for all RCF layers in this table and the previous one, except for the last position of this table where is was further increased due to the low signal level.

The agreement between experimental results and monochromatic beam simulations run with TraceWin is more evident in the second layer of the stack (see table 4.3) as here the energy range of particles loosing energy in the sensitive layer of the film is narrower than in the case of the first layer. A good correlation can also be inferred on the first layer, if the shape of the signal observed on the second one is neglected. In order to highlight the agreement between experimental data and simulations, in the fourth column of the tables are shown profiles obtained from our realistic TNSA beam simulated in Simion. In the first table, the least energetic particles having energies within $[3.66 - 4]$ MeV are plotted in blue (hence the shape is similar to the TraceWin profile), while above this range protons are represented with a colorscale related to their density. In the second table, the plots have simply a density scale for all particles reaching the active layer of the second film (above the corresponding minimum energy required, and below the proton beam cutoff energy), that is to say in the range 6.48 MeV to 8 MeV.

The experimental traces have an evident rotation, which is probably due to an imperfect alignment of the PMQ system with the input beam, emphasizing the skew quadrupole components already considered in the field maps used for the simulations. The first layer of the stack placed at the output of the system shows a poor beam uniformity, presumably because the skew components act on the beam in an unpredictable way on some of the lower energy components, apparently splitting and concentrating them along four distinct curves. The beam tilt is present on most of the films, but the distortion is even more noticeable when the beam has some sharp features (first layers) or is narrowed in one axis (second layer of the third and last stack).

Output beam spatial properties

The transport system consists in a set of four PMQs with alternating polarity, aligned on the target normal axis (see Fig. 4.14). The first quadrupole (PMQ1) is placed 5 cm behind the target, the shortest possible distance considering the mechanical constraints. Despite the high beam divergence (see Fig. 3.18), this enables to collect all the protons above 4 MeV at the bore entrance of PMQ1, which includes all the particles that have a sufficient energy to reach the output sample. The simulated envelopes, along with the particle losses for a 5 MeV beam, are shown in Figure 4.17.

The aim of this configuration was to limit the losses along the transport, while obtaining a relatively large output beam with a low divergence. The goal was also to filter the beam in energy to get a narrow output energy spectrum. Most of the losses occur in the first PMQ as protons are defocused along the x axis, but the transmission efficiency of 15 % for the selected energy of 5 MeV is remarkable. The usable beam size obtained in the biological sample plane located in air at 56 cm from the last PMQ is 10 mm $\times$ 15 mm (area delimited by the white rectangle in Figure 4.18a), with a 20 % standard deviation in the dose deposition profile measured experimentally from the IP scan. The chromaticity of the transport line induces a tighter focus at the sample position of the energy components around 5 MeV, while the higher energies are spread out over a larger beam size. The intense and central signal with a X shape in the output profile presented in Figure 4.18a, is due to the energy deposition of the transmitted protons in the lower energy range. Such a configuration is preferable to the reverse situation with a stronger focus of the higher energies, because the concentrated dose deposition from low energy particles can easily be suppressed. This was verified experimentally, as demonstrated in Figure 4.18b, using 104 µm of aluminium placed just before the IP. The filter allows only protons with energies higher than 3.5 MeV to pass through, which corresponds to protons with an initial energy above 6 MeV considering the energy loss occurring while they propagate in the various absorbing elements at the end of the beamline. Comparing the isodose lines at half the maximum signal on

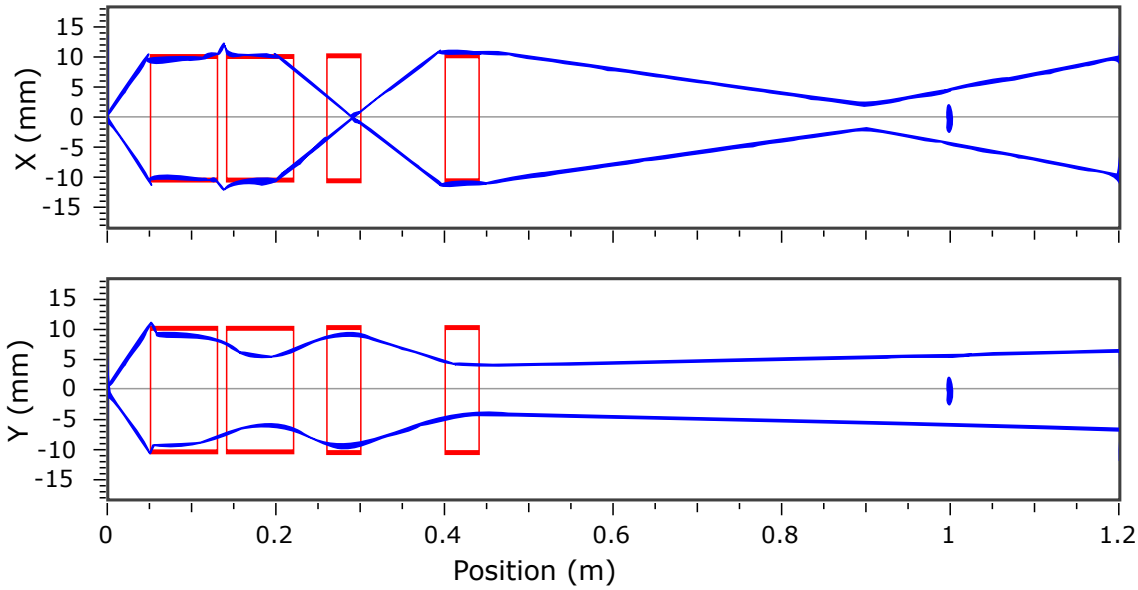

(a) Multiparticle longitudinal envelope calculated in the x and y directions.

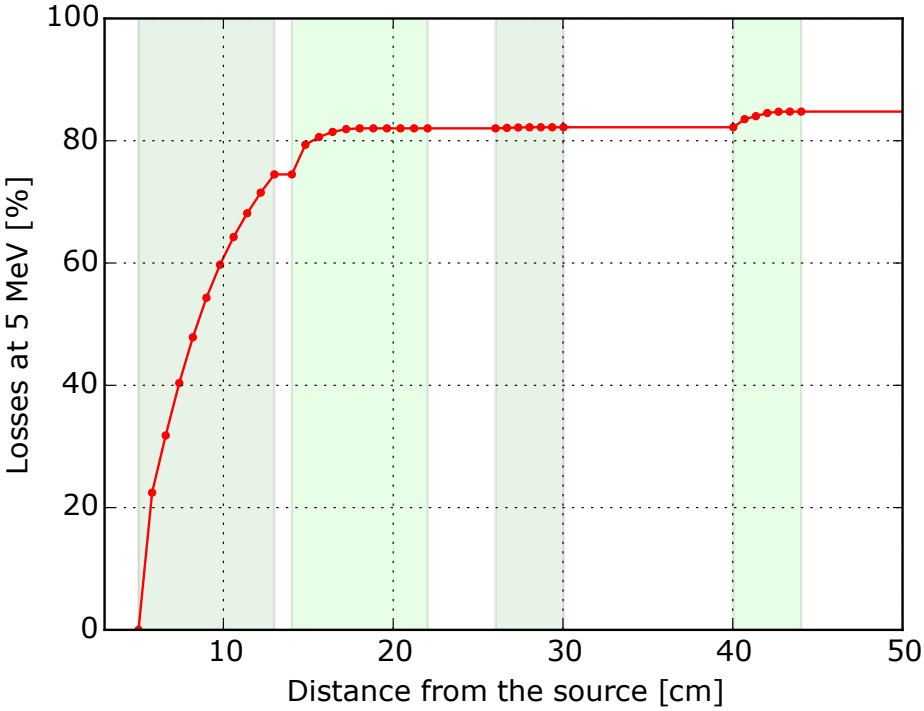

(b) Particle losses along the beam path. The shaded areas represent the PMQs.

FIGURE 4.17: 5 MeV proton beam simulations performed with the TraceWin Multiparticle tool in the described PMQ setup.

each IP (in black), it can clearly be seen that the shape of the energy deposition is different and more homogeneous with the additional filter, but it is inevitably less intense. The encompassed area has an average signal 39 % smaller in (b) compared to (a), with a surface 49 % larger but an integrated signal only 8.9 % smaller and with a significant 25 % reduction in its standard deviation.

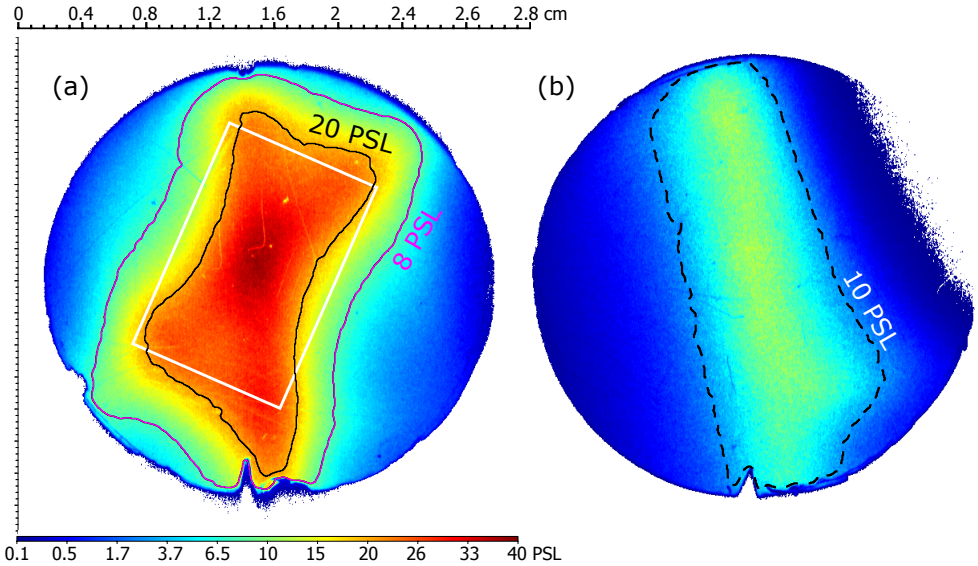

FIGURE 4.18: Transverse profile of the output proton beam energy deposition, recorded on 28 mm diameter Imaging Plates. The IPs were placed in air at the sample location, 1 m away from the target. The original image on the left (a) presents a central X-shape structure, that is not visible on the IP scan on the right (b), for which a 104 µm aluminium filter, blocking protons with energies lower than 3.5 MeV (that is to say protons with an initial energy below 6 MeV), was inserted in front of the IP. The isodose curves at 20 PSL and 8 PSL (i.e. 50 % and 20 % of the maximum recorded signal in (a)) are represented by the black and purple solid lines, while the dashed contour represents the 10 PSL isoline (i.e. 50 % of the maximum in (b)). The white rectangle marks the 1.5 cm^2 area where the biological sample response was studied.

Energy selection and output spectrum

The effect of the PMQ system on the final spectrum, inferred through beam propagation simulations from the measured proton spectrum as input, is shown in Figure 4.19. The simulation codes used proved to be reliable, as it was seen in a previous section that their results were matching well experimental observations. As expected, the transmission efficiency increases sharply at higher energies (Fig. 4.19a). The output proton spectrum is narrower and centered around an initial proton energy of 5 MeV (Fig. 4.19b).

Even though some carbon and oxygen ions are detected by the TPS, no ions other than protons will be found in the beam propagating in air as all heavy ions at the considered sub-MeV energies are stopped in the Mylar window. Concerning protons, they need to have an energy greater than 4.4 MeV to propagate through the entire system without being stopped before depositing energy in the output sample. Relativistic electrons are also generated during the

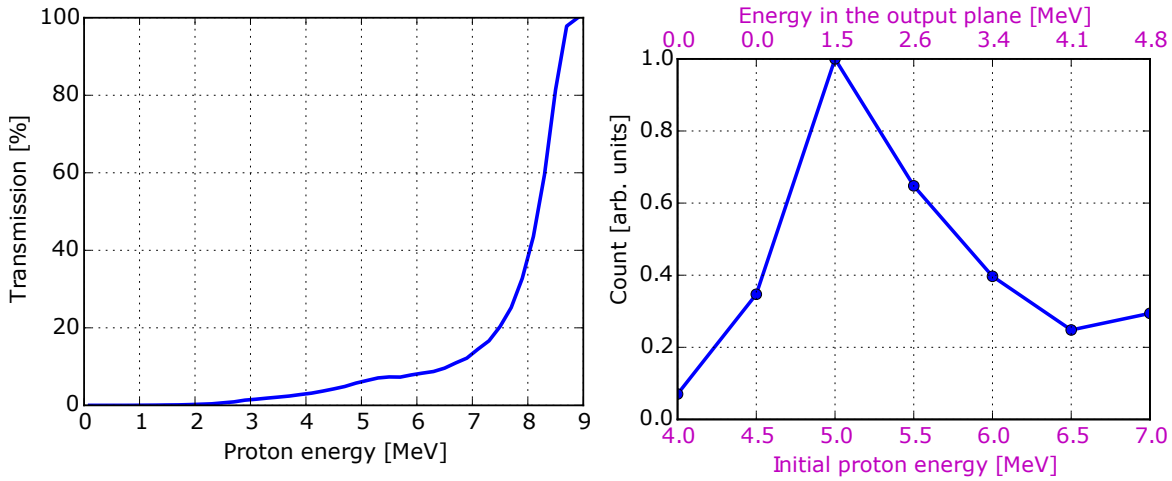

(a) Transmission efficiency of the PMQ system as function of the initial proton energy.

(b) Relative energy spectrum of the proton beam reaching the 1.5 cm^2 output sample area, obtained from multiple monochromatic simulations. The bottom scale shows the initial proton energy, while the top scale shows the energy of these same particles when they reach the sample layer after crossing the absorbing elements present at the end of the beamline.

FIGURE 4.19: Simulated properties of the beam transported by the radiobiology setup.

laser-plasma interaction, but due to the fact that their weight is much smaller than that of protons, they are completely rejected by the magnetic field of the PMQ system. According to simulations, electrons with initial energies lower than 10 MeV are not able to reach the vacuum chamber exit. X-ray signal is emitted from the plasma in 4π sr so some of it reaches the sample, which is in a direct line of sight of the source point. Its intensity was recorded on an IP in a configuration not transmitting particles and the measurement was three orders of magnitude lower than the proton signal obtained in regular conditions.

4.2.4 Pepperpot characterisation

The *pepper-pot* (2D version of the *slits*) method can be used to characterize the emittance of beams of diverse natures. For instance, the transverse emittance of laser wakefield electron bunches was studied after propagation through a triplet of permanent quadrupole magnets, and the pepper-pot tool also enabled to check for misalignments of the magnetic system [Manahan et al., (2014)].

The pepper-pot that we used is made out of a 1 mm thick aluminium plate, in which a grid pattern of holes with 0.5 mm diameter have been drilled with a pitch of 1 mm (see a picture in Figure 4.20). The grid was placed before the first, third and fourth PMQ, as well as after the fourth which is the last one, at respective distances from the target of 45, 255, 390 and 448 mm. As the pepperpot was always located against a PMQ, which has a 2 cm bore diameter, up to 20 beamlets could be created along the horizontal and vertical central line. The transverse profile of the resulting proton beam is measured with a stack of RCF EBT3 films placed 70 cm from the target. Beam envelopes are simulated with TraceWin for the cutoffs corresponding to the

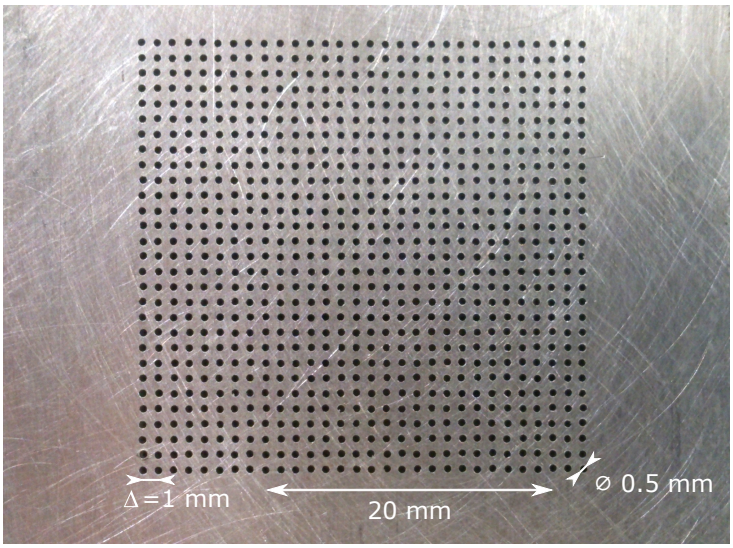

FIGURE 4.20: Picture of the pepperpot used in the characterisation presented here.

minimum energies required for protons to reach the active layer of the first three films making the stack (the ones in which signal was observed), namely 3.2, 6.2 and 8.3 MeV, as sketched in Figure 4.22. Owed to the Bragg peak feature, the signal observed is expected to come mainly from the beam energy component around these energies. The simulated transverse profile of the proton beam (without pepperpot) in the plane where the RCF stack was placed is shown in Figure 4.23.

A clear correlation can be seen between the number of beamlets visible along each axis, and the simulated beam profile. For example, there are 1×11 beamlets (horizontal x vertical) spreading in the vertical direction in the first layer of Figure 4.21a, which is coherent with the envelope of the 3.2 MeV protons represented in blue in Figure 4.22. Indeed, it stays confined in the y direction from the first pepperpot plane to the exit of the PMQ system, from which it diverges leaving a wide vertical imprint of many beamlets on the RCF. However in the x direction, the envelope expands much outside the physical boundaries of the PMQ bores after passing the pepperpot, hence the beam is clipped except for the central beamlets present along the $x = 0$ axis. For the same pepperpot position the closest to the source but looking at the highest energy component 8.3 MeV (red curve in Fig. 4.22) recorded on the third layer of Figure 4.21a, the pattern looks like a magnification $\times 10$ of the original grid with some distortions. Up to 4×6 beamlets are visible in the x and y directions, which is coherent with the simulated envelope that is always maintained tightly around the y axis and diverges slowly after the PMQs, while it spreads to a larger width inside the second PMQ in the x direction before reaching a width similar to the y size in the plane of detection.

The rotation of the entire grid pattern could be due to misalignment of the individual PMQ with respect to each other, whereas a misalignment of the entire assembly with respect to the beam axis would result in deformations along only one axis, according to [Manahan et al., (2014)]. The distortions are more pronounced for the first pepperpot position, which suggest that one or both of the first two PMQs might be skewed. Misalignments of these first two PMQs would also have more effects on the beam since they are twice longer than the last two PMQs for a similar field strength.

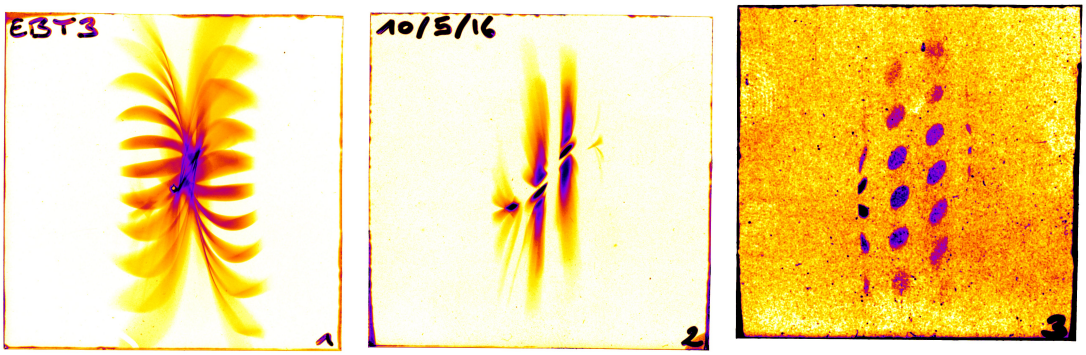

(a) Pepper-pot placed 45 mm behind the ion beam source, in front of the first PMQ.

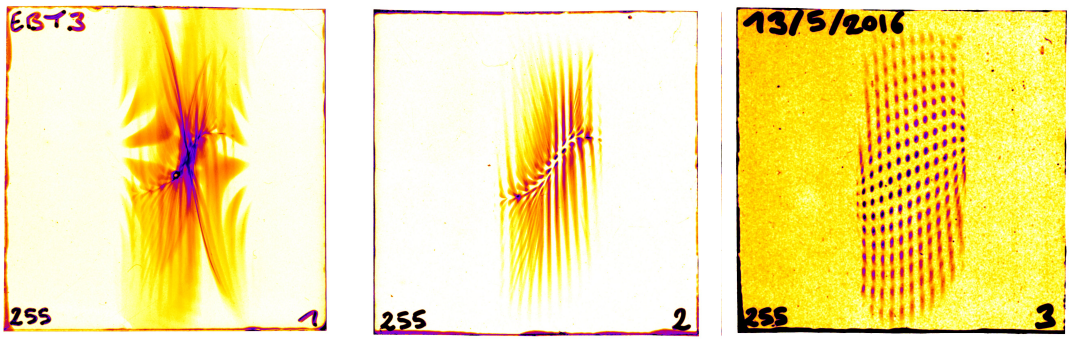

(b) Pepper-pot placed 255 mm from the source, in front of the third PMQ.

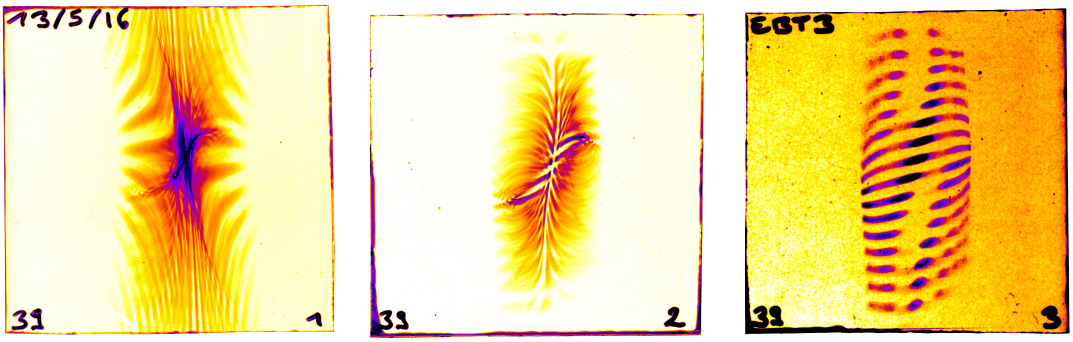

(c) Pepper-pot placed 390 mm from the source, in front of the fourth PMQ.

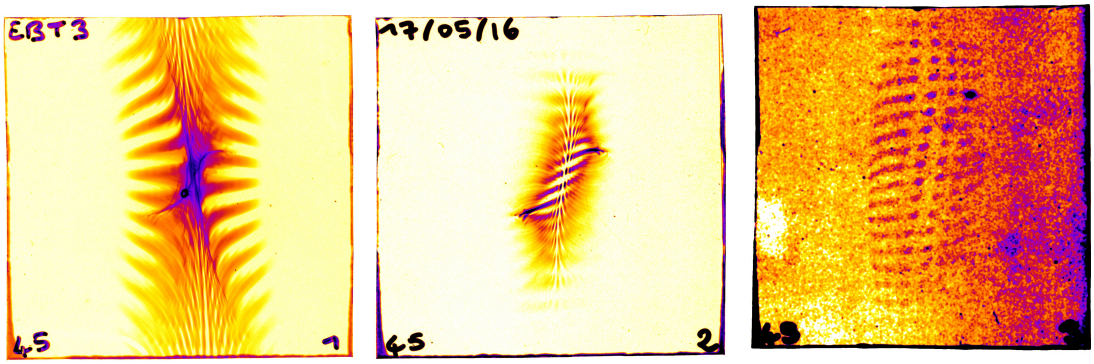

(d) Pepper-pot placed 448 mm from the source, behind the fourth PMQ.

FIGURE 4.21: Pepper-pot beam analysis with 3 layer stacks of 6 cm side square RCF EBT3 placed 70 cm downstream from the source, after the 4 PMQ system. The minimum energy of the protons reaching the active layer of each stack film is respectively 3.2, 6.2 and 8.3 MeV. The ion beam signal of 25 consecutive shots was accumulated on each stack. The contrast of the scanned images was enhanced and rendered in false colors to help visualisation.

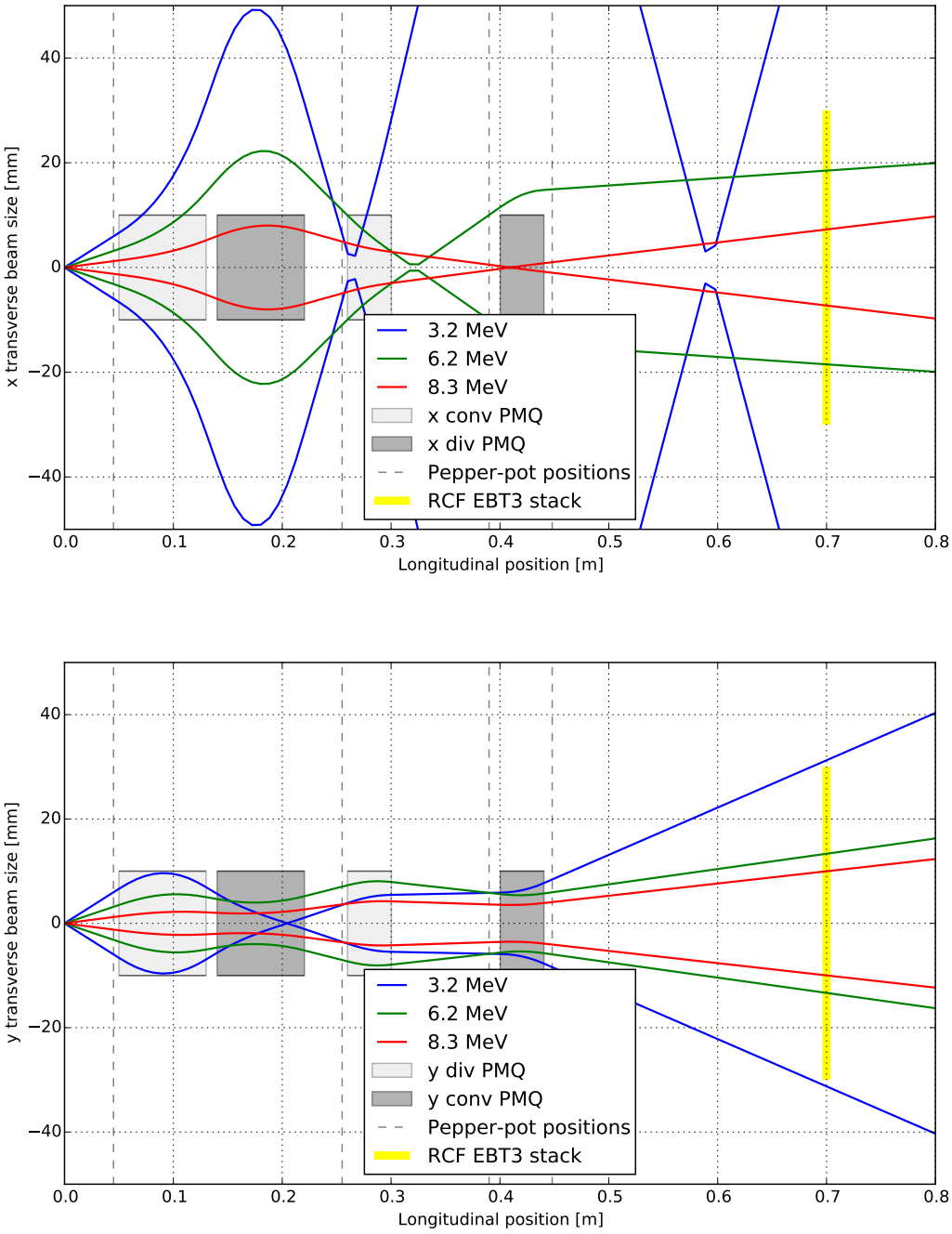

FIGURE 4.22: Multiparticle beam envelope simulations in the two transverse directions for different proton energies with TraceWin. The vertical dash lines mark the various planes where the pepper-pot was placed. The graph shows the full beam envelope as if there was no clipping of the beam due to the finite PMQ bore (in particular the profile of the low energies would be much affected in the x direction otherwise).

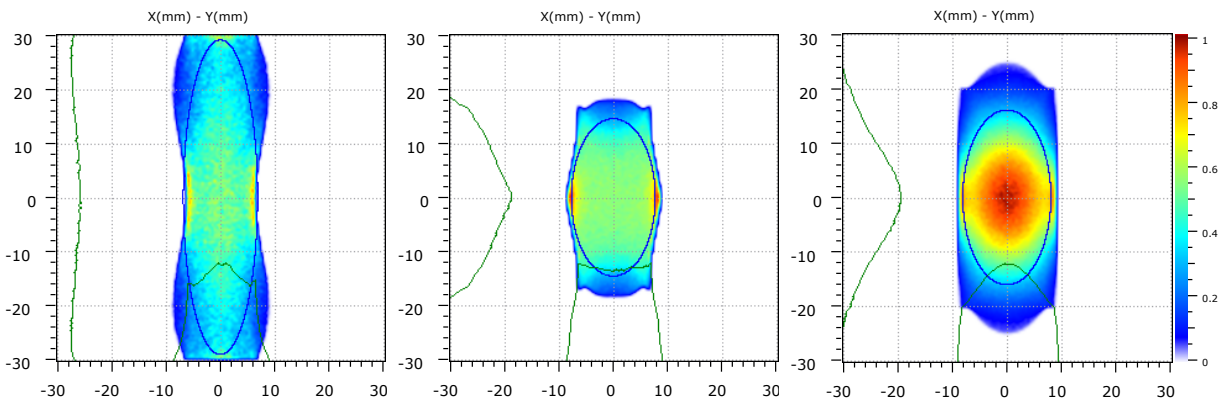

(a) 3.2 MeV (b) 6.2 MeV (c) 8.3 MeV

FIGURE 4.23: Transverse beam profile, in the RCF plane 70 cm behind the source, simulated with TraceWin for different energies corresponding to the proton cutoff on each layer of the RCF stack.

A theoretical formula gives the emittance of a beam as function of the slit positions and beamlet spots parameters on an observation screen [Zhang, (1996)]:

$$\epsilon_x^2 = \langle x^2 \rangle \langle x'^2 \rangle - \langle x x' \rangle^2 \tag{4.13}$$

$$= \frac{1}{N^2} \left\{ \left[\sum_{j=1}^{p} n_j \left(x_{sj} - \bar{x} \right)^2 \right] \left[\sum_{j=1}^{p} \left(n_j \sigma_{x'_j}^2 + n_j \left(\bar{x'_j} - \bar{x'} \right)^2 \right) \right] \left[\sum_{j=1}^{p} n_j x_{sj} \bar{x'_j} - N \bar{x} \bar{x'} \right]^2 \right\} \tag{4.14}$$

where N is the number of particles behind the slit; x_{sj} the position of the jth slit; n_j the number of particles passing through the jth slit and hitting the screen (practically it is a weighting of spot intensity); $\bar{x}$ the mean position of all beamlets; $\bar{x'_j}$ the mean divergence of jth beamlet; $\bar{x'}$ the mean divergence of all beamlets; $\sigma_{x'_j}$ the rms divergence of jth beamlet.

However in our case, the presence of significant distortions and the overlap of several beamlets (for the lower energy component observed in the first layer) prevent from interpreting well the data and retrieve emittance values from the images. The measurement of the beam divergence after the PMQ system from Figure 4.21d would be easier for the higher energy component, given the relatively simple pattern of the 8.3 MeV protons, but the signal is too low to be able to analyse accurately the spots size and their surrounding shadow area.

4.3 Conclusion

In conclusion, I presented in this chapter a detailed study of proton beam propagation through permanent magnetic quadrupoles (first order focusing), after a brief description of a previous attempt involving a chicane (zero order). I demonstrated experimentally the possibility to focus an energy component, opening the prospect of energy filtering and obtaining quasi-monochromatic output from a laser-driven proton beams. I also described how to efficiently transport a limited range of the energy spectrum over a 1 m length, to provide an output beam with a relatively wide and uniform transverse profile, suitable to perform cell irradiation experiments. Finally, a pepperpot characterisation experiment enabled to diagnose misalignment in the elements of the transport system and to calculate beam emittance values in theory.

The combined use of both devices could open prospects for future experiments. The PMQs would serve as a focusing system, providing a narrow collimated beam to the following chicane, which would operate a fine energy selection. A pulsed solenoid could also be placed first, between the source and the PMQs, to better collect the emitted particles, as described in [Maggiore et al., (2013); Schillaci et al., (2015a)]. Nonetheless, such a beamline would probably be longer that the radius of the current experimental chamber in SAPHIR (76 cm), requiring the addition of an extension pipe or a careful design to make the whole system compact enough. Besides, improved laser parameters and interaction conditions enable to consider other PMQ configurations taking advantage of the increased fluence and higher proton energies available. In perspective, one could also consider using higher order poles such as octupoles (third order focusing) to achieve a better beam profile uniformity [Meads, (1983); Tsoupas et al., (1991)].

Chapter 5

Dosimetry

This chapter is dedicated to the dosimetry measurements performed on the laser accelerator beam, and to the protocol thus defined to monitor the dose delivered to the biological samples, during radiobiology assays. After a brief presentation of the detector used, the experiment performed to calibrate it is described. Then, the simulation studies pursed to deduce the absolute dose deposition in the cell samples are explained. Finally, the selected irradiation conditions for systematic studies are detailed.

Contents

5.1 Dose integrating devices **110**

Ionization chambers 110

5.2 TIC calibration experiment at CPO in Orsay **111**

5.3 Simulations for absolute dose retrieval **114**

5.4 Irradiation conditions **116**

5.5 Conclusion **118**

5.1 Dose integrating devices

The use of accelerated proton beams for practical applications requires a precise measurement of the deposited doses. Several parameters can fluctuate from shot-to-shot and influence the energy deposition at the irradiated target. In order to monitor the proton source for variations, due for instance to the laser parameters as well as target positioning and surface inhomogeneities, a transmission monitor chamber is used, allowing precise normalisation of the final dose. A PTW transmission monitor ionization chamber model 786[1] is associated with a PTW electrometer UNIDOS® E Universal Dosemeter to read the measurements.

The advantages of such a thin flat *transmission ionization chamber* (TIC) is that it can provide an online monitoring of the beam passing through it, on its way to the region of practical use. The TIC can be permanently installed while the output beam can still be used for the desired application. It can monitor either a specific segment of a large beam, or as in our setup, the whole beam. This was easily ensured, as the 155 mm diameter sensitive area of the TIC is larger than the 30 mm diameter window through which the beam exits the vacuum chamber, and on which the TIC is centred.

Ionization chambers

As the earliest constructed and the simplest of all gas-filled radiation detectors, **ionization chambers** (ICs) are widely used for the detection and measurement of ionizing radiation. An IC consists of an air-filled chamber at atmospheric pressure containing two electrodes to which a voltage is applied. They collect the charges created when air molecules, exposed to radiations, are directly ionized. ICs operate at a low electric field strength, so that no gas multiplication takes place and only the discrete ion pairs created by each interaction between the incident radiation and the gas are measured (gas multiplication factor $a = 1$, see Figure 5.1). The electric field must be above a certain threshold to ensure that the generated ions have a sufficient drift velocity to prevent elimination of some ion pairs by recombination. Other radiation instruments, such as the proportional counter ($a > 1$) or the Geiger-Müller counter ($a \gg 1$), involve *gas multiplication* via secondary ionizations.

On the one hand, the advantages of ICs are their ease of use and their capability to give instant readings with good accuracy. The total charge is independent of the applied voltage over a wide range, and it is proportional to the energy deposited by the incident radiation in the air volume. They can measure very high radiation rates, and sustained high radiation levels without degradation of the fill gas. On the other hand, ICs have some limitations. They have a low sensitivity, as the current measured is extremely low and detecting individual particles is difficult, especially with ordinary air at atmospheric pressure. Their response may change with atmospheric conditions, such as temperature and pressure, but the effect will only matter for high resolution systems. The low electronic output requires expensive and sophisticated electrometer circuits. They operate as a dose integrator not providing any spatial information. More details about ICs principle of operation and type of designs can be found in [Ahmed, (2014)].

[1] vented sensitive volumes of 94 cm^3, designed as twin-chambers with 2.5 mm measuring depth each and a diameter of 155 mm ; the chamber walls and the electrodes are made of polyimide of 25 µm thickness each with graphite layer ; more details at: http://www.ptw.de/fileadmin/data/download/catalogviewer/DETECTORS_Cat_en_16522900_09/blaetterkatalog/index.html?startpage=54

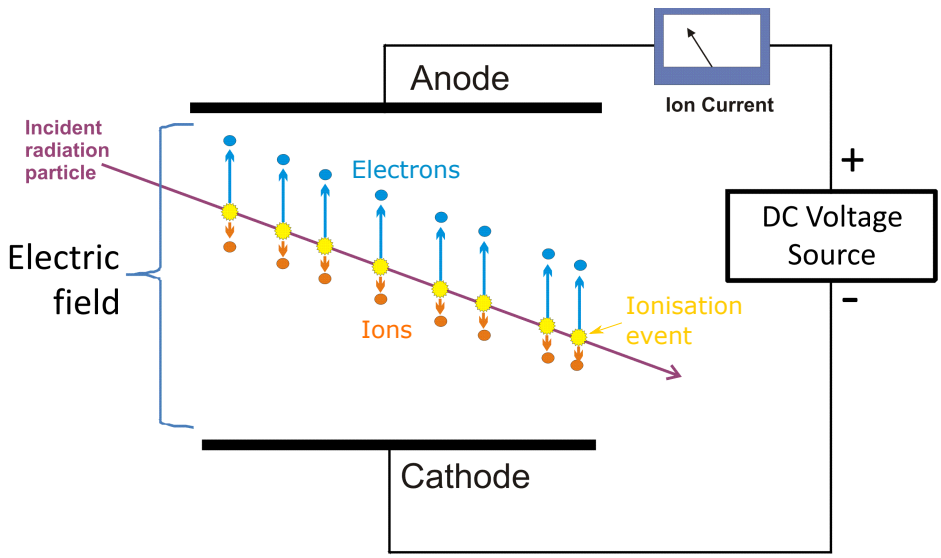

FIGURE 5.1: Schematic operation principle of an ionization chamber. An incident radiation particle leaves a trail of ion pairs in its path as it collides with atoms of the gas through which it is travelling. Each ion pair consists of a free electron, which is attracted to the anode, and a positive ion, which is attracted to the cathode by the influence of the electric field. This ion drift ensures that electrons and positive ions do not recombine, so that the ionisation current generated is proportional to the number of pairs created.

Special care will be taken in this chapter to note the various quantities and units described. For instance, the charge collected by the TIC should not be confused with the charge of the ion beam, so annotations will be added to ease the understanding.

5.2 TIC calibration experiment at CPO in Orsay

In order to relate the recorded values of charge in our ionization chamber with the actual dose deposition inside it, a calibration campaign has been performed at the Institut Curie's Proton Therapy Center in Orsay, France. The source is an IBA C230 isochronous cyclotron, which generates a continuous proton beam with an initial energy of 235 MeV. The beam energy is lowered to 201 MeV right at the cyclotron output and further reduced down to 76 MeV as per treatment protocol of eye tumours. This second attenuation is achieved with 175 mm of polycarbonate (Lexan) and 1 mm of lead placed about 1 m after the beam exits the transport line under vacuum, and 5 m before the irradiation spot.

At the end of the transport, the beam is routinely characterised by energy deposition in a water tank, as a function of the depth, but the proton energy is never measured directly along the beamline of the protontherapy facility. The calibrated beam charge reference is set on the dose in the distal 80 % of the energy deposition curve, i.e. on the far decreasing slope of the Bragg peak. During normal operation, the dose to be delivered by the beamline is quantified in *monitor units* (MU). It is calibrated so as to obtain the conversion factor from the MU unit, measure of the output from the clinical accelerator, to the actual dose deposition in Gray received at the irradiation position at the end of the line. The measure is obtained with a compact thimble air ionization chamber CC13 (IBA) having an air active volume of 0.13 cm^3. It is located in the middle of the spread-out Bragg peak of the 76 MeV beam at a depth of 31.6 mm in the water

tank, as sketched in Figure 5.2 (the projected range of a 76 MeV proton in water is 47 mm).

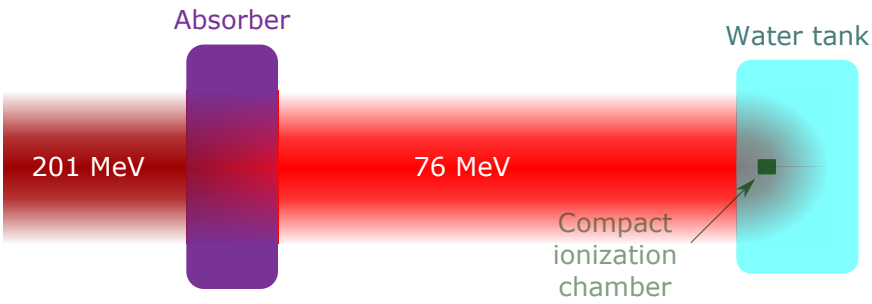

FIGURE 5.2: CPO beamline calibration setup.

The current measured by the CC13 during the experiment was 80 pA, corresponding to a dose rate in air of $3\,\mathrm{Gy}\cdot\mathrm{min}^{-1}$. This dose calibration leads to the relationship $1.2\,\mathrm{MU} = 1.12\,\mathrm{cGy}_{\mathrm{CC13}}$, hence the conversion ratio :

$$\eta_C = \frac{Dose_{CC13}}{Dose_{MU}} = \frac{1.12\,\mathrm{cGy}_{\mathrm{CC13}}}{1.2\,\mathrm{MU}} = 0.93 \pm 0.02\ \mathrm{cGy}_{\mathrm{CC13}}/\mathrm{MU}, \tag{5.1}$$

where subscripts have been added to some units to remind to which element they are associated to.

Our equipment was then calibrated to obtain the conversion factor from MUs to the charge collected in the TIC. To get closer to the operating conditions in SAPHIR and its range of proton energies generated, this was performed with an additional attenuation to 20 MeV, using 36.1 mm of Poly(methyl methacrylate) (PPMA or Plexiglas) attenuator placed in front of the TIC. The beam was also shaped with a collimator to a square aperture of side 2 cm (see a drawing of the setup in Figure 5.3 and the energy deposition transverse profile of the CPO beam in Figure 5.6). The readings on the electrometer of the charge collected inside the TIC were recorded for a range

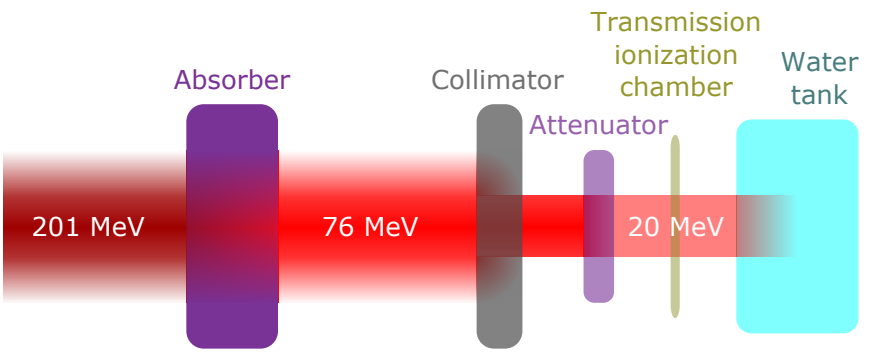

FIGURE 5.3: Schematic of the TIC calibration setup.

of MU values shown in Figure 5.4. According to a linear fit, $10\,\mathrm{nC}_{\mathrm{TIC}} = 17.4\,\mathrm{MU}$, and the slope is:

$$\eta_{TM} = \frac{Q_{TIC}}{Dose_{MU}} = \frac{10\,\mathrm{nC}_{\mathrm{TIC}}}{17.4\,\mathrm{MU}} = 0.57 \pm 0.01\ \mathrm{nC}_{\mathrm{TIC}}/\mathrm{MU}. \tag{5.2}$$

Combining the results of both measurements, the dose deposition at a 30 mm depth in water in the homogeneous section of the beam for the first setup (Fig. 5.2) is related to the charge

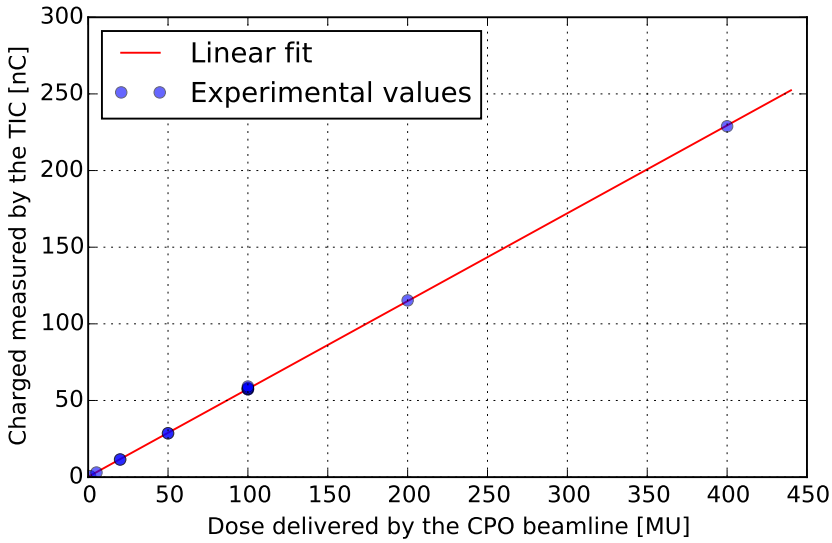

FIGURE 5.4: Schematic of the TIC calibration setup.

measured in the TIC for the second setup (Fig. 5.3). The linear relationship is:

$$\eta_{indirect} = \frac{Dose_{CC13}}{Q_{TIC}} = 1.6 \pm 0.1 \text{ cGy}_{\text{CC13}}/\text{nC}_{\text{TIC}}. \tag{5.3}$$

The water thickness equivalent to the TIC in terms of energy absorption was evaluated repeating a dose deposition measurement, with and without the TIC inserted in front of the water tank, for a beam energy reduced to 76 MeV. The energy deposition of the protons passing through the TIC was deduced to be equivalent to the propagation in 0.10 mm to 0.12 mm of water from the shift in the measured curves (see Figure 5.5). Geant4 simulations confirmed a 105 µm TIC equivalent water thickness.

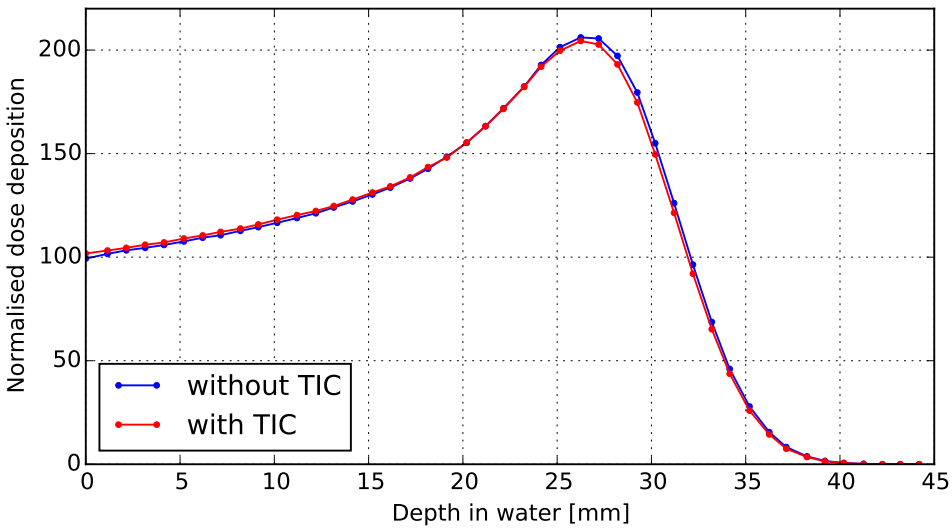

FIGURE 5.5: Dose deposition in water of the 76 MeV ICPO proton beam. The TIC projected density is equivalent to 0.11 ± 0.01 mm of water, from the shift measured in the energy deposition curves.

5.3 Simulations for absolute dose retrieval

So as to retrieve the dose deposition at the lower energies provided by the laser-plasma accelerator in the samples irradiated during radiobiological experiments, Monte Carlo simulations have been run with the *Geant4* toolkit [Agostinelli et al., (2003)] developed by CERN for the simulations of the passage of particles through matter. All three setups considered for the calibration were simulated, and the energy deposition per proton in each element was recorded.

In a first step, both CPO calibration setups were combined to get the absolute dose calibration of the TIC. The first and second setups, associated to Figures 5.2 and 5.3, were used to get the energy deposited inside the 5.2 mm and 5 mm air thickness of respectively the CC13 and TIC sensitive volume. The initial energy was set to the original 201 MeV from the cyclotron and the thick filters were taken into account. The average simulated energy deposited per primary proton in the CC13 and TIC volumes are respectively 8.5 keV/proton and 18.7 keV/proton. The corresponding doses, via normalisation to the contained volume of air at atmospheric pressure with a density of $1.2\,\mathrm{kg}\cdot\mathrm{m}^{-3}$, are respectively $Dose^{Simu}_{CC13} = 8.7\,\mathrm{nGy/proton}$ and $Dose^{Simu}_{TIC} = 1.2\,\mathrm{nGy/proton}$, giving a ratio of:

$$R^{CPO}_{dose} = \frac{Dose^{Simu}_{TIC}}{Dose^{Simu}_{CC13}} = 0.14 \tag{5.4}$$

The proton beam fluence was well uniform in the area imposed by the 2 cm side square collimator aperture, as indicated by the scan of the RCF EBT2 stack placed behind it and displayed in Figure 5.6. Indeed, the FWHM of the dose deposition signal is 24.7 mm and the signal has a 20 mm width at 70 % of the maximum intensity. The ratio of total deposited dose

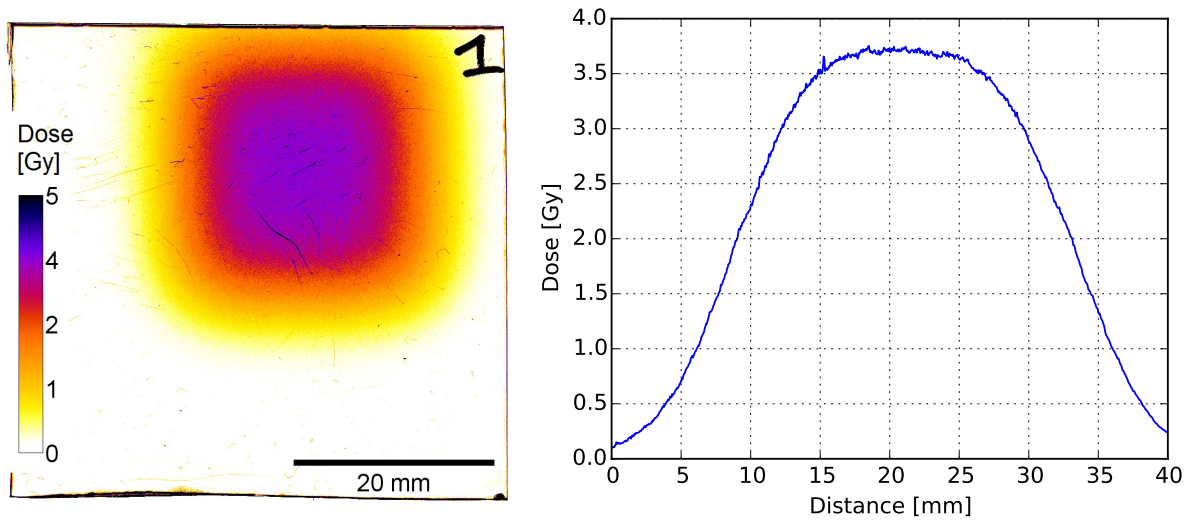

FIGURE 5.6: Transverse dose deposition profile of the CPO proton beam recorded on a RCF EBT2 placed behind the collimator. A dose of 300 MU was delivered by the beamline in approximately 56 s. The graph on the right shows an averaged horizontal lineout of the dose map.

in the ionization chambers should take in account the geometrical factor of irradiated areas. In fact while the CC13, surface $5 \times 5\,\mathrm{mm}^2$, was fully illuminated, the beam cross section is considerably smaller than the TIC active surface, which limits the irradiation to $2 \times 2\,\mathrm{cm}^2$ of its

useful diameter, as set by the square beam collimator. The illuminated section ratio is:

$$R_{surf} = \frac{S_{TIC}}{S_{CC13}} = \frac{4}{0.25} = 16, \tag{5.5}$$

which gives for the comparison of the two setups with the same initial beam, the dose ratio:

$$\eta_{dose} = R_{surf} \times R_{dose}^{CPO} = 2.3. \tag{5.6}$$

Finally, combining the TIC indirect calibration in Equation (5.3) with the above dose ratio, the *intrinsic TIC calibration* represented by the factor correlating the charged measured in the TIC with the dose deposition inside its active air volume is obtained:

$$\eta_{TIC} = \frac{Dose_{TIC}}{Q_{TIC}} = \eta_{dose} \times \eta_{indirect} = 3.7\,\mathrm{cGy_{TIC}/nC_{TIC}}. \tag{5.7}$$

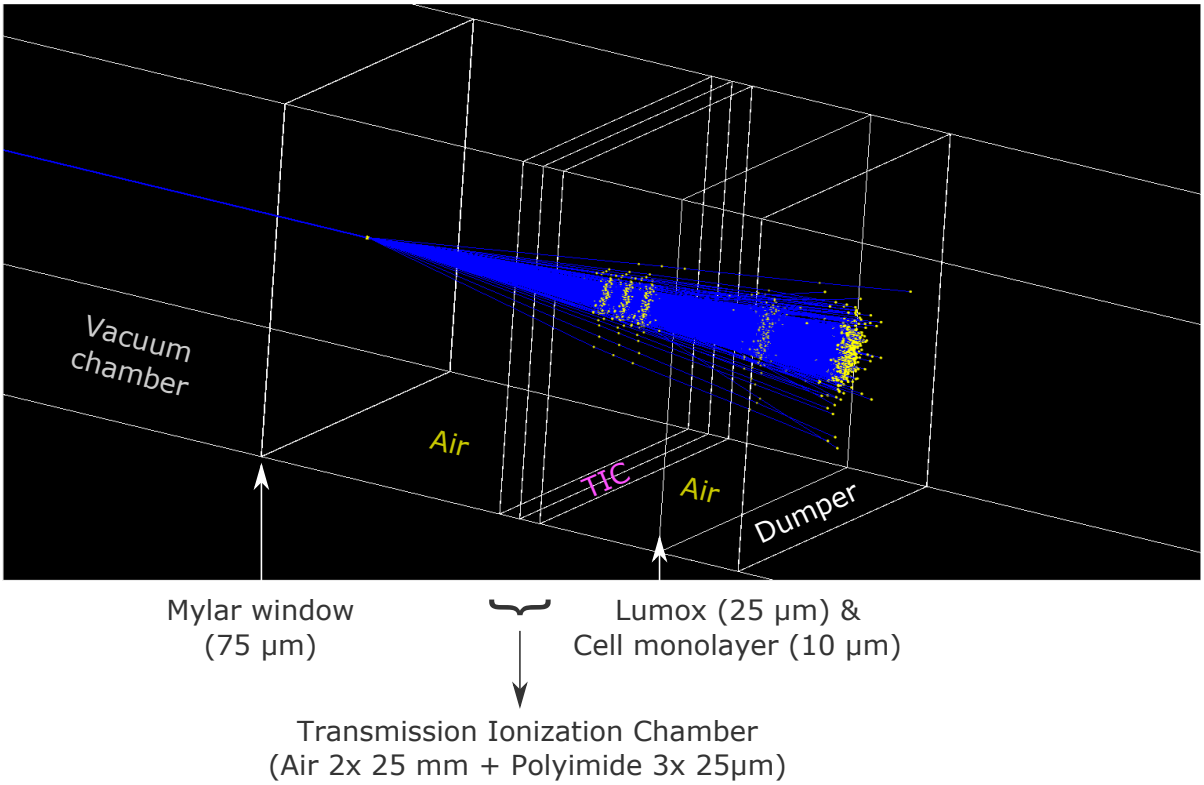

FIGURE 5.7: Visualisation of the propagation of a 5 MeV proton beam simulated in Geant4. The blue lines represent the proton trajectories and the yellow points are the actual step points.

In a second step, the absorbing elements of the SAPHIR beamline (Fig. 4.14) were implemented to simulate the relative energy deposition in the TIC and the cell monolayer sample, as illustrated in Figure 5.7. A realistic spatially dependent spectrum was computed coupling these *Geant4* energy deposition simulations with the energy-dependent spatial distribution obtained by propagating our proton source beam through the system with *TraceWin*. The 1.5 cm^2 sample area was divided into a 3x3 grid, and the average spectrum in each of the 9 sections was calculated. The average spectrum over the full sample surface, delimited by the white rectangle in Fig. 4.18, is shown in Figure 4.19b. The The average energy deposition ratio between the sample area and the TIC is $E_{Cell/TIC} = 1.02$. Applying a $W_{TIC/Cell} = 3.03$ normalization factor

accounting for the weight ratio of the TIC irradiated air volume at atmospheric pressure, and the cell sample regarded as water (dose is inversely proportional to mass), leads to an average dose ratio of:

$$R_{dose}^{Saphir} = \frac{Dose_{Cell}^{Simu}}{Dose_{TIC}^{Simu}} = W_{TIC/Cell} \times E_{Cell/TIC} = 3.1. \tag{5.8}$$

The final calibration, relating the average dose deposition in the biological sample with the charge measured in the TIC, is deduced combining equations (5.7) and (5.8):

$$\eta_{Cell} = \frac{Dose_{Cell}}{Q_{TIC}} = R_{dose}^{Saphir} \times \eta_{TIC} = 11.5 \pm 5.9\ \mathrm{cGy_{Cell}/nC_{TIC}}. \tag{5.9}$$

The figures given previously are averaged on the 9 individual calibration values obtained from the spatially-resolved simulations performed for each grid area of the sample. The indicated 51 % error is associated to the spatial variations observed over the 9 sample sections. However, it is overestimated due to the spatial beam features that are blurred after the beam propagates through the absorbing elements at the end of the beamline, but that are not included in TraceWin which is simulating beam propagation only in vacuum. Indeed, the standard deviation calculated from the signal recorded on the IP (in the white rectangle corresponding to the sample area illustrated in Fig. 4.18) is only 22 %. This latter value is retained as the calibration error, and notice that it is comparable to previous experiments reported in the literature. The absolute dosimetry error in Bin et al., [2012] was ±20 % and the regions of interest had a size of only $142 \times 106\,\mu m^2 = 1.5 \times 10^{-4}\,cm^2$. Yogo et al., [2011b] and Doria et al., [2012] had dose errors of about ±8 % and ±10 % respectively, but their sample areas were restricted to 5 mm and 2.5 mm diameter discs, corresponding to surfaces of respectively $0.79\,cm^2$ and $0.2\,cm^2$. The dose error in Zeil et al., [2012] was also ±10 % and the sample size $2 \times 6\,mm^2 = 0.12\,cm^2$.

5.4 Irradiation conditions

In this section, simple approximate calculations are done to estimate the number of output protons, assuming that all of them have the same initial energy of 5 MeV which corresponds to the peak in the output spectrum. Such a 5 MeV proton crosses the transmission ionization chamber at 4 MeV because of energy lost in the 75 µm thick Mylar separation film and during drift of a few centimeters in air, as illustrated in the graph in Figure 5.8. The total energy deposition of this proton, while passing through the 5 mm of air of the TIC twin-chambers with 2.5 mm measuring depth each, is $E_{TIC}^{air} = 60\,keV$. The dose deposition calculated in the $m_{iT} = 2.4\,mg$ TIC volume (with the $2 \times 2\,cm^2$ cross section considered in the calibration) yields:

$$D_{TIC}^{1H^+} = E_{TIC}^{air}/m_{iT} = 4.0\,nGy. \tag{5.10}$$

The charge measured experimentally was of the order of $Q_{TIC}^{exp} = 10\,nC$ per laser shot, with a standard deviation of $\sigma = 15\,\%$ for a typical day with over a hundred shots, so according to the calibration (5.7) for our output proton beam passing through the TIC, it corresponds to a dose deposition in it of:

$$D_{TIC}^{exp} = Q_{TIC}^{exp} \times \eta_{TIC} = 37 \pm 5.6\,cGy. \tag{5.11}$$

Hence, according to the calibration in (5.9), the average dose per shot received by the analysed biological sample area (with the experimentally measured error) is:

$$D_{Cell}^{exp} = \eta_{Cell} \times Q_{TIC}^{exp} = 1.15 \pm 0.25\,Gy/shot, \tag{5.12}$$

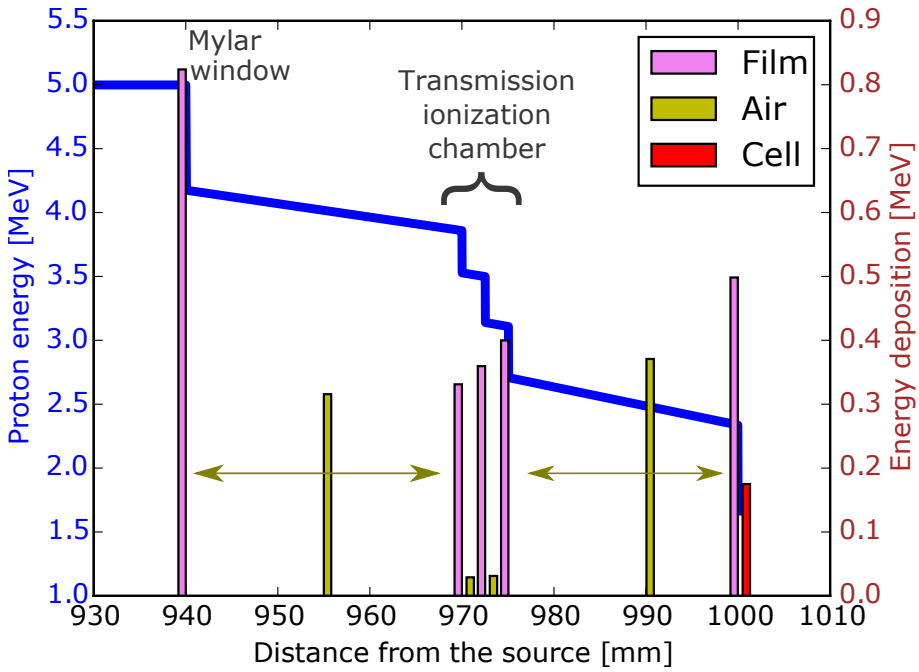

FIGURE 5.8: Graph depicting the energy decrease (blue curve, vertical scale on the left) of an instance proton with a 5 MeV initial energy, as it propagates along the beamline. The energy deposited in the various absorbing elements encountered on its path is represented by the bar plot (vertical scale on the right). Each bar is centered in its energy deposition longitudinal range to preserve proportionality between the energy deposition value and the area of the corresponding bar.

and the number of protons can be estimated to:

$$N_{H^+}^{Cell} = \frac{D_{TIC}^{exp}}{D_{TIC}^{1H^+}} = \frac{0.37}{4.0 \times 10^{-9}} = (9.3 \pm 3.3) \times 10^7 \text{ protons per shot,} \tag{5.13}$$

with a 35 % error taking into account the experimental fluctuations and the error due to the monochromatic approximation. The average energy of the protons reaching the sample area is 2.8 MeV and their average LET is 137 MeV $\cdot$ cm^{-1} (or 14 keV $\cdot$ µm^{-1}).

The energy deposition profile of the output proton beam, at the biological sample position 1 m from the source where its energy spectrum peaks at 1.5 MeV[2], was recorded on an Image Plate. Assuming linearity of the IP dose response as claimed in [Bonnet et al., (2013)], the energy deposition ending up in the $A_S = 1.5\,\text{cm}^2$ central most intense portion of the beam, where the biological sample response was studied and which is delimited by the white rectangle on top of the IP scan in Figure 4.18, represents $r_S = 50\,\%$ of the total. This leads to a doubled number of protons per shot actually received by the full IP surface, that is to say :

$$N_{H^+}^{IP} = N_{H^+}^{Cell}/r_S = (1.8 \pm 0.6) \times 10^8 \textit{ output protons per shot}. \tag{5.14}$$

The mean energy required to produce an ion pair in air being $E_{ioniz}^{air} = 34\,\text{J} \cdot \text{C}^{-1}$ [Paganetti, (2011)], each of these 1.5 MeV protons will generate a charge, that is collected by the ionization chamber, of about:

$$Q_{TIC}^{1H^+} = \frac{E_{TIC}^{air}}{E_{ioniz}^{air}} = 2.0 \times 10^{-16}\,\text{C}/H^+. \tag{5.15}$$

[2]corresponding to a linear energy transfer in water of 200 MeV $\cdot$ cm^{-1}

The ballpark number of protons deduced that way is coherent, within the same order of magnitude as the first estimation:

$$N_{H^+}^{TIC} = \frac{Q_{TIC}^{exp}}{Q_{TIC}^{1H^+}} = 5 \times 10^7\, H^+/\text{shot}. \tag{5.16}$$

The area above 20 % of the maximum PSL signal (reaching 40 for the considered scan), and concentrating $r_{20} = 88\,\%$ of the integrated signal on the entire IP, has an area of $A_{20} = 3.4\,\text{cm}^2$. It is delimited by the solid purple contour line in Figure 4.18a. These values are also used to evaluate the total number of protons getting to the sample and the considered area, leading to *fluences* of:

$$\begin{aligned} F_{Cell} &= \frac{N_{H^+}^{Cell}}{A_{Cell}} = 6.2 \times 10^7\,\text{protons/cm}^2, \\ F_{20} &= \frac{r_{20} \times N_{H^+}^{IP}}{A_{20}} = 4.8 \times 10^7\,\text{protons/cm}^2. \end{aligned} \tag{5.17}$$

The accelerated proton bunch has an emission duration at the source in the order of a few picoseconds [Dromey et al., (2016)]. After propagation over the one meter path length to reach the sample, the transmitted protons of the beam in the 4.5 MeV to 6.5 MeV energy range are spread out in space due to their speed differential, and irradiate the sample for a duration of $\Delta t = 5.7\,\text{ns}$. Hence, the *peak dose rate* inflicted to the biological samples is estimated to be:

$$\phi_S = \frac{D_{Cell}^{exp}}{\Delta t} = 2.0 \times 10^8\,\text{Gy/s}, \tag{5.18}$$

which is many orders of magnitude higher than what is provided by conventional accelerator. Typical dose rates used nowadays in protontherapy are around 3 Gy/min or 5×10^{-2} Gy/s.

5.5 Conclusion

A rigorous method was established to monitor the output dose. An ionization chamber was calibrated to be used as an online diagnostic. Combined with the results of probabilistic simulations, it enables to retrieve the absolute dose received by the cell samples. An article related to this activity has been accepted for publication in the PRAB journal [Pommarel et al., (2017)].

Several factors could alter the calibration of the transmission ionisation chamber but were not considered here. For instance humidity, temperature and atmospheric pressure would influence the charge collected by the TIC, hence changing the calibration to some extent [Mijnheer, (1985); Vynckier et al., (1991); Medin et al., (1995)]. The largest variations might be due to the electronic response of the electrometer, which could not easily be simulated. Hence, a thorough calibration experiment in different conditions would be helpful to examine the effect of the mentioned parameters, in order to give more accurate dose estimations.

Chapter 6

Radiobiology Experiments on SAPHIR

Laser-driven proton beams have found interest with potential applications in medicine, and preliminary studies are presented in this last chapter. The biological protocol to which the cell samples were subjected is described first. The results of the radiobiological experiments pursued in SAPHIR are then discussed and balanced against results obtained using conventional radiation sources. In the end, some prospects for further screening the radiobiological effects of laser-accelerated protons are addressed.

Contents

6.1 Cell handling : material and methods 120
- 6.1.1 Cell lineage culture 120
- 6.1.2 Cell irradiation 120
- 6.1.3 Cell survival assay 120
- 6.1.4 DNA damage foci immunofluorescent staining 122
- Automated counting of DNA damage foci 122

6.2 Experimental results 123
- 6.2.1 Foci analysis 124
- 6.2.2 Survival assay 124
- 6.2.3 Exploratory work and outlook 128
- Cadence effect 128
- Irradiation of spheroid cell samples 130

6.3 Conclusion 132

6.1 Cell handling : material and methods

6.1.1 Cell lineage culture

Two phenotypes of the **colorectal cancer cell line HCT116** were cultured, the *wild type* (WT) and the mutated for the tumour suppressor gene *p53* ($p53^{-/-}$) that is known to be more radioresistant. They were grown as monolayers in plastic tissue culture disposable flasks (TPP) in McCoy's 5A (Modified) Medium with GlutaMAXTM (ThermoFisher Scientific), supplemented with 10 % fetal calf serum (PAA) and 1 % penicillin and streptomycin (ThermoFisher Scientific).

Human glioblastoma cell lines SF763 and U87MG were from the tissue bank of the Brain Tumor Research Center (University of California–San Francisco, San Francisco, CA). Cells were grown as monolayer in Dulbecco's modified Eagle's minimum medium with glutamax (Life technologies), added with 10 % foetal calf serum (PAA) and 1 % penicillin and streptomycin (Life technologies). These brain tumor cells are recognised as even more radioresistant than the HCT116-p53.

To produce **spheroids**, U87 cells were grown in suspension (5×10^4 cells/mL as starting concentration in 100 mL) in spinner (Techne) for 6 days. Spheroids were harvested by centrifugation (500 rpm, 1 min).

All cell lineages were grown at 37 °C in a humidified atmosphere of 5 % CO_2 in air.

6.1.2 Cell irradiation

The cell containers used for irradiation were lumox® dish 35 (Sarstedt) exhibiting a 25 µm thick gas-permeable lumox® film base. Cells were grown overnight. Culture dish was positioned vertically behind the exit window, outside of the vacuum chamber and just after the ionization chamber (see Figure 6.1). Appropriate control samples were treated under the same conditions including bringing the cell culture dish in a vertical position as for irradiation.

The dishes were hold in place thanks to a homemade mount fixed on a magnetic base (see Fig. 4.15b). It enabled a quick replacement of the dish while ensuring each time a precise and exactly reproducible sample positioning.

For the latest experiments with variable paces, to remove any effect of temperature change or tissue drying through the gas-permeable lumox membrane, the dish was filled with culture medium (3 mL) and surrounded by Parafilm (see Figure 6.2) to prevent any leaking when the samples are irradiated in the vertical position.

6.1.3 Cell survival assay

Depending on beam form and position deducted from image plate acquisition, a 9 mm × 18 mm area was delimited on the inside face of lumox® with Creamy Color long lasting lip pencil (Kiko) in which 6×10^4 cells were seeded in 200 µL of medium. Cells were exposed to a variable number of successive shots ranging from 1 to 12, with a mean frequency of 0.025 Hz. After exposure to laser-driven protons, 1 mL of medium was added and the cell monolayers were incubated for 4 hours in standard conditions. Cells were harvested with Accutase (Merck), dispatched into 3 different wells of 12-well plate (TPP) in 2.5 mL of medium and grown for five generations corresponding to five days (replication time below 20 h), except for the lineage U87

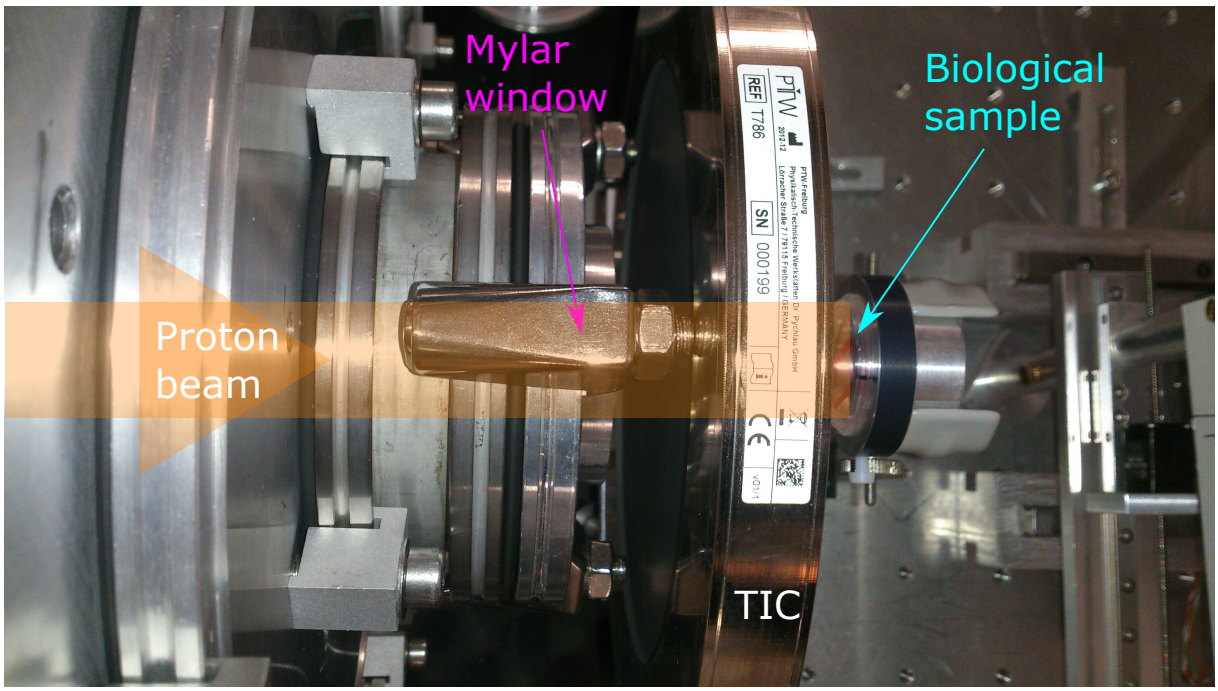

FIGURE 6.1: Picture of the transmission ionization chamber inserted between the biological sample (on the right) and the vacuum chamber (on the left).

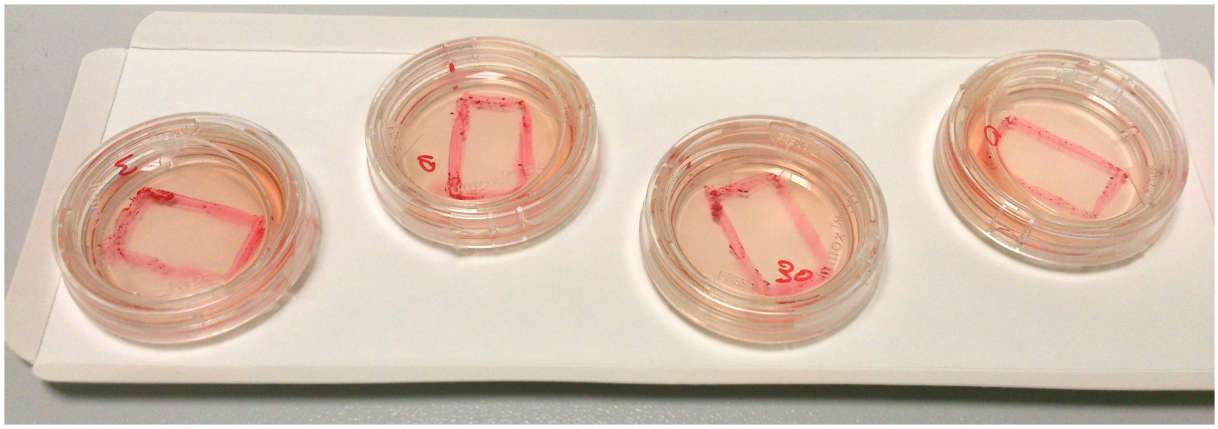

FIGURE 6.2: Picture of the 3 cm diameter cell sample dishes hosting a cell monolayer and filled with culture medium.

which requires 6 days (replication time of approximately 24 h). After this period, cells were harvested with 250 µL of Accutase inactivated with 250 µL of 1X PBS (ThermoFisher Scientific) supplemented with 10 % fetal calf serum. Final volume was adjusted to 1 mL with 1X PBS and 200 µL of each well were dispatched into a non-sterile U-bottom 96-well plate (TPP). In each well, 2 µL of a propidium iodide solution (Sigma, 100 µg · mL^{-1} in 1X PBS) were added just before counting by flow cytometry technology. Cell acquisition was performed using Guava® and the data analysis carried out with GuavaSoft (Merck Millipore).

Concerning spheroids, after a wash in 1X PBS, they were dissociated in 800 µL of Acctutase (Merck, solution for gentle and effective cell detachment and tissue dissociation of adherent cells) for 30 min at 37°C under agitation (950 rpm). 50 000 cells were then seeded in 6 well plates and grown as for monolayers for 5 generations, 6 days for the U87MG cell line.

6.1.4 DNA damage foci immunofluorescent staining

For DNA damage foci analysis, 4×10^5 cells were seeded on the entire lumox® surface of the dish in 2 mL of medium. Just before irradiation 1.8 mL of medium was removed. Cells were subjected to different numbers of successive shots. The cells were incubated 1 or 24 hours post irradiation at 37 °C and then were washed with 1 mL of 1X PBS and fixed in 1 mL of 4 % Formaline solution (Sigma) for 15 min at room temperature. The cells were then washed twice with 1X PBS before incubation for 10 min in 1 mL of permeabilization buffer (0.5 % Triton X-100 in 1X PBS). After a 20 min saturation in 1 mL of 1X PBS supplemented with 2 % SVF, saturation buffer was entirely removed. Opened Lumox® dishes were incubated 5 min under chemical hood to eliminated liquid excess. Irradiation surface was delimitated and subdivided in two equal area for immunostaining with Dako Pen (Agilent).

The cells were incubated for one hour at room temperature with a rabbit polyclonal antibody against 53BP1 (Bethyl) or a mouse monoclonal antibody against γH2AX (Merck) diluted in in PBS/SVF (1/1000, 30 µL per area). The cells were then washed twice with PBS/SVF before incubation in a 50 µL dilution of secondary antibody (Alexafluor 488 goat anti rabbit antibody or Alexafluor 546 goat anti mouse antibody, ThermoFisher Scientific, 1/500 in PBS/SVF). After a wash with 1X PBS, the cells were incubated in 1X PBS supplemented with DAPI (ThermoFisher Scientific, 0.1 µg · mL^{-1}) for 10 min at room temperature and were finally washed once again with 1X PBS. Liquid excess was removed by a 5 min incubation under chemical hood, irradiation area was cut following Dako Pen delimitation and Lumox® was mounted on glass microscopy slides using Prolong® Gold Antifade (ThermoFisher Scientific). Picture Acquisition was performed using DMi8 microscope and LASX software (Leica) at 40x magnification.

Automated counting of DNA damage foci

Foci were automatically counted in each nucleus, using a home-made ImageJ macro operating in two steps. Firstly, the nuclear image is processed. Potential uneven illumination was corrected by dividing the original nuclear image by a duplicate convolved by a Gaussian filter (radius: of 20 pixels). The resulting image intensities were enhanced using a gamma transform (gamma: 0.5) and smoothed by a median filter (radius: 5 pixels). Automated thresholding was applied, followed by morpho-mathematics operations (close, dilate, fill holes and watershed). The "analyze particle" function was used to isolate individual nuclei and retrieve their contours.

Secondly for foci counting, the outline of each nucleus was drawn onto the image of DNA repair foci. As foci were characterized as local maxima, the corresponding ImageJ function was used to identify and count them (noise parameter: 10). Eventually, a montage was created, presenting each nucleus with foci overlaid for visual inspection and assessment of the detection, as shown in Figure 6.3. For each data point, the average count of foci per cell was determined from at least 200 nuclei.

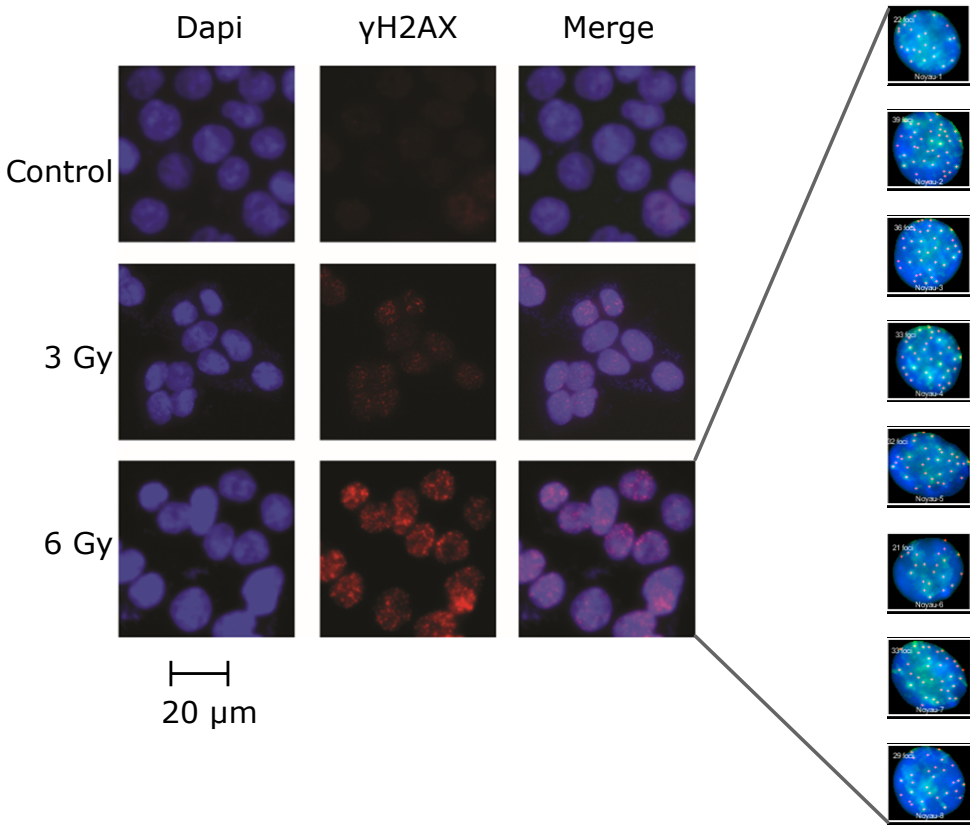

FIGURE 6.3: Immunostaining of radiation-induced γH2AX foci (second column, each red dot marks a DNA double-strand break), counterstaining with Dapi (first column, showing cell nuclei) and merged images are shown for HCT116 cells subjected to different doses of laser-pulsed proton beams. An example of automated foci counting is depicted on the right.

6.2 Experimental results

Radiobiological experiments were carried out using the laser-accelerated proton beam generated in SAPHIR and described in the previous chapters. For comparison, assays were also performed using three conventional radiation sources by Frédérique Mégnin-Chanet and Émilie Bayart from the Gustave-Roussy Institute. One is the **cyclotron** of the *Institut Curie Proton Therapy Center* that provides a 20 MeV *proton beam* at a dose rate of $3\,\mathrm{Gy}\cdot\mathrm{min}^{-1}$ [Calugaru et al., (2011); Calugaru et al., (2014)]. Another is a ^{137}**Cesium** source integrated in an IBL 637 n°9418 device manufactured by CIS Bio. It emits 662 keV *gamma ray* at $1.4\,\mathrm{Gy}\cdot\mathrm{min}^{-1}$. The last one is a Varian NDI 226 **x-ray tube** generating photons with an average energy of 72.5 keV. In standard conditions, a tension of 200 kV and an intensity of 15 mA are applied.

6.2.1 Foci analysis

As shown in Figure 6.4, increasing doses led to increasing amounts of detected foci in cell nuclei. For each irradiation condition, similar amounts of foci were counted in the two HCT116 cell lines. These results suggest that despite the theoretical importance of the error on the dose, the DNA damage generated by laser pulsed protons showed a great reproducibility of the dose delivered to the sample.

One hour after irradiation, the number of detected foci increases with the applied dose. For the glioblastoma cells, it reaches a plateau around 3 Gy, which is a commonly observed phenomenon [Torudd et al., (2005); Short et al., (2007)]. This higher bound results from the saturation of the DNA damage signalling pathways as well as from reaching the limits of the detection method (foci are getting closer to each other, becoming harder to distinguish).

24 hours after irradiation, most of the damages should naturally be repaired. Hence, as expected, there is consistently less foci measured at 24 h compared to 1 h after irradiation. At doses up to 3 Gy, most of the damages are repaired 24 h post-irradiation except for U87, with average numbers of foci per cell comparable to the background levels observed in the control unirradiated samples (which is non null, as mentioned in section 2.2.2). At higher doses, residual damages are still observed after 24 h as the DNA repair machinery gets saturated with more numerous and closer damages that become harder to repair.

Finally, the data coming from the irradiation of samples using conventional sources matches well the values obtained with the SAPHIR proton beam, confirming the dosimetry estimations. However, more data points at low doses would be necessary to see if the plateau is reached in the same way for each radiation source.

6.2.2 Survival assay

For each experiment the dose giving 10 % of cell survival (D_{10}) was calculated using the α and β parameters determined from curves drawn for best fit to the experimental data (Kaleidagraph and GraphPad Prism softwares). Cell survival values obtained in response to increasing doses of irradiation with laser accelerated protons allowed to perform a reliable linear quadratic regression analysis (Fig.6.5C), as for ^{137}Cesium or 20 MeV conventional protons (Fig.6.5A and 6.5B). As shown in Figure 6.5D, the D_{10} ratio between HCT116-WT and HCT116-p53$^{-/-}$ corresponding to pulsed-protons (0.62 ± 0.4) appears to be reduced compared to those of 20 MeV conventional protons and 662 keV photons (0.75 and 0.72 ± 0.06 respectively). However, this apparent reduction in effectiveness of the pulsed protons was not statistically significant (p-value $P > 0.05$). It results probably from the relatively large error on the delivered dose, but it was acceptable for the proof of principle experiments for use of SAPHIR facility for radiobiological studies. All together, these results reflected the good control of the dosimetry to sample and the stability of the beam.

The glioblastoma cells that are more radioresistant behave much in the same way whatever the nature of the radiation, as shown in Figure 6.6. Table 6.1 summarises the D_{10} values obtained for each cell line and irradiation source.

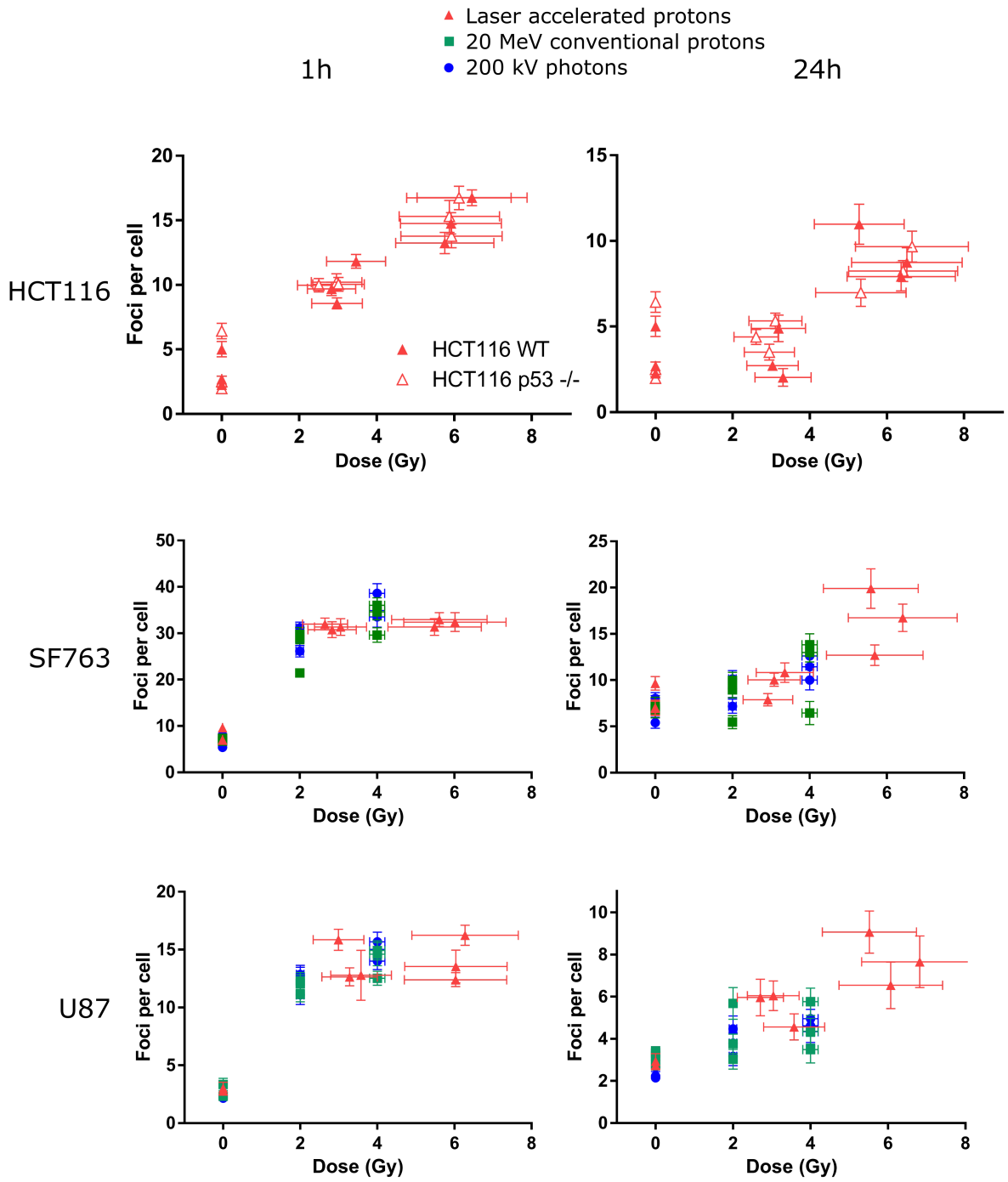

FIGURE 6.4: Number of γH2AX foci generated in the different cell lines irradiated with an increasing dose provided by several bunches of laser-accelerated protons ($n = 3$). The right and left columns represent the damages measured respectively 1 h and 24 h after irradiation. Foci counts measured in cells irradiated with conventional sources are also displayed when available, with 20 MeV continuous protons in green and 200 kV x-rays in blue.

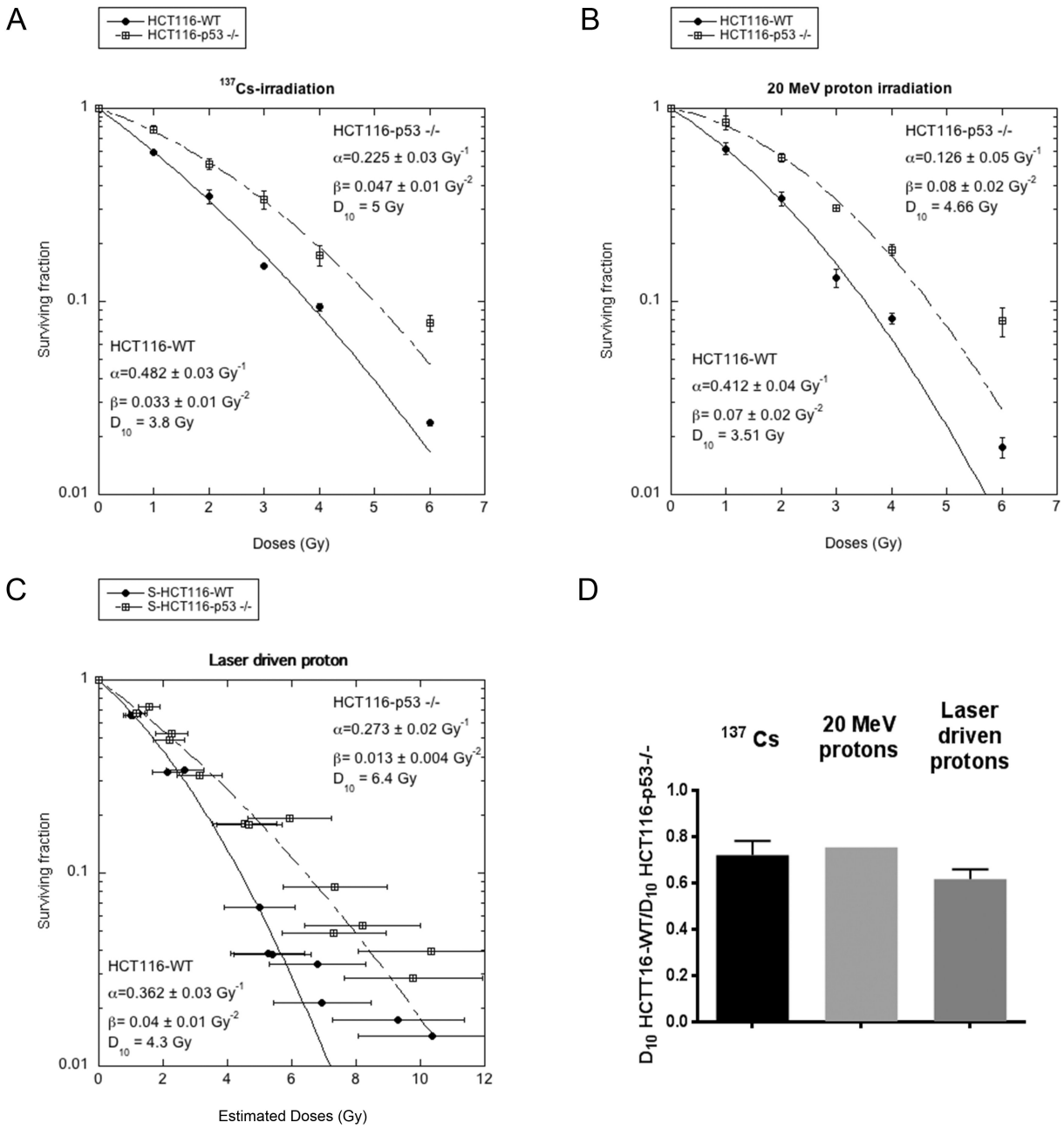

FIGURE 6.5: Survival curves of HCT116-WT and p53$^{-/-}$ cells after ^{137}Cs (A, mean ± SD of 3 independent experiments), 20 MeV proton (B, mean ± SD of 2 independent experiments) or laser-driven irradiations (C, mean ± SD of 3 independent experiments). D: Calculated D10 ratio between HCT116-WT and p53$^{-/-}$ cells for each irradiation condition.

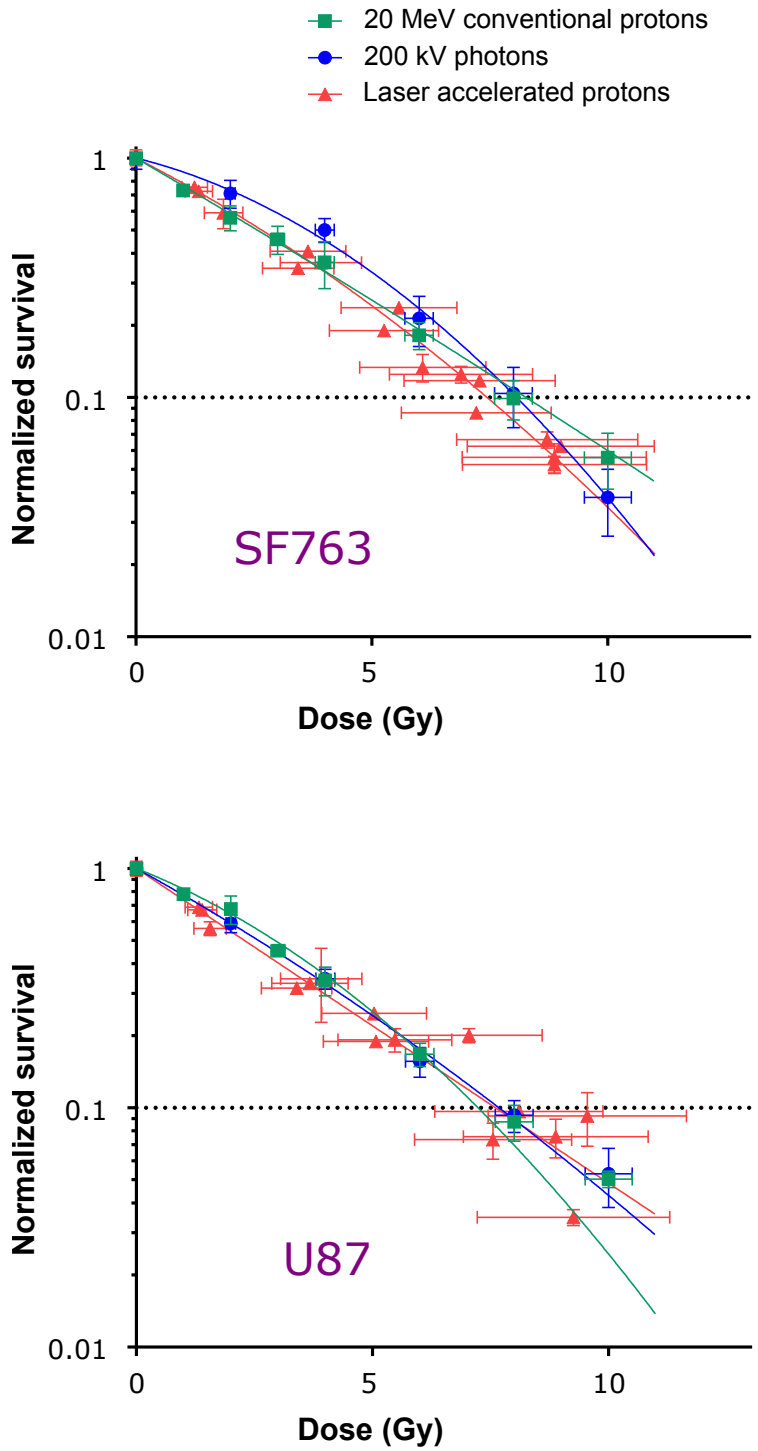

FIGURE 6.6: Survival curves of the glioblastoma cell lines, subjected to irradiation from conventional sources and laser-accelerated protons.

Cell line	Proton sources		Photon sources	
	Laser pulsed	20 MeV continuous	^{137}Cs γ at 662 keV	200 kV x-rays
HCT116 WT	3.88 ± 0.74	3.5 ± 0.4	3.8 ± 0.4	
HCT116 p53	6.28 ± 0.78	4.7 ± 0.7	5 ± 0.4	
SF763	7.30 ± 0.52	7.90 ± 0.36		7.95 ± 0.42
U87	7.47 ± 0.56	7.11 ± 0.27		7.74 ± 0.16

TABLE 6.1: Summary of 10 % survival doses in Gray for the different cell lines and irradiation sources. The errors represent standard deviations of the survival for 3 independent experiments.

The biological effectiveness on live cells of laser-driven proton beams at extreme dose rates above 10^8 Gy $\cdot$ s^{-1} appears similar to that of conventional sources, in agreement with previous studies [Auer et al., (2011); Doria et al., (2012)]. Earlier experiments were already performed at very high dose rates on conventional accelerator and concluded in the same direction of no significant dose rate effect on biological responses. In [Yashkin et al., (1995)], the radiation source was a 179 MeV proton beam generated by a medical synchrotron facility, at a peak dose rates of 10^6 Gy $\cdot$ s^{-1} with a mean rate of 1.2 Gy $\cdot$ min^{-1} (10^{-7} s pulse duration at a frequency of 0.25 Hz).

6.2.3 Exploratory work and outlook

Cadence effect

We investigated the possible effects of varying the *pace* at which the shots are fired. A total of 6 shots were delivered to each HCT116 sample, while 9 shots were delivered to SF763 and U87 samples, which corresponds to doses of respectively 6 Gy and 9 Gy. The time delay between shots was kept constant during the irradiation of each sample, but varied between samples among the following values: 2 s, 3 s, 10 s, 30 s, 45 s and 60 s. Each setting was repeated for 3 independent experiments. To eliminate effects related to variations in the total absorbed dose, the results are represented as function of the dose applied per minute, as shown in Figure 6.7.

A fit is superimposed on top of the experimental data for HCT116 and SF763, as a bell curve behaviour seems to emerge. It would indicate an increased cell survival around 15 Gy $\cdot$ min^{-1}, which corresponds to a pace of about 5 s (the average dose per shot was 1.2 Gy). However, the effect is less evident for U87. The survival evolution of this cell line, which is the most radioresistant one, looks flat. The insensitivity of this cell line to the variation of the pace could result from a particular genetic characteristic.

Another group performed the same kind of experiment. They exposed other cell lines to split-dose of pulsed 3.5 MeV electron radiation at relatively high dose rates of 12 or 120 Gy $\cdot$ s^{-1}, and also observed variations in survival response [Ponette et al., (2000); Fernet et al., (2000)]. It was called the *W effect*, and it is reproduced in Figure 6.8. The curve include a bell shape that could reflects the behaviour observed in our experiments. The oscillatory radiation response did not correlate with more DNA damages, but with phenotypic alterations related to delayed cell death. The range over which we performed our study was not spread over such an extended range, but what we observed could correspond to be the central peak of the "W". It is therefore important to scan the pace over a wider range to find which value is maximising cell death.

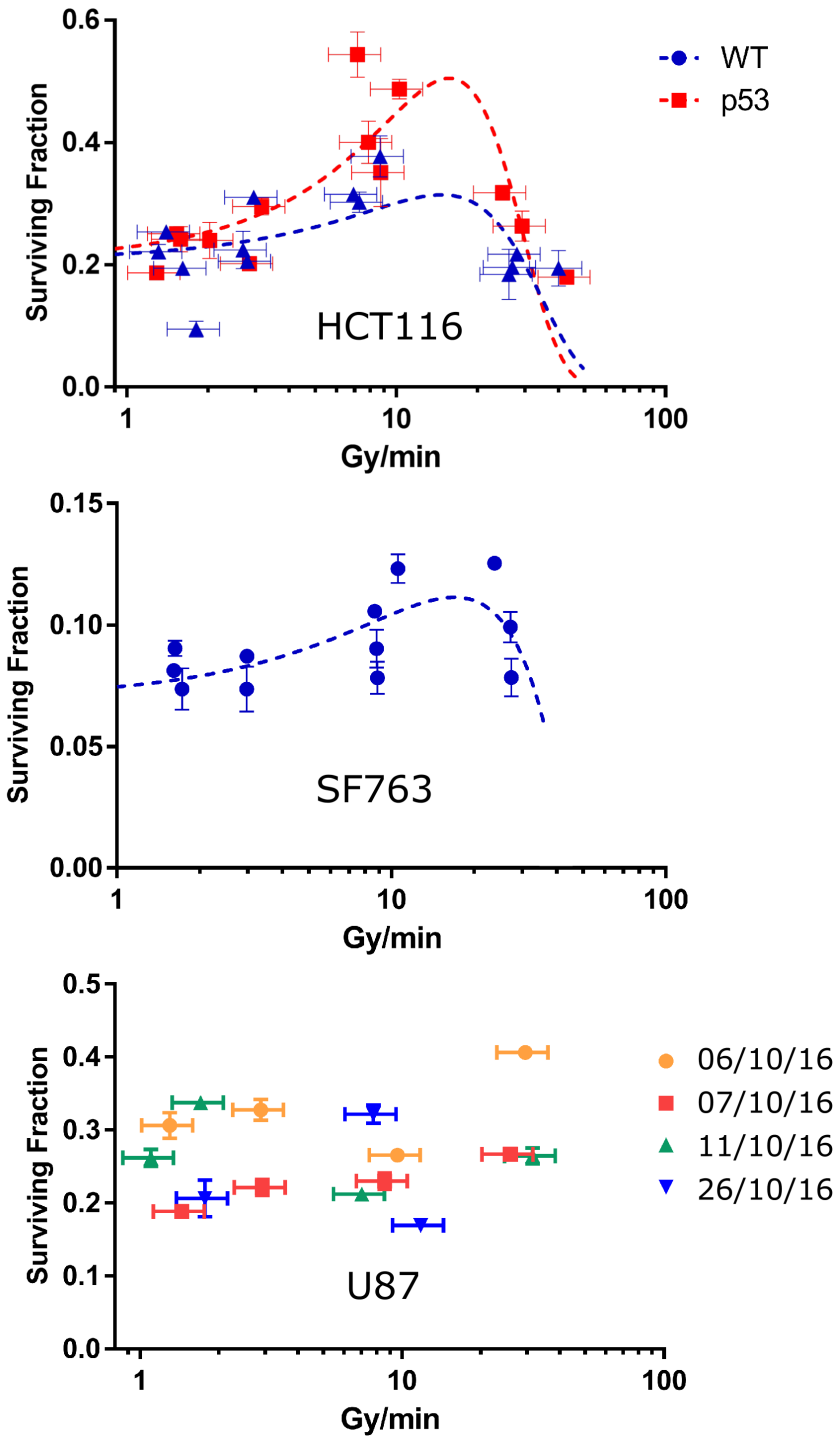

FIGURE 6.7: Cell survival as function of the dose absorbed per minute. The pace of the shots was changed from 3 s to 1 min. 6 (for HCT116) and 9 (for glioblastomas) shots were applied. The graphs are semi-logarithmic plot to permit a distinction between data points related to large delays between shots. Each of the 3 series for SF763 was normalised with respect to the survival curve obtained with a pace of 30 s that is presented in the previous section.

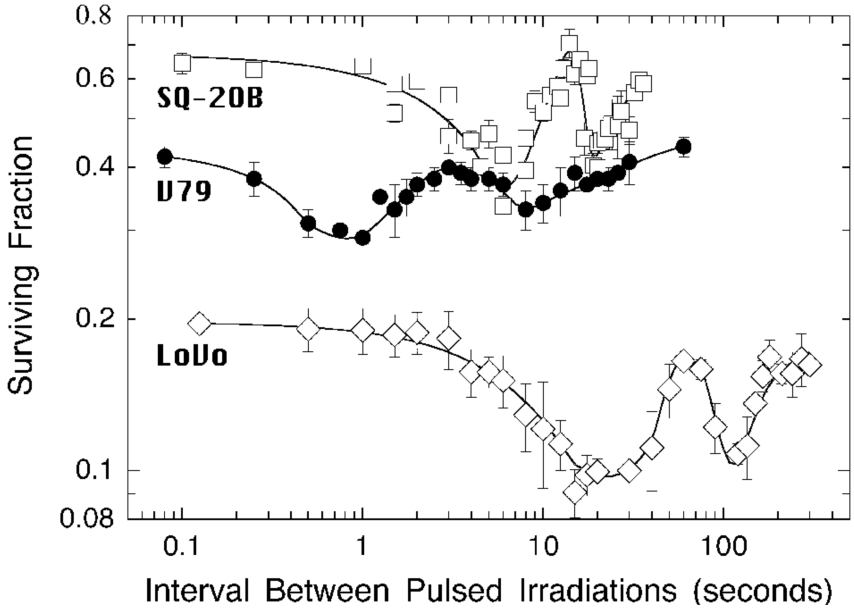

FIGURE 6.8: Time-dependent profile of the clonogenic survival of different cells following pulsed, split-dose exposure to 2 shots of 3.5 MeV electrons at a dose rate of $12\,\mathrm{Gy}\cdot\mathrm{s}^{-1}$. (Adapted from Ponette et al., [2000])

Irradiation of spheroid cell samples

An attempt to study the behaviour of 3D structures was undertaken (see a picture of the samples in Figure 6.9). A tumour inside the body is volumetric indeed, so the reaction of 3D tissues can differ compared with monolayers. Due to a latent state caused by nutriment and oxygen deprivation (hypoxia), the innermost cells are less sensitive to radiation than well-oxygenated cells [Khaitan et al., (2006)]. They were subject to the irradiation protocol as for the monolayers, but a flat survival curve was observed (data not shown).

This can be explained by the fact that the peak in the proton spectrum of the setup used is only 1.5 MeV (see Fig. 4.19b) at the forefront of the biological sample, so most of the protons stopped in the first 50 µm of the sample volume. The spheroids were quite big, between 200 µm and 500 µm, hence a majority of the cells were not irradiated. The survival rate being measured after potentially 5 cell divisions, the non-irradiated part of the sample completely overwhelmed the small irradiated fraction, explaining the result that was obtained.

For later experiments of this type, the setup should be optimised to bring protons with energies up to at least 6 MeV to the sample, that is to say with an initial energy of 8 MeV for the current setup, in order to irradiate the sample over a thickness of 500 µm (see the proton range in a cell sample, considered as water, in Figure 6.10).

If not much higher proton energies can be generated to irradiate 3D samples, an alternative to relax the constraints could be to use a thinner (and reduced in diameter as the aperture size is not fully used) window to extract the protons from the vacuum chamber, hence limiting the energy lost by the proton beam while exiting the chamber.

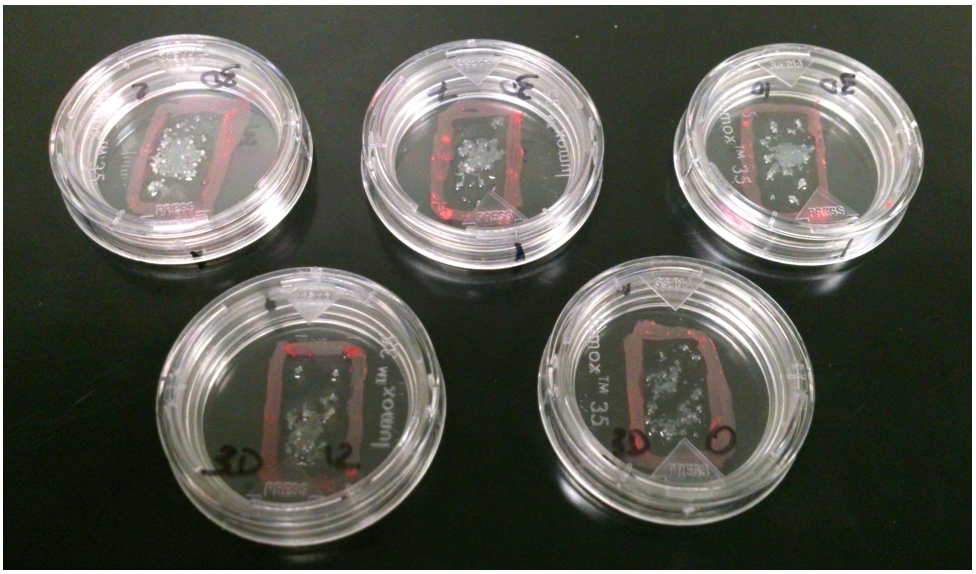

FIGURE 6.9: Picture of 3 cm diameter dishes hosting spheroids samples. The 3D structures are visible as small lumps on the bottom membrane in the rectangular area of interest delimited in red.

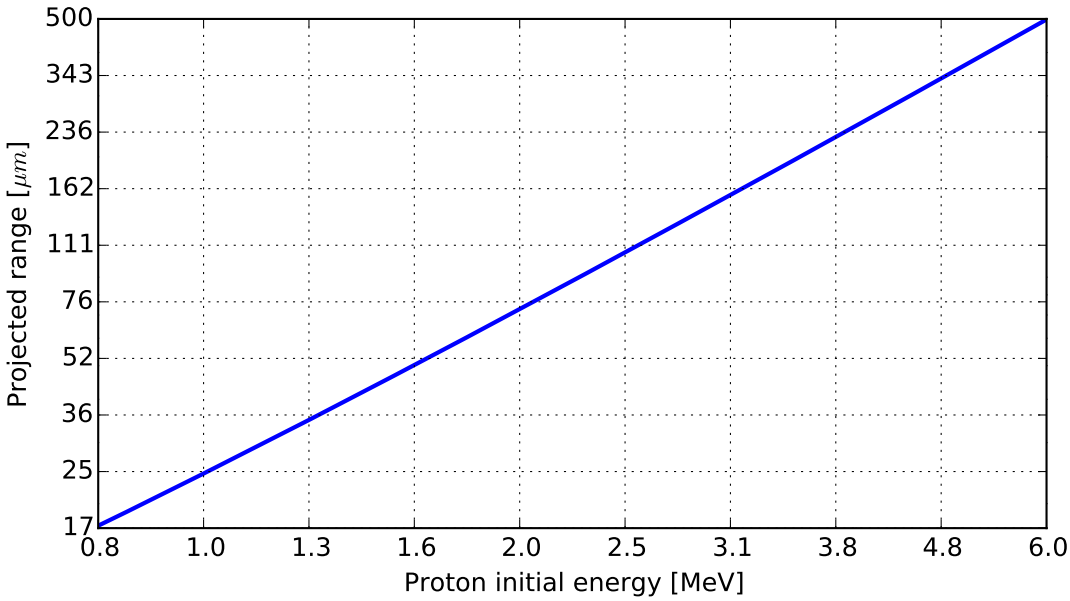

FIGURE 6.10: Log-log plot of the projected range of protons in water as function of their initial energy. Calculated from the data provided by the NIST PSTAR database [Berger et al., (1999)].

6.3 Conclusion

In this chapter, the radiobiological experiments performed using the laser-driven proton beams generated in the SAPHIR facility were presented. The biological protocol for cell culture and analysis was described. DNA damages were measured by immunofluorescence and the energy-dependent cell survival was assessed for different cell lines. All the results indicate no significant difference in relative biological effectiveness between these pulsed proton beams and continuous radiation coming from conventional sources.

Cell response was also evaluated for different paces, and a trend seems to come out. A more in depth study over a wider range of delays between shots would be useful to make a better diagnostic and validate the hypothesis. If this phenomenon is confirmed, it would really demonstrate the interest of using pulsed radiation sources in radiotherapy. They could allow for the definition of new clinical protocols more efficient than the current ones that are based on continuous beams generated by conventional accelerators.

The following step will be to look into the response of healthy tissues, with the objective of developing treatment plans that maximise the dose delivered to the tumour to destroy it, potentially increasing the chance of a cure, while limiting the amount of radiation received by the nearby healthy tissue to reduce side effects and the risk of radiation-induced cancer. 3D samples will allow to study oxygen effects and the reaction of cells irradiated in hypoxia conditions. Getting closer to in vivo conditions, the behaviour of irradiated tumour cells in their microenvironment could be examined, considering the activation of the immune system after they were deposited on lymphocytes (white blood cells, playing a major role in the immune system).

Conclusion

This section summarises the main results of the studies presented in this thesis and some future prospects are then addressed. The work exposed is the outcome of three years of numerical and experimental efforts dedicated to the spatial and spectral shaping of laser-accelerated proton beams for their application to radiobiology experiments.

Firstly, I presented in chapter 3 a comprehensive characterisation of the ion beams accelerated from solid targets by the SAPHIR laser, using appropriate diagnostic devices. The 3 J laser energy per pulse of 25 fs duration enables the acceleration of ions in the TNSA regime from solid titanium targets with a 5 µm thickness. Ion energy spectra were measured using a Thomson Parabola spectrometer and proton energy cutoffs were observed above 7 MeV. The energy-resolved beam source divergence was inferred from the irradiation of stacks of radiochromic films placed behind the source. The divergence decreases as the energy increases, and for instance the 5 MeV proton component is emitted in a cone with a FWHM angle of 24°.

Using this description, I showed in chapter 4 that a good control on the proton beam can be achieved thanks to a transport beamline made of four permanent magnet quadrupoles. I showed the possibility to focus an energy component via simulations, and demonstrated experimentally getting a spot size down to a millimetric scale at 44 cm behind the source. This feature paves the way for energy filtering using an aperture placed in the focus plane, making use of the chromatic property of PMQs. I also optimised the transport system in order to deliver a proton beam in air, with a spectrum peaking at 1.5 MeV at a distance of 1 m from the target, with a size and homogeneity suitable for pursing radiobiogical studies. Moreover, the predictions of particle beam transport simulations were in good agreement with the experimental behaviours recorded as transverse beam profiles along the beam path.

In chapter 5 I presented the meticulous dosimetry approach that was implemented on our setup. It allowed to determine the dose deposition of the laser-driven proton beam in a cell sample placed at the output in air, and evaluate the fluctuations in real time. On a surface of 1.5 cm^2, an average dose of 1.1 Gy/shot is delivered to the cell monolayer samples with a standard deviation of 22 %. The monitoring method depended on the absolute calibration of a transmission ionisation chamber, using a medical cyclotron facility. The procedure was detailed, including the experimental layout and the Monte-Carlo simulations required to derive the final dose in SAPHIR.

Finally, in chapter 6 I disclosed the results of monolayer cell irradiation experiments performed using our laser-based proton accelerator that provides utmost dose rates above 10^8 Gy/s. Several human cancer cell lines were scrutinised, namely colorectal cancer cells HCT116 (wild type and p53 mutated) and glioblastoma cell lines SF763 and U87MG. DNA damages were measured by immunofluorescence staining technique and cell survival rates were recorded for different applied doses. The effects of the pulsed protons on the behaviour and biological response of the samples seemed in both cases analogous to irradiation using continuous proton beams coming from conventional accelerators at the same dose level. A preliminary inquiry of how the pace at which the pulses are fired on the samples could affect the biological response

was exposed. A trend seems to turn up and follow previous studies in the literature. If confirmed, this discovery would reveal an additional advantage of using laser-accelerated proton beams in medicine.

Perspectives

With the recent developments in laser technology, laser pulses are delivered at higher intensities and repetition rates. The energetic ion beams that can be accelerated up to several tens of MeV with reasonable size facilities could offer a potentially more compact and cost-effective mean of delivering particle beams for medical applications. These laser based proton accelerators represent a promising new method of accelerating charged particles to energies that might become high enough for therapeutic use in the treatment of cancers with hadrontherapy. TNSA, the prevailing acceleration mechanism nowadays, shows some limitations in some key elements such as the highest energies achieved. However, new regimes are under study and may overcome the addressed problems to accelerate ions to high energies with higher efficiencies and better collimation. Emerging scaling laws indicate possible realization of an ion therapy facility with compact, cost-efficient lasers [Malka et al., (2004); Tajima et al., (2009)].

On more practical aspects, one of the main issues associated with laser-based accelerator systems is the shot-to-shot fluctuations. Even if the transport system contributes to stabilise the output spectrum against variations in the proton energy cutoff, an improved stability could enable studies of the biological effect of the dose applied per pulse. A solution could be attained with a new target mounting process such as tape targets. This could also help in decreasing the time between shots down to the 5 Hz laser repetition rate, to be able to scan pace effects over a larger range than what was already done. Moreover, faster shot series would be made easier with the complete automation of the target alignment.

The PMQ transport system used until now could be improved in several ways. Better transport efficiency could be achieved with a solenoid added right behind the target to ensure a better initial collection by focusing the beam in all radial directions. If a monochromatic beam was preferred for the irradiation of cell monolayers, it is not the rule when one wants to move towards conditions closer to therapy, as for the irradiation of more complex, three dimensional volumes. Employing pulsed solenoids opens the way for active shaping of the proton energy spectrum, which would be particularly useful for the irradiation of volumetric samples. A homogeneous proton depth dose distribution could thus be applied to a tumour without the need to shape the energy distribution directly in the plasma acceleration process [Burris-Mog et al., (2011); Zeil et al., (2012)]. Another option to obtain such a spread-out Bragg peak (SOBP) could be accomplished with a magnetic chicane [Yoo et al., (2014)]. Combined with the use of a scattering material (wedge or slices), it would allow to shape the beam spectrum so that a full SOBP could be delivered in a single shot [Schell and Wilkens, (2009)]. The possibility to select a range of energies to naturally produce SOBPs would increases the particle efficiency of the whole system, highlighting the fit between laser accelerators and their application in radiation therapy.

On the subject of dosimetry, improvements on the value of the dose delivered on the sample area could be achieved with more homogeneous beam distributions. If higher proton energies are generated at the source, different PMQ setups could be used to provide output beams with a better uniformity. The PMQ positions could also be adjusted to tune the output dose delivered per pulse. Higher instantaneous dose rates would allow to investigate possible collective effects predicted by Fourkal et al., [2011]. Besides, some factors could induce variations in the

calibration of the transmission ionisation chamber. A comprehensive calibration experiment could help in taking them into account in order to give a more precise evaluation of the dose.

Simulating the entire system in Geant4 would also lead to better estimations of the dose deposition in the samples. Integrating the quadrupole field maps and the beam source modelled from its characterised energy spectrum and spatial divergence would allow to obtain within a single software the spatially dependent dose deposition more accurately.

For the first time at LOA, a synergy between physics and biology was created in the scope of the SAPHIR project. A common language was elaborated in order to run successful radiobiological experiments. The next step will be a strict collaboration with clinicians and radiotherapists to study and define protocols for patient treatment. Though the practical realisation of laser-driven medical facility may take several decades, methods of beam delivery and treatment planning that are specifically adapted to laser accelerated particles have already been presented [Schell and Wilkens, (2010)]. The challenges remain to deliver stable and reproducible proton beams at higher energies up to 200 MeV and with a modulated energy spectrum, which should be reachable with the upcoming generations of compact laser systems.

Bibliography

Agostinelli, S., J. Allison, K. Amako, J. Apostolakis, H. Araujo, P. Arce, M. Asai, D. Axen, S. Banerjee, G. Barrand, et al. (2003). "Geant4—a simulation toolkit". In: *Nuclear Instruments and Methods in Physics Research Section A: Accelerators, Spectrometers, Detectors and Associated Equipment* 506.3, pp. 250–303. ISSN: 0168-9002. DOI: 10.1016/S0168-9002(03)01368-8 (cit. on p. 114).

Agostini, P., G. Barjot, J. Bonnal, G. Mainfray, C. Manus, and J. Morellec (1968). "Multiphoton ionization of hydrogen and rare gases". In: *IEEE Journal of Quantum Electronics* 4.10, pp. 667–669. ISSN: 0018-9197. DOI: 10.1109/JQE.1968.1074955 (cit. on p. 15).

Ahmed, Syed Naeem (2014). *Physics and Engineering of Radiation Detection*. Elsevier. ISBN: 978-0-12-801644-2 (cit. on p. 110).

Albright, B. J., L. Yin, B. M. Hegelich, Kevin J. Bowers, T. J. T. Kwan, and J. C. Fernández (2006). "Theory of Laser Acceleration of Light-Ion Beams from Interaction of Ultrahigh-Intensity Lasers with Layered Targets". In: *Physical Review Letters* 97.11, p. 115002. DOI: 10.1103/PhysRevLett.97.115002 (cit. on pp. 21, 27).

Albright, B. J., L. Yin, Kevin J. Bowers, B. M. Hegelich, K. A. Flippo, T. J. T. Kwan, and J. C. Fernández (2007). "Relativistic Buneman instability in the laser breakout afterburner". In: *Physics of Plasmas (1994-present)* 14.9, p. 094502. ISSN: 1070-664X, 1089-7674. DOI: 10.1063/1.2768933 (cit. on p. 28).

Almomani, A., M. Droba, U. Ratzinger, and I. Hofmann (2012). "Matching the laser generated p bunch into a crossbar-H drift tube linac". In: *Physical Review Special Topics - Accelerators and Beams* 15.5, p. 051302. DOI: 10.1103/PhysRevSTAB.15.051302 (cit. on p. 78).

Attanasi, F., N. Belcari, A. Del Guerra, W. Enghardt, S. Moehrs, K. Parodi, V. Rosso, and S. Vecchio (2009). "Comparison of two dedicated 'in beam' PET systems via simultaneous imaging of 12C-induced beta+-activity". In: *Physics in Medicine and Biology* 54.2, N29. ISSN: 0031-9155. DOI: 10.1088/0031-9155/54/2/N01 (cit. on p. 28).

Attanasi, F., N. Belcari, S. Moehrs, V. Rosso, S. Vecchio, G. A. P. Cirrone, G. Cuttone, P. Lojacono, F. Romano, N. Lanconelli, and A. Del Guerra (2010). "Characterization of an In-Beam PET Prototype for Proton Therapy With Different Target Compositions". In: *IEEE Transactions on Nuclear Science* 57.3, pp. 1563–1569. ISSN: 0018-9499. DOI: 10.1109/TNS.2010.2048124 (cit. on p. 28).

Attix, Frank Herbert (1986). *Introduction to Radiological Physics and Radiation Dosimetry*. Wiley. ISBN: 978-3-527-61714-2 (cit. on p. 32).

Auer, Susanne, Volker Hable, Christoph Greubel, Guido A. Drexler, Thomas E. Schmid, Claus Belka, Günther Dollinger, and Anna A. Friedl (2011). "Survival of tumor cells after proton irradiation with ultra-high dose rates". In: *Radiation Oncology* 6.1, p. 139. ISSN: 1748-717X. DOI: 10.1186/1748-717X-6-139 (cit. on p. 128).

Batani, D., R. Jafer, M. Veltcheva, R. Dezulian, O. Lundh, F. Lindau, A. Persson, K. Osvay, C.-G. Wahlström, D. C. Carroll, P. McKenna, A. Flacco, and V. Malka (2010). "Effects of laser prepulses on laser-induced proton generation". In: *New Journal of Physics* 12.4, p. 045018. ISSN: 1367-2630. DOI: 10.1088/1367-2630/12/4/045018 (cit. on p. 49).

Berdermann, E., M. Pomorski, W. de Boer, M. Ciobanu, S. Dunst, C. Grah, M. Kiš, W. Koenig, W. Lange, W. Lohmann, R. Lovrinčić, P. Moritz, J. Morse, S. Mueller, A. Pucci, M. Schreck, S.

Rahman, and M. Träger (2010). "Diamond detectors for hadron physics research". In: *Diamond and Related Materials*. Proceedings of Diamond 2009, The 20th European Conference on Diamond, Diamond-Like Materials, Carbon Nanotubes and Nitrides, Part 1 19.5–6, pp. 358–367. ISSN: 0925-9635. DOI: 10.1016/j.diamond.2009.11.019 (cit. on p. 69).

Berger, Martin J., J S. Coursey, and M A. Zucker (1999). *ESTAR, PSTAR, and ASTAR: Computer Programs for Calculating Stopping-Power and Range Tables for Electrons, Protons, and Helium Ions (version 1.21)* (cit. on pp. 33, 131).

Bin, Jianhui, Klaus Allinger, Walter Assmann, Günther Dollinger, Guido A. Drexler, Anna A. Friedl, Dieter Habs, Peter Hilz, Rainer Hoerlein, Nicole Humble, et al. (2012). "A laser-driven nanosecond proton source for radiobiological studies". In: *Applied Physics Letters* 101.24, p. 243701. ISSN: 0003-6951, 1077-3118. DOI: 10.1063/1.4769372 (cit. on pp. 8, 116).

Bolton, P. R., M. Borghesi, C. Brenner, D. C. Carroll, C. De Martinis, F. Fiorini, A. Flacco, V. Floquet, J. Fuchs, P. Gallegos, et al. (2014). "Instrumentation for diagnostics and control of laser-accelerated proton (ion) beams". In: *Physica Medica* 30.3, pp. 255–270. ISSN: 1120-1797. DOI: 10.1016/j.ejmp.2013.09.002 (cit. on p. 54).

Bonnet, T., M. Comet, D. Denis-Petit, F. Gobet, F. Hannachi, M. Tarisien, M. Versteegen, and M. M. Aleonard (2013). "Response functions of Fuji imaging plates to monoenergetic protons in the energy range 0.6–3.2 MeV". In: *Review of Scientific Instruments* 84.1, p. 013508. ISSN: 00346748. DOI: 10.1063/1.4775719 (cit. on pp. 58, 117).

Borghesi, M., D. H. Campbell, A. Schiavi, M. G. Haines, O. Willi, A. J. MacKinnon, P. Patel, L. A. Gizzi, M. Galimberti, R. J. Clarke, F. Pegoraro, H. Ruhl, and S. Bulanov (2002a). "Electric field detection in laser-plasma interaction experiments via the proton imaging technique". In: *Physics of Plasmas (1994-present)* 9.5, pp. 2214–2220. ISSN: 1070-664X, 1089-7674. DOI: 10.1063/1.1459457 (cit. on p. 28).

Borghesi, M., S. Bulanov, D. H. Campbell, R. J. Clarke, T. Zh. Esirkepov, M. Galimberti, L. A. Gizzi, A. J. MacKinnon, N. M. Naumova, F. Pegoraro, H. Ruhl, A. Schiavi, and O. Willi (2002b). "Macroscopic Evidence of Soliton Formation in Multiterawatt Laser-Plasma Interaction". In: *Physical Review Letters* 88.13, p. 135002. DOI: 10.1103/PhysRevLett.88.135002 (cit. on p. 28).

Borghesi, M., J. Fuchs, S. V. Bulanov, A. J. MacKinnon, P. K. Patel, and M. Roth (2006). "Fast ion generation by high-intensity laser irradiation of solid targets and applications". In: *ResearchGate* 49.3. ISSN: 1536-1055 (cit. on pp. 20, 23, 24).

Borghesi, Marco (2014). "Laser-driven ion acceleration: State of the art and emerging mechanisms". In: *Nuclear Instruments and Methods in Physics Research Section A: Accelerators, Spectrometers, Detectors and Associated Equipment*. Proceedings of the first European Advanced Accelerator Concepts Workshop 2013 740, pp. 6–9. ISSN: 0168-9002. DOI: 10.1016/j.nima.2013.11.098 (cit. on p. 20).

Boutoux, G., N. Rabhi, D. Batani, A. Binet, J.-E. Ducret, K. Jakubowska, J.-P. Nègre, C. Reverdin, and I. Thfoin (2015). "Study of imaging plate detector sensitivity to 5-18 MeV electrons". In: *Review of Scientific Instruments* 86.11, p. 113304. ISSN: 0034-6748, 1089-7623. DOI: 10.1063/1.4936141 (cit. on p. 58).

Brunel, F. (1987). "Not-so-resonant, resonant absorption". In: *Physical Review Letters* 59.1, pp. 52–55. DOI: 10.1103/PhysRevLett.59.52 (cit. on pp. 18, 19).

— (1988). "Anomalous absorption of high intensity subpicosecond laser pulses". In: *Physics of Fluids (1958-1988)* 31.9, pp. 2714–2719. ISSN: 0031-9171. DOI: 10.1063/1.867001 (cit. on p. 18).

Bulanov, S. V. and V. S. Khoroshkov (2002). "Feasibility of using laser ion accelerators in proton therapy". In: *Plasma Physics Reports* 28.5, pp. 453–456. ISSN: 1063-780X, 1562-6938. DOI: 10.1134/1.1478534 (cit. on p. 28).

Burris-Mog, T., K. Harres, F. Nürnberg, S. Busold, M. Bussmann, O. Deppert, G. Hoffmeister, M. Joost, M. Sobiella, A. Tauschwitz, B. Zielbauer, V. Bagnoud, T. Herrmannsdoerfer, M. Roth, and T. E. Cowan (2011). "Laser accelerated protons captured and transported by a pulse power solenoid". In: *Physical Review Special Topics - Accelerators and Beams* 14.12, p. 121301. DOI: 10.1103/PhysRevSTAB.14.121301 (cit. on pp. 7, 134).

Bychenkov, V. Yu, W. Rozmus, A. Maksimchuk, D. Umstadter, and C. E. Capjack (2001). "Fast ignitor concept with light ions". In: *Plasma Physics Reports* 27.12, pp. 1017–1020. ISSN: 1063-780X, 1562-6938. DOI: 10.1134/1.1426135 (cit. on p. 28).

Calugaru, Valentin, Catherine Nauraye, Georges Noël, Nicole Giocanti, Vincent Favaudon, and Frédérique Mégnin-Chanet (2011). "Radiobiological Characterization of Two Therapeutic Proton Beams With Different Initial Energy Spectra Used at the Institut Curie Proton Therapy Center in Orsay". In: *International Journal of Radiation Oncology • Biology • Physics* 81.4, pp. 1136–1143. ISSN: 0360-3016. DOI: 10.1016/j.ijrobp.2010.09.003 (cit. on p. 123).

Calugaru, Valentin, Catherine Nauraye, Fabrice P. Cordelières, Denis Biard, Ludovic De Marzi, Janet Hall, Vincent Favaudon, and Frédérique Mégnin-Chanet (2014). "Involvement of the Artemis Protein in the Relative Biological Efficiency Observed With the 76-MeV Proton Beam Used at the Institut Curie Proton Therapy Center in Orsay". In: *International Journal of Radiation Oncology • Biology • Physics* 90.1, pp. 36–43. ISSN: 0360-3016. DOI: 10.1016/j.ijrobp.2014.05.018 (cit. on p. 123).

Ceccotti, T., A. Lévy, H. Popescu, F. Réau, P. D'Oliveira, P. Monot, J. P. Geindre, E. Lefebvre, and Ph. Martin (2007). "Proton Acceleration with High-Intensity Ultrahigh-Contrast Laser Pulses". In: *Physical Review Letters* 99.18, p. 185002. DOI: 10.1103/PhysRevLett.99.185002 (cit. on p. 22).

Ceccotti, T., V. Floquet, A. Sgattoni, A. Bigongiari, O. Klimo, M. Raynaud, C. Riconda, A. Heron, F. Baffigi, L. Labate, et al. (2013). "Evidence of Resonant Surface-Wave Excitation in the Relativistic Regime through Measurements of Proton Acceleration from Grating Targets". In: *Physical Review Letters* 111.18, p. 185001. DOI: 10.1103/PhysRevLett.111.185001 (cit. on p. 23).

Chen, Francis F. (1984). *Introduction to Plasma Physics and Controlled Fusion*. 2nd. Vol. 1. Springer. ISBN: 978-0-306-41332-2 (cit. on p. 14).

Choppin, G., J. O. Liljenzin, J. Rydberg, and C. Ekberg (2013). *Radiochemistry and Nuclear Chemistry*. Elsevier Science. ISBN: 978-0-12-397868-4 (cit. on p. 34).

Cirrone, Giuseppe A. P., Massimo Carpinelli, Giacomo Cuttone, Santo Gammino, S. Bijan Jia, Georg Korn, Mario Maggiore, Lorenzo Manti, Daniele Margarone, Jan Prokupek, Marcella Renis, Francesco Romano, Francesco Schillaci, Barbara Tomasello, Lorenzo Torrisi, Antonella Tramontana, and Andriy Velyhan (2013). "ELIMED, future hadrontherapy applications of laser-accelerated beams". In: *Nuclear Instruments and Methods in Physics Research Section A: Accelerators, Spectrometers, Detectors and Associated Equipment*. Proceedings of the 9th International Conference on Radiation Effects on Semiconductor Materials Detectors and Devices October 9-12 2012 Dipartimento di Fisica e Astronomia - Sezione di Astronomia e Scienza dello Spazio - Largo Enrico Fermi, 2, 50125 Firenze Organized by : Università degli Studi di Firenze with the support of Istituto Nazionale di Fisica Nucleare 730, pp. 174–177. ISSN: 0168-9002. DOI: 10.1016/j.nima.2013.05.051 (cit. on p. 83).

Clark, E. L., K. Krushelnick, M. Zepf, F. N. Beg, M. Tatarakis, A. Machacek, M. I. K. Santala, I. Watts, P. A. Norreys, and A. E. Dangor (2000a). "Energetic Heavy-Ion and Proton Generation from Ultraintense Laser-Plasma Interactions with Solids". In: *Physical Review Letters* 85.8, pp. 1654–1657. DOI: 10.1103/PhysRevLett.85.1654 (cit. on p. 20).

Clark, E. L., K. Krushelnick, J. R. Davies, M. Zepf, M. Tatarakis, F. N. Beg, A. Machacek, P. A. Norreys, M. I. K. Santala, I. Watts, and A. E. Dangor (2000b). "Measurements of Energetic Proton Transport through Magnetized Plasma from Intense Laser Interactions with Solids".

In: *Physical Review Letters* 84.4, pp. 670–673. DOI: 10.1103/PhysRevLett.84.670 (cit. on p. 20).

Cohen, Robert S., Lyman Spitzer, and Paul McR. Routly (1950). "The Electrical Conductivity of an Ionized Gas". In: *Physical Review* 80.2, pp. 230–238. DOI: 10.1103/PhysRev.80.230 (cit. on p. 18).

Cormack, A. M. and A. M. Koehler (1976). "Quantitative proton tomography: preliminary experiments". In: *Physics in Medicine and Biology* 21.4, p. 560. ISSN: 0031-9155. DOI: 10.1088/0031-9155/21/4/007 (cit. on p. 28).

Cowan, T. E., J. Fuchs, H. Ruhl, A. Kemp, P. Audebert, M. Roth, R. Stephens, I. Barton, A. Blazevic, E. Brambrink, J. Cobble, J. Fernández, J.-C. Gauthier, M. Geissel, M. Hegelich, J. Kaae, S. Karsch, G. P. Le Sage, S. Letzring, M. Manclossi, S. Meyroneinc, A. Newkirk, H. Pépin, and N. Renard-LeGalloudec (2004). "Ultralow Emittance, Multi-MeV Proton Beams from a Laser Virtual-Cathode Plasma Accelerator". In: *Physical Review Letters* 92.20, p. 204801. DOI: 10.1103/PhysRevLett.92.204801 (cit. on p. 28).

Cox, James D. and Kie Kian Ang (2009). *Radiation Oncology: Rationale, Technique, Results*. Elsevier Health Sciences. ISBN: 978-0-323-07660-9 (cit. on p. 30).

Denavit, J. (1992). "Absorption of high-intensity subpicosecond lasers on solid density targets". In: *Physical Review Letters* 69.21, pp. 3052–3055. DOI: 10.1103/PhysRevLett.69.3052 (cit. on p. 25).

Dendy, R. O. (1995). *Plasma Physics: An Introductory Course*. Cambridge University Press. ISBN: 978-0-521-48452-7 (cit. on p. 18).

d'Humières, Emmanuel (2012). *Ion Acceleration by High Intensity Short Pulse Lasers*. InTech. ISBN: 978-953-51-0796-5 (cit. on p. 20).

d'Humières, Emmanuel, Erik Lefebvre, Laurent Gremillet, and Victor Malka (2005). "Proton acceleration mechanisms in high-intensity laser interaction with thin foils". In: *Physics of Plasmas (1994-present)* 12.6, p. 062704. ISSN: 1070-664X, 1089-7674. DOI: 10.1063/1.1927097 (cit. on p. 20).

Ditmire, T., J. W. G. Tisch, E. Springate, M. B. Mason, N. Hay, R. A. Smith, J. Marangos, and M. H. R. Hutchinson (1997). "High-energy ions produced in explosions of superheated atomic clusters". In: *Nature* 386.6620, pp. 54–56. DOI: 10.1038/386054a0 (cit. on p. 20).

Doria, D., K. F. Kakolee, S. Kar, S. K. Litt, F. Fiorini, H. Ahmed, S. Green, J. C. G. Jeynes, J. Kavanagh, D. Kirby, K. J. Kirkby, C. L. Lewis, M. J. Merchant, G. Nersisyan, R. Prasad, K. M. Prise, G. Schettino, M. Zepf, and M. Borghesi (2012). "Biological effectiveness on live cells of laser driven protons at dose rates exceeding 109 Gy/s". In: *AIP Advances* 2.1, p. 011209. ISSN: 2158-3226. DOI: 10.1063/1.3699063 (cit. on pp. 116, 128).

Dromey, B., M. Coughlan, L. Senje, M. Taylor, S. Kuschel, B. Villagomez-Bernabe, R. Stefanuik, G. Nersisyan, L. Stella, J. Kohanoff, M. Borghesi, F. Currell, D. Riley, D. Jung, C.-G. Wahlström, C. L. S. Lewis, and M. Zepf (2016). "Picosecond metrology of laser-driven proton bursts". In: *Nature Communications* 7, p. 10642. DOI: 10.1038/ncomms10642 (cit. on p. 118).

Durrani, Saeed A. and Richard K. Bull (1987). *Solid State Nuclear Track Detection: Principles, Methods, and Applications*. Pergramon Press. ISBN: 978-0-08-020605-9 (cit. on p. 57).

Einstein, A. (1916). "Die Grundlage der allgemeinen Relativitätstheorie". In: *Annalen der Physik* 354, pp. 769–822. ISSN: 0003-3804. DOI: 10.1002/andp.19163540702 (cit. on p. 10).

Elkind, M. M. and Harriet Sutton (1959). "X-Ray Damage and Recovery in Mammalian Cells in Culture". In: *Nature* 184.4695, pp. 1293–1295. ISSN: 0028-0836. DOI: 10.1038/1841293a0 (cit. on p. 41).

Esirkepov, T., M. Borghesi, S. V. Bulanov, G. Mourou, and T. Tajima (2004). "Highly Efficient Relativistic-Ion Generation in the Laser-Piston Regime". In: *Physical Review Letters* 92.17, p. 175003. DOI: 10.1103/PhysRevLett.92.175003 (cit. on p. 25).

Esirkepov, T., M. Yamagiwa, and T. Tajima (2006). "Laser Ion-Acceleration Scaling Laws Seen in Multiparametric Particle-in-Cell Simulations". In: *Physical Review Letters* 96.10, p. 105001. DOI: 10.1103/PhysRevLett.96.105001 (cit. on pp. 23, 26).

Esirkepov, T. Zh, Y. Sentoku, K. Mima, K. Nishihara, F. Califano, F. Pegoraro, N. M. Naumova, S. V. Bulanov, Y. Ueshima, T. V. Liseikina, V. A. Vshivkov, and Y. Kato (1999). "Ion acceleration by superintense laser pulses in plasmas". In: *Journal of Experimental and Theoretical Physics Letters* 70.2, pp. 82–89. ISSN: 0021-3640, 1090-6487. DOI: 10.1134/1.568134 (cit. on p. 20).

Esirkepov, Timur Zh., James K. Koga, Atsushi Sunahara, Toshimasa Morita, Masaharu Nishikino, Kei Kageyama, Hideo Nagatomo, Katsunobu Nishihara, Akito Sagisaka, Hideyuki Kotaki, Tatsufumi Nakamura, Yuji Fukuda, Hajime Okada, Alexander S. Pirozhkov, Akifumi Yogo, Mamiko Nishiuchi, Hiromitsu Kiriyama, Kiminori Kondo, Masaki Kando, and Sergei V. Bulanov (2014). "Prepulse and amplified spontaneous emission effects on the interaction of a petawatt class laser with thin solid targets". In: *Nuclear Instruments and Methods in Physics Research Section A: Accelerators, Spectrometers, Detectors and Associated Equipment* 745, pp. 150–163. ISSN: 0168-9002. DOI: 10.1016/j.nima.2014.01.056 (cit. on p. 23).

Fedosejevs, R., I. V. Tomov, N. H. Burnett, G. D. Enright, and M. C. Richardson (1977). "Self-Steepening of the Density Profile of a CO2-Laser-Produced Plasma". In: *Physical Review Letters* 39.15, pp. 932–935. DOI: 10.1103/PhysRevLett.39.932 (cit. on p. 17).

Fernet, M., V. Ponette, E. Deniaud-Alexandre, J. Ménissier-De Murcia, G. De Murcia, N. Giocanti, F. Megnin-Chanet, and V. Favaudon (2000). "Poly(ADP-ribose) polymerase, a major determinant of early cell response to ionizing radiation". In: *International Journal of Radiation Biology* 76.12, pp. 1621–1629. ISSN: 0955-3002. DOI: 10.1080/09553000050201118 (cit. on p. 128).

Fernández-Varea, J. M., P. Andreo, and T. Tabata (1996). "Detour factors in water and plastic phantoms and their use for range and depth scaling in electron-beam dosimetry". In: *Physics in Medicine and Biology* 41.7, p. 1119. ISSN: 0031-9155. DOI: 10.1088/0031-9155/41/7/004 (cit. on p. 33).

Fews, A. P., P. A. Norreys, F. N. Beg, A. R. Bell, A. E. Dangor, C. N. Danson, P. Lee, and S. J. Rose (1994). "Plasma Ion Emission from High Intensity Picosecond Laser Pulse Interactions with Solid Targets". In: *Physical Review Letters* 73.13, pp. 1801–1804. DOI: 10.1103/PhysRevLett.73.1801 (cit. on p. 20).

Fiuza, F., A. Stockem, E. Boella, R. A. Fonseca, L. O. Silva, D. Haberberger, S. Tochitsky, C. Gong, W. B. Mori, and C. Joshi (2012). "Laser-Driven Shock Acceleration of Monoenergetic Ion Beams". In: *Physical Review Letters* 109.21, p. 215001. DOI: 10.1103/PhysRevLett.109.215001 (cit. on p. 25).

Flacco, A., F. Sylla, M. Veltcheva, M. Carrié, R. Nuter, E. Lefebvre, D. Batani, and V. Malka (2010). "Dependence on pulse duration and foil thickness in high-contrast-laser proton acceleration". In: *Physical Review E* 81.3, p. 036405. DOI: 10.1103/PhysRevE.81.036405 (cit. on p. 23).

Flacco, Alessandro (2008). "Experimental Study of Proton Acceleration with Ultra-High Intensity, High Contrast Laser Beam". PhD thesis. Ecole Polytechnique X (cit. on p. 21).

Fleischer, R. L., P. B. Price, and R. M. Walker (1965). "Ion Explosion Spike Mechanism for Formation of Charged-Particle Tracks in Solids". In: *Journal of Applied Physics* 36.11, pp. 3645–3652. ISSN: 0021-8979, 1089-7550. DOI: 10.1063/1.1703059 (cit. on p. 57).

Fourkal, E., J. S. Li, M. Ding, T. Tajima, and C.-M. Ma (2003). "Particle selection for laser-accelerated proton therapy feasibility study". In: *Medical Physics* 30.7, pp. 1660–1670. ISSN: 0094-2405. DOI: 10.1118/1.1586268 (cit. on pp. 81, 83).

Fourkal, E., I. Velchev, C.-M. Ma, and J. Fan (2011). "Linear energy transfer of proton clusters". In: *Physics in Medicine and Biology* 56.10, p. 3123. ISSN: 0031-9155. DOI: 10.1088/0031-9155/56/10/015 (cit. on p. 134).

Franklin, M., A. Fry, K. K. Gan, S. Han, H. Kagan, S. Kanda, D. Kania, R. Kass, S. K. Kim, R. Malchow, F. Morrow, S. Olsen, W. F. Palmer, L. S. Pan, F. Sannes, S. Schnetzer, R. Stone, Y.

Sugimoto, G. B. Thomson, C. White, and S. Zhao (1992). "Development of diamond radiation detectors for SSC and LHC". In: *Nuclear Instruments and Methods in Physics Research Section A: Accelerators, Spectrometers, Detectors and Associated Equipment* 315.1, pp. 39–42. ISSN: 0168-9002. DOI: 10.1016/0168-9002(92)90677-V (cit. on p. 69).

Freidberg, J. P., R. W. Mitchell, R. L. Morse, and L. I. Rudsinski (1972). "Resonant Absorption of Laser Light by Plasma Targets". In: *Physical Review Letters* 28.13, pp. 795–799. DOI: 10.1103/PhysRevLett.28.795 (cit. on p. 18).

Fritzler, S., V. Malka, G. Grillon, J. P. Rousseau, F. Burgy, E. Lefebvre, E. d'Humières, P. McKenna, and K. W. D. Ledingham (2003). "Proton beams generated with high-intensity lasers: Applications to medical isotope production". In: *Applied Physics Letters* 83.15, pp. 3039–3041. ISSN: 0003-6951, 1077-3118. DOI: 10.1063/1.1616661 (cit. on p. 28).

Fuchs, J., Y. Sentoku, S. Karsch, J. Cobble, P. Audebert, A. Kemp, A. Nikroo, P. Antici, E. Brambrink, A. Blazevic, E. M. Campbell, J. C. Fernández, J.-C. Gauthier, M. Geissel, M. Hegelich, H. Pépin, H. Popescu, N. Renard-LeGalloudec, M. Roth, J. Schreiber, R. Stephens, and T. E. Cowan (2005). "Comparison of Laser Ion Acceleration from the Front and Rear Surfaces of Thin Foils". In: *Physical Review Letters* 94.4, p. 045004. DOI: 10.1103/PhysRevLett.94.045004 (cit. on p. 25).

Fuchs, J., P. Antici, E. d'Humières, E. Lefebvre, M. Borghesi, E. Brambrink, C. A. Cecchetti, M. Kaluza, V. Malka, M. Manclossi, S. Meyroneinc, P. Mora, J. Schreiber, T. Toncian, H. Pépin, and P. Audebert (2006). "Laser-driven proton scaling laws and new paths towards energy increase". In: *Nature Physics* 2.1, pp. 48–54. ISSN: 1745-2473. DOI: 10.1038/nphys199 (cit. on p. 23).

Fujioka, Shinsuke, Zhe Zhang, Kazuhiro Ishihara, Keisuke Shigemori, Youichiro Hironaka, Tomoyuki Johzaki, Atsushi Sunahara, Naoji Yamamoto, Hideki Nakashima, Tsuguhiro Watanabe, Hiroyuki Shiraga, Hiroaki Nishimura, and Hiroshi Azechi (2013). "Kilotesla Magnetic Field due to a Capacitor-Coil Target Driven by High Power Laser". In: *Scientific Reports* 3. ISSN: 2045-2322. DOI: 10.1038/srep01170 (cit. on p. 78).

Gaillard, S. A., T. Kluge, K. A. Flippo, M. Bussmann, B. Gall, T. Lockard, M. Geissel, D. T. Offermann, M. Schollmeier, Y. Sentoku, and T. E. Cowan (2011). "Increased laser-accelerated proton energies via direct laser-light-pressure acceleration of electrons in microcone targetsa)". In: *Physics of Plasmas (1994-present)* 18.5, p. 056710. ISSN: 1070-664X, 1089-7674. DOI: 10.1063/1.3575624 (cit. on p. 23).

Gibbon, Paul (2005). *Short Pulse Laser Interactions with Matter: An Introduction*. Imperial College Press. ISBN: 978-1-86094-135-1 (cit. on pp. 15, 17).

Haberberger, Dan, Sergei Tochitsky, Frederico Fiuza, Chao Gong, Ricardo A. Fonseca, Luis O. Silva, Warren B. Mori, and Chan Joshi (2012). "Collisionless shocks in laser-produced plasma generate monoenergetic high-energy proton beams". In: *Nature Physics* 8.1, pp. 95–99. ISSN: 1745-2473. DOI: 10.1038/nphys2130 (cit. on p. 25).

Hall, Eric J. and Amato J. Giaccia (2012). *Radiobiology for the Radiologist*. Wolters Kluwer Health. ISBN: 978-1-4511-5418-4 (cit. on pp. 32, 37, 39).

Hannachi, F., M. M. Aléonard, M. Gerbaux, F. Gobet, G. Malka, C. Plaisir, J. N. Scheurer, M. Tarisien, P. Audebert, E Brambrink, V. Méot, P. Morel, Ph Nicolaï, and V. Tikhonchuk (2007). "Prospects for nuclear physics with lasers". In: *Plasma Physics and Controlled Fusion* 49.12B, B79. ISSN: 0741-3335. DOI: 10.1088/0741-3335/49/12B/S06 (cit. on p. 28).

Harres, K., M. Schollmeier, E. Brambrink, P. Audebert, A. Blažević, K. Flippo, D. C. Gautier, M. Geißel, B. M. Hegelich, F. Nürnberg, J. Schreiber, H. Wahl, and M. Roth (2008). "Development and calibration of a Thomson parabola with microchannel plate for the detection of laser-accelerated MeV ions". In: *Review of Scientific Instruments* 79.9, p. 093306. ISSN: 0034-6748, 1089-7623. DOI: 10.1063/1.2987687 (cit. on pp. 54, 57).

Harres, K., I. Alber, A. Tauschwitz, V. Bagnoud, H. Daido, M. Günther, F. Nürnberg, A. Otten, M. Schollmeier, J. Schütrumpf, M. Tampo, and M. Roth (2010). "Beam collimation and transport of quasineutral laser-accelerated protons by a solenoid field". In: *Physics of Plasmas (1994-present)* 17.2, p. 023107. ISSN: 1070-664X, 1089-7674. DOI: 10.1063/1.3299391 (cit. on p. 78).

Hatchett, Stephen P., Curtis G. Brown, Thomas E. Cowan, Eugene A. Henry, Joy S. Johnson, Michael H. Key, Jeffrey A. Koch, A. Bruce Langdon, Barbara F. Lasinski, Richard W. Lee, Andrew J. Mackinnon, Deanna M. Pennington, Michael D. Perry, Thomas W. Phillips, Markus Roth, T. Craig Sangster, Mike S. Singh, Richard A. Snavely, Mark A. Stoyer, Scott C. Wilks, and Kazuhito Yasuike (2000). "Electron, photon, and ion beams from the relativistic interaction of Petawatt laser pulses with solid targets". In: *Physics of Plasmas (1994-present)* 7.5, pp. 2076–2082. ISSN: 1070-664X, 1089-7674. DOI: 10.1063/1.874030 (cit. on p. 20).

Hegelich, B. M., B. Albright, P. Audebert, A. Blazevic, E. Brambrink, J. Cobble, T. Cowan, J. Fuchs, J. C. Gauthier, C. Gautier, M. Geissel, D. Habs, R. Johnson, S. Karsch, A. Kemp, S. Letzring, M. Roth, U. Schramm, J. Schreiber, K. J. Witte, and J. C. Fernández (2005). "Spectral properties of laser-accelerated mid-ZMeV/u ion beams". In: *Physics of Plasmas (1994-present)* 12.5, p. 056314. ISSN: 1070-664X, 1089-7674. DOI: 10.1063/1.1915350 (cit. on p. 22).

Hegelich, B. M., B. J. Albright, J. Cobble, K. Flippo, S. Letzring, M. Paffett, H. Ruhl, J. Schreiber, R. K. Schulze, and J. C. Fernández (2006). "Laser acceleration of quasi-monoenergetic MeV ion beams". In: *Nature* 439.7075, pp. 441–444. ISSN: 0028-0836. DOI: 10.1038/nature04400 (cit. on p. 23).

Hegelich, B. M., D. Jung, B. J. Albright, J. C. Fernandez, D. C. Gautier, C. Huang, T. J. Kwan, S. Letzring, S. Palaniyappan, R. C. Shah, H.-C. Wu, L. Yin, A. Henig, R. Hörlein, D. Kiefer, J. Schreiber, X. Q. Yan, T. Tajima, D. Habs, B. Dromey, and J. J. Honrubia (2011). "Experimental demonstration of particle energy, conversion efficiency and spectral shape required for ion-based fast ignition". In: *Nuclear Fusion* 51.8, p. 083011. ISSN: 0029-5515. DOI: 10.1088/0029-5515/51/8/083011 (cit. on p. 27).

Hegelich, Björn Manuel (2002). "Acceleration of heavy Ions to MeV/nucleon Energies by Ultrahigh-Intensity Lasers". Text.PhDThesis. Ludwig-Maximilians-Universität München (cit. on p. 22).

Hegelich, M., S. Karsch, G. Pretzler, D. Habs, K. Witte, W. Guenther, M. Allen, A. Blazevic, J. Fuchs, J. C. Gauthier, M. Geissel, P. Audebert, T. Cowan, and M. Roth (2002). "MeV Ion Jets from Short-Pulse-Laser Interaction with Thin Foils". In: *Physical Review Letters* 89.8, p. 085002. DOI: 10.1103/PhysRevLett.89.085002 (cit. on p. 22).

Henig, A., D. Kiefer, K. Markey, D. C. Gautier, K. A. Flippo, S. Letzring, R. P. Johnson, T. Shimada, L. Yin, B. J. Albright, K. J. Bowers, J. C. Fernández, S. G. Rykovanov, H.-C. Wu, M. Zepf, D. Jung, V. Kh. Liechtenstein, J. Schreiber, D. Habs, and B. M. Hegelich (2009a). "Enhanced Laser-Driven Ion Acceleration in the Relativistic Transparency Regime". In: *Physical Review Letters* 103.4, p. 045002. DOI: 10.1103/PhysRevLett.103.045002 (cit. on p. 28).

Henig, A., D. Kiefer, M. Geissler, S. G. Rykovanov, R. Ramis, R. Hörlein, J. Osterhoff, Zs. Major, L. Veisz, S. Karsch, F. Krausz, D. Habs, and J. Schreiber (2009b). "Laser-Driven Shock Acceleration of Ion Beams from Spherical Mass-Limited Targets". In: *Physical Review Letters* 102.9, p. 095002. DOI: 10.1103/PhysRevLett.102.095002 (cit. on p. 25).

Henig, A., S. Steinke, M. Schnürer, T. Sokollik, R. Hörlein, D. Kiefer, D. Jung, J. Schreiber, B. M. Hegelich, X. Q. Yan, J. Meyer-ter-Vehn, T. Tajima, P. V. Nickles, W. Sandner, and D. Habs (2009c). "Radiation-Pressure Acceleration of Ion Beams Driven by Circularly Polarized Laser Pulses". In: *Physical Review Letters* 103.24, p. 245003. DOI: 10.1103/PhysRevLett.103.245003 (cit. on p. 25).

Henshaw, D. L. (1982). "Applications of CR-39 nuclear track detector in medicine and technology". In: *Physics in Technology* 13.6, p. 266. ISSN: 0305-4624. DOI: 10.1088/0305-4624/13/

6/I02 (cit. on p. 57).

Hofmann, Ingo (2013). "Performance of solenoids versus quadrupoles in focusing and energy selection of laser accelerated protons". In: *Physical Review Special Topics - Accelerators and Beams* 16.4, p. 041302. DOI: 10.1103/PhysRevSTAB.16.041302 (cit. on p. 77).

Hong, Wan, Hyung-Joo Woo, Han-Woo Choi, Young-Suk Kim, and Gi-dong Kim (2001). "Optical property modification of PMMA by ion-beam implantation". In: *Applied Surface Science* 169–170, pp. 428–432. ISSN: 0169-4332. DOI: 10.1016/S0169-4332(00)00698-X (cit. on p. 28).

IAEA (2010). *Radiation Biology: A Handbook for Teachers and Students*. Training Course Series No. 42 (cit. on p. 36).

Joiner, M. C. and H. Johns (1987). "Renal Damage in the Mouse: The Effect of d(4)-Be Neutrons". In: *Radiation Research* 109.3, pp. 456–468. ISSN: 0033-7587. DOI: 10.2307/3577046 (cit. on p. 41).

Jullien, A., O. Albert, G. Chériaux, J. Etchepare, S. Kourtev, N. Minkovski, and S. M. Saltiel (2006). "Two crystal arrangement to fight efficiency saturation in cross-polarized wave generation". In: *Optics Express* 14.7, pp. 2760–2769. ISSN: 1094-4087. DOI: 10.1364/OE.14.002760 (cit. on p. 50).

Jullien, A., L. Canova, O. Albert, D. Boschetto, L. Antonucci, Y.-H. Cha, J. P. Rousseau, P. Chaudet, G. Chériaux, J. Etchepare, S. Kourtev, N. Minkovski, and S. M. Saltiel (2007). "Spectral broadening and pulse duration reduction during cross-polarized wave generation: influence of the quadratic spectral phase". In: *Applied Physics B* 87.4, pp. 595–601. ISSN: 0946-2171, 1432-0649. DOI: 10.1007/s00340-007-2685-8 (cit. on p. 50).

Jullien, Aurélie, Olivier Albert, Frédéric Burgy, Guy Hamoniaux, Jean-Philippe Rousseau, Jean-Paul Chambaret, Frédérika Augé-Rochereau, Gilles Chériaux, Jean Etchepare, Nikolay Minkovski, and Solomon M. Saltiel (2005). "10^-10 temporal contrast for femtosecond ultraintense lasers by cross-polarized wave generation". In: *Optics Letters* 30.8, pp. 920–922. ISSN: 0146-9592, 1539-4794. DOI: 10.1364/OL.30.000920 (cit. on p. 50).

Jung, D., R. Hörlein, D. Kiefer, S. Letzring, D. C. Gautier, U. Schramm, C. Hübsch, R. Öhm, B. J. Albright, J. C. Fernandez, D. Habs, and B. M. Hegelich (2011). "Development of a high resolution and high dispersion Thomson parabola". In: *Review of Scientific Instruments* 82.1, p. 013306. ISSN: 0034-6748, 1089-7623. DOI: 10.1063/1.3523428 (cit. on p. 55).

Jung, Daniel (2012). "Ion acceleration from relativistic laser nano-target interaction". Text.PhDThesis. LMU Munich Germany: Ludwig-Maximilians-Universität München (cit. on p. 27).

Kaluza, M., J. Schreiber, M. I. K. Santala, G. D. Tsakiris, K. Eidmann, J. Meyer-ter-Vehn, and K. J. Witte (2004). "Influence of the Laser Prepulse on Proton Acceleration in Thin-Foil Experiments". In: *Physical Review Letters* 93.4, p. 045003. DOI: 10.1103/PhysRevLett.93.045003 (cit. on p. 49).

Kar, S., K. F. Kakolee, B. Qiao, A. Macchi, M. Cerchez, D. Doria, M. Geissler, P. McKenna, D. Neely, J. Osterholz, R. Prasad, K. Quinn, B. Ramakrishna, G. Sarri, O. Willi, X. Y. Yuan, M. Zepf, and M. Borghesi (2012). "Ion Acceleration in Multispecies Targets Driven by Intense Laser Radiation Pressure". In: *Physical Review Letters* 109.18, p. 185006. DOI: 10.1103/PhysRevLett.109.185006 (cit. on p. 25).

Kar, Satyabrata, Hamad Ahmed, Rajendra Prasad, Mirela Cerchez, Stephanie Brauckmann, Bastian Aurand, Giada Cantono, Prokopis Hadjisolomou, Ciaran L. S. Lewis, Andrea Macchi, Gagik Nersisyan, Alexander P. L. Robinson, Anna M. Schroer, Marco Swantusch, Matt Zepf, Oswald Willi, and Marco Borghesi (2016). "Guided post-acceleration of laser-driven ions by a miniature modular structure". In: *Nature Communications* 7, p. 10792. ISSN: 2041-1723. DOI: 10.1038/ncomms10792 (cit. on pp. 78, 79).

Karsch, S., S. Düsterer, H. Schwoerer, F. Ewald, D. Habs, M. Hegelich, G. Pretzler, A. Pukhov, K. Witte, and R. Sauerbrey (2003). "High-Intensity Laser Induced Ion Acceleration from Heavy-Water Droplets". In: *Physical Review Letters* 91.1, p. 015001. DOI: 10.1103/PhysRevLett.91.015001 (cit. on p. 20).

Key, M. H., M. D. Cable, T. E. Cowan, K. G. Estabrook, B. A. Hammel, S. P. Hatchett, E. A. Henry, D. E. Hinkel, J. D. Kilkenny, J. A. Koch, et al. (1998). "Hot electron production and heating by hot electrons in fast ignitor research". In: *Physics of Plasmas (1994-present)* 5.5, pp. 1966–1972. ISSN: 1070-664X, 1089-7674. DOI: 10.1063/1.872867 (cit. on p. 19).

Khaitan, Divya, Sudhir Chandna, MB Arya, and BS Dwarakanath (2006). "Establishment and characterization of multicellular spheroids from a human glioma cell line; Implications for tumor therapy". In: *Journal of Translational Medicine* 4, p. 12. ISSN: 1479-5876. DOI: 10.1186/1479-5876-4-12 (cit. on p. 130).

Kim, I Jong, Ki Hong Pae, Chul Min Kim, Hyung Taek Kim, Jae Hee Sung, Seong Ku Lee, Tae Jun Yu, Il Woo Choi, Chang-Lyoul Lee, Kee Hwan Nam, Peter V. Nickles, Tae Moon Jeong, and Jongmin Lee (2013). "Transition of Proton Energy Scaling Using an Ultrathin Target Irradiated by Linearly Polarized Femtosecond Laser Pulses". In: *Physical Review Letters* 111.16, p. 165003. DOI: 10.1103/PhysRevLett.111.165003 (cit. on p. 23).

Kim, I. Jong, Ki Hong Pae, Il Woo Choi, Chang-Lyoul Lee, Hyung Taek Kim, Himanshu Singhal, Jae Hee Sung, Seong Ku Lee, Hwang Woon Lee, Peter V. Nickles, Tae Moon Jeong, Chul Min Kim, and Chang Hee Nam (2016). "Radiation pressure acceleration of protons to 93 MeV with circularly polarized petawatt laser pulses". In: *Physics of Plasmas (1994-present)* 23.7, p. 070701. ISSN: 1070-664X, 1089-7674. DOI: 10.1063/1.4958654 (cit. on p. 23).

Klassen, Norman V., Len van der Zwan, and Joanna Cygler (1997). "GafChromic MD-55: Investigated as a precision dosimeter". In: *Medical Physics* 24.12, pp. 1924–1934. ISSN: 0094-2405. DOI: 10.1118/1.598106 (cit. on p. 58).

Klimo, O., J. Psikal, J. Limpouch, and V. T. Tikhonchuk (2008). "Monoenergetic ion beams from ultrathin foils irradiated by ultrahigh-contrast circularly polarized laser pulses". In: *Physical Review Special Topics - Accelerators and Beams* 11.3, p. 031301. DOI: 10.1103/PhysRevSTAB.11.031301 (cit. on p. 25).

Klug, J. N., J. Lutz, and J. B. Meijer (2011). "N-type doping of silicon by proton implantation". In: *Proceedings of the 2011-14th European Conference on Power Electronics and Applications (EPE 2011)*, pp. 1–7 (cit. on p. 28).

Kodama, R., K. Takahashi, K. A. Tanaka, M. Tsukamoto, H. Hashimoto, Y. Kato, and K. Mima (1996). "Study of Laser-Hole Boring into Overdense Plasmas". In: *Physical Review Letters* 77.24, pp. 4906–4909. DOI: 10.1103/PhysRevLett.77.4906 (cit. on p. 17).

Koenig, M., A. Benuzzi-Mounaix, A. Ravasio, T. Vinci, N. Ozaki, S. Lepape, D. Batani, G. Huser, T. Hall, D. Hicks, A MacKinnon, P. Patel, H. S. Park, T. Boehly, M. Borghesi, S. Kar, and L. Romagnani (2005). "Progress in the study of warm dense matter". In: *Plasma Physics and Controlled Fusion* 47.12B, B441. ISSN: 0741-3335. DOI: 10.1088/0741-3335/47/12B/S31 (cit. on p. 28).

Kraft, S. D., C. Richter, K. Zeil, M. Baumann, E. Beyreuther, S. Bock, M. Bussmann, T. E. Cowan, Y. Dammene, W. Enghardt, U. Helbig, L. Karsch, T. Kluge, L. Laschinsky, E. Lessmann, J. Metzkes, D. Naumburger, R. Sauerbrey, M. Schürer, M. Sobiella, J. Woithe, U. Schramm, and J. Pawelke (2010). "Dose-dependent biological damage of tumour cells by laser-accelerated proton beams". In: *New Journal of Physics* 12.8, p. 085003. ISSN: 1367-2630. DOI: 10.1088/1367-2630/12/8/085003 (cit. on p. 8).

Kruer, W. L. and Kent Estabrook (1985). "J×B heating by very intense laser light". In: *Physics of Fluids* 28.1, pp. 430–432. ISSN: 0031-9171. DOI: 10.1063/1.865171 (cit. on p. 18).

Kruer, William L. (2003). *The Physics of Laser Plasma Interactions*. First. Westview Press. ISBN: 978-0-8133-4083-8 (cit. on p. 17).

Krushelnick, K., E. L. Clark, Z. Najmudin, M. Salvati, M. I. K. Santala, M. Tatarakis, A. E. Dangor, V. Malka, D. Neely, R. Allott, and C. Danson (1999). "Multi-MeV Ion Production from High-Intensity Laser Interactions with Underdense Plasmas". In: *Physical Review Letters* 83.4, pp. 737–740. DOI: 10.1103/PhysRevLett.83.737 (cit. on p. 20).

Krushelnick, K., E. L. Clark, R. Allott, F. N. Beg, C. N. Danson, A. Machacek, V. Malka, Z. Najmudin, D. Neely, P. A. Norreys, M. R. Salvati, M. I. K. Santala, M. Tatarakis, I. Watts, M. Zepf, and A. E. Dangor (2000). "Ultrahigh-intensity laser-produced plasmas as a compact heavy ion injection source". In: *IEEE Transactions on Plasma Science* 28.4, pp. 1110–1155. ISSN: 0093-3813. DOI: 10.1109/27.893296 (cit. on p. 28).

Kumar, Vinit (2009). "Understanding the focusing of charged particle beams in a solenoid magnetic field". In: *American Journal of Physics* 77.8, pp. 737–741. ISSN: 0002-9505, 1943-2909. DOI: 10.1119/1.3129242 (cit. on p. 77).

Ledingham, K. W. D., P. McKenna, T. McCanny, S. Shimizu, J. M. Yang, L. Robson, J. Zweit, J. M. Gillies, J. Bailey, G. N. Chimon, R. J. Clarke, D. Neely, P. A. Norreys, J. L. Collier, R. P. Singhal, M. S. Wei, S. P. D. Mangles, P. Nilson, K Krushelnick, and M. Zepf (2004). "High power laser production of short-lived isotopes for positron emission tomography". In: *Journal of Physics D: Applied Physics* 37.16, p. 2341. ISSN: 0022-3727. DOI: 10.1088/0022-3727/37/16/019 (cit. on p. 28).

Ledingham, Ken W. D., Paul R. Bolton, Naoya Shikazono, and C.-M. Charlie Ma (2014). "Towards Laser Driven Hadron Cancer Radiotherapy: A Review of Progress". In: *Applied Sciences* 4.3, pp. 402–443. DOI: 10.3390/app4030402 (cit. on p. 7).

Lezius, M., S. Dobosz, D. Normand, and M. Schmidt (1998). "Explosion Dynamics of Rare Gas Clusters in Strong Laser Fields". In: *Physical Review Letters* 80.2, pp. 261–264. DOI: 10.1103/PhysRevLett.80.261 (cit. on p. 20).

Li, C. K., F. H. Séguin, J. A. Frenje, R. D. Petrasso, P. A. Amendt, R. P. J. Town, O. L. Landen, J. R. Rygg, R. Betti, J. P. Knauer, D. D. Meyerhofer, J. M. Soures, C. A. Back, J. D. Kilkenny, and A. Nikroo (2009). "Observations of Electromagnetic Fields and Plasma Flow in Hohlraums with Proton Radiography". In: *Physical Review Letters* 102.20, p. 205001. DOI: 10.1103/PhysRevLett.102.205001 (cit. on p. 28).

Lim, J. K., P. Frigola, G. Travish, J. B. Rosenzweig, S. G. Anderson, W. J. Brown, J. S. Jacob, C. L. Robbins, and A. M. Tremaine (2005). "Adjustable, short focal length permanent-magnet quadrupole based electron beam final focus system". In: *Physical Review Special Topics - Accelerators and Beams* 8.7, p. 072401. DOI: 10.1103/PhysRevSTAB.8.072401 (cit. on p. 75).

Lindau, F., O. Lundh, A. Persson, P. McKenna, K. Osvay, D. Batani, and C.-G. Wahlström (2005). "Laser-Accelerated Protons with Energy-Dependent Beam Direction". In: *Physical Review Letters* 95.17, p. 175002. DOI: 10.1103/PhysRevLett.95.175002 (cit. on p. 59).

Luo, Wei, Eugene Fourkal, Jinsheng Li, and Chang-Ming Ma (2005). "Particle selection and beam collimation system for laser-accelerated proton beam therapy". In: *Medical Physics* 32.3, pp. 794–806. ISSN: 0094-2405. DOI: 10.1118/1.1861772 (cit. on p. 81).

Luther-Davies, B. and J. L. Hughes (1976). "Observations of MeV ions emitted from a laser produced plasma". In: *Optics Communications* 18.3, pp. 351–353 (cit. on p. 20).

Macchi, Andrea and Carlo Benedetti (2010). "Ion acceleration by radiation pressure in thin and thick targets". In: *Nuclear Instruments and Methods in Physics Research Section A: Accelerators, Spectrometers, Detectors and Associated Equipment*. COULOMB09Ions Acceleration with high Power Lasers: Physics and Applications 620.1, pp. 41–45. ISSN: 0168-9002. DOI: 10.1016/j.nima.2010.01.057 (cit. on p. 26).

Macchi, Andrea, Federica Cattani, Tatiana V. Liseykina, and Fulvio Cornolti (2005). "Laser Acceleration of Ion Bunches at the Front Surface of Overdense Plasmas". In: *Physical Review Letters* 94.16, p. 165003. DOI: 10.1103/PhysRevLett.94.165003 (cit. on p. 25).

Macchi, Andrea, Silvia Veghini, and Francesco Pegoraro (2009). “"Light Sail” Acceleration Reexamined”. In: *Physical Review Letters* 103.8, p. 085003. DOI: 10.1103/PhysRevLett.103.085003 (cit. on p. 26).

Macchi, Andrea, Silvia Veghini, Tatyana V. Liseykina, and Francesco Pegoraro (2010). “Radiation pressure acceleration of ultrathin foils”. In: *New Journal of Physics* 12.4, p. 045013. ISSN: 1367-2630. DOI: 10.1088/1367-2630/12/4/045013 (cit. on p. 26).

Macchi, Andrea, Marco Borghesi, and Matteo Passoni (2013). “Ion acceleration by superintense laser-plasma interaction”. In: *Reviews of Modern Physics* 85.2, pp. 751–793. DOI: 10.1103/RevModPhys.85.751 (cit. on p. 20).

Maggiore, M., G. a. P. Cirrone, M. Carpinelli, G. Cuttone, F. Romano, F. Schillaci, V. Scuderi, and A. Tramontana (2013). “Beam handling and transport solutions”. In: *AIP Conference Proceedings*. Vol. 1546. AIP Publishing, pp. 34–43. DOI: 10.1063/1.4816603 (cit. on p. 108).

Maiman, Theodore H. (1960). “Stimulated Optical Radiation in Ruby”. In: *Nature* 187.4736, pp. 493–494. DOI: 10.1038/187493a0 (cit. on p. 10).

Mainfray, G. and G. Manus (1991). “Multiphoton ionization of atoms”. In: *Reports on Progress in Physics* 54.10, p. 1333. ISSN: 0034-4885. DOI: 10.1088/0034-4885/54/10/002 (cit. on p. 15).

Maksimchuk, A., S. Gu, K. Flippo, D. Umstadter, and V. Yu. Bychenkov (2000). “Forward Ion Acceleration in Thin Films Driven by a High-Intensity Laser”. In: *Physical Review Letters* 84.18, pp. 4108–4111. DOI: 10.1103/PhysRevLett.84.4108 (cit. on p. 20).

Malka, Victor, Sven Fritzler, Erik Lefebvre, Emmanuel d’Humières, Régis Ferrand, Georges Grillon, Claude Albaret, Samuel Meyroneinc, Jean-Paul Chambaret, Andre Antonetti, and Danièle Hulin (2004). “Practicability of protontherapy using compact laser systems”. In: *Medical Physics* 31.6, pp. 1587–1592. ISSN: 0094-2405. DOI: 10.1118/1.1747751 (cit. on pp. 7, 134).

Malka, Victor, Jérôme Faure, Yann A. Gauduel, Erik Lefebvre, Antoine Rousse, and Kim Ta Phuoc (2008). “Principles and applications of compact laser–plasma accelerators”. In: *Nature Physics* 4.6, pp. 447–453. ISSN: 1745-2473. DOI: 10.1038/nphys966 (cit. on p. 28).

Manahan, G. G., E. Brunetti, C. Aniculaesei, M. P. Anania, S. Cipiccia, M. R. Islam, D. W. Grant, A. Subiel, R. P. Shanks, R. C. Issac, G. H. Welsh, S. M. Wiggins, and D. A. Jaroszynski (2014). “Characterization of laser-driven single and double electron bunches with a permanent magnet quadrupole triplet and pepper-pot mask”. In: *New Journal of Physics* 16.10, p. 103006. ISSN: 1367-2630. DOI: 10.1088/1367-2630/16/10/103006 (cit. on pp. 103, 104).

Mančić, A., J. Fuchs, P. Antici, S. A. Gaillard, and P. Audebert (2008). “Absolute calibration of photostimulable image plate detectors used as (0.5–20MeV) high-energy proton detectors”. In: *Review of Scientific Instruments* 79.7, p. 073301. ISSN: 0034-6748, 1089-7623. DOI: 10.1063/1.2949388 (cit. on p. 58).

Mančić, A., A. Lévy, M. Harmand, M. Nakatsutsumi, P. Antici, P. Audebert, P. Combis, S. Fourmaux, S. Mazevet, O. Peyrusse, V. Recoules, P. Renaudin, J. Robiche, F. Dorchies, and J. Fuchs (2010). “Picosecond Short-Range Disordering in Isochorically Heated Aluminum at Solid Density”. In: *Physical Review Letters* 104.3, p. 035002. DOI: 10.1103/PhysRevLett.104.035002 (cit. on p. 28).

Margarone, D., J. Krása, L. Giuffrida, A. Picciotto, L. Torrisi, T. Nowak, P. Musumeci, A. Velyhan, J. Prokůpek, L. Láska, T. Mocek, J. Ullschmied, and B. Rus (2011). “Full characterization of laser-accelerated ion beams using Faraday cup, silicon carbide, and single-crystal diamond detectors”. In: *Journal of Applied Physics* 109.10, p. 103302. ISSN: 0021-8979, 1089-7550. DOI: 10.1063/1.3585871 (cit. on p. 69).

Marx, G. (1966). “Interstellar Vehicle Propelled By Terrestrial Laser Beam”. In: *Nature* 211.5044, pp. 22–23. DOI: 10.1038/211022a0 (cit. on p. 25).

Masood, U., M. Bussmann, T. E. Cowan, W. Enghardt, L. Karsch, F. Kroll, U. Schramm, and J. Pawelke (2014). "A compact solution for ion beam therapy with laser accelerated protons". In: *Applied Physics B* 117.1, pp. 41–52. ISSN: 0946-2171, 1432-0649. DOI: 10.1007/s00340-014-5796-z (cit. on p. 7).

McAlister, A. J. and E. A. Stern (1963). "Plasma Resonance Absorption in Thin Metal Films". In: *Physical Review* 132.4, pp. 1599–1602. DOI: 10.1103/PhysRev.132.1599 (cit. on p. 18).

McKenna, P., K. W. D. Ledingham, T. McCanny, R. P. Singhal, I. Spencer, M. I. K. Santala, F. N. Beg, K. Krushelnick, M. Tatarakis, M. S. Wei, E. L. Clark, R. J. Clarke, K. L. Lancaster, P. A. Norreys, K. Spohr, R. Chapman, and M. Zepf (2003). "Demonstration of Fusion-Evaporation and Direct-Interaction Nuclear Reactions using High-Intensity Laser-Plasma-Accelerated Ion Beams". In: *Physical Review Letters* 91.7, p. 075006. DOI: 10.1103/PhysRevLett.91.075006 (cit. on p. 28).

McKenna, P., K. W. D. Ledingham, J. M. Yang, L. Robson, T. McCanny, S. Shimizu, R. J. Clarke, D. Neely, K. Spohr, R. Chapman, R. P. Singhal, K. Krushelnick, M. S. Wei, and P. A. Norreys (2004). "Characterization of proton and heavier ion acceleration in ultrahigh-intensity laser interactions with heated target foils". In: *Physical Review E* 70.3, p. 036405. DOI: 10.1103/PhysRevE.70.036405 (cit. on p. 22).

Meads, P. F. (1983). "A Nonlinear Lens System to Smooth the Intensity Distribution of a Gaussian Beam". In: *IEEE Transactions on Nuclear Science* 30.4, pp. 2838–2840. ISSN: 0018-9499. DOI: 10.1109/TNS.1983.4332972 (cit. on p. 108).

Medin, J., P. Andreo, E. Grusell, O. Mattsson, A. Montelius, and M. Roos (1995). "Ionization chamber dosimetry of proton beams using cylindrical and plane parallel chambers. N w versus N K ion chamber calibrations". In: *Physics in Medicine and Biology* 40.7, p. 1161. ISSN: 0031-9155. DOI: 10.1088/0031-9155/40/7/002 (cit. on p. 118).

Melngailis, J., A. A. Mondelli, Ivan L. Berry Iii, and R. Mohondro (1998). "A review of ion projection lithography". In: *Journal of Vacuum Science & Technology B* 16.3, pp. 927–957. ISSN: 2166-2746, 2166-2754. DOI: 10.1116/1.590052 (cit. on p. 28).

Mijnheer, B. J. (1985). "Variations in response to radiation of a nylon-walled ionization chamber induced by humidity changes". In: *Medical Physics* 12.5, pp. 625–626. ISSN: 0094-2405. DOI: 10.1118/1.595683 (cit. on p. 118).

Miyahara, Junji, Kenji Takahashi, Yoshiyuki Amemiya, Nobuo Kamiya, and Yoshinori Satow (1986). "A new type of X-ray area detector utilizing laser stimulated luminescence". In: *Nuclear Instruments and Methods in Physics Research Section A: Accelerators, Spectrometers, Detectors and Associated Equipment* 246.1, pp. 572–578. ISSN: 0168-9002. DOI: 10.1016/0168-9002(86)90156-7 (cit. on p. 58).

Mora, P. (2003). "Plasma Expansion into a Vacuum". In: *Physical Review Letters* 90.18, p. 185002. DOI: 10.1103/PhysRevLett.90.185002 (cit. on p. 22).

Mourou, Gerard A., Toshiki Tajima, and Sergei V. Bulanov (2006). "Optics in the relativistic regime". In: *Reviews of Modern Physics* 78.2, pp. 309–371. DOI: 10.1103/RevModPhys.78.309 (cit. on p. 20).

Muench, Philip James, Ali S. Meigooni, Ravinder Nath, and William L. McLaughlin (1991). "Photon energy dependence of the sensitivity of radiochromic film and comparison with silver halide film and LiF TLDs used for brachytherapy dosimetry". In: *Medical Physics* 18.4, pp. 769–775. ISSN: 0094-2405. DOI: 10.1118/1.596630 (cit. on p. 58).

Mulser, Peter and Dieter Bauer (2010). *High Power Laser-Matter Interaction*. Vol. 238. Springer Tracts in Modern Physics. Berlin, Heidelberg: Springer Berlin Heidelberg. ISBN: 978-3-540-50669-0 978-3-540-46065-7 (cit. on p. 17).

Murakami, Masao, Yoshio Hishikawa, Satoshi Miyajima, Yoshiko Okazaki, Kenneth L. Sutherland, Mitsuyuki Abe, Sergei V. Bulanov, Hiroyuki Daido, Timur Zh Esirkepov, James Koga,

Mitsuru Yamagiwa, and Toshiki Tajima (2008). "Radiotherapy using a laser proton accelerator". In: *arXiv:0804.3826 [physics]* 1024, pp. 275–300. ISSN: 0094243X. DOI: 10.1063/1.2958203 (cit. on p. 7).

Nagy, Sandor (2009). *Radiochemistry and Nuclear Chemistry - Volume II*. Vol. 2. EOLSS Publications. ISBN: 978-1-84826-127-3 (cit. on p. 38).

Neely, D., P. Foster, A. Robinson, F. Lindau, O. Lundh, A. Persson, C.-G. Wahlström, and P. McKenna (2006). "Enhanced proton beams from ultrathin targets driven by high contrast laser pulses". In: *Applied Physics Letters* 89.2, p. 021502. ISSN: 0003-6951, 1077-3118. DOI: 10.1063/1.2220011 (cit. on p. 49).

Nishiuchi, M., I. Daito, M. Ikegami, H. Daido, M. Mori, S. Orimo, K. Ogura, A. Sagisaka, A. Yogo, A. S. Pirozhkov, et al. (2009). "Focusing and spectral enhancement of a repetition-rated, laser-driven, divergent multi-MeV proton beam using permanent quadrupole magnets". In: *Applied Physics Letters* 94.6, p. 061107. ISSN: 0003-6951, 1077-3118. DOI: 10.1063/1.3078291 (cit. on p. 90).

Nishiuchi, M., H. Sakaki, T. Hori, K. Ogura, A. Yogo, A. S. Pirozhkov, A. Sagisaka, S. Orimo, M. Mori, H. Sugiyama, et al. (2010). "Toward laser driven proton medical accelerator". In: *Journal of Physics: Conference Series* 244.2, p. 022051. ISSN: 1742-6596. DOI: 10.1088/1742-6596/244/2/022051 (cit. on p. 90).

Oksenhendler, T., D. Kaplan, P. Tournois, G. M. Greetham, and F. Estable (2006). "Intracavity acousto-optic programmable gain control for ultra-wide-band regenerative amplifiers". In: *Applied Physics B* 83.4, pp. 491–494. ISSN: 0946-2171, 1432-0649. DOI: 10.1007/s00340-006-2231-0 (cit. on p. 46).

Oksenhendler, T., S. Coudreau, N. Forget, V. Crozatier, S. Grabielle, R. Herzog, O. Gobert, and D. Kaplan (2010). "Self-referenced spectral interferometry". In: *Applied Physics B* 99.1-2, pp. 7–12. ISSN: 0946-2171, 1432-0649. DOI: 10.1007/s00340-010-3916-y (cit. on p. 52).

Ottevaere, H., B. Volckaerts, J. Lamprecht, J. Schwider, A. Hermanne, I. Veretennicoff, and H. Thienpont (2002). "Two-dimensional plastic microlens arrays by deep lithography with protons: fabrication and characterization". In: *Journal of Optics A: Pure and Applied Optics* 4.4, S22. ISSN: 1464-4258. DOI: 10.1088/1464-4258/4/4/354 (cit. on p. 28).

Paganetti, Harald (2011). *Proton Therapy Physics*. CRC Press. ISBN: 978-1-4398-3645-3 (cit. on p. 117).

— (2014). "Relative biological effectiveness (RBE) values for proton beam therapy. Variations as a function of biological endpoint, dose, and linear energy transfer". In: *Physics in Medicine and Biology* 59.22, R419. ISSN: 0031-9155. DOI: 10.1088/0031-9155/59/22/R419 (cit. on p. 41).

Passoni, M. and M. Lontano (2004). "One-dimensional model of the electrostatic ion acceleration in the ultraintense laser–solid interaction". In: *Laser and Particle Beams* 22.02, pp. 163–169. ISSN: 1469-803X. DOI: 10.1017/S026303460422211X (cit. on p. 21).

Patel, P. K., A. J. Mackinnon, M. H. Key, T. E. Cowan, M. E. Foord, M. Allen, D. F. Price, H. Ruhl, P. T. Springer, and R. Stephens (2003). "Isochoric Heating of Solid-Density Matter with an Ultrafast Proton Beam". In: *Physical Review Letters* 91.12, p. 125004. DOI: 10.1103/PhysRevLett.91.125004 (cit. on p. 78).

Paterson, I. J., R. J. Clarke, N. C. Woolsey, and G. Gregori (2008). "Image plate response for conditions relevant to laser–plasma interaction experiments". In: *Measurement Science and Technology* 19.9, p. 095301. ISSN: 0957-0233. DOI: 10.1088/0957-0233/19/9/095301 (cit. on p. 58).

Petrov, G. M. and J. Davis (2009). "Laser acceleration of light ions from high-intensity laser-target interactions". In: *Applied Physics B* 96.4, pp. 773–779. ISSN: 0946-2171, 1432-0649. DOI: 10.1007/s00340-009-3624-7 (cit. on p. 20).

Pfotenhauer, S. M., O. Jäckel, A. Sachtleben, J. Polz, W. Ziegler, H.-P. Schlenvoigt, K.-U. Amthor, M. C. Kaluza, K. W. D. Ledingham, R. Sauerbrey, P. Gibbon, A. P. L. Robinson, and H. Schwoerer (2008). "Spectral shaping of laser generated proton beams". In: *New Journal of Physics* 10.3, p. 033034. ISSN: 1367-2630. DOI: 10.1088/1367-2630/10/3/033034 (cit. on p. 78).

Podhorecka, Monika, Andrzej Skladanowski, and Przemyslaw Bozko (2010). "H2AX Phosphorylation: Its Role in DNA Damage Response and Cancer Therapy". In: *Journal of Nucleic Acids* 2010, e920161. ISSN: , DOI: 10.4061/2010/920161 (cit. on p. 37).

Pommarel, Loann, Benjamin Vauzour, Frédérique Mégnin-Chanet, Emilie Bayart, Olivier Delmas, Farid Goudjil, Catherine Nauraye, Virgile Letellier, Frédéric Pouzoulet, Francesco Schillaci, Francesco Romano, Valentina Scuderi, G. A. Pablo Cirrone, Eric Deutsch, Alessandro Flacco, and Victor Malka (2017). "Spectral and spatial shaping of a laser-produced ion beam for radiation-biology experiments". In: *Physical Review Accelerators and Beams* 20.2 (cit. on p. 118).

Ponette, V., C. Le Péchoux, E. Deniaud-Alexandre, M. Fernet, N. Giocanti, H. Tourbez, and V. Favaudon (2000). "Hyperfast, early cell response to ionizing radiation". In: *International Journal of Radiation Biology* 76.9, pp. 1233–1243. ISSN: 0955-3002, 1362-3095. DOI: 10.1080/09553000050134465 (cit. on pp. 128, 130).

Pukhov, A. and J. Meyer-Ter-Vehn (1997). "Laser Hole Boring into Overdense Plasma and Relativistic Electron Currents for Fast Ignition of ICF Targets". In: *Physical Review Letters* 79.14, pp. 2686–2689. DOI: 10.1103/PhysRevLett.79.2686 (cit. on p. 17).

Rajta, I., I. Gómez-Morilla, M. H. Abraham, and Á. Z. Kiss (2003). "Proton beam micromachining on PMMA, Foturan and CR-39 materials". In: *Nuclear Instruments and Methods in Physics Research Section B: Beam Interactions with Materials and Atoms*. 8th International Conference of Nuclear Microprobe Technology and Applications 210, pp. 260–265. ISSN: 0168-583X. DOI: 10.1016/S0168-583X(03)01025-5 (cit. on p. 28).

Rax, Jean-Marcel (2005). *Physique des plasmas: cours et applications*. Dunod. ISBN: Paper 978-2-10-007250-7 ; ebook 9782100527878 (cit. on p. 17).

Rhee, M. J. (1984). "Compact Thomson spectrometer". In: *Review of Scientific Instruments* 55.8, pp. 1229–1234. ISSN: 0034-6748, 1089-7623. DOI: 10.1063/1.1137927 (cit. on p. 54).

Rogakou, Emmy P., Duane R. Pilch, Ann H. Orr, Vessela S. Ivanova, and William M. Bonner (1998). "DNA Double-stranded Breaks Induce Histone H2AX Phosphorylation on Serine 139". In: *Journal of Biological Chemistry* 273.10, pp. 5858–5868. ISSN: 0021-9258, 1083-351X. DOI: 10.1074/jbc.273.10.5858 (cit. on p. 37).

Rossbach, J and Schmüser, P (1994). "Basic course on accelerator optics - CERN Document Server". In: *CAS - CERN Accelerator School : 5th General Accelerator Physics Course, Jyväskylä, Finland, 7 - 18 Sep 1992, pp.17-88 (CERN-1994-001)*. Accelerators and Storage Rings. DOI: 10.5170/CERN-1994-001.17 (cit. on p. 77).

Roth, M., T. E. Cowan, M. H. Key, S. P. Hatchett, C. Brown, W. Fountain, J. Johnson, D. M. Pennington, R. A. Snavely, S. C. Wilks, K. Yasuike, H. Ruhl, F. Pegoraro, S. V. Bulanov, E. M. Campbell, M. D. Perry, and H. Powell (2001). "Fast Ignition by Intense Laser-Accelerated Proton Beams". In: *Physical Review Letters* 86.3, pp. 436–439. DOI: 10.1103/PhysRevLett.86.436 (cit. on p. 28).

Roth, M., M. Allen, P. Audebert, A. Blazevic, E. Brambrink, T. E. Cowan, J. Fuchs, J.-C. Gauthier, M. Geißel, M Hegelich, S. Karsch, J. Meyer-ter-Vehn, H. Ruhl, T. Schlegel, and R. B. Stephens (2002). "The generation of high-quality, intense ion beams by ultra-intense lasers". In: *Plasma Physics and Controlled Fusion* 44.12B, B99. ISSN: 0741-3335. DOI: 10.1088/0741-3335/44/12B/308 (cit. on p. 22).

Rygg, J. R., F. H. Séguin, C. K. Li, J. A. Frenje, M. J.-E. Manuel, R. D. Petrasso, R. Betti, J. A. Delettrez, O. V. Gotchev, J. P. Knauer, D. D. Meyerhofer, F. J. Marshall, C. Stoeckl, and W. Theobald (2008). "Proton Radiography of Inertial Fusion Implosions". In: *Science* 319.5867,

pp. 1223–1225. ISSN: 0036-8075, 1095-9203. DOI: 10.1126/science.1152640 (cit. on p. 28).

Sakaki, Hironao, Mamiko Nishiuchi, Toshihiko Hori, Paul R. Bolton, Motonobu Tampo, Akifumi Yogo, Kiminori Kondo, Shunichi Kawanishi, Hiroshi Iwase, and Koji Niita (2010). "Simulation of Laser-Accelerated Proton Focusing and Diagnosis with a Permanent Magnet Quadrupole Triplet". In: *Plasma and Fusion Research* 5, pp. 009–009. ISSN: 1880-6821. DOI: 10.1585/pfr.5.009 (cit. on p. 80).

Sarkisov, G. S., V. Yu. Bychenkov, V. N. Novikov, V. T. Tikhonchuk, A. Maksimchuk, S.-Y. Chen, R. Wagner, G. Mourou, and D. Umstadter (1999). "Self-focusing, channel formation, and high-energy ion generation in interaction of an intense short laser pulse with a He jet". In: *Physical Review E* 59.6, pp. 7042–7054. DOI: 10.1103/PhysRevE.59.7042 (cit. on p. 20).

Schell, S. and J. J. Wilkens (2009). "Modifying proton fluence spectra to generate spread-out Bragg peaks with laser accelerated proton beams". In: *Physics in Medicine and Biology* 54.19, N459. ISSN: 0031-9155. DOI: 10.1088/0031-9155/54/19/N04 (cit. on p. 134).

Schell, Stefan and Jan J. Wilkens (2010). "Advanced treatment planning methods for efficient radiation therapy with laser accelerated proton and ion beams". In: *Medical Physics* 37.10, pp. 5330–5340. ISSN: 0094-2405. DOI: 10.1118/1.3491406 (cit. on p. 135).

Schillaci, F., G. A. P. Cirrone, G. Cuttone, M. Maggiore, L. Andó, A. Amato, M. Costa, G. Gallo, G. Korn, G. Larosa, R. Leanza, R. Manna, D. Margarone, G. Milluzzo, S. Pulvirenti, F. Romano, S. Salamone, M. Sedita, V. Scuderi, and A. Tramontana (2015a). "Design of the ELIMAIA ion collection system". In: *Journal of Instrumentation* 10.12, T12001. ISSN: 1748-0221. DOI: 10.1088/1748-0221/10/12/T12001 (cit. on pp. 78, 108).

Schillaci, F., M. Maggiore, D. Rifuggiato, G. A. P. Cirrone, G. Cuttone, and D. Giove (2015b). "Errors and optics study of a permanent magnet quadrupole system". In: *Journal of Instrumentation* 10.05, T05001. ISSN: 1748-0221. DOI: 10.1088/1748-0221/10/05/T05001 (cit. on pp. 78–80, 90).

Schillaci, F., L. Pommarel, F. Romano, G. Cuttone, M. Costa, D. Giove, M. Maggiore, A. D. Russo, V. Scuderi, Malka, V., B. Vauzour, A. Flacco, and G. A. P. Cirrone (2016). "Characterization of the ELIMED Permanent Magnets Quadrupole system prototype with laser-driven proton beams". In: *Journal of Instrumentation* 11.07, T07005. ISSN: 1748-0221. DOI: 10.1088/1748-0221/11/07/T07005 (cit. on p. 87).

Schlessinger, L. and J. Wright (1979). "Inverse-bremsstrahlung absorption rate in an intense laser field". In: *Physical Review A* 20.5, pp. 1934–1945. DOI: 10.1103/PhysRevA.20.1934 (cit. on p. 18).

Schollmeier, M., S. Becker, M. Geißel, K. A. Flippo, A. Blažević, S. A. Gaillard, D. C. Gautier, F. Grüner, K. Harres, M. Kimmel, F. Nürnberg, P. Rambo, U. Schramm, J. Schreiber, J. Schütrumpf, J. Schwarz, N. A. Tahir, B. Atherton, D. Habs, B. M. Hegelich, and M. Roth (2008). "Controlled Transport and Focusing of Laser-Accelerated Protons with Miniature Magnetic Devices". In: *Physical Review Letters* 101.5, p. 055004. DOI: 10.1103/PhysRevLett.101.055004 (cit. on p. 80).

Schreiber, J., F. Bell, F. Grüner, U. Schramm, M. Geissler, M. Schnürer, S. Ter-Avetisyan, B. M. Hegelich, J. Cobble, E. Brambrink, J. Fuchs, P. Audebert, and D. Habs (2006). "Analytical Model for Ion Acceleration by High-Intensity Laser Pulses". In: *Physical Review Letters* 97.4, p. 045005. DOI: 10.1103/PhysRevLett.97.045005 (cit. on pp. 21, 23).

Schwoerer, H., S. Pfotenhauer, O. Jäckel, K.-U. Amthor, B. Liesfeld, W. Ziegler, R. Sauerbrey, K. W. D. Ledingham, and T. Esirkepov (2006). "Laser-plasma acceleration of quasi-monoenergetic protons from microstructured targets". In: *Nature* 439.7075, pp. 445–448. ISSN: 0028-0836. DOI: 10.1038/nature04492 (cit. on p. 23).

Scuderi, V., S. Bijan Jia, M. Carpinelli, G. A. P. Cirrone, G. Cuttone, G. Korn, T. Licciardello, M. Maggiore, D. Margarone, P. Pisciotta, F. Romano, F. Schillaci, C. Stancampiano, and A. Tramontana (2014). "Development of an energy selector system for laser-driven proton beam

applications". In: *Nuclear Instruments and Methods in Physics Research Section A: Accelerators, Spectrometers, Detectors and Associated Equipment*. Proceedings of the first European Advanced Accelerator Concepts Workshop 2013 740, pp. 87–93. ISSN: 0168-9002. DOI: 10.1016/j.nima.2013.10.037 (cit. on p. 81).

Sekine, M., S. Ikeda, M. Romanelli, M. Kumaki, Y. Fuwa, T. Kanesue, N. Hayashizaki, R. Lambiase, and M. Okamura (2015). "Plasma shape control by pulsed solenoid on laser ion source". In: *Nuclear Instruments and Methods in Physics Research Section A: Accelerators, Spectrometers, Detectors and Associated Equipment* 795, pp. 151–155. DOI: http://dx.doi.org/10.1016/j.nima.2015.05.030 (cit. on p. 77).

Sentoku, Y., T. E. Cowan, A. Kemp, and H. Ruhl (2003). "High energy proton acceleration in interaction of short laser pulse with dense plasma target". In: *Physics of Plasmas (1994-present)* 10.5, pp. 2009–2015. ISSN: 1070-664X, 1089-7674. DOI: 10.1063/1.1556298 (cit. on p. 25).

Sentoku, Y., V. Y. Bychenkov, K. Flippo, A. Maksimchuk, K. Mima, G. Mourou, Z. M. Sheng, and D. Umstadter (2014). "High-energy ion generation in interaction. of short laser pulse with high-density plasma". In: *Applied Physics B* 74.3, pp. 207–215. ISSN: 0946-2171, 1432-0649. DOI: 10.1007/s003400200796 (cit. on p. 17).

Shapiro, Jacob (2002). *Radiation Protection: A Guide for Scientists, Regulators, and Physicians*. La Editorial, UPR. ISBN: 978-0-674-00740-6 (cit. on p. 32).

Short, Susan C., Christine Martindale, Sara Bourne, Geoff Brand, Mick Woodcock, and Peter Johnston (2007). "DNA repair after irradiation in glioma cells and normal human astrocytes". In: *Neuro-Oncology* 9.4, pp. 404–411. ISSN: 1522-8517. DOI: 10.1215/15228517-2007-030 (cit. on p. 124).

Sigmund, Peter (2006). *Particle Penetration and Radiation Effects: General Aspects and Stopping of Swift Point Charges*. Springer Science & Business Media. ISBN: 978-3-540-31718-0 (cit. on p. 31).

Silva, Luís O., Michael Marti, Jonathan R. Davies, Ricardo A. Fonseca, Chuang Ren, Frank S. Tsung, and Warren B. Mori (2004). "Proton Shock Acceleration in Laser-Plasma Interactions". In: *Physical Review Letters* 92.1, p. 015002. DOI: 10.1103/PhysRevLett.92.015002 (cit. on p. 25).

Smith, David P. (1971). "Analysis of surface composition with low-energy backscattered ions". In: *Surface Science* 25.1, pp. 171–191. ISSN: 0039-6028. DOI: 10.1016/0039-6028(71)90214-7 (cit. on p. 28).

Snavely, R. A., M. H. Key, S. P. Hatchett, T. E. Cowan, M. Roth, T. W. Phillips, M. A. Stoyer, E. A. Henry, T. C. Sangster, M. S. Singh, S. C. Wilks, A. MacKinnon, A. Offenberger, D. M. Pennington, K. Yasuike, A. B. Langdon, B. F. Lasinski, J. Johnson, M. D. Perry, and E. M. Campbell (2000). "Intense High-Energy Proton Beams from Petawatt-Laser Irradiation of Solids". In: *Physical Review Letters* 85.14, pp. 2945–2948. DOI: 10.1103/PhysRevLett.85.2945 (cit. on p. 20).

Spitzer, Lyman and Richard Härm (1953). "Transport Phenomena in a Completely Ionized Gas". In: *Physical Review* 89.5, pp. 977–981. DOI: 10.1103/PhysRev.89.977 (cit. on p. 18).

Sprawls, Perry (1995). *The Physical Principles of Medical Imaging*. 2nd Ed. Medical Physics Pub Corp. ISBN: ISBN-10: 0944838545, ISBN-13: 978-0944838549 (cit. on p. 32).

Strickland, Donna and Gerard Mourou (1985). "Compression of amplified chirped optical pulses". In: *Optics Communications* 56.3, pp. 219–221. ISSN: 0030-4018. DOI: 10.1016/0030-4018(85)90120-8 (cit. on p. 13).

Svelto, Orazio (2010). *Principles of Lasers*. 5th Edition. Springer US. ISBN: Hardcover 978-1-4419-1301-2, eBook 978-1-4419-1302-9 (cit. on p. 11).

Szydlowski, A., J. Badziak, J. Fuchs, M. Kubkowska, P. Parys, M. Rosinski, R. Suchanska, J. Wolowski, P. Antici, and A. Mancic (2009). "Application of solid-state nuclear track detectors of the CR-39/PM-355 type for measurements of energetic protons emitted from plasma produced by an ultra-intense laser". In: *Radiation Measurements*. Proceedings of the 24th

International Conferenceon Nuclear Tracks in Solids 44.9–10, pp. 881–884. ISSN: 1350-4487. DOI: 10.1016/j.radmeas.2009.08.008 (cit. on p. 57).

Tajima, Toshiki, Dietrich Habs, and Xueqing Yan (2009). "Laser Acceleration of Ions for Radiation Therapy". In: *Reviews of Accelerator Science and Technology* 02.01, pp. 201–228. ISSN: 1793-6268. DOI: 10.1142/S1793626809000296 (cit. on p. 134).

Thomson, Joseph John (1911). "XXVI. Rays of positive electricity". In: *Philosophical Magazine Series 6* 21.122, pp. 225–249. ISSN: 1941-5982. DOI: 10.1080/14786440208637024 (cit. on p. 54).

Toncian, Toma, Marco Borghesi, Julien Fuchs, Emmanuel d'Humières, Patrizio Antici, Patrick Audebert, Erik Brambrink, Carlo Alberto Cecchetti, Ariane Pipahl, Lorenzo Romagnani, and Oswald Willi (2006). "Ultrafast Laser-Driven Microlens to Focus and Energy-Select Mega-Electron Volt Protons". In: *Science* 312.5772, pp. 410–413. ISSN: 0036-8075, 1095-9203. DOI: 10.1126/science.1124412 (cit. on p. 78).

Torudd, J., M. Protopopova, R. Sarimov, J. Nygren, S. Eriksson, E. Marková, M. Chovanec, G. Selivanova, and I. Y. Belyaev (2005). "Dose-response for radiation-induced apoptosis, residual 53BP1 foci and DNA-loop relaxation in human lymphocytes". In: *International Journal of Radiation Biology* 81.2, pp. 125–138. ISSN: 0955-3002. DOI: 10.1080/09553000500077211 (cit. on p. 124).

Tournois, Pierre (1997). "Acousto-optic programmable dispersive filter for adaptive compensation of group delay time dispersion in laser systems". In: *Optics Communications* 140.4, pp. 245–249. ISSN: 0030-4018. DOI: 10.1016/S0030-4018(97)00153-3 (cit. on p. 46).

Tsoupas, N., R. Lankshear, CL Jr Snead, T. E. Ward, M. Zucker, and H. A. Enge (1991). "Uniform beam distributions using octupoles". In: *Conference Record of the 1991 IEEE Particle Accelerator Conference*. San Francisco, California, USA: IEEE, p. 1695. ISBN: 0-7803-0135-8. DOI: 10.1109/PAC.1991.164748 (cit. on p. 108).

Tubiana, M. (2008). *Radiobiologie: radiothérapie et radioprotection : bases fondamentales*. 3rd ed. Hermann. ISBN: 978-2-7056-7810-4 (cit. on p. 41).

Tuvè, C., M. Angelone, V. Bellini, A. Balducci, M. G. Donato, G. Faggio, M. Marinelli, G. Messina, E. Milani, M. E. Morgada, M. Pillon, R. Potenza, G. Pucella, G. Russo, S. Santangelo, M. Scoccia, C. Sutera, A. Tucciarone, and G. Verona-Rinati (2007). "Single crystal diamond detectors grown by chemical vapor deposition". In: *Nuclear Instruments and Methods in Physics Research Section A: Accelerators, Spectrometers, Detectors and Associated Equipment*. Proceedings of the 7th International Conference on Large Scale Applications and Radiation Hardness of Semiconductor Detectors 570.2, pp. 299–302. ISSN: 0168-9002. DOI: 10.1016/j.nima.2006.09.043 (cit. on p. 69).

Volpe, L., R. Jafer, B. Vauzour, Ph Nicolai, J. J. Santos, F. Dorchies, C. Fourment, S. Hulin, C. Regan, F. Perez, et al. (2011). "Proton radiography of cylindrical laser-driven implosions". In: *Plasma Physics and Controlled Fusion* 53.3, p. 032003. ISSN: 0741-3335. DOI: 10.1088/0741-3335/53/3/032003 (cit. on p. 28).

Vynckier, S., D. E. Bonnett, and D. T. L. Jones (1991). "Code of practice for clinical proton dosimetry". In: *Radiotherapy and Oncology* 20.1, pp. 53–63. ISSN: 0167-8140. DOI: 10.1016/0167-8140(91)90112-T (cit. on p. 118).

Wagner, F., O. Deppert, C. Brabetz, P. Fiala, A. Kleinschmidt, P. Poth, V. A. Schanz, A. Tebartz, B. Zielbauer, M. Roth, T. Stöhlker, and V. Bagnoud (2016). "Maximum Proton Energy above 85 MeV from the Relativistic Interaction of Laser Pulses with Micrometer Thick ${\mathrm{CH}}_{2}$ Targets". In: *Physical Review Letters* 116.20, p. 205002. DOI: 10.1103/PhysRevLett.116.205002 (cit. on p. 23).

Wiedemann, Helmut (2007). *Particle Accelerator Physics*. Springer Science & Business Media. ISBN: 978-3-540-49045-6 (cit. on pp. 75, 76).

Wilks, S. C., W. L. Kruer, M. Tabak, and A. B. Langdon (1992). "Absorption of ultra-intense laser pulses". In: *Physical Review Letters* 69.9, pp. 1383–1386. DOI: 10.1103/PhysRevLett.69.1383 (cit. on p. 17).

Wilks, S. C., A. B. Langdon, T. E. Cowan, M. Roth, M. Singh, S. Hatchett, M. H. Key, D. Pennington, A. MacKinnon, and R. A. Snavely (2001). "Energetic proton generation in ultra-intense laser–solid interactions". In: *Physics of Plasmas (1994-present)* 8.2, pp. 542–549. ISSN: 1070-664X, 1089-7674. DOI: 10.1063/1.1333697 (cit. on pp. 20, 22).

Wille, Klaus (2000). *The Physics of Particle Accelerators: An Introduction*. Oxford University Press. ISBN: 978-0-19-850549-5 (ISBN-10: 0198505493 ; 0198505507, 9780198505501) (cit. on pp. 74, 76).

Yamanaka, C., T. Yamanaka, T. Sasaki, K. Yoshida, M. Waki, and H. B. Kang (1972). "Anomalous Heating of a Plasma by a Laser". In: *Physical Review A* 6.6, pp. 2335–2342. DOI: 10.1103/PhysRevA.6.2335 (cit. on p. 20).

Yan, X. Q., C. Lin, Z. M. Sheng, Z. Y. Guo, B. C. Liu, Y. R. Lu, J. X. Fang, and J. E. Chen (2008). "Generating High-Current Monoenergetic Proton Beams by a CircularlyPolarized Laser Pulse in the Phase-StableAcceleration Regime". In: *Physical Review Letters* 100.13, p. 135003. DOI: 10.1103/PhysRevLett.100.135003 (cit. on p. 26).

Yang, J. M., P. McKenna, K. W. D. Ledingham, T. McCanny, S. Shimizu, L. Robson, R. J. Clarke, D. Neely, P. A. Norreys, M.-S. Wei, K. Krushelnick, P. Nilson, S. P. D. Mangles, and R. P. Singhal (2004). "Nuclear reactions in copper induced by protons from a petawatt laser-foil interaction". In: *Applied Physics Letters* 84.5, pp. 675–677. ISSN: 0003-6951, 1077-3118. DOI: 10.1063/1.1645314 (cit. on p. 28).

Yashkin, Pavel N., Dimitry I. Silin, Vladmir A. Zolotov, Valery I. Kostjuchenko, Dimitry F. Nichiporov, Tatiana P. Feoktistova, Kyrill S. Martirosov, Yelizaveta I. Minakova, Vladimir S. Khoroshkov, Pavel B. Polonski, and Ludmila V. Zinovyeva (1995). "Relative biological effectiveness of proton medical beam at Moscow synchrotron determined by the Chinese hamster cells assay". In: *International Journal of Radiation Oncology*Biology*Physics* 31.3, pp. 535–540. ISSN: 0360-3016. DOI: 10.1016/0360-3016(94)00381-T (cit. on p. 128).

Yin, L., B. J. Albright, B. M. Hegelich, and J. C. Fernández (2006). "GeV laser ion acceleration from ultrathin targets: The laser break-out afterburner". In: *Laser and Particle Beams* 24.02, pp. 291–298. ISSN: 1469-803X. DOI: 10.1017/S0263034606060459 (cit. on p. 27).

Yin, L., B. J. Albright, B. M. Hegelich, K. J. Bowers, K. A. Flippo, T. J. T. Kwan, and J. C. Fernández (2007). "Monoenergetic and GeV ion acceleration from the laser breakout afterburner using ultrathin targets". In: *Physics of Plasmas (1994-present)* 14.5, p. 056706. ISSN: 1070-664X, 1089-7674. DOI: 10.1063/1.2436857 (cit. on p. 27).

Yogo, A., K. Sato, M. Nishikino, M. Mori, T. Teshima, H. Numasaki, M. Murakami, Y. Demizu, S. Akagi, S. Nagayama, et al. (2009). "Application of laser-accelerated protons to the demonstration of DNA double-strand breaks in human cancer cells". In: *Applied Physics Letters* 94.18, p. 181502. ISSN: 0003-6951, 1077-3118. DOI: 10.1063/1.3126452 (cit. on p. 8).

Yogo, A., T. Maeda, T. Hori, H. Sakaki, K. Ogura, M. Nishiuchi, A. Sagisaka, P. R. Bolton, M. Murakami, S. Kawanishi, and K. Kondo (2011a). "Development of laser-driven quasi-monoenergetic proton beam line for radiobiology". In: *Nuclear Instruments and Methods in Physics Research Section A: Accelerators, Spectrometers, Detectors and Associated Equipment* 653.1, pp. 189–192. ISSN: 0168-9002. DOI: 10.1016/j.nima.2010.12.016 (cit. on p. 81).

Yogo, A., T. Maeda, T. Hori, H. Sakaki, K. Ogura, M. Nishiuchi, A. Sagisaka, H. Kiriyama, H. Okada, S. Kanazawa, T. Shimomura, Y. Nakai, M. Tanoue, F. Sasao, P. R. Bolton, M. Murakami, T. Nomura, S. Kawanishi, and K. Kondo (2011b). "Measurement of relative biological effectiveness of protons in human cancer cells using a laser-driven quasimonoenergetic proton beamline". In: *Applied Physics Letters* 98.5, p. 053701. ISSN: 0003-6951, 1077-3118. DOI: 10.1063/1.3551623 (cit. on p. 116).

Yoo, Seung Hoon, Ilsung Cho, Sungho Cho, Yongkeun Song, Won-Gyun Jung, Dae-Hyun Kim, Dongho Shin, Se Byeong Lee, Ki-Hong Pae, and Sung Yong Park (2014). "Effective generation of the spread-out-Bragg peak from the laser accelerated proton beams using a carbon–proton mixed target". In: *Australasian Physical & Engineering Sciences in Medicine* 37.4, pp. 635–644. ISSN: 0158-9938, 1879-5447. DOI: 10.1007/s13246-014-0292-7 (cit. on p. 134).

Young, P. E., G. Guethlein, S. C. Wilks, J. H. Hammer, W. L. Kruer, and K. G. Estabrook (1996). "Fast Ion Production by Laser Filamentation in Laser-Produced Plasmas". In: *Physical Review Letters* 76.17, pp. 3128–3131. DOI: 10.1103/PhysRevLett.76.3128 (cit. on p. 20).

Zeil, K., M. Baumann, E. Beyreuther, T. Burris-Mog, T. E. Cowan, W. Enghardt, L. Karsch, S. D. Kraft, L. Laschinsky, J. Metzkes, D. Naumburger, M. Oppelt, C. Richter, R. Sauerbrey, M. Schürer, U. Schramm, and J. Pawelke (2012). "Dose-controlled irradiation of cancer cells with laser-accelerated proton pulses". In: *Applied Physics B* 110.4, pp. 437–444. ISSN: 0946-2171, 1432-0649. DOI: 10.1007/s00340-012-5275-3 (cit. on pp. 8, 116, 134).

Zepf, M., E. L. Clark, F. N. Beg, R. J. Clarke, A. E. Dangor, A. Gopal, K. Krushelnick, P. A. Norreys, M. Tatarakis, U. Wagner, and M. S. Wei (2003). "Proton Acceleration from High-Intensity Laser Interactions with Thin Foil Targets". In: *Physical Review Letters* 90.6, p. 064801. DOI: 10.1103/PhysRevLett.90.064801 (cit. on p. 20).

Zhang, Min (1996). "Emittance formula for slits and pepper-pot measurement". In: *Fermilab-TM-1988, October* (cit. on p. 107).

Zhao, Kun, Qi Zhang, Michael Chini, Yi Wu, Xiaowei Wang, and Zenghu Chang (2012). "Tailoring a 67 attosecond pulse through advantageous phase-mismatch". In: *Optics Letters* 37.18, pp. 3891–3893. ISSN: 1539-4794. DOI: 10.1364/OL.37.003891 (cit. on p. 10).

Zhu, Lijun, Pang-Chen Sun, Dirk-Uwe Bartsch, William R. Freeman, and Yeshaiahu Fainman (1999). "Wave-front generation of Zernike polynomial modes with a micromachined membrane deformable mirror". In: *Applied Optics* 38.28, pp. 6019–6026. ISSN: 0003-6935, 1539-4522. DOI: 10.1364/AO.38.006019 (cit. on p. 52).

université PARIS-SACLAY

ÉCOLE DOCTORALE
Ondes et Matière
(EDOM)

Titre : Transport et contrôle de faisceaux de protons accélérés par laser pour une application à la radiobiologie

Mots-clefs : *Accélération de Protons, Interaction Laser Plasma, Transport de Faisceau, Dosimétrie, Expérience de Radiobiologie*

Résumé : L'accélération de particules par interaction laser-plasma est une alternative prometteuse aux accélérateurs conventionnels qui permettrait de rendre plus compactes les machines du futur dédiées à la protonthérapie. Des champs électriques extrêmes de l'ordre du TV/m sont créés en focalisant une impulsion laser ultra-intense sur une cible solide mince de quelques micromètres d'épaisseur, ce qui produit un faisceau de particules de haute énergie. Ce dernier contient des protons ayant une énergie allant jusqu'à la dizaine de mégaélectron-volts, et est caractérisé par une forte divergence angulaire et un spectre en énergie très étendu.

Le but de cette thèse est de caractériser parfaitement un accélérateur laser-plasma afin de produire un faisceau de protons stable, satisfaisant les critères d'énergie, de charge et d'homogénéité de surface requis pour son utilisation en radiobiologie. La conception, la réalisation et l'implé-mentation d'un système magnétique, constitué d'aimants permanents quadripolaires ont été optimisés au préalable avec des simulations numériques.

Ce système permet d'obtenir un faisceau de protons ayant un spectre en énergie qui à été mise en forme, et dont le profil est uniforme sur une surface de taille adaptée aux échantillons biologiques.

Une dosimétrie absolue et en ligne a également été établie, permettant le contrôle de la dose délivrée en sortie. Pour cela, une chambre d'ionisation à transmission, précédemment calibrée sur un accélérateur à usage médical de type cyclotron, a été mise en place sur le trajet du faisceau de protons. Des simulations Monte Carlo ont ensuite permis de calculer la dose déposée dans les échantillons. Ce système compact autorise maintenant de définir un protocole expérimental rigoureux pour la poursuite d'expériences in vitro de radiobiologie. De premières irradiations de cellules cancéreuses ont été ainsi réalisées in vitro, ouvrant la voie à l'exploration des effets de rayonnements ionisants pulsés à haut débit de dose sur les cellules vivantes.

Title : Transport and control of a laser-accelerated proton beam for application to radiobiology

Keywords : *Proton Acceleration, Laser Plasma Interaction, Beam Transport, Dosimetry, Radiobiology Experiment*

Summary : Particle acceleration by laser-plasma interaction is a promising alternative to conventional accelerators that could make future devices dedicated to protontherapy more compact. Extreme electric fields in the order of TV/m are created when an ultra-intense laser pulse is focused on a thin solid target with a thickness of a few micrometers, which generates a beam of highly energetic particles. The latter includes protons with energies up to about ten megaelectron-volts and characterised by a wide angular divergence and a broad energy spectrum.

The goal of this thesis is to fully characterise a laser-based accelerator in order to produce a stable proton beam meeting the energy, charge and surface homogeneity requirements for radiobiological experiments. The design, realisation and implementation of a magnetic system made of permanent magnet quadrupoles were optimised beforehand through numerical simulations. It enables to obtain a beam with a shaped energy spectrum and with a uniform profile over a surface with a size adapted to the biological samples.

Deferred and online dosimetry was setup to monitor the delivered output dose. For that purpose, a transmission ionisation chamber, previously calibrated absolutely on a medical proton accelerator, was used. Monte Carlo simulations enabled to compute the dose deposited into the samples. This compact system allows now to define a rigorous experimental protocol for in vitro radiobiological experiments. First experiments of cancer cell irradiation have been carried out, paving the way for the exploration of the effects of pulsed ionizing radiations at extremely high dose rates on living cells.

Université Paris-Saclay
Espace Technologique / Immeuble Discovery
Route de l'Orme aux Merisiers RD 128 / 91190 Saint-Aubin, France